# HYPERFINE INTERACTION STUDIES USING LOW TEMPERATURE NUCLEAR ORIENTATION

- by -

P. D. JOHNSTON

Pembroke College, Oxford

A Thesis submitted for the degree of Doctor of Philosophy, September 1972

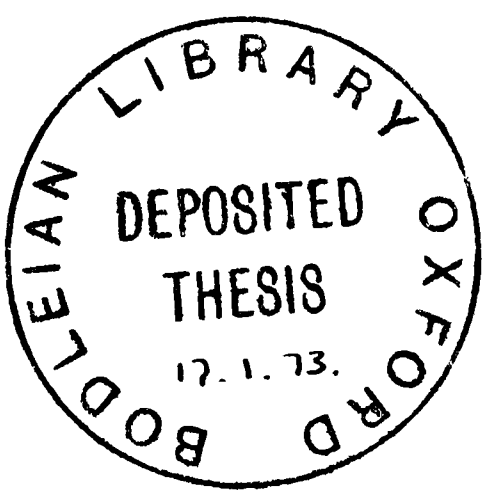


Table of Contents


Abstract

Chapter 1: Nuclear Orientation and Nuclear Magnetic Resonance

1.1 Introduction ..... 1
1.2 The hyperfine Interaction ..... 2
1.3 Nuclear Orientation ..... 6
1.4 Nuclear Magnetic Resonance on oriented nuclei .....12

Chapter 2: The Experimental Method

2.1 Introduction .....31
2.2 The adiabatic demagnetisation apparatus .....32
2.3 Radio frequency apparatus .....40
2.4 Detectors and counting equipment .....42
2.5 Thermometry .....48
2.6 The Resonance Method .....50
2.7 Typical resonance measurements on simple systems $\underline{Fe}^{60}Co$; $\underline{Co}^{60}Co$; and $\underline{Fe}^{96}Tc$ .....53
2.8 Conclusion .....62

Chapter 3: Nuclear orientation and nuclear magnetic resonance of $\underline{^{110}Ag^{m}}$ in iron and nickel .

3.1 Introduction .....63
3.2 Sample preparation for alloys of $^{110}Ag^{m}$ in iron and nickel ...
a) Preparation of alloys for conventional nuclear orientation .....65
b) Preparation of thin foil samples for resonance .....66
3.3 N.M.R./O.N. measurements in Fe and Ni .....68
3.4 Comparison of the nuclear orientation results on several alloys .....73
3.5 Nuclear orientation measurements on $^{110}Ag^{m}$ in iron ....75
3.6 Comparison of the M1/E2 mixing ratios with other experimental results.....94
3.7 The excited state structure of $^{110}Cd$ .....98

Chapter 3(a)

3.8 Nuclear orientation of $^{109}Cd$ and $^{109}Ag^{m}$ in nickel ... 99
3.9 Nuclear orientation measurements .....100
3.10 Discussion of the relaxation measurement .....103

Chapter 4: Theoretical models for the interaction of impurities with the ferromagnetic host electrons

4.1 Introduction .....105
4.2 The formation of a virtual bound state on an impurity 107
4.3 The formation of a local spin magnetic moment .....112
4.4 The orbital angular momentum of impurities .....116
4.5 The hyperfine interaction .....119
4.6 Conclusion .....121

Chapter 5: The measurement of mixed M1/E2 hyperfine interactions

5.1 Introduction .....123
5.2 The mixed E2/M1 hyperfine interaction .....123
5.3 Small quadrupole effects in conventional nuclear orientation .....126
5.4 The Effect of a quadrupole splitting upon the N.M.R./O.N. resonance line .....132
5.5 The effect of inhomogeneous broadening .....138
5.6 The effect of incomplete resonance saturation on the observed N.M.R./O.N. lineshape for a small quadrupole splitting .....144
5.7 Conclusions .....147

Chapter 6: Nuclear magnetic resonance of gold impurities in iron cobalt and nickel

6.1 Introduction .....148
6.2 The hyperfine anomaly .....149
6.3 N.M.R./O.N. measurements of $^{199}Au$ in iron .....156
6.4 N.M.R./O.N. measurements of $^{199}Au$ and $^{198}Au$ in cubic cobalt .....166
6.5 N.M.R./O.N. of Ni $^{198}Au$ .....175
6.6 The variation of $H_{eff}$ with the saturation moment of the host .....180
6.7 Conclusions .....183

**Chapter 7: Nuclear magnetic resonance studies on iridium impurities**

7.1 Introduction ..... 184
7.2 Sample preparation ..... 187
7.3 N.M.R./O.N. measurements on Ni $^{192}$Ir ..... 191
7.4 Summary and analysis of the measurements of the contributions to the hyperfine interaction in nickel, from an unquenched orbital magnetic moment ..... 197
7.5 The measurement of the hyperfine field of iridium in cubic cobalt by N.M.R./O.N. ..... 202
7.6 The magnetic hyperfine interaction on iridium and the $^{192}$Ir g factor ..... 205
7.7 Conclusions ..... 207

**Chapter 8: Nuclear Orientation measurements on $^{192}$Ir**

8.1 Introduction ..... 208
8.2 Comparison of measurements using various techniques ... 209
8.3 Sample preparation ..... 212
8.4 Gamma-ray spectroscopy ..... 214
8.5 The interpretation of the nuclear orientation measurements on Ni $^{192}$Ir ..... 216
8.6 Comparison with other measurements and the theoretical estimates ..... 228
8.7 The hyperfine interaction of $^{192}$Ir in iron ..... 231

**Appendix A: Least squares fitting to measured gamma-ray anisotropies** 233

## ACKNOWLEDGEMENTS

I would like to thank the following people whose help has made this work possible.

Professor Bleaney, for extending to me the facilities of the Clarendon Laboratory.

Dr.N.J.Stone, for his supervision throughout the period of this work.

Dr.A.D.Spanjaard, for many stimulating discussions and his collaboration in several experiments.

Members of the Low Temperature group for many useful discussions and their encouragement, in particular Dr.R.A.Fox, Dr.B.W.Marsden, Dr.J.D.Marsh, Mr.P.T.Callaghan, Mr.C.J.Sanctuary, Mr.P.A.Hensel and Mr.P.Kittel.

The technical staff of the Clarendon Laboratory for their constant assistance.

The Science Research Council for a maintainance grant.

# HYPERFINE INTERACTION STUDIES USING LOW TEMPERATURE NUCLEAR ORIENTATION

- by -

P. D. Johnston

## A B S T R A C T

Experiments are described in this thesis using the techniques of nuclear orientation and nuclear magnetic resonance to study the hyperfine interactions of dilute impurities in ferromagnetic metal hosts. The work is particularly concerned with the study of systems for which the more accurate measurement of the hyperfine interaction by the observation of nuclear magnetic resonance provides more information about the hyperfine interaction, and the nuclear parameters of the radioactive impurity, than can be obtained by a nuclear orientation experiment alone. The two aspects of this theme are combined in several experiments, where an accurate description of the decay transitions depends on the ability to provide a complete description of the orientation of the parent nucleus, from the resonance experiment.

The experimental results can be considered in two parts. The use of the nuclear resonance technique to study the hyperfine interactions of dilute impurities, has concentrated on the observation and measurement of contributions to the hyperfine interaction from localised orbital magnetic moments on heavy impurities in the three cubic ferromagnetic lattices, iron, cobalt and nickel. The mechanism of the formation of localised magnetic moments at impurity atoms is discussed in chapter four. The cubic symmetry of the three host lattices will tend to quench the orbital angular momentum of a substitutional ion, but the strong spin-orbit interaction associated with heavy impurities will compete with the crystal field, and tend to produce a small orbital magnetic moment localised at the impurity site. Such an effect can be observed through the detection and measurement of either the magnetic orbital dipolar hyperfine interaction or an electric quadrupole interaction.

The nuclear resonance technique is sensitive to both these interactions in the appropriate circumstances. The two impurities studied have provided an example of each measurement. Two isotopes of gold, dissolved as dilute impurities in iron, cobalt and nickel, have enabled the magnetic orbital dipolar hyperfine fields to be studied through the measurement of the hyperfine anomaly. The comparison of the measured value of the hyperfine anomaly in these hosts with the known value associated with a pure S-electron contact hyperfine field, allows the contribution to the hyperfine fields from a non-contact, orbital field, to be separated and measured. Since both a magnetic orbital dipolar field and an electric quadrupole interaction will arise from the unquenching of the orbital angular momentum, the effect of both contributions on the ratio of the observed nuclear resonance frequencies of $^{198}Au$ and $^{199}Au$ must be measured. The table below shows the measured values for the hyperfine fields on these two isotopes

Table 1

| Isotope | Host | $H_{Total}$ | $H_{Contact}$ | $H_{Orbital\ dipolar}$ |
|---|---|---|---|---|
| $^{198}Au$ | Fe | -1169(1) | -1389 (30) | +220(30) |
| | Co | - 732 (1) | - 792 (30) | + 60 (30) |
| | Ni | - 365·2(8) | | |
| $^{199}Au$ | Fe | -1233(1) | -1453(30) | +220(30) |
| | Co | - 769 (1) | - 829 (30) | + 60 (30) |
| | Ni | | | |

The other systems studied have been dilute impurities of iridium in nickel and cobalt. The interaction of the host conduction electrons of a nickel lattice with an iridium impurity has been shown by Demangeat and Gautier [64] to result in the formation of a localised magnetic moment on the impurity. This has been detected in the N.M.R/O.N. experiments by the finite electric quadrupole interaction resulting from

the unquenching of the orbital angular momentum, through the spin-orbit interaction. The comparison with other measurements, and with the estimate of the orbital dipolar hyperfine field, from the Mossbauer measurements of the hyperfine anomaly between the ground and first excited states of $^{193}$Ir, have suggested a magnitude for the orbital magnetic moment of $+0.2\mu_B$.

The second aspect of this study has used the knowledge of the hyperfine interaction from a nuclear resonance experiment to analyse nuclear orientation measurements on two isotopes, $^{110}$Ag$^m$ and $^{192}$Ir, in terms of the M1/E2 mixing ratios of several of the gamma-ray transitions in the decay. Both of the decay products of these isotopes fall into mass regions where the excited states can be represented, to first order, by collective vibrational harmonic oscillations about a spherical equilibrium nuclear shape. Measurements of M1 admixtures, into the pure E2 transitions predicted on the basis of a perfect harmonic oscillator model, are of value in comparison with theories including a pairing-plus-quadrupole force [ 54]. The results from the nuclear orientation experiments are compared with similar measurements by the gamma-gamma correlation technique, and are found to be in general agreement, with frequently a much improved accuracy. The results, particularly for $^{110}$Cd suggest large perturbations of simple harmonic oscillator excitations.

Previous nuclear orientation experiments on these isotopes have suffered from an inaccurate, and often very wrong, value for the hyperfine interaction, due to a non-unique distribution of hyperfine fields in the alloys used. The comparison with the nuclear magnetic resonance experiments has enabled good alloys, with impurity concentrations less than $10^{-3}$ at %, to be used, and the distribution of hyperfine fields in more concentrated, and non-substitutional alloys to be studied.

The theoretical basis of the nuclear orientation, and the observation of nuclear magnetic resonance by the perturbation of the thermal equilibrium gamma-ray anisotropic distribution from a system of oriented nuclei, is discussed in chapter one. The cryogenic apparatus and the experimental procedure is discussed in chapter two, including nuclear magnetic resonance measurements on three simple systems Fe $^{60}$Co, Co $^{60}$Co, and Fe $^{96}$Tc. Nuclear magnetic resonance studies on impurities of silver, gold, and irridium are presented in chapters three, six and seven.

# CHAPTER 1

# NUCLEAR ORIENTATION AND NUCLEAR MAGNETIC RESONANCE

The experiments described in this thesis involve the use of the techniques of Nuclear Orientation and Nuclear Magnetic Resonance to study the hyperfine interactions of impurities in the three common ferromagnetic metals, iron cobalt and nickel. The existence of large magnetic hyperfine interactions at a wide range of impurity nuclei in these host lattices was first demonstrated by Khutsishvili in 1956 [ 1 ], and Samoilov in 1958 [ 2 ]. These large magnetic interactions can be used to give considerable degrees of nuclear polarisation in the accessible temperature range from $0.1^{\circ}K$ to $0.01^{\circ}K$. The technique of nuclear orientation involves the measurement of the anisotropic angular distribution of the $\gamma$-ray emission from oriented radioactive nuclei, as a function of the temper ature, to estimate the magnitude of the hyperfine interaction. This method has been extensively used in the study of hyperfine interactions, and also for the measurement of the nuclear decay parameters involved in the observed and unobserved decay transitions.

The technique of nuclear magnetic resonance on oriented nuclei (N.M.R./O.N.), suggested by Bloembergen and Temmer [ 3 ], and first realised by Matthias and Halliday [ 4 ] in 1967, uses the disturbance of the thermal equilibrium gamma-ray anisotropy from the oriented nuclei, by resonant absorption of power from the radio frequency field, to detect the nuclear resonance. The measurement of the frequency of the nuclear resonance gives a very accurate measurement of the hyperfine interaction. This can be combined with the nuclear orientation measurements to give a complete description of the orientation of the parent nucleus and the multipolarities of the decay transitions of the impurity.

The work described in this thesis falls into two main categories. The N.M.R./O.N. technique has been combined with the nuclear orientation technique to provide a better understanding of the hyperfine interactions of the silver isotopes $^{110}Ag^{m}$, and $^{109}Ag$ in iron and nickel, and the isotope $^{192}Ir$ in nickel. The accurate measurement of the hyperfine interaction enables the nuclear orientation measurements to be interpreted in terms of the gamma and beta decay multipolarities. The second group of experiments uses the N.M.R./O.N. technique by itself to study the contributions to the hyperfine interaction from localised magnetic moments on heavy impurities. The theory associated with the formation of such magnetic moments is discussed in chapter four. In this chapter a description of the origin of the hyperfine interactions is followed by the theory of nuclear orientation and the observation of nuclear magnetic resonance on oriented nuclei.

## 1.2 The hyperfine interaction

The dominant hyperfine interaction at impurity sites in the magnetically ordered systems, such as the ferromagnetic metals, is the the Fermi-'contact' interaction, arising from the net spin magnetisation of the S-electrons at the impurity nucleus. The interaction was first proposed by Fermi [ 5 ], and applies only to S-electrons and $p_{\frac{1}{2}}$ electrons, the latter through relativistic effects. The hyperfine magnetic field associated with an electronic magnetism $M_o$ at the nucleus is given by

$$B = \frac{\mu_o}{4\pi} \cdot \frac{8\pi}{3} M_o$$

where $M_o = - g_s \beta \underline{S} \left| \Psi_s(o) \right|^2$

The interaction with the nuclear magnetic moment can be written in the form

$$W_o = \frac{\mu_o}{4\pi} \frac{8\pi}{3} g_s \beta \, (\mu_I \cdot S) \left| \Psi_s(o) \right|^2$$

In the ferromagnetic metal hosts, the S-electron magnetisation at the impurity nucleus results from a combination of the polarisation of the closed electronic shells of the core at the nucleus through the exchange interaction with polarised conduction electrons of the host, and the polarisation of the S-type conduction electrons at the impurity site.

Core polarisation

The exchange interaction between unfilled electron shells and the closed S-shells of the core, has the effect of attracting the core electrons with spin parallel to the net spin of the magnetic shells, and repelling those of antiparallel spin. This effect causes small changes in the density of the spin up and spin down closed shells at the nucleus, with a consequent non-zero Fermi hyperfine interaction. The contribution to the hyperfine field from closed shells inside the magnetic shell of the host will usually be negative with respect to the external magnetisation. This is shown diagramatically in Fig.1.1.

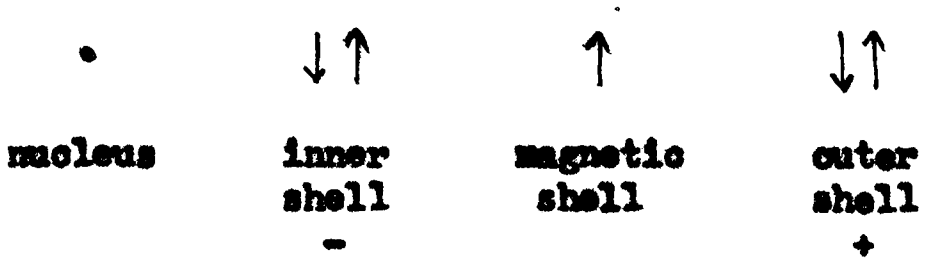



Fig. 1.1

The magnitude of the contributions is difficult to calculate, since it consists of large, nearly equal, cancelling terms from each sense of

polarisation. The results of calculations by Watson and Freeman [ 6 ], using a self-consistent Hartree-Fock calculation, show hyperfine fields in general agreement with the order of magnitude found by experiment.

Conduction electron polarisation

This contribution to the hyperfine field results from the interaction with the S-electrons of the conduction band. The spin-up and spin down halves of the condudion band are unequally populated because the exchange interaction splits the band base energies of the two sub-bands by an energy $2\epsilon$. The sub-bands are both filled to the Fermi energy, giving a net spin magnetisation due to the greater population of the spin up sub-band. The interaction of the impurity electron shells with the polarised conduction band provides the mechanism for transferring the spin polarisation into the region of the impurity nucleus. Models for the scattering of the conduction electrons at the impurity, providing the screening of the excess charge on the impurity, have been proposed by Daniel and Friedel [ 7 ], Campbell [ 8 ], and others. In the model proposed by Daniel and Friedel the magnitude of the conduction-electron-polarisation hyperfine interaction is proportional to the difference in the densities of the spin $\uparrow$ and spin $\downarrow$ conduction electrons at the impurity. The conduction electrons are treated as Bloch waves in the nearly free approximation, scattered by the spin dependent square well potentials $V_{\uparrow}$ and $V_{\downarrow}$ at the impurity site. In the theory of Campbell, the conduction electrons are treated in a tight binding approximation, using the expressions developed by Clogston [ 9 ], Woolf [ 10 ] and Kamamori [ 11 ] for the screened charge and the electron density. These models are discussed in more detail in Chapter four, with reference to the formation of localised spin magnetic

moments on the impurity atom. The predictions of the tight binding model of Campbell for the hyperfine fields of S-p type impurities in iron agree very well with the experimental results. The mechanism of conduction electron polarisation is the dominant interaction mechanism for many impurities, the core-polarisation becoming dominant only when large magnetic moments exist on the impurity atom. A comparison of the two interactions is given by Shirley et al [12].

The orbital dipolar and spin dipolar hyperfine interactions

These two additional interactions are associated with the interaction between the nuclear magnetic moment and the orbital angular momentum, and the distribution of the spin magnetisation of the non-S type wavefunctions of the impurity. The quenching of the orbital angular momentum in the cubic symmetry of the host lattices means that both will give zero contributions to the total hyperfine interaction in the absence of a strong spin orbit interaction. The Hamiltonians are given below and are discussed in Chapter 4. [13]

$$\mathcal{H}_{O.D.} = 2\beta\left(\frac{\mu}{I}\right)\left\langle r_l^{-3}\right\rangle \quad (\underline{L}.\underline{I})$$

$$\mathcal{H}_{S.D.} = 2\beta\left(\frac{\mu}{I}\right)\left\langle r_s^{-3}\right\rangle [L(L+1)(\underline{I}.\underline{S}) - \tfrac{3}{2}(\underline{L}.\underline{I})(\underline{L}.\underline{S}) - \tfrac{3}{2}(\underline{L}.\underline{S})(\underline{L}-\underline{I})]$$

[13]

The total hyperfine interactions may also include the effect of an electric field gradient at the impurity nucleus, from either the crystal environment or the electronic orbitals of the impurity. This is also further discussed in chapter four.

## 1.3 Nuclear orientation

The term, orientation, refers to the unequal population of the magnetic substates of the nuclear spin. Nuclear alignment is used to describe the situation where the populations of the $\pm M_I$ substates are equal, and nuclear polarisation to describe the more general situation.

The effect of the large magnetic hyperfine field on the impurity nucleus is to split the nuclear ground state into 2I+1 equally spaced energy levels, separated by the Zeeman energy $\mu_N . H_{eff}/I_n$. The general interaction will include a small electric field gradient, and can be represented by the Hamiltonian.

$$\mathcal{H}_n = - \frac{\mu_N H_{eff} M_s}{I_n} + P[M_z^2 - \tfrac{1}{3} I (I+1)]$$

At temperatures such that $\mu_N H/I_N \sim kT$, the thermal equilibrium Boltzmann distribution of the populations of the split nuclear magnetic substates produces a significant preferential population of the lower energy states. For a predominantly magnetic interaction, the unequal populations of the $M_s$ substates produces a net nuclear magnetism associated with the unequal populations of the $\pm M_s$ states. Nuclear alignment, produced by an electric field gradient alone, where the populations of the $\pm M_s$ states are equal, will only give a non-zero value of $\langle | M_z^2 | \rangle$. For the large magnetic fields produced by the hyperfine interaction in ferromagnetic lattices, temperatures of the order of $0.01^{\circ}K$ will generally give a substantial degree of nuclear polarisation.

The angular distribution of the gamma-ray emission from systems of oriented nuclei is considered in detail by Blin Stoyle and Grace [14]. At high temperatures the random distribution of the population over the magnetic substates in a system of radioactive nuclei will produce an isotropic distribution of the decay products. At low temperatures the

unequal population distribution throughout the nuclear substates will give rise to an anisotropic distribution for the beta and gamma-ray emission, but preserving cylindrical symmetry about the axis of orientation. The anisotropy is a function of the degree of polarisation, or alignment; $\mu H/IKT$ and $e^2Q\ V_{zz}/4I(2I-1)kT$, and of the multipolarities of the observed and previous unobserved decay transitions. All the experiments in this thesis involve the observation of the gamma rays following the decay of a parent nucleus, by beta emission or electron capture, to an excited state of the daughter nucleus. The decay to the ground state of the daughter is by emission of one or more observed gamma rays. The gamma emission intensity at an angle $\Theta$ to the axis of orientation can be written in the form

$$W(\Theta) = \sum_{K\ \text{even}} B_K\ U_K\ F_K\ Q_K\ P_K(\cos\Theta) \qquad \ldots \qquad 1$$

The summation over K is limited to even values by the requirement of parity conservation for the electromagnetic interactions of the decay mechanism. The maximum value of K is determined by the minimum value of $(2L, 2I_o)$ where L is the multipolarity of the transition, and $I_o$ the spin of the parent nucleus, but, for the spins and temperature range used for these experiments only the K = 2 and K = 4 terms need be considered. The terms in the above expression are explained below.

$B_K$ are the parameters describing the expectation values of $\langle |M_z^K| \rangle$ associated with the population distribution of the magnetic substates of the parent nucleus. The half-lives of the intermediate states populated in the decay process are assumed to be sufficiently short that no re-distribution of the populations occurs through relaxation mechanisms in the intermediate states. When this condition is not satisfied, an integration over the population distribution during the half-life of the intermediate state must be used. Such a situation is described in

chapter three. Closed forms are available for the $B_K$ parameters in terms of the nuclear spin I and the substate populations [15]

$$B_2(I) = 6\left[\frac{5(2I+1)(2I-2)!}{(2I+3)!}\right]^{\frac{1}{2}} \sum_M [M^2 - \tfrac{1}{3} I(I+1)]\, W(M)$$

$$B_4(I) = 210\left[\frac{(2I+1)(2I-4)!}{(2I+5)!}\right]^{\frac{1}{2}} \sum_M \left[M^4 - \frac{(6I^2+6I-5)}{7} M^2 + \frac{3I(I-1)(I+1)(I+2)}{35}\right] W(M)$$

W(M) are the populations of the $M_z$ magnetic substates, given by the Boltzmann distribution

$$W(M) = \exp(-E_M/kT) \Big/ \sum_M \exp(-E_M/kT)$$

$$E_M = \left(-\frac{\mu_n H}{IkT}\right) M_z + P\,(M_z^2 - \tfrac{1}{3} I(I+1))$$

The parameters $Q_K$ represent the corrections for the finite solid angle subtended by the gamma-ray detector at the nucleus. They are functions only of K, and the shape and efficiency of the detector. For a particular detector the values of $Q_K$ are tabulated as a function of K, the distance of the detector from the gamma-ray source, and the gamma-ray energy. The latter parameter allows for the energy dependence of the detector efficiency.

The angular distribution parameters $P_K$ are the Legendre polynomials:

$$P_2 = \tfrac{1}{2}(3\cos^2\theta - 1) \quad P_4 = \tfrac{1}{8}[35\cos^4\theta - 30\cos^2\theta + 3]$$

The greatest sensitivity to the gamma-ray anisotropy is obtained at $\theta = 0$ when $P_2 = P_4 = 1$. This is the usual counting arrangement used in the experiments. Because of the different temperature dependences of the

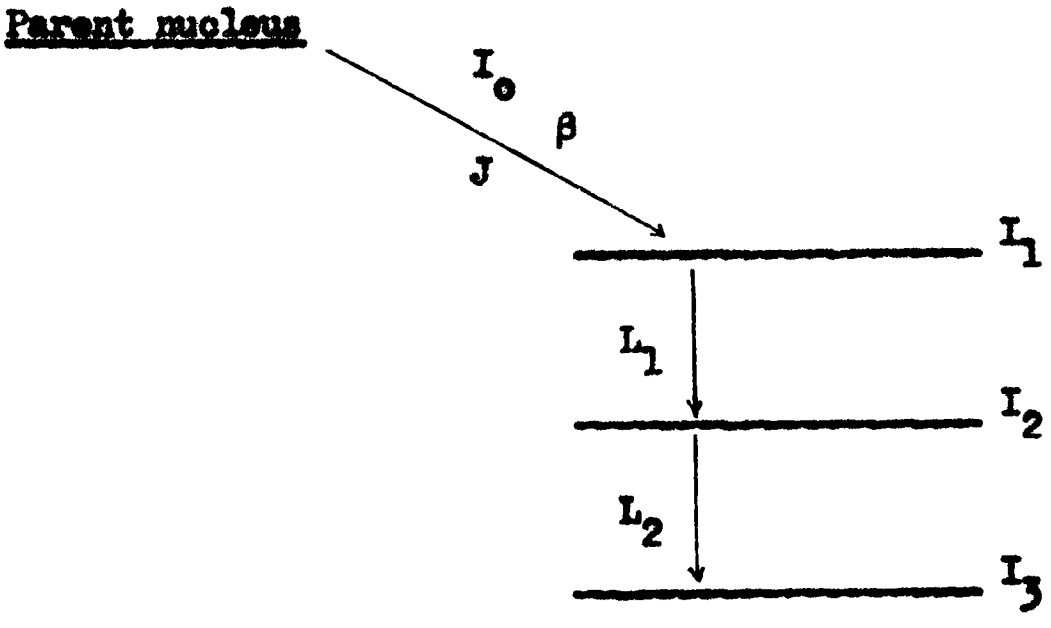
$B_2$ and $B_4$ parameters, such an arrangement enables $Q_2U_2F_2$ and $Q_4U_4F_4$ to be measured independently. A useful check is provided by an equatorial counter at $\Theta = \pi/2$ where $P_2 = -\frac{1}{2}$ and $P_4 = +3/8$. The comparison with the axial count rate gives independent measurements of $Q_K\ U_K\ F_K$ at each temperature.

The coefficients $U_K$ and $F_K$ describe the redistribution of the magnetic substate populations produced by the preceding unobserved transitions and the angular distribution associated with the multipolarity of the observed transition respectively. The $F_K$ coefficients are functions of the angular momentum removed in the observed transition and the spins of the excited states involved. The values of $F_K$ are given by the expression

$$F_K\ (LI_1I_2) = (-1)^{I_2-I_1-1}(2L-1)^{\frac{1}{2}}\ C(LLL_1-1/K\ o)W(I_1I_2LL;KL)$$

where C is the Clebsh-Gordon coefficient and W is the Racah coefficient associated with the observed decay. L is the angular momentum removed in the decay and $I_1$ and $I_2$ are the nuclear spins of the initial and final states. The values of $F_K$ are tabulated for transitions of single multipolarity [ 16 ].

The unobserved transitions preceding the observed gamma-ray will influence the population distribution in the magnetic substates of the exicted state emitting the gamma-ray. The value of $U_K$ used in expression (1) is the product of the appropriate $U_K$ coefficients for each preceding transition.



The values of $U_K$ are tabulated, as for the $F_K$ coefficients, as a function of K, $I_o$ and $I_1$ and the multipolarity of the decay. The values are derived from the expression

$$U_K = (2I_o + 1)(2I_1 + 1)^{\frac{1}{2}}(-1)^{I_o+I_1+1} W(I_o I_o I_1 I_1; KJ)$$

A number of the experiments in this thesis involve the observation of decay transitions of mixed multipolarity. The emitted quanta are classified as electic or magnetic $2^L$-pole according to the parity change and the angular momentum L involved in the decay. The angular momentum must satisfy the condition that

$$L \geqslant |I_1 - I_2|$$

More than one multipole order is often possible in a transition, but since the transition probabilities fall off rapidly with increasing L, only the two lowest orders will give a significant contribution. The multipolarities and parity changes are shown in table 1.1: [17]

| classification | L | (parity change) |
|---|---|---|
| E1 | 1 | Yes |
| M1 | | No |
| E2 | 2 | No |
| M2 | | Yes |
| E3 | 3 | Yes |
| M3 | | No |
| E4 | 4 | No |
| M4 | | Yes |

The transition probability for given multipolarity is greater for the electric transition by a factor of order $10^4$, therefore a mixed multipolarity will usually only occur when the selection rules allow M(L) and E(L+1).

The $F_K$ coefficients are thus given by

$$F_K^{\delta}(L,L+1) = \frac{F_K(1) + 2\delta\, F_K(L, L+1) + \delta^2 F_K(L+1)}{1+\delta^2}$$

The parameter of $\delta$ is defined such that $\delta^2 = x/(100-x)$, where x is the percentage of the (L+1) multipolarity. There is no mixed term in $2\delta$ for the similar $U_K$ coefficients.

$$U_K^{\delta}(L, L+1) = \frac{U_K(L) + \delta^2 U_K(L+1)}{1+\delta^2}$$

The sign of $\delta$ can be determined from nuclear orientation measurements only for directly observed transitions. The knowledge of the hyperfine field from a nuclear magnetic resonance experiment enables the temperature dependence of the gamma-ray anisotropies to be used to determine the values of $U_K F_K Q_K$ and thus the multipolarities and value of $\delta$ for the gamma and beta transitions.

In these formulations, the sign of $\delta$ is as defined in the work of Biedenharn and Rose [18]. This means that when comparing values of $\delta$ with those from angular correlation measurements in which the transition is first in the cascade, there will be a difference in sign given by $(-1)^{L_1-L_{11}}$, where $L_1$ and $L_{11}$ are the competing multipole orders. This has been discussed by Brink and Rose [19]. For transitions of mixed M1 and E2 multipolarity, which are mainly discussed in chapters three and eight, a sign change will arise only when the angular correlation measurement is on the first decay in the cascade. For the comparison of the nuclear orientation data with such measurements in chapter three and eight, all the signs of $\delta$ are converted to the convention of

Biedenham and Rose.

1.4 Nuclear magnetic resonance on oriented nuclei (N.M.R/O.N.)

The possibility of the resonant destruction of the gamma-ray anistropy for systems of oriented nuclei in the ferromagnetic lattices was demonstrated by Matthias and Holliday in 1967. The technique has since been applied to a wide range of impurities, providing a very accurate method of measuring the hyperfine interaction, with impurity concentrations several orders of magnitude smaller than those required for conventional N.M.R. or spin Echo measurements. The long relaxation times of tens of seconds characteristic of impurity nuclei in ferromagnetic metals at the temperatures normally used, and the ferromagnetic enhancement of the applied R.F. field, mean that low R.F. powers, compatible with the maintenance of the low temperatures, will produce sufficient saturation of the nuclear resonance to produce a measureable change in the gamma-ray anisotropies. The nuclei can be considered as free spins precessing about the effective magnetic field $\underline{H}_{eff}$ with a frequency, $\omega_n$, equal to $\frac{\mu_n \cdot H}{2\pi KI}$. The effect of an applied R.F field of frequency $\omega$ of amplitude $H_1$ perpendicular to the axis of $\underline{H}_{eff}$ can be seen by transforming to the Larmor frame rotating with angular frequency $\omega$ about the axis of $\underline{H}_{eff}$. In this frame the nuclei will precess about the resultant field $\underline{H}_L$ given by:

$$\underline{H}_L = \left(H_{eff} + \frac{\omega}{\gamma_n}\right)\underline{K} + H_1\,\underline{i} + H_1\left[\cos 2\omega t\,\underline{i} + \sin 2\omega t\,\underline{j}\right]$$

where the R.F. field is resolved into two circularly polarised counter-rotating components.

If $\omega_1 = -\gamma_n H_1$; and neglecting the counter rotating component this becomes

$$\underline{H}_L = \left[(\Omega - \omega_n)\underline{K} - \omega_1\,\underline{i}\right]/\gamma_n$$

resonance will occur when $w-\omega_n = 0$. When the R.F. frequency, w, is well away from $\omega_n$ the R.F. field will have very little effect on the nuclear spins but on resonance the projection of the nuclear magnetism along, K, the axis of orientation will change. This classical treatment gives the same resonance conditions as the selection rule $M_z = \pm 1$ and the energy requirement for a quantised angular momentum.

$$\hbar w = - \gamma \beta_n H_{eff}$$

The observed nuclear resonances show a large degree of inhomogenous broadening giving a linewidth $10^3 \longrightarrow 10^4$ times greater than the intrinsic linewidth associated with the relaxation mechanisms.

Ferromagnetic enhancement

The R.F field experienced by the impurity nuclei is considerably greater than that applied to the ferromagnetic host because of the enhancement by the hyperfine interaction. The externally applied R.F. field acts on the electronic magnetism of the host lattice, producing a tilting of the axis of the electronic magnetisation of $\Theta = H_1/H_{EXT}$; where $H_1$ is the amplitude of the applied R.F field, and $H_{EXT}$ is the magnitude of the static polarising field. The nuclei will see the magnetic hyperfine field oscillating about the axis of polarisation with the amplitude $\Theta$ . The apparent amplitude of $H_1$ acting on the nuclei is then given by

$$H_1^n = H_1 [1 + H_{eff}/H_{EXT}]$$

The polarising field applied to the ferromagnetic lattice to produce almost complete saturation of the electronic magnetism is of the order of 2kOe $\longrightarrow$ 10 kOe. The strength of the hyperfine field is usually of the order 200kOe $\longrightarrow$ 1000kOe, giving an enhancement of about 100 to the R.F field. The resonance is detected, by an N.M.R/O.N experiment, for nuclei inside the magnetic domains of the lattice, not just

in the domain walls, so the technique is also applicable to impurities in saturated single crystals over a wide range of applied magnetic fields.

Inhomogeneous Broadening of the resonance line

The inhomogeneous broadening associated with a resonance at a frequency $\omega$ is important in this thesis in the observation of small electric quadrupole splittings on the resonance of some impurities. The quantity of data now available makes possible a study of the systematic variation of the observed linewidths as a function of $\omega$. The distribution of effective fields producing the resonance broadening can arise from three causes; a) variations in the external magnetic field due to inhomogeneities in the applied field and the local demagnetising field, due to irregularities in the surface of the sample, b) contributions to the effective field from the dipolar coupling with neighbouring nuclei, and electric field gradients from lattice imperfections, c) variations in the hyperfine field itself.

a) The polarising magnets used for these experiments give a field uniformity over the sample volume of better than 1%, representing a linewidth of order 30 Oe for typical polarising fields. The broadening from the variation of the demagnetising factor is not so small. The samples used for resonance generally consist of thin foils magnetised in the plane of the foil, giving a demagnetising field of less than 50 Oe. The variations in the demagnetising factor will be associated with the irregularities in the surface of the foil giving a local tilting of the foil with respect to the axis of magnetisation. The demagnetising field will tend to reduce the magnitude of the external field at the impurity site by an amount

$$\delta H_{D.M} \simeq M_S \sin^2\theta$$

where $\theta$ represents the angle of tilting, and $M_S$ is the lattice magentisation when completely saturated. The probable distribution

of values of $\Theta$ of range $\pm 10^{\circ}$ will give a linewidth of order 300 Oe for iron samples. This is not negligible in comparison with the observed linewidths of 1kOe to 5kOe but is not the major contribution. When the applied field is not sufficiently strong to saturate the magnetisation of the foils a similar broadening results from the variation in the orientation of the domains within the foil, since the foil will tend to magnetise most easily parallel to the plane of the surface. The distribution of fields will then follow the form:

$$\delta H \simeq H_{APP} [1-\cos[\Theta + f(\phi)]]$$

where $f(\phi)$ represents the distribution of orientation of the domains. All these terms will give a width of the resonance line, independent of the hyperfine interaction but proportional to $\mu/I$.

b) A rough estimate of the effect of the dipolar coupling assuming a typical neighbouring nucleus at a distance r with a magnetic moment $\mu$ is given by

$$H_{LOC} = \frac{\mu}{r^3}$$

using values of $r \sim 2\text{Å}$ and $\mu \sim 10^{-23}$ erg/gauss the distribution of fields would have a range of $\sim$ 1 gauss; obviously negligible compared with other contributions.

The breaking of the cubic symmetry of the impurity environment by magneto strictive effects and crystal defects will produce contributions to the inhomogeneous broadening from the anisotropic Knight shift, and the splitting of the nuclear magnetic resonance line by the nuclear electric quadrupole interaction with electric field gradients of varying magnitude and oreintation. Such an interaction will split the magnetic resonance line into 2I components separated by a frequency 2P where

$$P = \frac{3eQV_{zz}}{4I[2I-1]}$$

and $V_{zz}$ represents the component of the electric field gradient parallel to the applied magnetic field. The effect of such an interaction on the N.MoR/O.N. line is discussed in more detail in chapter 6; the result only being used here. At temperatures giving a large degree of nuclear orientation, a single resonance line is observed, shifted in frequency by $[2I-1]P$. For a given host lattice the variation of the magnitude of the quadrupole broadening with frequency is given by

$$\Gamma_Q \simeq \left(\frac{4\,\mu_n H}{A_Q Q}\right)^{-1} \nu \,/\, 2I+1$$

The contribution to the broadening from an anisotropic Knight shift will be very small, $\sim < 10^{-4}\nu$, and will depend on the magnetostriction and the strength of the applied polarising field.

c) The influence of dislocations, strains, and vacancies near the impurity atom will give a variation in the magnitude of the hyperfine interaction through local changes in the magnetisation and density of the host lattice. For each host the inhomogeneous linewidth will then be proportional to the hyperfine interaction and therefore the resonance frequency.

Table 1.2 shows the observed linewidths and resonance frequencies for the impurity systems considered in this thesis. The constancy of $\Gamma_n/\nu_n$ suggests that the variation of the magnetic hyperfine interaction provides the dominant inhomogeneous broadening mechanism.

Table 1.2

| Impurity | host | $\nu_n$ | $\Gamma_n$ | $\frac{\Gamma_n}{\nu_n}$ % |
|---|---|---|---|---|
| $^{60}Co$ | Fe | 166.0 | 0.90 | 0.54 |
| $^{96}Tc$ | Fe | 174.0 | 0.40 | 0.23 |
| $^{110}Ag^{m}$ | Fe | 204.75 | 0.90 | 0.44 |
| $^{199}Au$ | Fe | 167.7 | 1.00 | 0.60 |
| $^{198}Au$ [20] | Fe | 260.3 | 1.7 | 0.65 |
| $^{60}Co$ | Co | 123.7 | 1.3 | 1.05 |
| $^{198}Au$ | Co | 162.5 | 0.8 | 0.50 |
| $^{199}Au$ | Co | 104.3 | 0.8 | 0.75 |
| $^{192}Ir$ | Co | 349.5 | 2.15 | 0.61 |
| $^{190}Ag^{m}$ | Ni | 55 .0 | 0.45 | 0.70 |
| $^{198}Au$ | Ni | 81.5 | 2.15 | 2.60 |
| $^{192}Ir^{1}$ | Ni* | 165.4* | 0.9 | 0.54 |

*Single crystal. The resonance frequency give is for the Zeeman splitting only.

Frequency Modulation

The solution of the Bloch equations for the evolution of the components of the nuclear magnetism at a time sufficiently long for the transient exponentials to have decayed, when an R.F field of amplitude $H_1$ and frequency w, near $w_n$, is applied, gives the steady state solutions:- [21]

$$\bar{M}_x = \frac{\Delta w \gamma H_1 T_2^2}{1+[T_2 \Delta w]^2 + \gamma^2 H_1^2 T_1 T_2} M_o$$

$$M_z = \frac{1 + [\Delta w T_2]^2}{1 + [\Delta w T_2]^2 + \gamma^2 H_1^2 T_1 T_2} M_o$$

The observation of the nuclear resonance through the second rank tensor $B_{20}$, relating the gamma-ray anistropy to the population distribution of the present nuclear substate, will show a resonance lineshape that is not Lorentzian but has a multiplet character. An estimate of the width of the resonance can however be made from the solutions of the Bloch equations using typical relaxation times. The linewidth associated with the resonance of a nuclear spin having a longditudinal relaxation time $T_1$ and a transverse relaxation time $T_2$ is given by

$$\Gamma_n = (2\pi)^{-1} \left[ \frac{1}{T_2^2} + \gamma_1^2 H_1^2 \, T_1/T_2 \right]^{\frac{1}{2}}$$

For the degree of saturation of the resonance achieved in most N.M.R./O.N. experiments $\gamma_1^2 H_1^2 T_1 T_2 \gg 1$. The above expression then approximates to

$$\Gamma_n \simeq \gamma_1 H_1 T_1^{\frac{1}{2}} / 2\pi T_2^{\frac{1}{2}}$$

Typical R.F. power levels give a value of $H_1$ of order 300mOe after enhancement, and for the measured relaxation times, this expression

indicates a linewidth of order 200Hz for $^{60}Co$ in iron. This is very small compared with the observed inhomogeneous linewidth of $\sim$ 1MHz for this system. To produce resonance in a large proportion of the $^{60}Co$ nuclei the R.F field must be modulated over a frequency range comparable with the inhomogeneous linewidth. For a frequency modulation of frequency $w_F$ and amplitude $\Delta w$ about the centre frequency $w_o$, the R.F field can be described by the form

$$H_1 = \cos w_o \left[t + \frac{A}{w_F} F(t)\right] \quad A = \Delta w / w.$$

To produce a nearly uniform resonance effect over the frequency range from $w_o - \Delta w$ to $w_o + \Delta w$, the form, F(t), of the frequency modulation is chosen as a saw-tooth sweep. The Fourier analysis of the resulting R.F field shows a frequency distribution given by

$$H(t) = \sum_{n=-\infty}^{\infty} H_1 J_n(x) \cos (w_o + n w_F)t$$

where

$$J_n(x) = \left[\frac{2}{\pi x}\right]^{\frac{1}{2}} \left[ P_n(x) \cos \left(x - \frac{n\pi}{2} - \frac{\pi}{4}\right) - Q_n(x) \sin \left(x - \frac{n\pi}{2} - \frac{\pi}{4}\right)\right]$$

$P_n(x)$ and $Q_n(x)$ are given by the converging series for $x = \frac{\Delta w}{w_F}$

$$P_n(x) = 1 - \frac{(4n^2-1)(4n^2-9)}{2!(8x)^2} + \frac{(4n^2-1)(4n^2-9)(4n^2-25)(4n^2-49)}{4!(8x)^4} \cdots\cdots$$

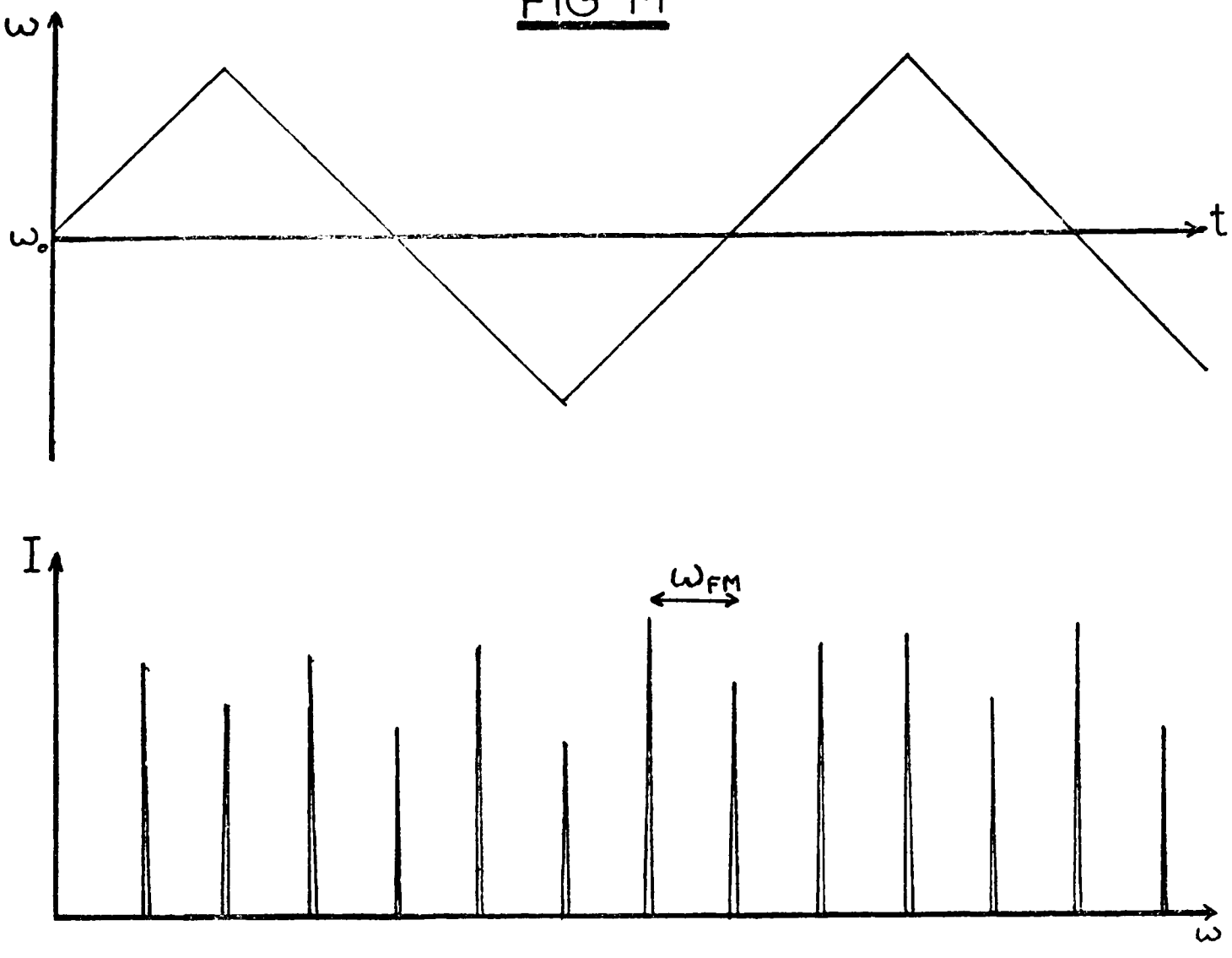
$$Q_n(x) = \frac{4n^2-1}{8x} - \frac{(4n^2-1)(4n^2-9)(4n^2-25)}{3!(8x)^3} \cdots\cdots$$

For small values of $n \ll x$ i.e. near the centre of the frequency distribution, theexpression can be simplified to

$$J_n(x) \rightarrow \left[\frac{2}{\pi x}\right]^{\frac{1}{2}} \cos \left(x - \frac{n\pi}{2} - \frac{\pi}{4}\right)$$

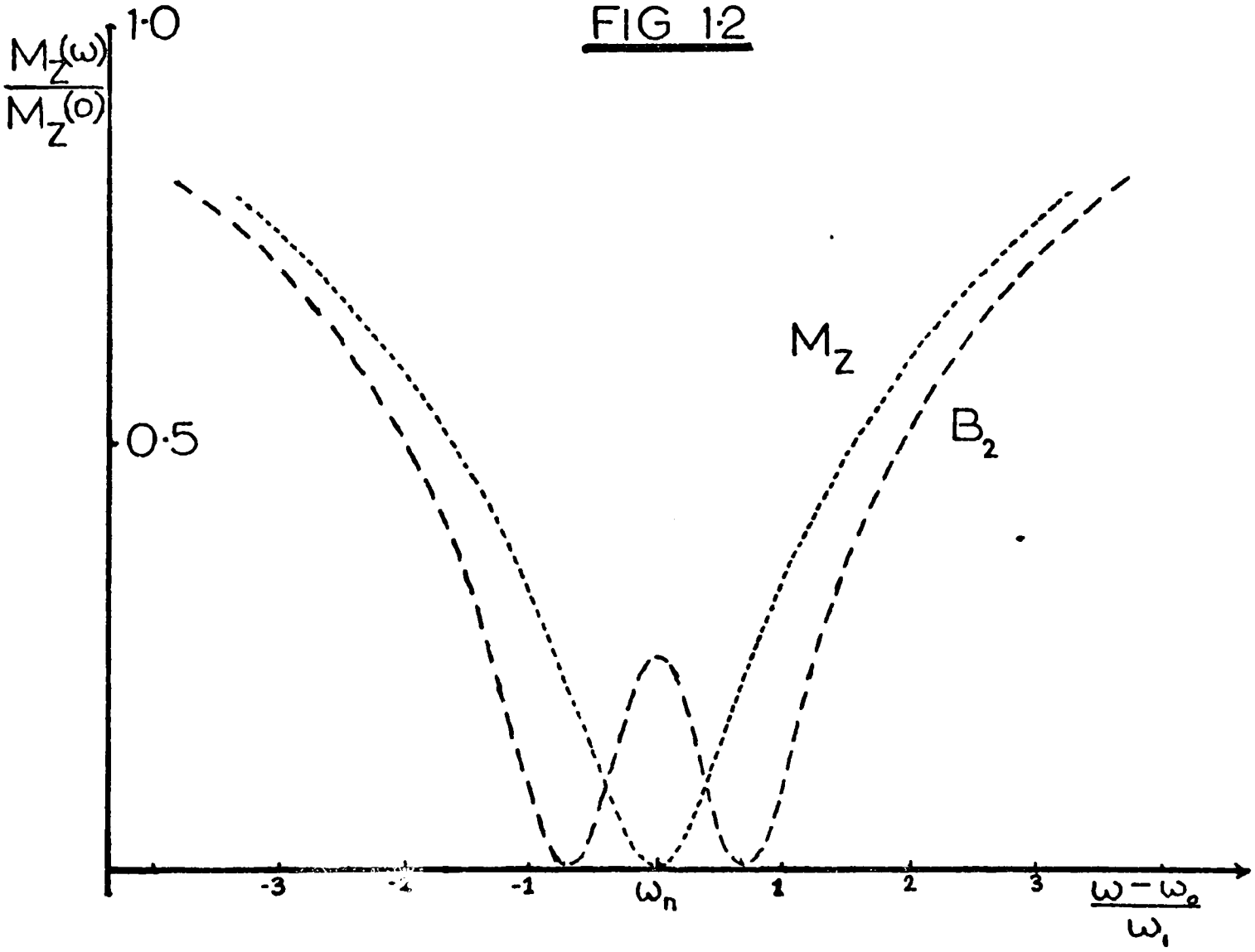
The physical interpretation of these results is shown in Fig.1.1. The R.F. field appears at a comb of frequencies, separated in frequency

FIG 1·1




Frequency modulation and R.F spectrum

FIG 1·2



by $w_F$, with an amplitude envelope given by $J_n(x)$. The mean value of $J_n(x)$ is $\sqrt{w_F/\Delta w}$ giving the same power spread over the frequency range as in the unmodulated R.F. carrier wave. We are now in a position to give four conditions that must be simultaneously satisfied in order to observe nuclear magnetic resonance on a system of oriented nuclei.

$$\Delta w \text{ [modulation amplitude]} \sim \Gamma_n \text{ [unhomogeneous]} \quad \ldots. 1$$

$$w_p \text{ [modulation frequency]} > \frac{1}{T_1} \quad \ldots. 2$$

$$w_F < \Gamma_n' \text{ where } \Gamma_n' = \gamma H_1 T_1^{\frac{1}{2}}/2\pi T_2^{\frac{1}{2}} \quad \ldots. 3$$

$$\frac{\gamma^2 H_1^2 T_1 T_2 w_F}{w} \gg 1 \quad \ldots. 4$$

The last condition is the requirement for saturation of the nuclear resonance. The third condition ensures that the separation of the components of the frequency spectrum is less than the natural linewidth of the resonance for each nucleus. If this condition is not satisfied only a proportion, $\Gamma_n'/w_F$, of the nuclei will experience a resonance effect.

The description of the modulated R.F field as a comb of frequencies is valid as a representation of the time averaged power distribution, but the value of $H_1$, included in the expression for the intrinsic power broadened linewidth in condition 3, is the total applied R.F amplitude, not merely the amplitude of a frequency component of the comb near the resonance frequency. This is because the linewidth is a function of the instantaneous precession frequency of the nuclear spin about the effective $H_1$ in the larmor frame as the frequency of the R.F field is swept through the resonance condition. The value of $\Gamma_n'$ deduced on such a basis for $^{60}Co$ in iron is in good agreement with the estimate of 1kHs obtained from the variation of the modulation frequency, and hence the spacingof the frequency components in the R.F spectrum [22].

The influence of an applied R.F. field on the observed gamma-ray anisotropy as the frequency is swept through the resonance condition, has been considered in detail by Barclay and Shirley [23 ] and by Spanjaard and Hartmann-Boutron [24 ]. The anisotropy gives a measure of the $b_2$ and $B_k$ parameters corresponding to the substate population distribution of the parent state. The variation with frequency of the applied R.F field near $\omega_0$ can best be considered by solving the equations for the evolution of the density matrix $\rho_K^q$ . This describes the population distribution of the parent states in a quantum mechanical way, analogous to the classical density of points in phase space. This is linked to the observed anisotropy through the expression

$$W(\theta,\phi) = \sqrt{2I+1} \sum_{kq} F_k \rho_k^q \sqrt{\frac{4\pi}{2K+1}} Y_k^q(\theta,\phi)$$

Because the resonance is primarily observed through changes in the second rank tensor $B_2$, the resonance line associated with each nuclear spin will not be a simple Lorentzian, but will show a multiple structure. This has the effect of changing the maximum degree of destruction of the anisotropy possible at the resonance condition. In the absence of relaxation processes, Barclay and Spanjaard have shown that the application of a large R.F field at $w_o$ will not produce complete destruction of the observed gamma-ray anisotropy. Spanjaard gives the expression for the density matrix after the nuclear spin has experienced a resonance effect for a time $\tau$

$$\rho_2^0(w_o) = \left[\frac{1}{4[1+\omega_1^2\tau^2]} + \frac{1}{4}\right] \rho_2^0(0)$$

This shows that after a long time; $w_1\tau \gg 1$; where $w_1$ is the nuclear precession frequence about $H_{RF}$, the gamma-ray anisotropy will show a "hard core" value of $1/4[1-W(0)]$. This 'hard core' anisotropy represents the classical situation of the nuclear spins precessing about the effective

field in the Larmor frame, corresponding to the resonance condition, which is perpendicular to the original axis of orientation. The detector will then see the nuclei randomly oriented about a circle, giving a different value of $B_2$ to the zero value corresponding to the random distribution about a sphere.

The introduction of the relaxation hamiltonian into the evolution equation for the population tensors, giving longditudinal and transverse relaxation times, $T_1$ and $T_2$ respectively, has the effect of reducing the hard core orientation. For the resonance of a nuclear state of half life $\tau$ Spanjaard gives the expression

$$\rho_{2,0(\text{Hard core})} = \frac{1}{4[3\tau/T_2+1]}\ \rho_{20}(0)$$

Fig.1.3 shows the typical time dependence of the second rank tensor $B_2$ as a function of the time after the R.F field is applied at the resonance frequency $w_o$. In practice the situation is complicated by the influence of several components of the R.F. frequency spectrum acting on each nucleus simultaneously. The superimposed precessions of the nuclear spin about the range of effective fields associated with the frequency spectrum will tend to smear out the hard core effect. The experimental investigation of hard core effects is difficult because of the problems in preparing perfect resonance samples in which all the impurity nuclei will experience a resonance effect. Some samples of $^{60}Co$ in iron appear to have shown more than the 75% destruction of the anisotropy associated with the hard core [25].

FIG 1·3

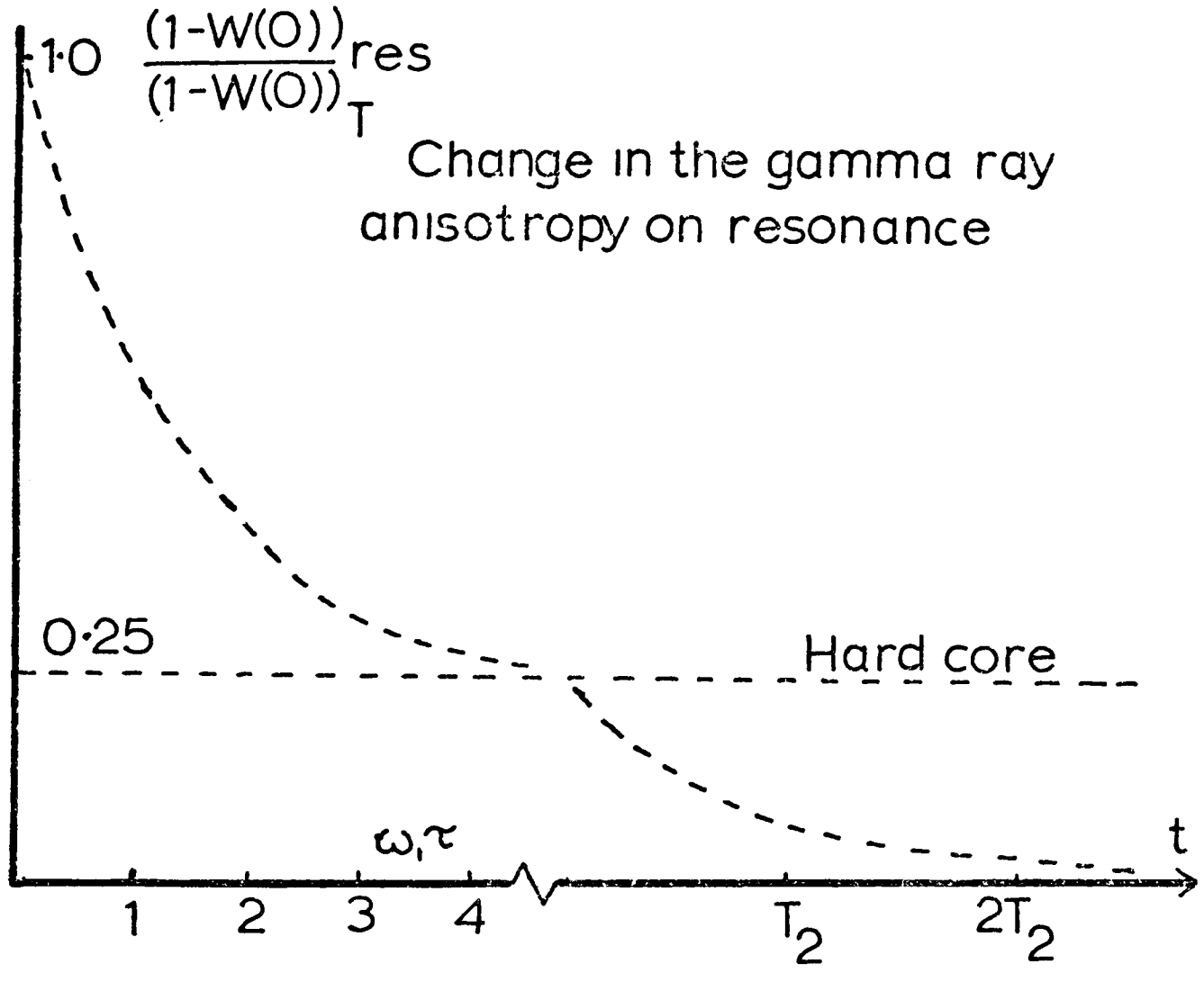
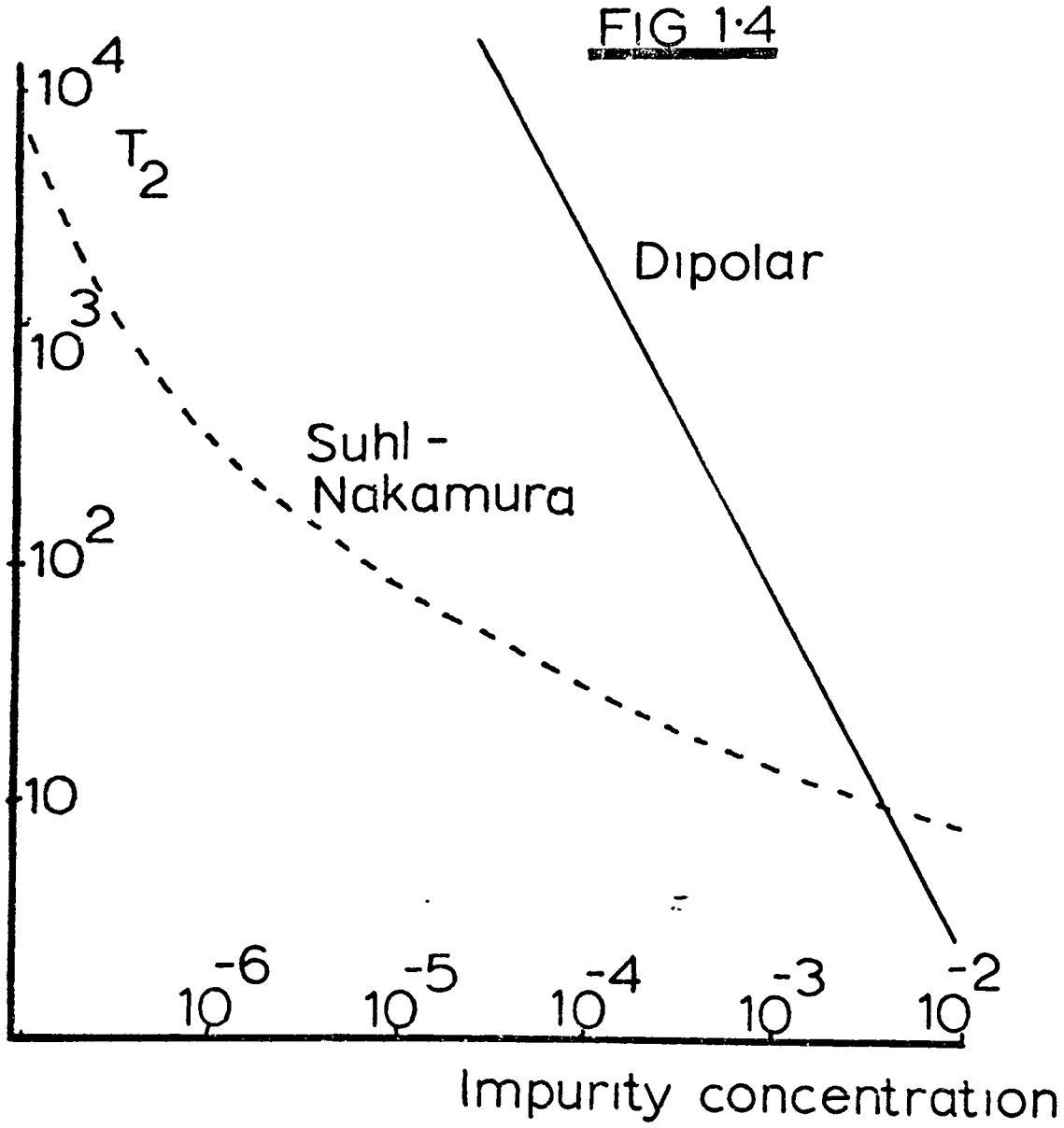

1·0
(1-W(0))res / (1-W(0))T
Change in the gamma ray anisotropy on resonance
0·25
Hard core
ω,τ
t
1
2
3
4
T2
2T2

FIG 1·4


10^4
T2
10^3
Suhl - Nakamura
10^2
10
Dipolar
10^-6
10^-5
10^-4
10^-3
10^-2
Impurity concentration

Effect of Relaxation on N.M.R/O.N.

Since the detection of the nuclear resonance involves the disturbance of the parent nuclear substate populations from their equilibrium values, the effect produced by the R.F field on resonance is in competition with the relaxation mechanisms acting on the impurity nuclei. The observation of the gamma-ray anisotropy after the removal of the R.F. field also provides a method of measuring the longditudinal relaxation time, $T_1$.

The dominant mechanism for the spin-lattice relaxation in ferromagnetic metals is usually represented by a spin-lattice coupling of the form

$$A.\underline{I}.\underline{S} = A[I_z S_z + \frac{1}{2}(I^+S^- + I^-S^+)]$$

where $\underline{S}$ is an effective spin operation for the conduction electrons, and I, the nuclear spin. Only transitions between adjacent nuclear substates are allowed involving electrons near the Fermi surface, where the initial and final states of energy E and $E \pm h\nu$ are occupied and empty respectively. Upward and downard transition probabilities have the form:

$$W_{m,m\pm1} = \frac{1}{2KC}|\langle m \pm 1 | I^{\mp} | m\rangle|^2 \int_0^{\infty} f(E)[1-f(E \mp h\nu)]\, dE$$

$$\text{where } f(E) = [1 + \exp{}^{(E-E_F)}/_{kT_L}]^{-1}$$

The spin-lattice, relaxation time may be defined by

$$\frac{1}{T_1} = W_+ + W_-$$

and has been shown to vary w ith the lattice temperature following the relationship [26]

$$\frac{1}{T_1} = \left(\frac{h\nu}{2kC}\right) \coth\left(\frac{h\nu}{2kT_L}\right)$$

This approximates to the Korringa form $T_1T = C_k$ at high temperatures. The $T_1$ as defined above is not directly related to the observables.

The experimentally observed relaxation time, $T_1$, is strongly influenced by the weighting of the $B_2$ tensor at high $I_z$ projections, and will tend to the limit at low temperatures

$$\lim_{T \to 0} \; T_1' = \frac{kC_K}{h\nu I}$$

It has been shown by Spanjaard, Barclay, [27 ] and Gabriel [28 ] that the determination of the true relaxation time, $T_1$, at low temperatures requires a multiexponential fit to the data, the amplitudes of the components depending on the initial conditions. The low temperature limit for $T_1$ is

$$\lim_{T \to 0} \; T_1 = \frac{2kC_K}{h\nu} = 2IT_1'$$

For nuclei of high spin the apparent relaxation time can therefore be an order of magnitude faster than the true value, and will show a deviation from the Korringa law at a higher temperature than $T_1$.

The interpretation of observed relaxation times depends sensitively on the initial conditions assumed for the steady state resonance condition. The question of the existence of a nuclear spin temperature has been discussed extensively for various situations of oriented nuclei, and is of obvious importance for the interpretation of relaxation measurements. and the comparison of the resonance effect at various temperatures. The dominant interactions associated with spin-spin relaxation mechanisms are the dipolar interaction and the Suhl Nakamura interaction. The analysis of the population redistributions through such interactions in terms of a $T_2$ relaxation time is most conveniently done using the method of the second moment [29 ] [30]. The relaxation time is defined by the equation

$$\frac{1}{T_2} = \frac{1}{2}\sqrt{\frac{\pi}{2\langle \Delta w^2 \rangle}} \; w_1^2$$

$$\text{where} \quad w_1 = \frac{2}{\hbar}\langle + - | H_{int} | - + \rangle$$

$$\langle \Delta w^2 \rangle = \langle w^2 \rangle - \langle w \rangle^2$$

The dipolar interaction takes the form: $\frac{\mu_1 \mu_2}{r^3}$, and shows a dependence of the relaxation time on the impurity concentration given by

$$\frac{1}{T_2(D)} \propto C^{3/2}$$

The order of magnitude calculation shown in Fig.1.4, shows that this mechanism becomes unimportant for concentrations below $10^{-3}$, compared with other terms in the full expression for $T_2$

$$\frac{1}{T_2} = \frac{1}{T_2(D)} + \frac{1}{T_2(S.N)} + \frac{1}{2T_1}$$

At low temperatures the number of thermally excited spin waves in the ferromagnetic metals is very small, but a powerful spin-spin interaction exists through the Suhl-Nakamura interaction, in which the magnons appear only as virtual excitations.

The Suhl-Nakamura interaction is temperature independent as long as the linear spin-wavetheory is valid. Energy conservation requires that the two nuclear transitions energies are identical, but the range of the interaction can be very large. The concentration dependence can be estimated using typical values for the nuclear hyperfine interaction and the properties of an iron lattice. For a nuclear spin of 1/2 and a value for the electronic spin s=5/2 the concentration dependence is

$$\frac{1}{T_2}(S.N.) \simeq C^{1/2} \exp\left(\frac{-C^{-1/3}}{15}\right)$$

The dependence shown in Fig.1.4 shows that this may be the dominant interaction for impurity concentrations of less than $10^{-3}$.

The Rudeiman-Kittel interaction provides an indirect coupling mechanism through the conduction electrons of the form

$$H_{Rk} = \Gamma_{R.K.} \underline{I}i \underline{I}_j$$

when $I_i$ and $I_j$ commute with $I_x$, there is no contribution to the second moment, but the contribution to the fourth moment causes a

narrowing of the central portion of the resonance line, and a broadening of the wings.

Typical concentrations of active $^{60}Co$ in a resonance iron foil of thickness 1μm giving an observed gamma-ray count rate of $1Ks^{-1}$ in a 3" x 3" NaI detector are $\sim 10^{-4} \longrightarrow 10^{-5}$. The Suhl-Nakamura interaction will give a spin-spin interaction independent of temperature corresponding to a value of $T_2$ of order 20 seconds. This is similar to the longitudinal relaxation time at a temperature of 30 mK. In this situation one may expect the nuclear substate population to be described by a spin temperature for typical counting periods for a resonance experiment. The situation for isotopes of shorter half life may be very different. An isotope of half life of 1 day for a similar activity will have a concentration of order $10^{-6} \longrightarrow 10^{-7}$, with a consequently weaker spin-spin interaction. Such a situation occurs for $^{109}Ag^{m}$ in iron and nickel, when the evolution of the substate population distribution must be considered without the existence of a spin temperature. This is discussed in chapter 3(b).

The R.F power required to produce saturation of the nuclear resonance depends on the relaxation times. Fig.1.5 shows the degree of saturation of the resonance as observed through the $B_2$ and $B_4$ orientation parameters, as a function of the effective radio frequency field amplitude experienced by the nuclei, and the spin lattice relaxation time. The effective R.F field is given by

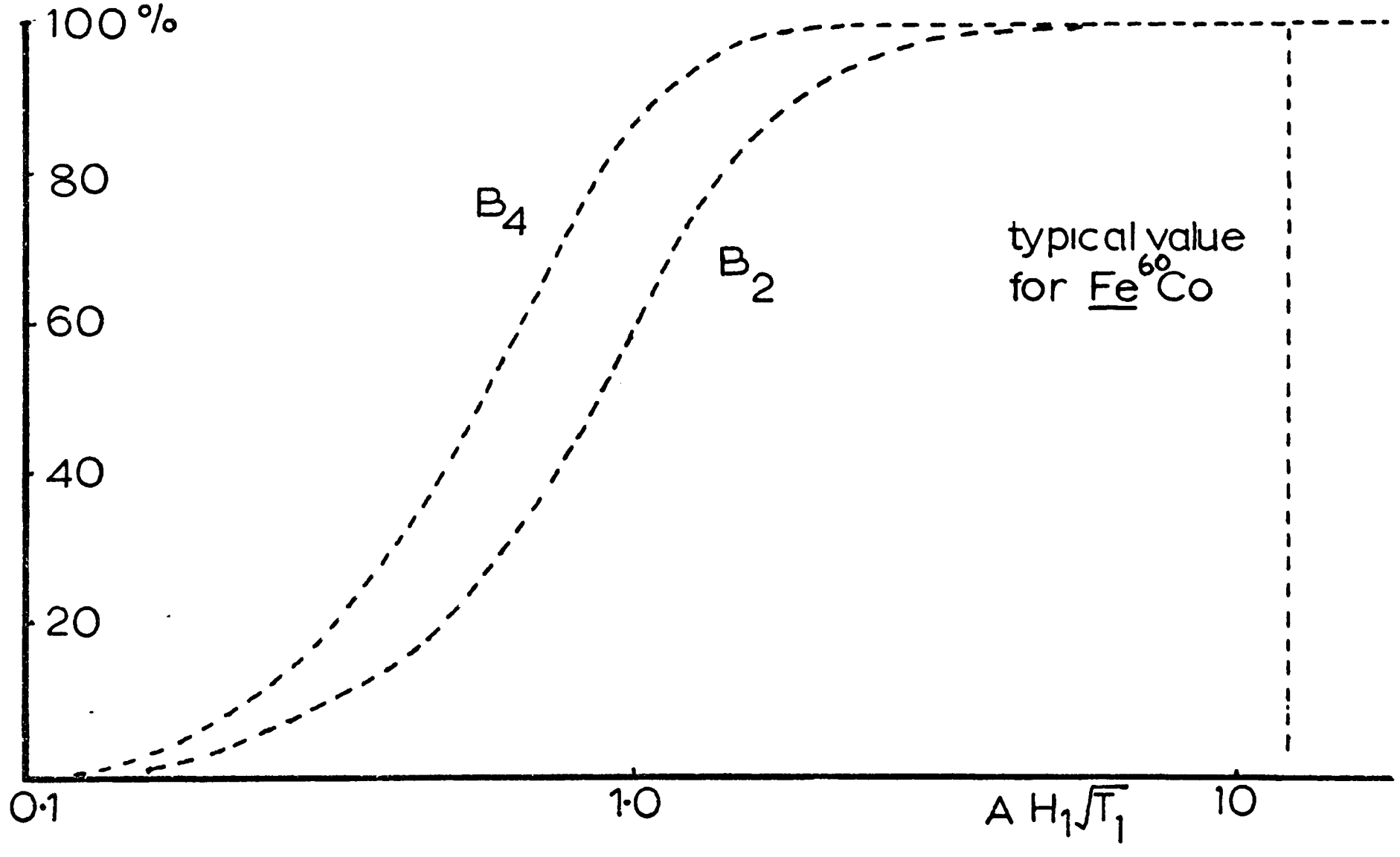
$$H_{R.F}^{eff} = H_{R.F}^{applied} \left[1 + \frac{H_{HF}}{H_{EXT}}\right] . \; n\sqrt{\frac{W_F}{\Delta w}}$$

$$A^{g} = \pi \delta \gamma_n^2 / 2$$

n is a small numerical factor representing the number of components in the R.F frequency spectrum, producing a resonance effect.

Change in the orientation parameters $B_2$ and $B_4$ as a function of the effective R.F. field amplitude.

FIG 1·5



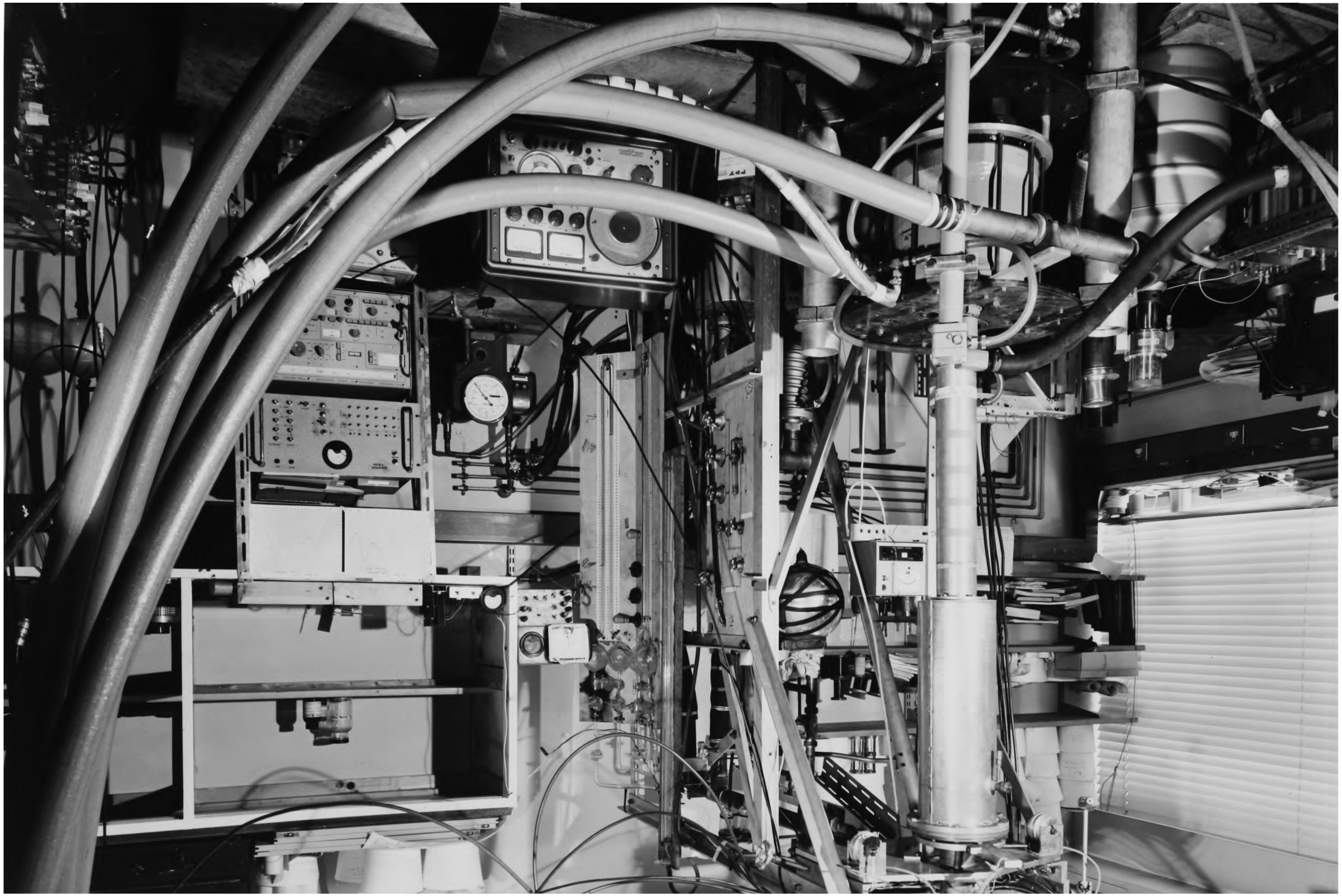
The dotted line shows a typical effective R.F field for the usual power level and modulation conditions for Fe $^{60}$Co. In the absence of "hard core" effects, the steady state population distribution for a system experiencing a pure magnetic hamiltonian and resonance absorption from an R.F. field will always tend to a spin temperature configuration. This effect is independent of the strength of spin-spin interactions, and is a result merely of the steady state population ratio established between each pair of nuclear substates through the competition between the resonance absorption and the spin-lattice relaxation. The attenuation of the applied R.F field within the metal surface will produce a range of degrees of saturation of the nuclear resonance experienced by nuclei throughout the sample, making the comparison of the resonance-induced change in the anisotropy at different temperatures a difficult problem. In the temperature range where the gamma-ray anisotropy is approximately linear in 1/T, the interpretation of the resonance signal as

$$\frac{W(o)_{RES} - W(o)_T}{1 - W(o)_T}$$

will give a reliable comparison between different temperatures for any degree of saturation. This approximation will not hold at lower temperatures and in the high temperature region where $1-W(o)$ is proportional to $1/T^2$.

## 2.1 The experimental method

In this chapter the experimental techniques are described for the production and maintainance of the low temperature required to produce a measurable degree of nuclear orientation. The description of the adiabatic demagnetisation technique is followed by a brief description of the gamma-ray detection and counting equipment for the measurement of the gamma-ray distribution. The measurement of the hyperfine interaction both with, and without, nuclear magnetic resonance is described, and some results from the detection of nuclear magnetic resonance in some simple systems are presented. Both techniques of measurement require the maintainance of ferromagnetic lattice temperatures in the range $1/T = 30K^{-1}$ to $1/T = 150\ K^{-1}$ for a sufficiently long time for accurate measurements of the angular distribution of the gamma-ray emission to be made. Thermal stability is provided by the large specific heat of a cooled paramagnetic salt associated with the entropy of the electronic spin system. After the demagnetisation a temperature variation can be provided either by the slow warming of the system from the unavoidable heat leaks, or by the introduction of heat through eddy current heating associated with an applied radiofrequency field.

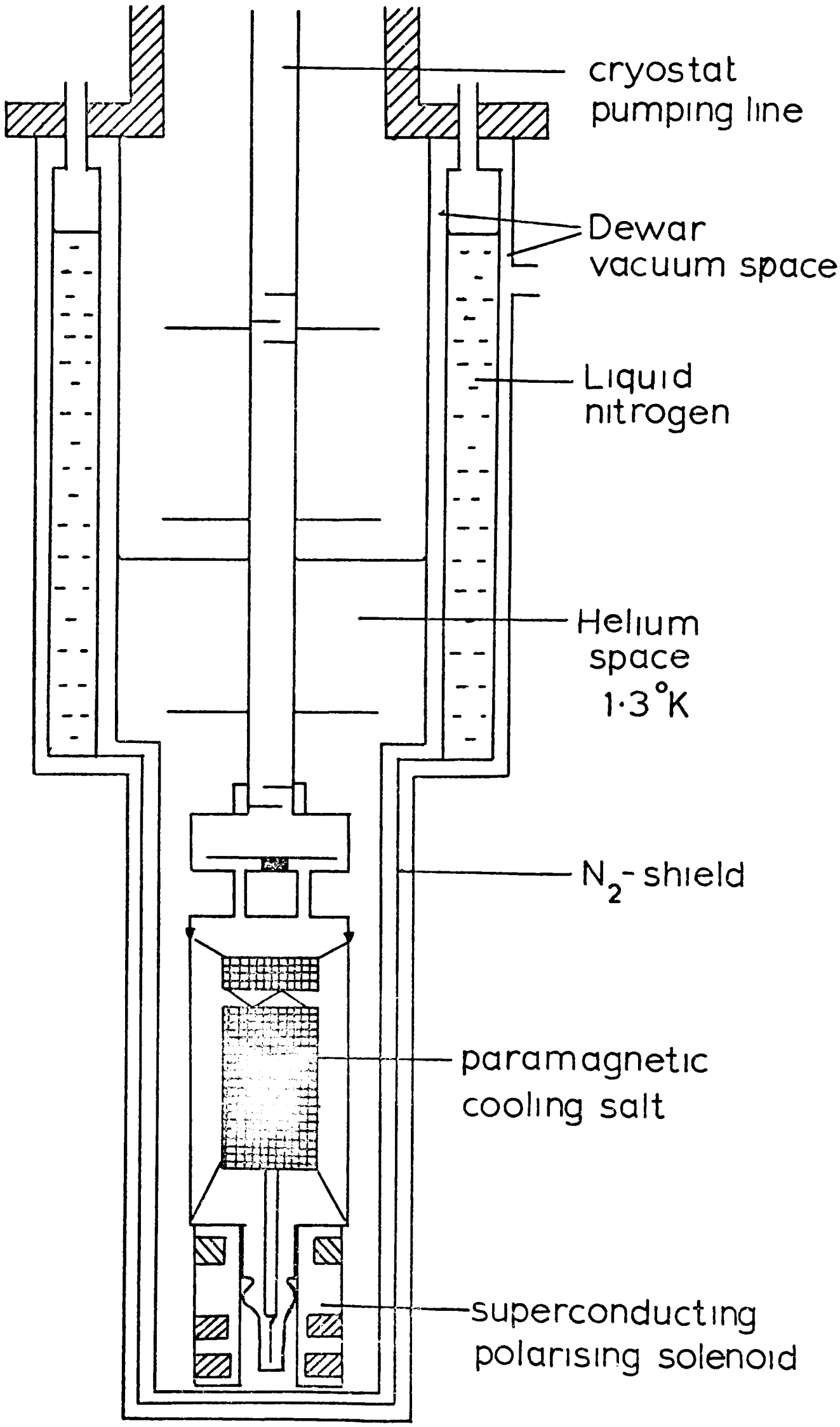


## 2.2 The adiabatic demagnetisation apparatus

The ferromagnetic samples containing dilute impurities of the radioactive isotopes are cooled by contact to the paramagnetic salt in the adiabatic demagnetisation cryostat. The paramagnetic salts used in the cooling process are chrome potassium alum ($CrK(SO_4)_2 \cdot 12 \cdot H_2O$) and cerium magnesium nitrate ($Ce_2Mg_3(NO_3)_{12}24H_2O$). Both have a small lattice entropy at $1^oK \rightarrow 1.3^oK$, the initial temperature of the demagnetisation process. The application of a large magnetic field produces a splitting of the [2J+1] fold spin degenerate ground state, greater than, or comparable to $K.T_i$. The removal of the magnetic field, when the salt is isolated at constant entropy, preserves the Boltzmann population distribution over the 2J+1 ionic levels, but the reduced Zeeman splitting represents a lower final temperature. The lattice cools through the spin-lattice relaxation mechanisms, and, because of the lattice specific heat, will reach a final temperature near that for an ideal adiabatic demagnetisation of the electronic spins. The demagnetisation must be sufficiently slow to make use of the larger specific heat associated with the spin system in high magnetic fields to cool the lattice efficiently. The cooling continues until the Zeeman splitting of the ionic levels is comparable with the zero-field splitting resulting from the interaction of the magnetic ions with their environment.

Thermal contact to the cooled paramagnetic salts was usually made through a large number of 49 s.w.g. enamelled copper wires embedded in a slurry of finely powdered chrome alum or C.M.N. mixed with a 50:50 glycerol/saturated-solution mixture. This arrangement provided a contact area of 6-10 thousand square centimeters between the copper and the salt; and, by using the finely powdered salt, reduced the effects of the poor thermal conductivity of the salt at low temperatures. The initial heat

FIG 2·2


cryostat
pumping line
Dewar
vacuum space
Liquid
nitrogen
Helium
space
1·3°K
$N_2$- shield
paramagnetic
cooling salt
superconducting
polarising solenoid

leak to the salt during the demagnetisation from cryopumping of residual Helium in the cryostat was reduced by the introduction of a second 'guard' pill above the cooling salt. The 200g of chrome alum used in the cooling salt maintained a temperature of less than 20mk for 12 hours or more, without R.F. heating; and 4 → 5 hours with the usual R.F. power levels used for resonance. A typical cooling specimen is shown in Fig.2.1. The ferromagnetic sample is soldered to the end of the cold finger made by compressing the free ends of the copper wires into a rigid rod.

Cerium magnesium nitrate can be cooled to below 0.02°K compared with 0.010 K for Chrome Alum, and can be used to extend the available temperature range below 10 mk. The C.M.N. cooling specimen was made from crystals grown from a saturated solution containing the molar proportions of cerium nitrate and magnesium nitrate. The hexagonal crystals were finely powdered and mixed with a glycerol/saturated solution mixture similar to that for chrome alum. Thermal contact was made through 30,000 49 s.w.g. copper wires in one specimen, and to 50, 25μm, copper fins in a second specimen. The latter system gave lower temperatures at the sample suggesting that contact to the clean copper surface was better than that to the varnished copper wires, despite the nominally greater surface area presented by the wires. The conditions required for a successful demagnetisation of CMN are more stringent than for chrome alum for three reasons:

1) The very poor thermal conductivity requires a finely powdered sample in intimate contact to the copper. The removal of the heat of magnetisation is much more difficult than for chrome alum, taking 30 to 60 minutes. The thermal contact at low temperatures follows a temperature dependence of the form [31]

$$\dot{Q} = KA\left(\frac{1}{T_s^3} - \frac{1}{T_c^3}\right)$$

For a constant heat leak to the copper cold finger a value of KA of 300°Kergs/sec is required to cool the copper to within 10% of the CMN; four times greater than that required for chrome alum.

2) The ground state of the $^2F_{5/2}$ state of $Ce^{3+}$ has an anisotropic g factor ($g_{\parallel} = 0.25$, $g_{\perp} = 1.84$). A polycrystalline salt pill will not make full use of the cooling power since crystal orientations showing small values of g will not allow all the entropy to be removed with the initial applied field at 1°K.

3) The specific heat of the demagnetised salt is very much smaller than that of chrome alum because of the smaller internal field splitting and the anisotropic g value. The salt does not have such a large heat capacity for cryopumping the residual exchange gas during the demagnetisation. Chrome alum 'guard pills' were included to reduce this heat leak.

The lowest temperature reached by the CMN pills was $\frac{1}{T} = 150\ k^{-1}$, representing a significant extension of the $\frac{1}{T} = 20$ to $\frac{1}{T} = 90\ k^{-1}$ temperature range for chrome alum, but not as good as the results obtained on the non-resonance apparatus with a lower initial temperature and smaller 'dead volume' in the cryostat. The smaller specific heat of the C.M.N. specimen made it less convenient for the resonance experiments in which a constant temperature must be maintained over long periods despite the R.F. eddy current heating. The cold finger separates the ferromagnetic sample from the cooling salt to reduce the stray field on the salt from the solenoid used to provide a polarising field on the nuclear orientation sample.

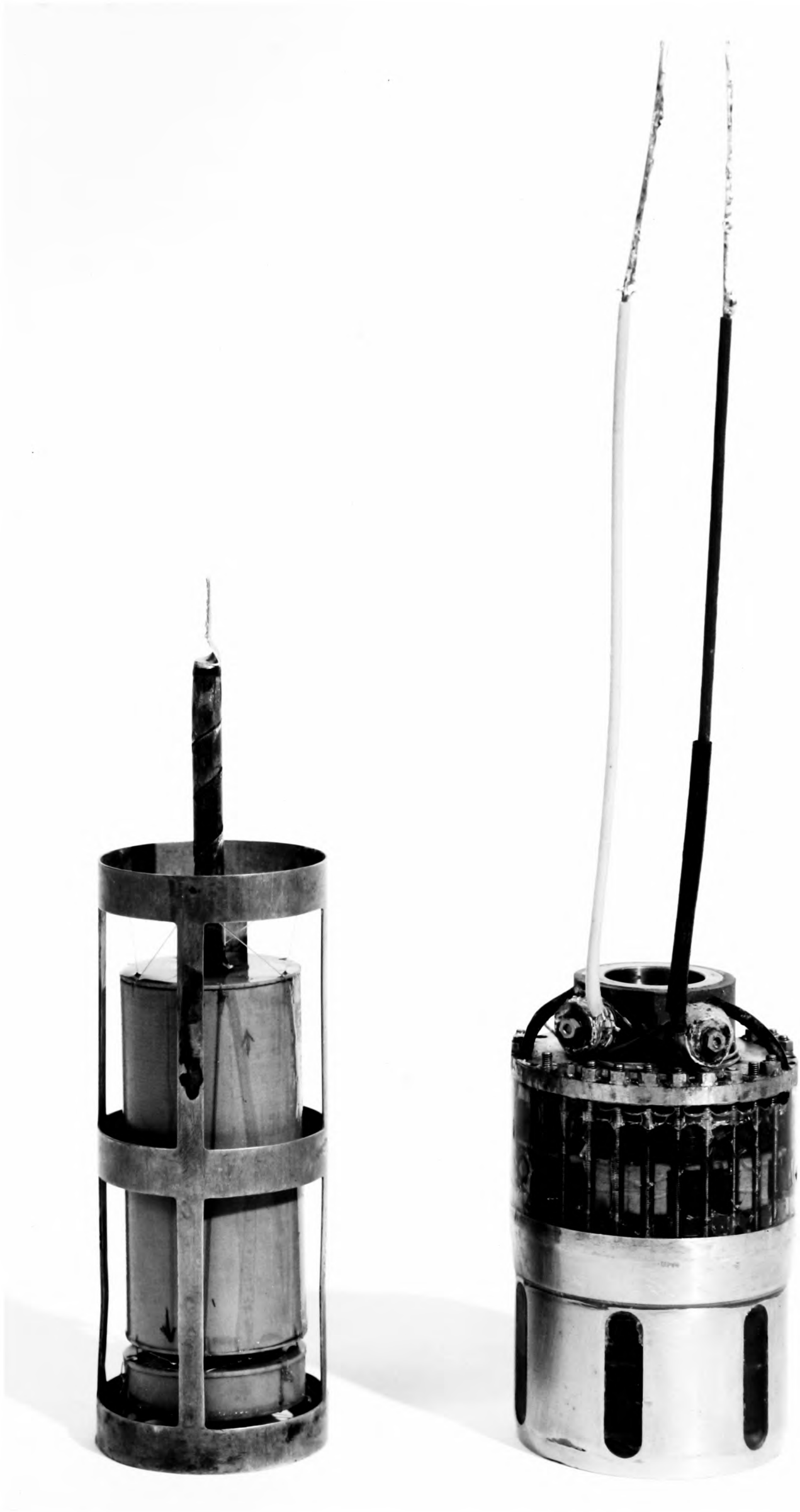
The apparatus is shown in Fig.2.2. It consists of a single He bath suspended in a nitrogen bath providing a 77°K shield, both insulated by a common vacuum space. The helium is pumped by an Edwards DB3 Booster pump backed by a 150 l/m rotary pump, producing a helium bath temperature

of 1.05°K to 1.30°K for 16 hours. The salt pill is suspended inside a separate vacuum jacket assembled at the Wood's metal seal before each experiment. The salt is cooled to the helium bath temperature by thermal contact through a pressure of $5 \times 10^{-4}$ τ of helium exchange gas, before, and during the magnetisation process. This space is pumped to $10^{-5}$τ before demagnetisation. The initial conditions of 40 kOe and 1.2°K consistently produced a temperature of 11 to 14 mK after demagnetisation using chrome alum, and 7 mK to 10 mK with C.M.N.

The magnetic field for a salt demagnetisation was provided by a 4" bore, water cooled, copper magnet, raised around the dewar and removed after demagnetisation. The electrical power was supplied by the 2MW DC generating facility of the Clarendon Laboratory and the magnet cooled by a 15HP pump providing 220 g.p.m. of de-ionised water. The solenoid consisted of four helical coils separated in pairs by 3 cms giving a field of 12 Oe/A. The magnet and cryostat pumping were controlled from a console outside the room.

The cryostat and magnet provided a simple and reliable method for the production and maintainance of the very low temperatures required for the experiments. In particular, the single helium bath construction and design of the demagnetisation cryostat both showed great reliability in assembly, and the absence of leaks.

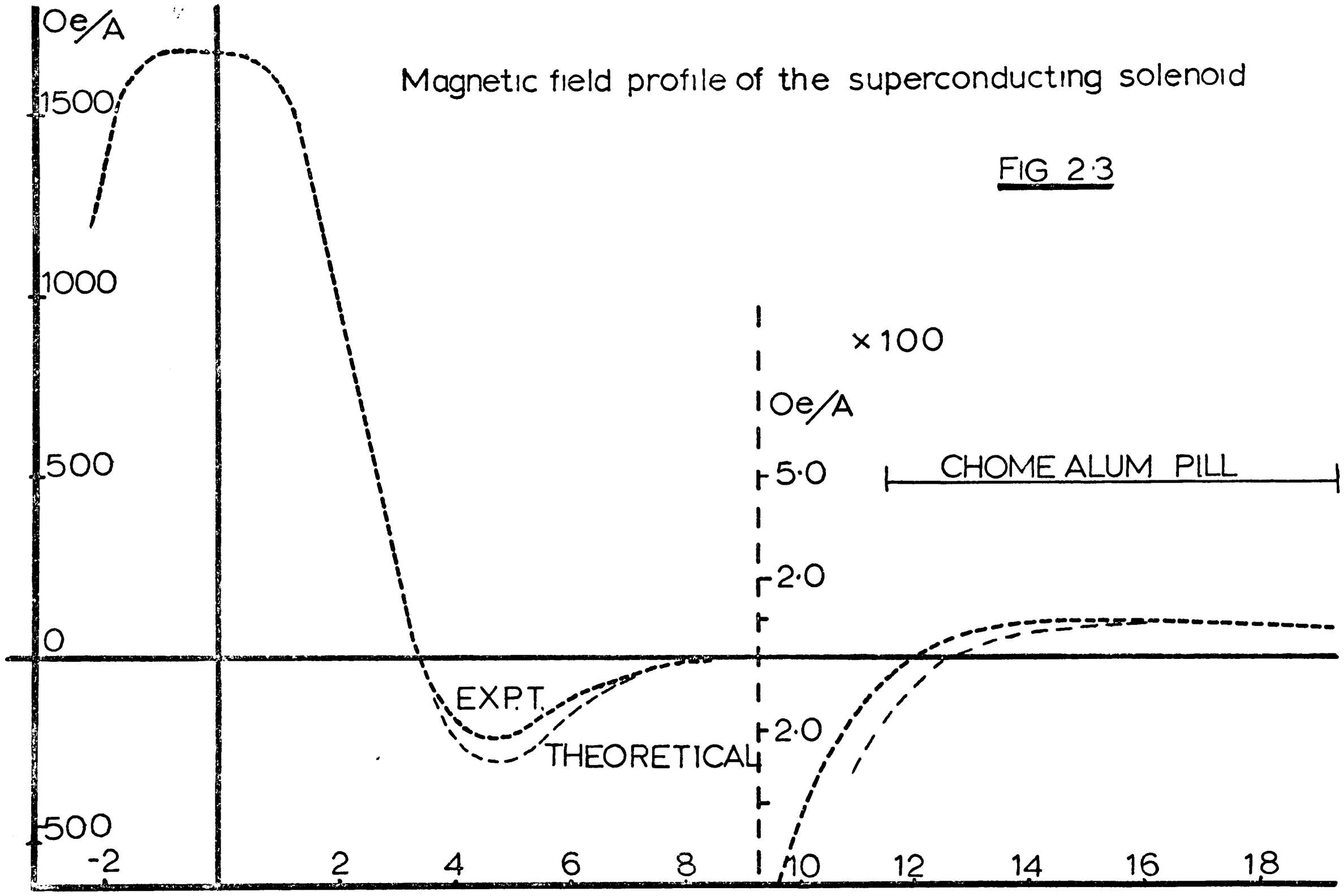
The paramagnetic salt was suspended from a metal cradle in the cryostat by a system of nylon threads. The monofilament nylon provided a rigid suspension at low temperatures with a high breaking force of order 20 kg, and poor thermal conductivity. The total estimated heat leak through the nylon suspension is of the order of 5 ergs/min. The vacuum jacket containing the salt was well protected from radiation at room temperature and nitrogen temperature by a system of baffles in the pumping lines and the helium space. The dominant heat leak was from



radiation from the 1.3K walls of the cryostat and conduction through, and cryopumping of, the residual helium exchange gas not removed by pumping. The total heat leak was of the order of 1 erg/sec, compared with the R.F. eddy current heating of 3 to 10 ergs/sec typical during a resonance experiment.

The polarising field applied to the ferromagnetic samples was provided by a superconducting solenoid, suspended from the bottom of the demagnetisation cryostat, in the helium bath. Two solenoids have been used, both with a counterwound compensating coil to minimise the stray field at the paramagnetic cooling salt. The magnet used for the resonance experiments is wound with 33 thou. Nicmax Nb/Ti filamentary wire giving a magnetic field of 448 (1)Oe/A in a bore of 2.3 cms. The nuclear magnetic resonance requires a uniform applied field over the sample to avoid additional inhomogeneous broadening of the resonance line. This magnet provides a uniform field to within 1% over a volume of $1cm^3$. The magnet was not run in a persistent mode because of the necessity of changing the field during an experiment, and the low inductance of the magnet produced a decay in the field of 2% per hour, with a resistance of $2 \times 10^{-7} \Omega$ at the soldered terminals, when in the persistent mode.

A high field polarising solenoid has been designed and built during the last 18 months. The independent measurement of the magnetic moment and the hyperfine field of an impurity depends on the accurate measurement of the shift of the nuclear resonance in an applied field. The magnet was designed to produce a field of 60 kOe on the nuclear orientation sample with less than 50 Oe on the paramagnetic salt.




Magnetic field profile of the superconducting solenoid

FIG 2·3

These conditions should make possible independent measurements of nuclear magnetic moments to better than 1%. The large field alone may provide sufficient nuclear polarisation to detect the nuclear magnetic resonance on isotopes for which a large hyperfine field is not available, or for which low solubility precludes the use of a ferromagnetic host. The field profile of the magnet is shown in Fig.2.3. The field homogeneity is 0.5% in a volume of $1cm^3$ with a gauss/amp of $1667\pm3$g/a.

The smaller superconducting solenoid is wound on a Tufnol former with no reinforcement between the winding, but the larger forces in the 60kOe solenoid require a more rigid construction. The wire is wound on a anodised Dural former and the finished magnet is encapsulated in araldite, inside a stainless steel case, to contain the large repulsive forces set up between the main coil and the compensating coil. This magnet has been tested up to 65 kOe at $4.2^{o}K$ but instabilities due to the forces on the current leads have so far restricted its operation to less than 50 kOe in the experimental arrangement.

The current leads for the magnets are composite copper - superconductor, designed to minimise the joule heating and the thermal conductivity, both of which increase the helium evaporation rate. The thermal conductivity in the superconducting state is very small, so ideally one requires superconducting wire in all regions where the temperature is less than $T_c$. The surface area of the leads is large, to increase the cooling effect of the cold helium gas above the liquid surface, and the leads are thermally anchored at $77^{o}K$ to minimise the heat flow by conduction from room temperature. Both the superconducting magnets require 40A to produce the maximum designed field. The current leads are capable of taking 25A with no effect on the helium boil off rate from the dewar, but higher currents produce a rise in the helium bath temperature.

## 2.3 Radio frequency apparatus

The optimum orientation for the applied R.F. field $H_1$, is in the plane of the surface of the metal foil sample, and perpendicular to the axis of static polarising field defining the axis of orientation. The R.F field is provided by two single loops either side of the specimen through which a small current is passed at the required frequency. The loops are mounted inside the polarising solenoid such that the glass end of the cryostat lies between them. The dimensions of the coils are designed to roughly match the impedance of the transmission cable. The measured R.Fresponse of the loops as a function of the applied frequency shows an oscillatory behaviour due to reflexions along the transmission cable but the response remains constant to within 20% over the range from 50 MHz to 450 MHz. The cable is standard 50$\Omega$ co-axial cable, except for a length of rigid German silver coaxial cable in the dewar, to reduce the heat influx to the helium by conduction down the copper conductors of the standard cable. The amplitude of $H_1$ applied to the sample can be calculated for a given voltage output of the R.F generator. The R.F. coils used in all the experiments described provide 12 mOe/Volt. The R.F. power level to observe resonance, but also maintain a sufficiently low level of eddy current heating in the cooper cold finger and sample, depends on the frequency. The typical value at 150MHz is 0.35v giving a R.F field amplitude of 4 mOe. The frequency dependence of the R.F heating should be proportional to $\nu^{\frac{1}{2}}$, but in practice, frequencies about 300 MHz appear to produce an unexpectedly large eddy current heating. This may be associated with resonant effects in the transmission cable. At high frequencies a reduced power level of 0.1v is required to maintain the low temperature, but this appears to be sufficient to observe the resonance of $^{192}Ir$ in cobalt at 350 MHz.

The radio frequency power is generated by a Solatron sweep oscillator and a Schlumberger F.S.M.500 R.F synthesiser. The solatron provides a basic frequency of 1MHz and a signal at a frequency between 21MHz and 22MHz. The Schlumberger gives a phase-locked output at any frequency from 27 MHz to 470MHz at a frequency $\nu_{SCH} + \delta\nu$ where $\delta\nu$ is the frequency increment above 21MHz supplied by the Solatron unit. The R.F. output is frequency modulated at 100Hz by a saw-tooth sweep generator controlling the frequency output of the solatron. The frequency calibration for the automatic frequency control is

$$\nu_{out} = 21\text{MHz} + (0.1\ V_{in})\text{MHz}$$

with a range 20.6 MHz to 22.4 MHz.

The R.F output level is continuously variable from 0 → 2V and is frequency independent. This arrangement allows an R.F signal of the chosen amplitude to be frequency modulated about any centre frequency from 27-470 MHz with an amplitude of frequency modulation of up to 400kHz. The stability of all the components gives a stable centre frequency to $10^{-7}$ and a stability of $10^{-5}$ in the frequency modulation amplitude and frequency.

## 2.4 Detectors and Counting Equipment

The Dewar containing the adiabatic demagnetisation cryostat was constructed with aluminium 'windows' in the tail to reduce the gamma-ray scattering, with the consequent large corrections involved in the spectrum analysis. The usual geometry involves a gamma-ray detector below the dewar, on the axis of the polarising field, and occasionally another detector in the equatorial plane of the sample and the polarising field.

Two types of gamma-ray detector were used, the choice depending on whether high resolution or high efficiency was required. The interactions of gamma-rays with the material of the detectors can occur through three mechanisms.

1) The photoelectric effect. This process is one in which a photon interacts with an atom in such a way that its total energy is absorbed by a single electron. The cross section for this process is proportional to the fifth power of Z of the interacting atom, and falls off rapidly with increasing energy. For the detectors used this process is only important for photon energies below 100 keV. [17]

2) Compton scattering. This form of interaction involves the scattering of a photon by an electron which absorbs part of the energy of the incoming photon. For the interaction with a free electron, the energy lost by the gamma-ray to the electron is given by

$$T = \frac{E_\gamma}{1 + m_o C^2/E_\gamma(1-\cos\phi)}$$

where $\phi$ is the angle between the incident and the scattered gamma-rays. The cross section for this process is proportional to Z, and, although it falls off with increasing energy, it is the dominant primary interaction for gamma-rays of energy between 0.5 and 5 MeV.

3) Pair production. This is only important for gamma-rays of energy greater than 1022 KeV, when a position and an electron can be created with a total energy equal to that of the photon.

Both types of solid state detector work with a combination of all three mechanisms; the main criterion for the measurement of the gamma-ray energy is that all the energy should be absorbed into electron energy in the detector. For a sufficiently large active volume in the detector, this will occur through multiple Compton scattering and photoelectric processes.

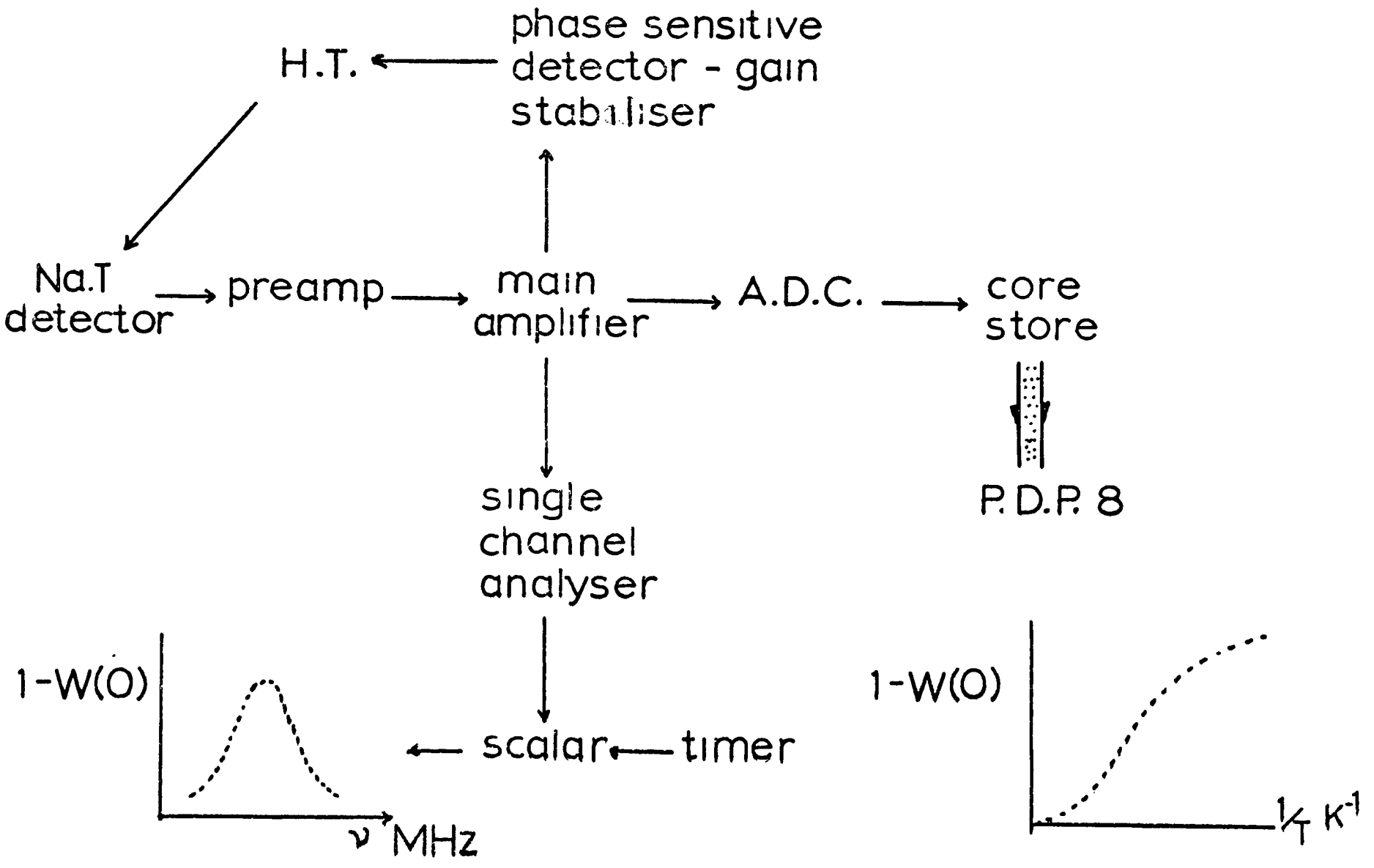
For the nuclear magnetic resonance experiments, a high detector efficiency is required to give a maximum count-rate and sensitivity. The resolution is of secondary importance, as the gamma-ray anisotropy is used only as a means by which the nuclear resonance can be observed. Sodium iodide (NaI) activated with thallium has a high probability of photoelectric emission because of the large Z of the iodine. The detector depends on the excitation of electrons to the conduction band. The lifetime of the electron states is very short owing to the high probability of trapping at luminescence centres. The de-excitation occurs with the emission of low energy photons which eject electrons from the photocathode of a photomultiplier tube. The amplification by secondary emission at each dynode stage gives a detectable voltage pulse of amplitude proportional to the incident gamma-ray energy. The typical resolution for the 3" x 3" detectors used was 8.5%.

For the experiments involving complex decay schemes where an accurate measurement of the gamma-ray anisotropies required high resolution, commercial lithium drifted germanium Ge(Li), detectors were used. The low recombination and trapping probabilities of intrinsic germanium give a sufficiently long lifetime, for electrons excited into the conduction band, to allow charge collection at the electrodes, and

detection of a charge pulse proportional to the incident $\gamma$-ray energy. A region of low intrinsic conductivity can be produced in the "depletion layer" formed at a reverse biased p-n junction in a germanium crystal. The Lithium provides an n type region in a predominantly p type germanium crystal. The detector is maintained and operated at 77°K to limit further diffusion of the Lithium and reduce thermal fluctuations. The resolution of the detectors used was 2keV to 3keV at a 1MeV incident gamma-ray energy, but the efficiency is limited by the volume of the useful depletion layer. Both Ge(Li) detectors had an operating volume of 40 cc giving an efficiency of 7.5% compared with a 3" x 3" NaI detector measured at 25 cms from the gamma-ray source. The charge pulse signal from the Ge(Li) detectors is initially amplified by low noise F.E.T. preamplifiers giving voltage output pulses. The detectors are stable against small bias voltage changes so no form of spectrum stabilisation was required.

Fig. 2.4 shows a block diagram of the counting arrangement for resonance and for nuclear orientation. The observation of the nuclear resonance requires a very stable pulse amplification and single channel analyser setting. The gamma-ray energy calibration of the NaI detector output varies critically with the H.T. applied to the photomultiplier, and is also very sensitive to small stray magnetic fields. The NaI gamma-ray spectrum was stabilised against changes in the H.T and amplification gain by a phase sensitive detector using a signal proportional to the countrate in an energy/voltage window modulated over a prominent peak in the spectrum. This provided a stability of better than 0.5% in the energy calibration over a period of 4 to 5 hours required for the experiment. Whenever possible the energy window of the single channel analyser was set between the half height energies of the observed peak to minimise the changes in count rate associated with gain changes in the spectrum.

FIG 2·4 Block diagram of the gamma-ray counting equipment



The photomultiplier tube of the NaI detectors was shielded against the stray axial field from the polarising solenoid by a cylinder of soft iron enclosing the tube, and another similar cylinder around the dewar in the region of the polarising solenoid. The output of the single channel analyser was displayed on a Nuclear Enterprises (N.E.) Scalar for counting periods of 100 secs.

The pulses from both the Ge(Li) and NaI preamplifiers were amplified using N.E. 4603 linear pulse amplifiers producing 0 to 10v output pulses for the gamma-ray energy range, with a rise time of 2 μsec or 5 μsec. The amplified pulses are analysed in either the Victoreen SCIPP 1600 multichannel analyser or the Nuclear Data 4096 channel analyser. In both instruments the pulses are converted by the A.D.C. into digital form, and a spectrum of count rate versus channel number is built up. The measurement of the nuclear orientation effect involves counts of 10 min to 30 min duration after which the spectrum is punched onto 8-hole tape, and the memory erased. Both instruments now work on a recycling mechanism, requiring very little attention during the counting period. The adequate reproduction of the 2keV to 3keV resolution from the Ge(Li) detectors requires accummulation into at least 1000 channels and high stability in the amplification and analog to digital conversion. This is provided by a Wensel amplifier and the Nuclear Data analyser. The SCIPP 1600 was mainly used for the accummulation of NaI spectra into 200 or 400 channels during the N.M.R./O.N. experiments.

The analysis of the spectra to produce the temperature dependence of the gamma-ray intensities as a function of the temperature requires several corrections:

1) Decay correction. This is only appreciable for the counting periods used if the half life is less than 50 days.

2) Background correction for degraded radiation from higher energy transitions under the required peak.

3) Sold angle corrections for the gamma-ray energy and detector geometry.

4) Applied field correction for the temperature calculated from the gamma-ray anisotropy of the Fe$^{60}$Co thermometer

Corrections 1) and 2) are included in the analysis of the $\gamma$-ray spectra using the P.D.P. 8L computer. The background corrections from a Ge(Li) detector simply involve the extrapolation of the background level at energies near that of the peak, but the poor resolution of the NaI detector requires an independent measurement of the background from the room (mainly from $^{40}$K in the walls at 1460 keV) and higher energy $^{60}$Co gamma rays. A correction for the anisotropy of the degraded $^{60}$Co radiation under the peak must also be included for a detailed analysis.

The solid angle corrections used for NaI are those calculated by Yates [33] and, for the Ge(Li) detectors, the value of $Q_{2,4}$ has been computed for various energies and distances. [34]

## 2.5 Thermometry

All the temperature measurements below 1°K were obtained from the anisotropy of the 1173 and 1333keV gamma transitions from the decay of $^{60}Co$. The decay scheme [Fig.2.5] gives unambiguous decay parameters for both transitions and identical anisotropies on both gamma rays. The hyperfine interaction is well known from the nuclear magnetic resonance of $\underline{Fe}^{60}CO$ (at 166.00±.05MHz) giving a hyperfine field of -290.1±1kOe. The thermometers used consisted of iron foils, 0.01 x 0.2 x 0.7cm$^3$, soft soldered to the end of the copper cold finger near the sample. The small radioactive heating of 0.2 ergs/min associated with the β decay of the 1μc of $^{60}Co$ gives a negligible temperature gradient between the sample and the copper cold finger. The only errors in the temperature measurement can arise from the statistical fluctuations of the gamma-ray countrate and incomplete polarisation of the iron host. Lines [35] has given a very full description of the saturation characteristics of iron foils when used for nuclear orientation measurements. The use of a thin iron foil, well annealed, and oriented with the long axis parallel to the applied polarising field, reduces the demagnetising field and gives a more rapid saturation of the magnetisation with the increase of applied field. Lines has shown that an iron sample of dimensions 0.5 x 0.3 x 0.05 cm$^3$ generally requires an applied field of 5kOe to produce greater than 99% saturation of the magnetisation. The saturation of the magnetisation varies as $A/H^2_{applied}$ near saturation but the gamma-ray anisotropy is proportional to $P_2 = 1/2(3\cos^2\theta - 1)$ which varies as $3A/H^2_{applied}$. The field requirement for complete saturation of the gamma-ray anisotropy is therefore more stringent than for the magnetisation. For most of the orientation experiments an applied field of 5 kOe or 10 kOe has been used. No difference in the degree of saturation has been detected between these two

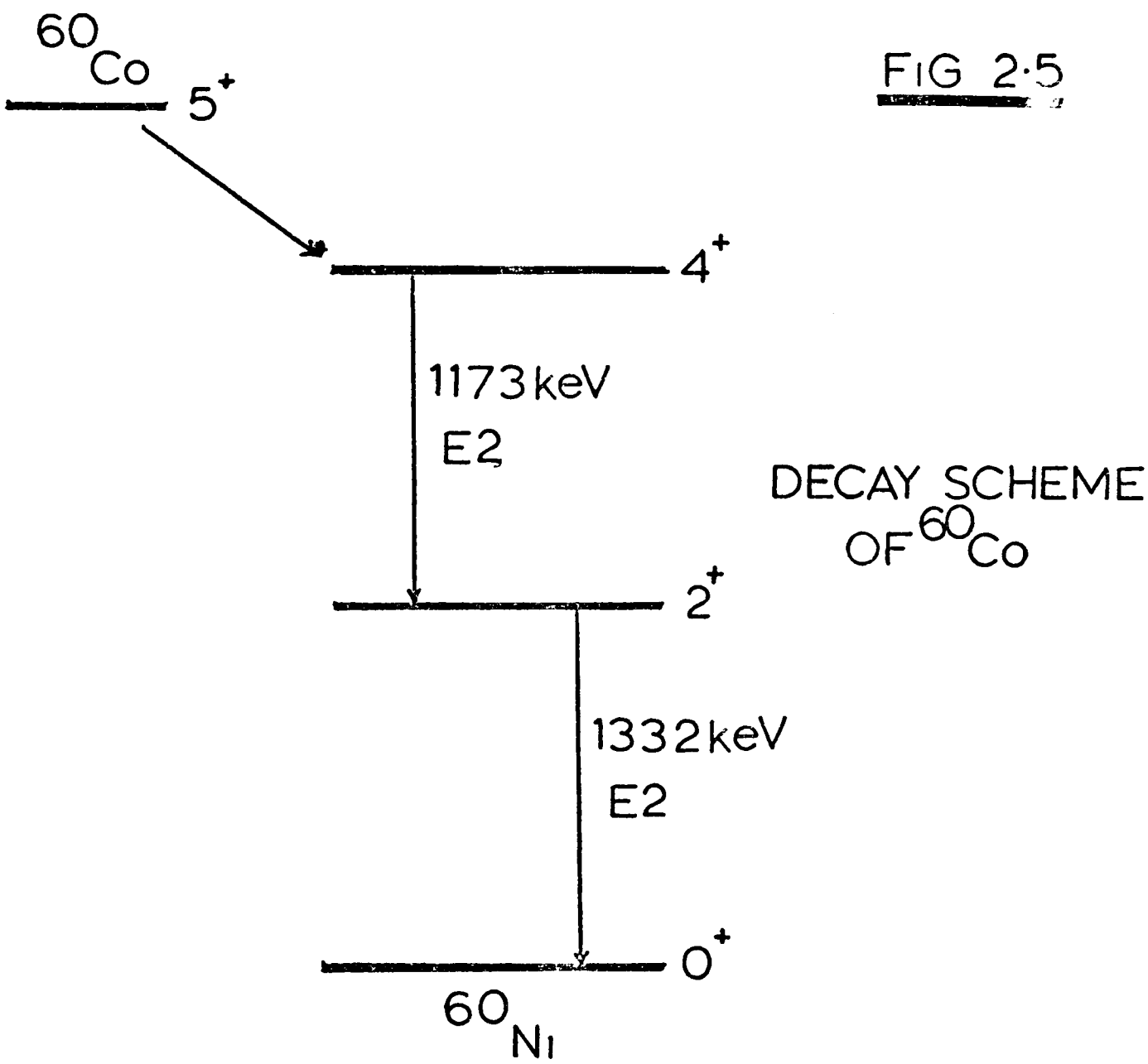
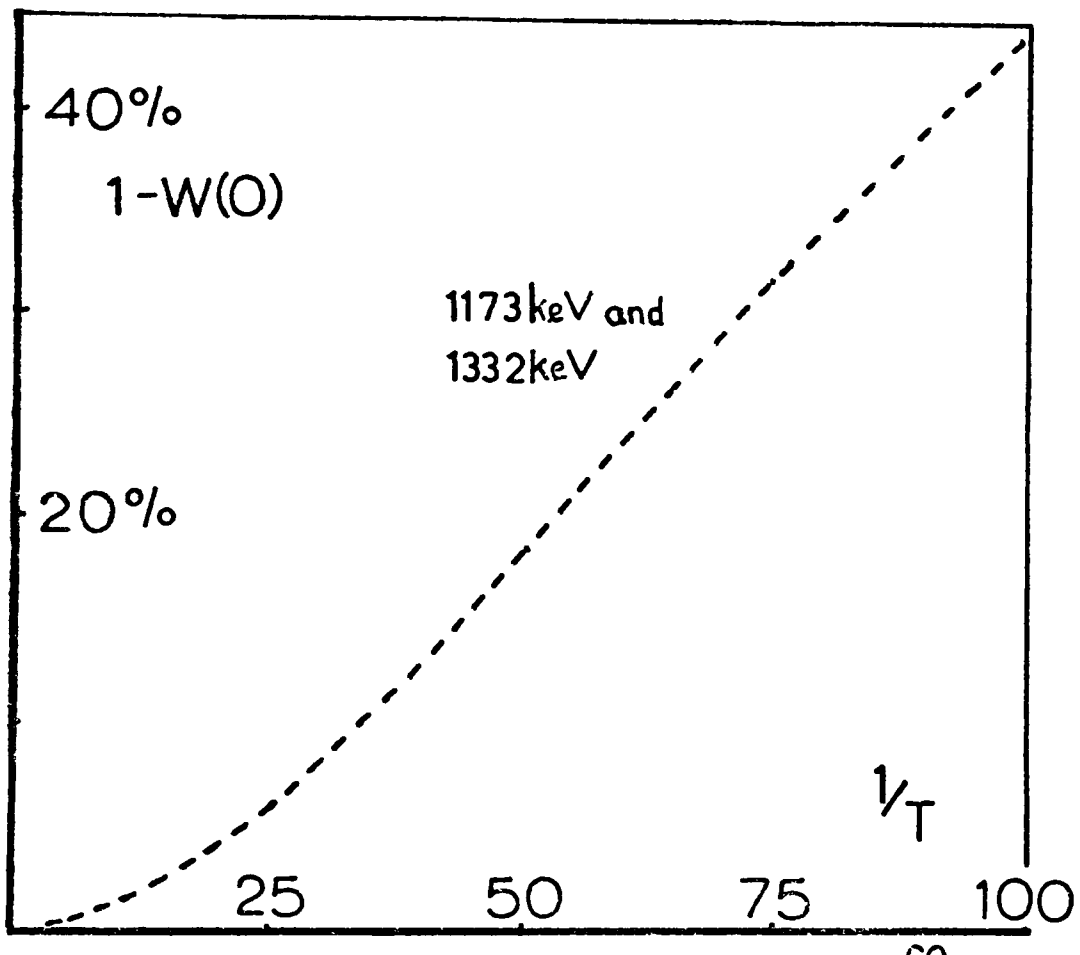



FIG 2·5

DECAY SCHEME OF $^{60}Co$




Axial gamma ray anisotropy of Fe $^{60}Co$ as a function of the temperature

fields with the thermometers used. This is consistent with the expectation that a field of 5kOe will produce at least 98% saturation of the gamma-ray anisotropy for the thermometers used. The temperature measurement on all orientation experiments shows a statistical fluctuation of $\pm 1$ in 1/T in the range $1/T = 30K^{-1}$ to $1/T = 130\ K^{-1}$.

Carbon resistance thermometers were used to help with the helium transfer to the dewar, and to observe the cooling of the paramagnetic salt after magnetisation; although the exchange gas pressure was found to give an adequate estimate of the temperature of the salt. The resistor in the salt pill lost contact with the salt temperature below $1^{o}K$ because of the resistive heating from the D.C. bridge current.

## 2.6 Resonance method

As discussed in chapter 1, the inhomogeneous broadening of the nuclear magnetic resonance line requires a frequency modulation of the R.F field to produce a measurable resonance effect. This has the indirect advantage of providing a check on the lattice temperature of the sample at each frequency with the same R.F power level by the observation of the gamma-ray anisotropy with only the R.F carrier wave applied to the sample. This is an important measurement because the imperfect matching of the R.F coils to the transmission cable will produce a fluctuating power level as a function of frequency, with an associated frequency dependence of the sample temperature. The R.F eddy current heating is frequently large enough to establish a large temperature gradient between the copper cold finger and the chrome alum salt, so [illegible] a change in the R.F power level has a more drastic effect than simply a change in the rate of warming. The resonance signal at each frequency is also influenced by the undisturbed thermal equilibrium anisotropy, so a correction must be included when the

anisotropy shown by the impurity gamma-rays changes significantly as the frequency is swept across the resonance line.

Because of the inhomogeneous broadening the anisotropy will not be completely destroyed at one frequency setting, even with modulation. The change in the anisotropy can be written as

$$\Delta(1-W_o) = \sum_i N_i \, S_i \, (H, T) . f(\nu)$$

The summation being over all the radioactive impurity nuclei. $N_i$ is the proportion of oriented impurity nuclei experiencing an R.F field of amplitude $H_1$ at the site i, and $S_i(H, T)$ is the degree of resonance saturation produced. The calculations of resonance saturation show that $S_i(H, T)$ is proportional to $1-W_o$ for the temperature range where $1-W(o)$ is proportional to $1/T$. To a good approximation the measurement of a resonance signal of $S = \frac{(1-W(o))_{FM}}{(1-W(o))_{CW}}$ will give an accurate representation of $f(\nu)$.

The inhomogeneous broadening mechanisms discussed in chapter 1 tend to give a gaussian form to the resonance lineshape. This is modified in practice by the amplitude of the frequency modulation which will give a resonance signal from an integration over the gaussian distribution from $\omega_{CW} - \Delta\omega$ to $\omega_{CW} + \Delta\omega$. This produces an apparent broadening of the resonance line, but the knowledge of the modulation amplitude and the observed linewidth enables the natural linewidth associated with the Gaussian distribution to be deduced. All the resonances in this thesis are fitted for computed lineshapes including the effect of the modulation.

The R.F. field has a phase and amplitude which are both a function of the depth from the surface of the metal host. The solution of Maxwells equations for the propogation of the magnetic field component of electromagnetic radiation into a conducting medium gives solutions

$$H_{//}(x) = H_{o//} \exp(-x/\delta) \exp i(\omega t - x/\delta)$$

where $\delta$ is given by

$$\delta = (\tfrac{1}{2}\sigma\omega\mu\mu_o)^{-\frac{1}{2}}$$

For a typical value of the resistivity for the iron foils, the skin depth, $\delta$, at 100 MHz, will vary from 0.5 to 5μm, increasing as the applied field and degree of saturation of the iron magnetisation increases, and the susceptibility, $\mu$, correspondingly falls. To produce a sufficiently large R.F field throughout the sample, thin foils of iron, cobalt and nickel must be used.

The foils used were prepared by either evaporation onto a cold substrate or by rolling. The rolling produced a more brittle foil through work hardening, and was limited to a minimum thickness of 2μm. The inhomogeneous broadening of the resonance line was very similar for both methods of preparation. The foils were tinned with Wood's metal solder on one side, while held flat on a copper substrate by a glue subsequently dissolved off in trichloroethane. The tinned foil was then soldered onto the end of the copper cold finger.

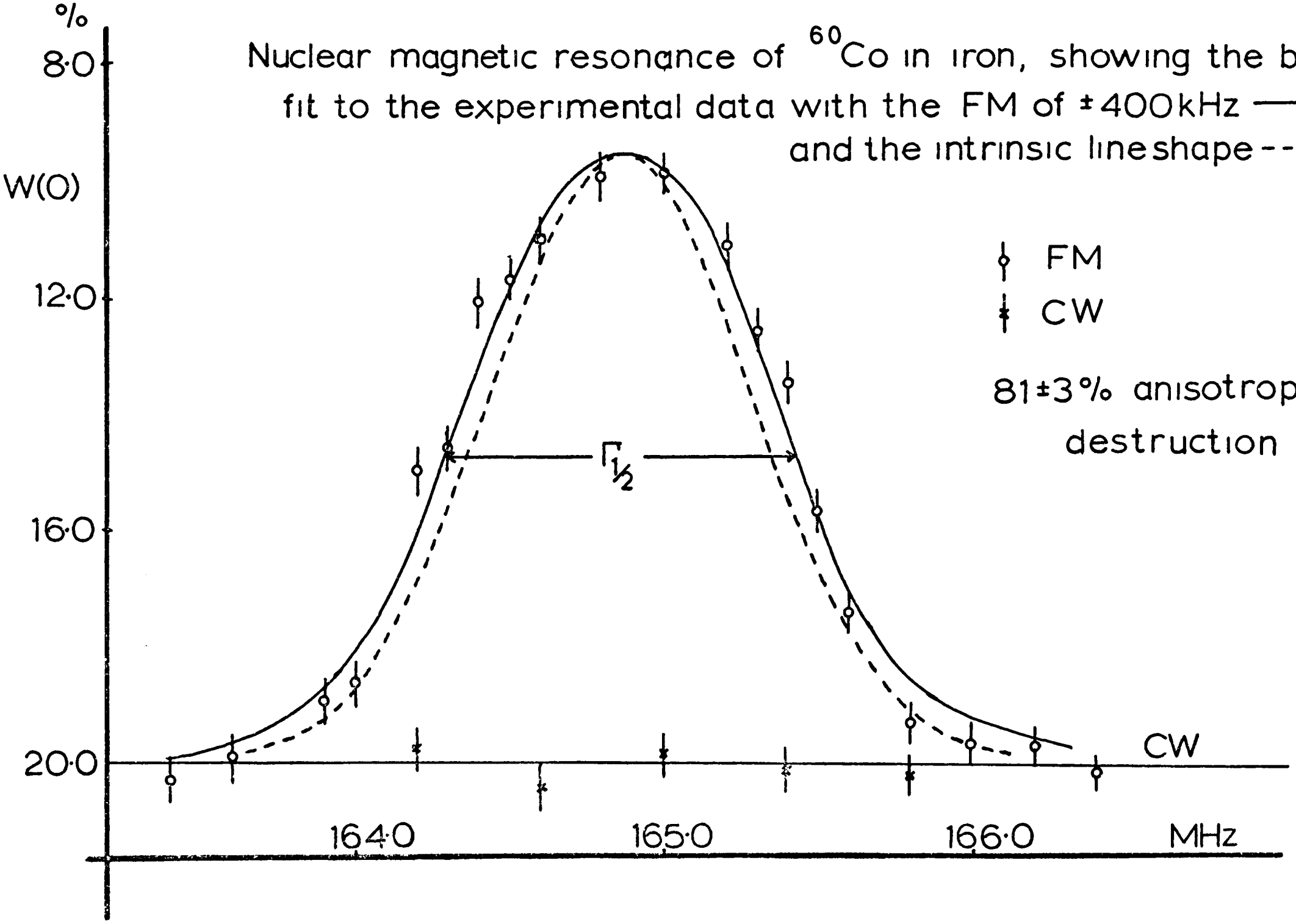
## 2.7 Typical resonance measurements on simple systems

Fe$^{60}$Co has been extensively studied by nuclear magnetic resonance as it provides an easily detectable resonance effect on the large gamma-ray anisotropies. Fig.2.6 shows a typical N.M.R/O.N. spectrum for a 1 μm iron foil containing 2 μC of $^{60}$Co. The experimental points are fitted by the calculated resonance curve for an inhomogeneous broadening of $\Gamma_{1/2}$ = 0.7 MHz with a frequency modulation of ±0.4MHz. The data shows the difference in the axial anisotropy between the frequency modulated situation and the pure carrier wave irradiation. A time of $3T_1$ was allowed after each frequency modulation count, to allow the population distribution of the $^{60}$Co nuclei to relax back to thermal equilibrium before the carrier wave count.

The sensitivity to the resonance is a rapidly varying function of the applied field; depending on the degree of magnetic saturation, determining the magnitude of the observed anisotropy; and the enhancement factor. Fig.2.7 shows the observed change in the axial ocuntrate for the $^{60}$Co resonance at 1/T = 50 as a function of the applied field. The three regions of the curve represent the magnetic saturation of the iron foil, 1, almost complete saturation of the resonance, 2, and the reduction of the resonance effect associated with the reduced enhancement factor in large external fields, 3.

The use of the nuclear orientation technique for impurities in cobalt hosts has been restricted by the difficulty in producing complete saturation of the host magnetisation. The resonance technique avoids this difficulty; incomplete saturation producing merely a broadening of the resonance line. Barclay [22] first observed the N.M.R/O.N. signal of Co$^{60}$Co using single crystal films of cobalt grown on a copper backing and annealed to remove the h.c.p.

FIG 2·6




Nuclear magnetic resonance of $^{60}Co$ in iron, showing the best fit to the experimental data with the FM of ±400kHz ——— and the intrinsic lineshape ------

FM

CW

81±3% anisotropy destruction

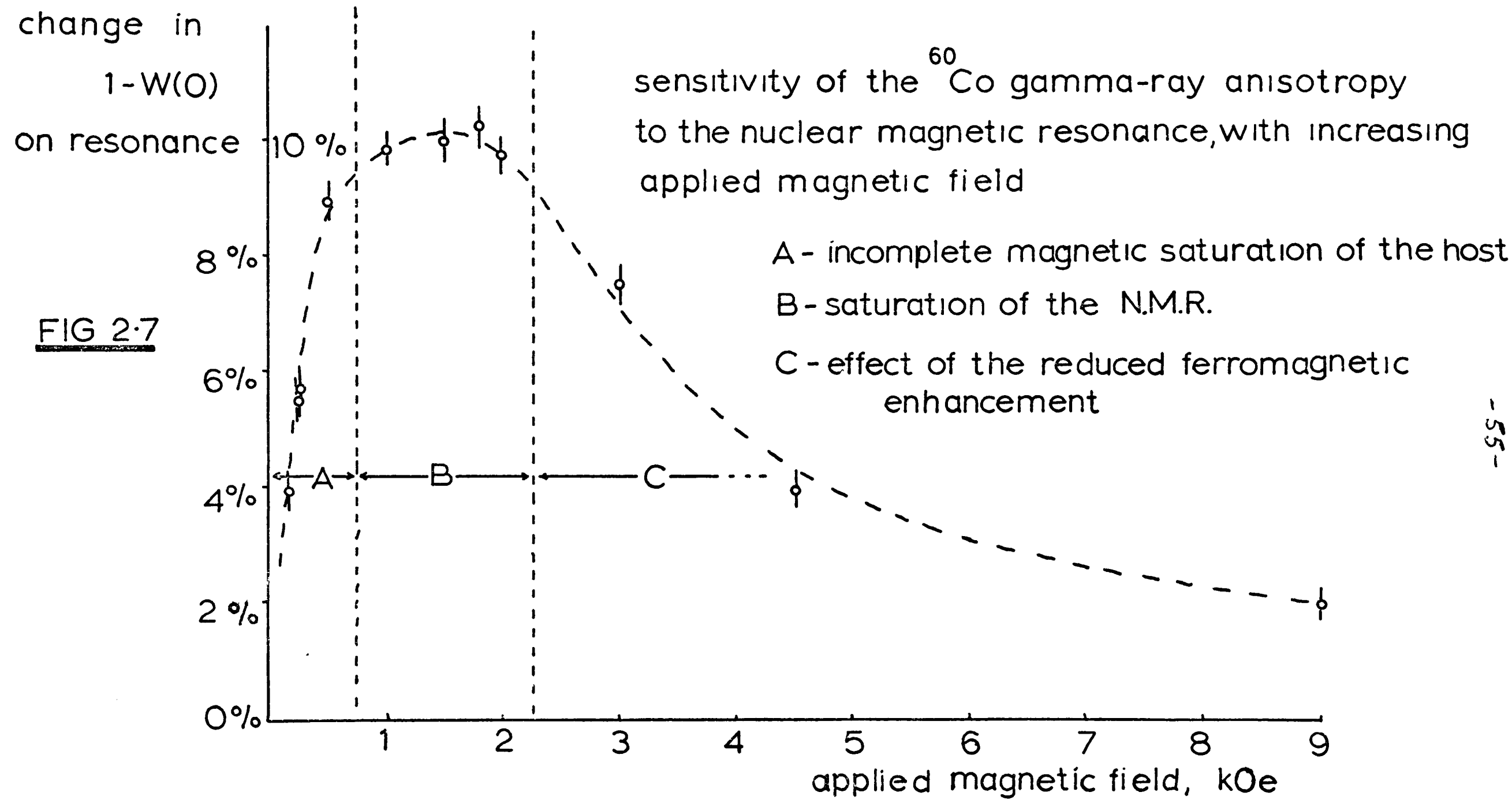



FIG 2·7

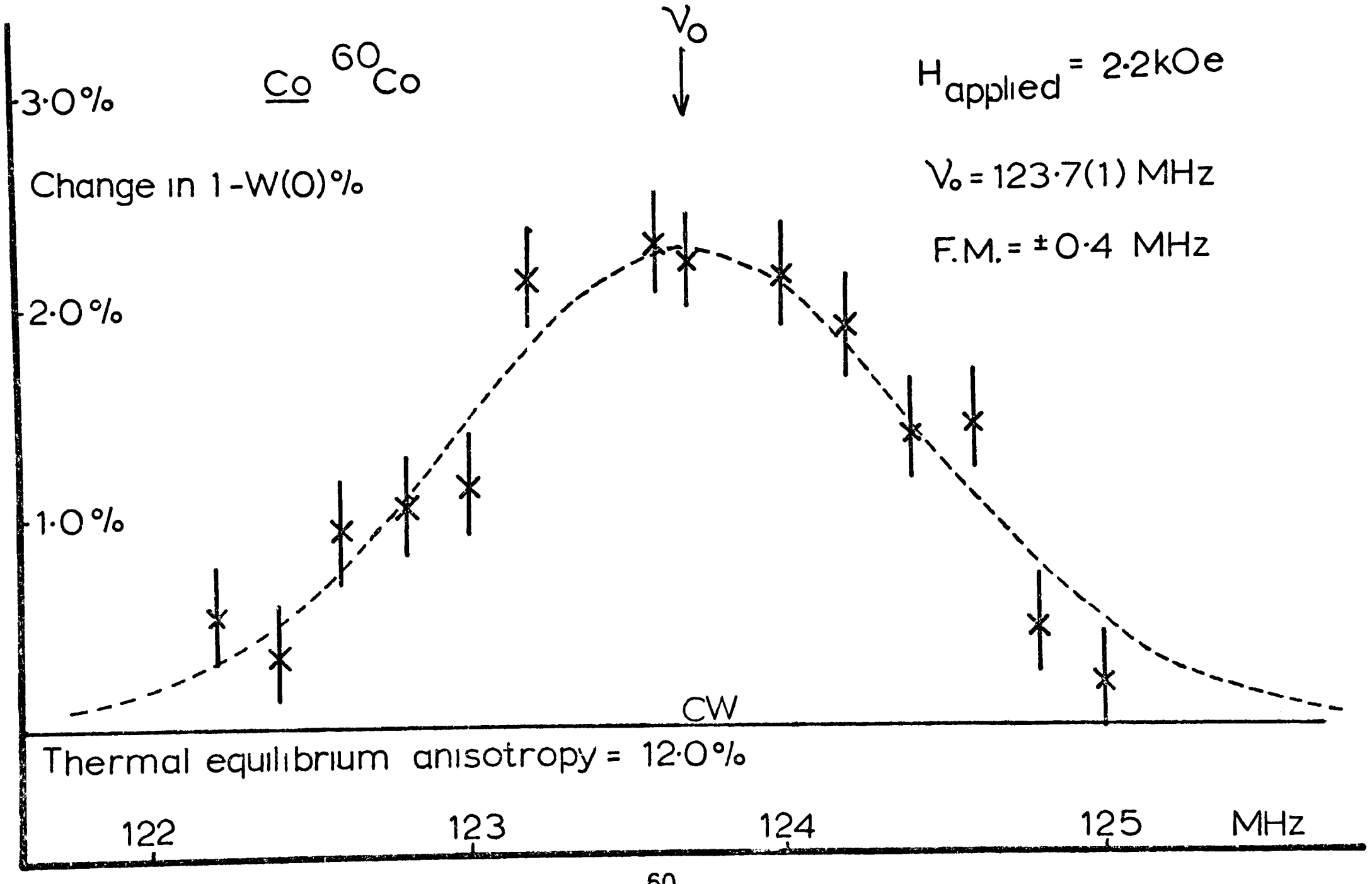
sensitivity of the $^{60}$Co gamma-ray anisotropy to the nuclear magnetic resonance, with increasing applied magnetic field

A - incomplete magnetic saturation of the host

B - saturation of the N.M.R.

C - effect of the reduced ferromagnetic enhancement

FIG 2·8




Nuclear magnetic resonance of $^{60}Co$ in cubic cobalt

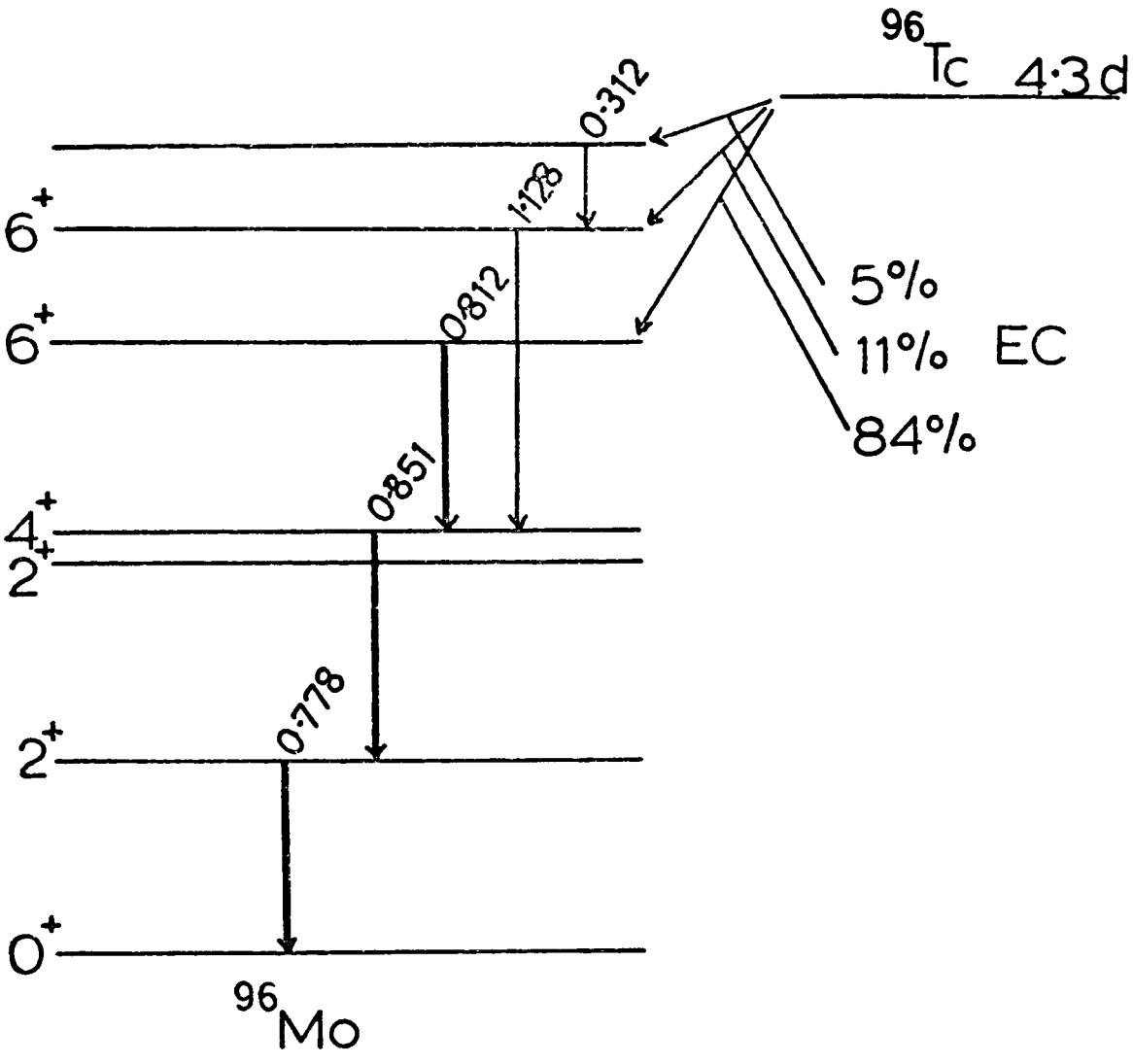
phase. The experiments performed on cobalt hosts, here, have used vacuum deposited polycrystaline cobalt foils into which the impurity is introduced by thermal diffusion. The heat treatment also serves to remove the h.c.p. phase producing a predominantly cubic lattice structure. The magnetic saturation of these foils is much harder than that of iron or nickel, requiring an external field of 10 kOe to ensure 95% saturation of the gamma-ray anisotropy. Fig. 2·8 shows the N.M.R./O.N. response for $Co^{60}Co$ in an applied field of 2.2 kOe. The resonance position of 124.95 ± .15 MHz corrected for the applied field gives a hyperfine field of -218.1 (3) kOe in good agreement with the conventional N.M.R. measurements for cubic cobalt extrapolated to $0^{\circ}K$. [ 36 ]. The resonance frequency in a higher applied field confirmed the negative sign, and showed a linear dependence of the resonance frequency with applied field, even for incomplete magnetic saturation of the cobalt host.

N.M.R./O.N. of $Fe^{96}Tc$

A good demonstration of the value of the N.M.R./O.N. techniques was provided by experiments performed in collaboration with C.Sanctuary with dilute impurities of $^{96}Tc$ in iron. Neither the nuclear magnetic moment nor the hyperfine field were known, but the temperature dependence of the gamma ray anisotropies gave a value for the product $\mu_N \cdot \mu H_{eff}$ of 1700 ± 100 $\mu_N$ kOe [ 37 ]. The decay scheme and $\gamma$-ray spectrum are shown in Fig.2.9. The aim of the N.M.R./O.N. experiment was to determine $\mu_N$ and $H_{eff}$ independently from the resonance frequency and the resonance frequency shift in a large external magnetic field.

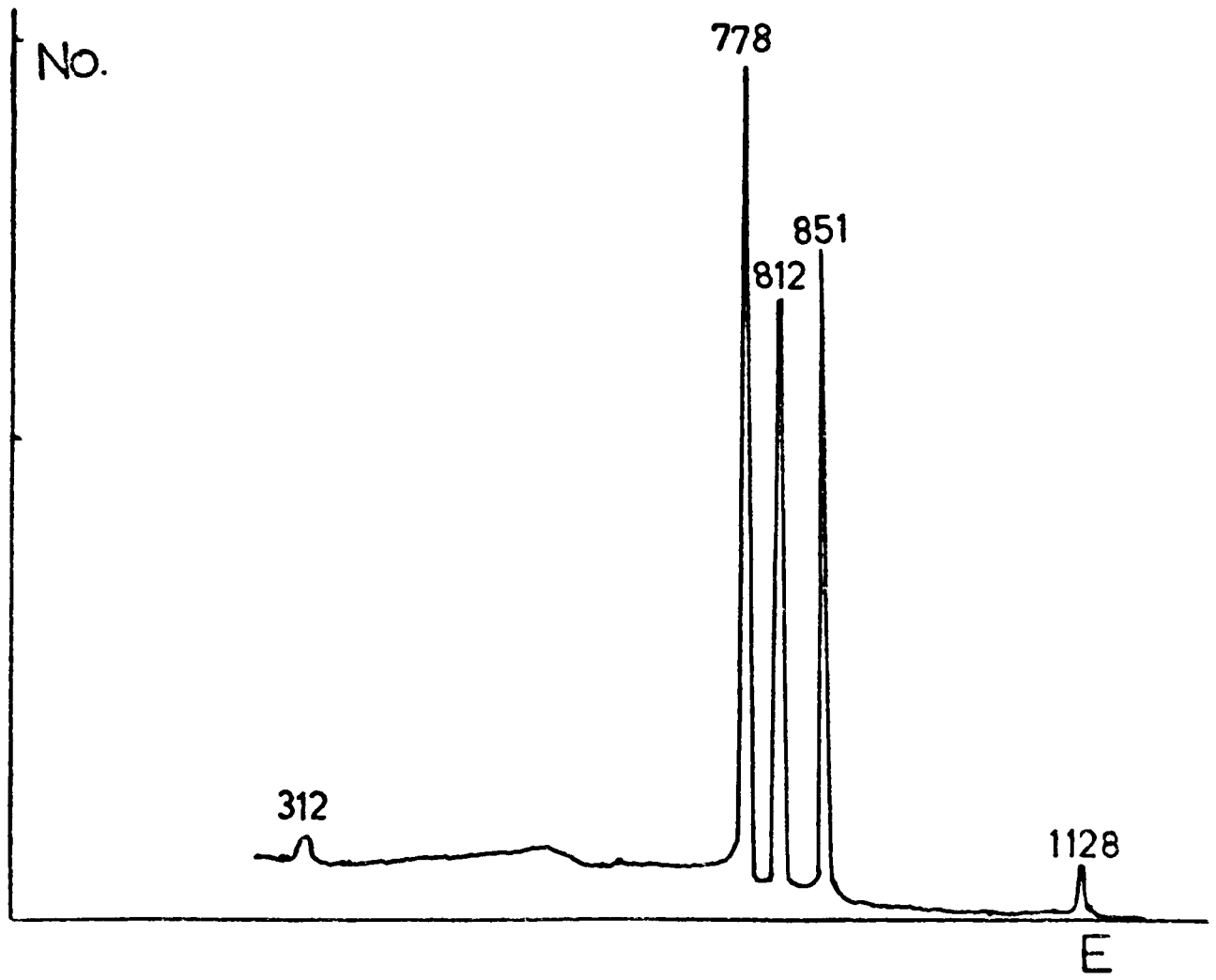
A 1 μm iron foil sample was pr epared by evaporating to dryness a few drops of a solution of active tetra-phenyl arsenium pertechnicate onto the surface of the foil. The $^{96}Tc$ activity was diffused into the

FIG 2·9




Decay scheme of $^{96}Tc$

Gamma ray spectrum



foil at 900°C for 12 hours under a reduced pressure of hydrogen. The foil was held flat in a soft iron holder and sealed in a quarts tube because of the high vapour pressure of the tetra-phenyl arsonium pertechnicate.

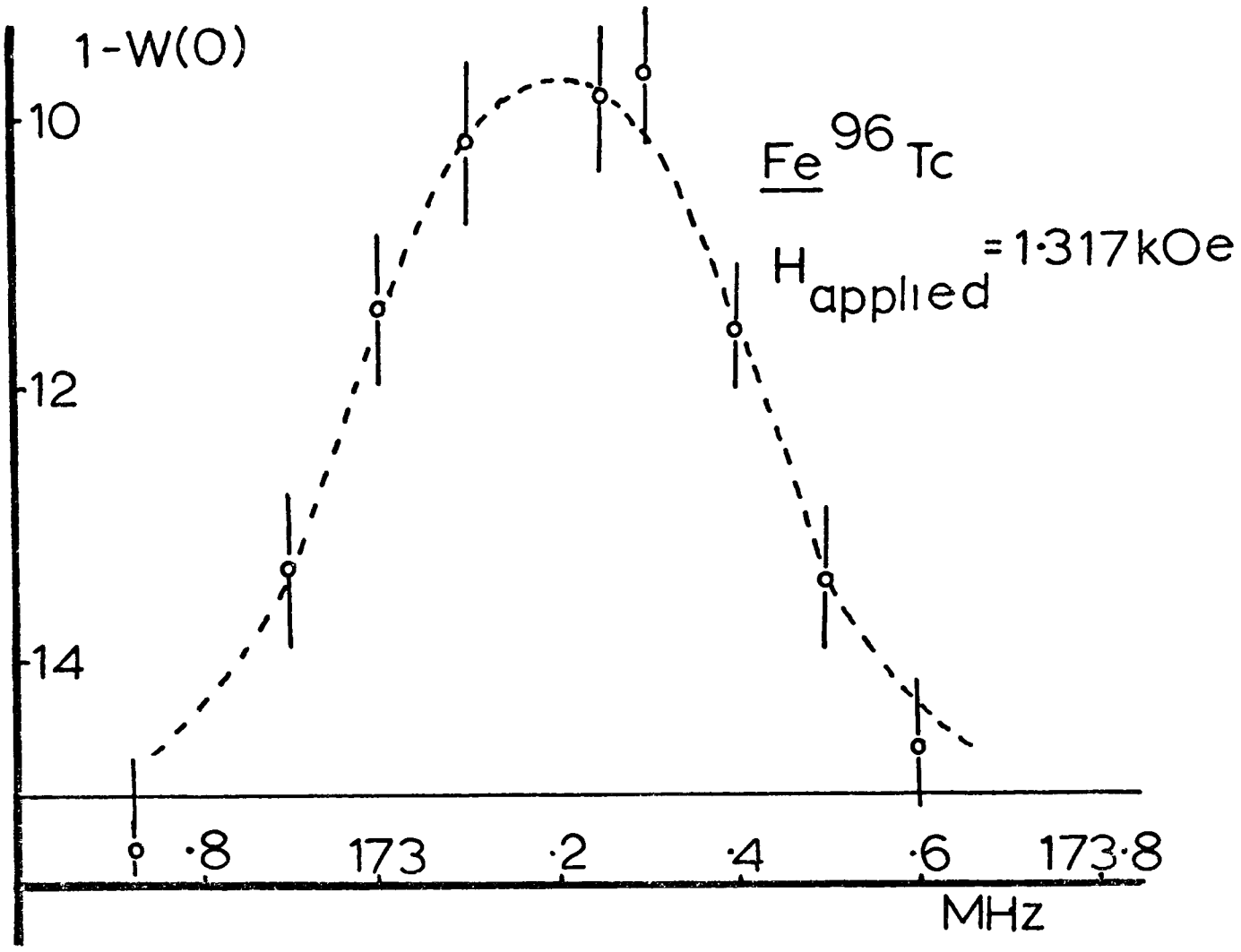
The sample was cooled to $1/T = 50^{\circ}K^{-1}$ by contact with chrome potassium alum where the axial countrate from the three gamma-rays at 779 keV, 812 KeV and 852 KeV, unresolved in the NaI spectrum, gave an anistropy of -15%. The range of the frequency search for the resonance was defined by the value of $\mu H/I$, estimated from the gamma-ray anisotropy measurements of Sanctuary, over the temperature range of $1/T = 300$ to $1/T = 30$. With a frequency modulation of $\pm$ 400 kHz at a frequency of 100 Hz, a 5% destruction of the axial anisotropy was found at 173 MHz. The resonance shows the smallest linewidth relative to the total interaction ever observed with a polycrystalline iron sample. After correction for the frequency-modulation amplitude, the natural resonance width from the inhomogeneous broadening is 0,35MHz, for the full width at half height. This may be a result of the solubility of $T_c$ in iron and the very similar atomic sizes, which will mean that the technicium will produce very little distortion of the lattice.

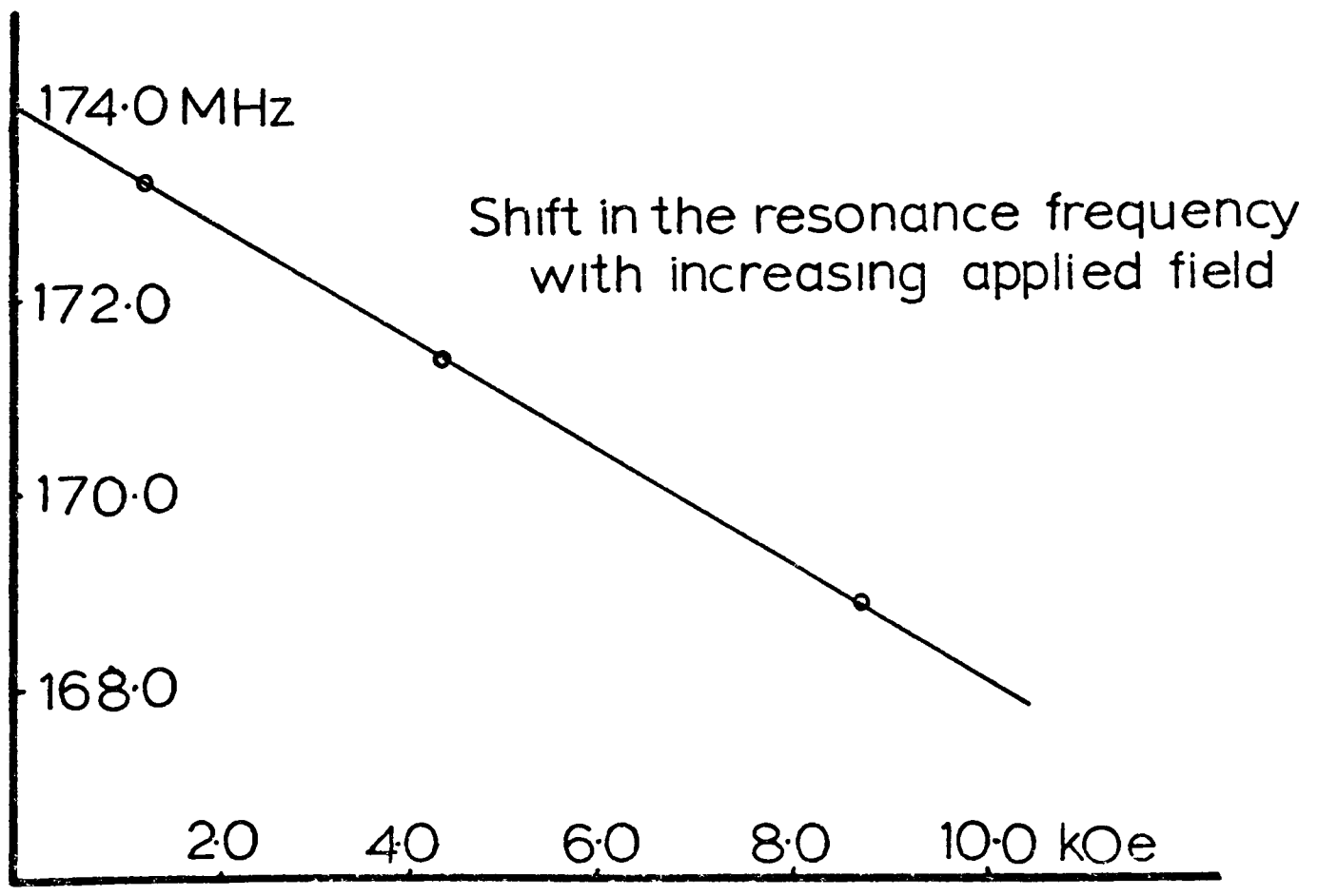
Measurements were made in polarising fields of 1.317 kOe, 4.39 kOe and 8.78 kOe, with frequency modulations of $\pm$200 kHz. The results are shown in the table below.

| $H_{applied}$ (kOe) | Frequency (MHz) | line width (MHz) observed with a frequency modulation of $\pm$ 200kHz |
|---|---|---|
| 1.317 | 173.23(5) | 0.52(6) |
| 4.39 | 171.45(5) | 0.53(8) |
| 8.78 | 168.88(8) | 0.75(20) |

FIG 2·10

Nuclear magnetic resonance of $^{96}$Tc in iron



A straight line fit through the points gives a zero applied field resonance frequency of 174.00(5) MHz, and, taking the ground state spin as 7 [38] the slope gives the magnetic moment of $^{96}$Tc to be

$$\mu = 5.37\ (17)\mu_N$$

The effective hyperfine field is then given by

$$h\nu = \mu H/I$$

From the deduced resonance frequency in zero field, and the magnetic moment, this gives

$$H_{eff} = -298\ (10)\ kOe$$

The errors in this measurement due to the Knight shift and uncertainty in the applied field amount to less than 0.5%.

The comparison of the hyperfine interaction measurement by N.M.R/O.N. with the nuclear orientation results enables more information to be obtained about the spins and multipolarities of the decay scheme. The resonance provides a measurement of μH/I, but the nuclear orientation measurements are sensitive to the value of μ.H. The comparison of these measurements with the gamma-ray anisotropies measured by C.J. Sanctuary have confirmed the spin assignment of the ground state of $^{96}$Tc as 7, and has enabled the transitions between the excited states of $^{96}$Mo to be studied.

## 2.8 Conclusion

This chapter has described the techniques involved in nuclear magnetic resonance on oriented nuclei, and has presented results demonstrating the sensitivity of the technique for the study of the hyperfine interactions of very dilute impurities in the ferromagnetic metals. The experiments described in the bulk of this thesis involve the use of this technique for the study of dilute alloy systems where nuclear orientation alone does not provide enough information, either through the greater inaccuracy of the measurements, or because the insolubility of the impurity results in an average over the hyperfine interactions at a range of impurity sites.

# CHAPTER 3

# NUCLEAR ORIENTATION AND NUCLEAR MAGNETIC RESONANCE OF $^{110}Ag^{m}$ IN IRON AND NICKEL

## 3.1 Introduction

The interest in the hyperfine interaction at nuclei of silver isotopes in iron and nickel hosts arises from two lines of work. The published measurements of the hyperfine field from nuclear orientation measurements on isotopes of silver are in poor agreement with the systematic variation of the hyperfine field on other elements of 4d, 5s electronic structure. This is a region of the periodic table where the variation of the conduction-electron-polarisation contribution to the hyperfine field is described quite well by the theory proposed by Campbell on the basis of the conduction electron scattering from the impurity. Silver should be a particularly simple case to study, with the atomic structure having one 5s electron outside the filled 4d shell. Shirley and Westenbarger [ 39 ] have predicted a hyperfine magnetic field of -400 kOe of silver in iron on the assumption of a conduction electron contribution to the hyperfine field that is proportional to the polarisation of the conduction electrons, the hyperfine coupling constant, and the number of contributing electrons. The more sophisticated model proposed by Campbell [ 40 ] also predicts a higher field than the value of -282(20) kOe quoted by Shirley, Rosenblum and Matthias [ 12 ], from the measurements of Shirley and Westenbarger [ 41 ]. We had reason to believe that the existing measurements were unreliable because of the discrepancy with the theoretical estimates and because of the problems involved in producing a good substitutional dilute alloy of silver in iron. The interest in a more accurate measurement lies in the comparison with the interactions of the neighbouring elements and the theoretical estimates, but also, the accurateknowledge of the

hyperfine field magnitude is essential to the interpretation of the nuclear orientation measurements of the many gamma-rays. The nuclear orientation technique provides a very sensitive method for the measurement of beta and gamma transition multipolarities when the hyperfine interaction is known. These measurements are useful in the identification of the spins and parities of excited states, and for comparison with E2/M1 mixing ratios calculated for particular nuclear structure models.

A major problem in the study of the hyperfine interaction of silver in iron is the very low solubility of the silver at almost all temperatures. The solubility limit of silver in iron below 1000°C is quoted by Hanson [ 42 ] as less than $10^{-3}$ at %. The effect of this limit for the preparation of dilute alloys is that, although an alloy of higher concentration may be produced by melting or diffusion of the silver at a high temperature, on cooling, the silver will tend to migrate to clusters of silver in the lattice, or will have more stable sites at interstitial positions. The existence of a unique hyperfine interaction depends on all the impurity silver atoms lying on substitutional lattice sites. This is particularly important for nuclear orientation measurements, where an average over the degree of orientation of all the impurity nuclei is observed. Any nuclei in low field interstitial sites, or clusters of impurities, will reduce the apparent hyperfine field. Very low concentrations of silver must therefore be used to ensure that a large proportion of the impurity nuclei see the unique hyperfine field associated with the substitutional sites.

The N.M.R./O.N. technique differs from nuclear orientation in that it is sensitive only to those nuclei in well defined hyperfine fields. In these normally substitutional alloys the technique provies a method of accurately measuring the hyperfine field of the nuclei in substitutional sites without any perturbation from other impurities. The comparison of

the N.M.R./O.N. measurement with the nuclear orientation effects from several alloys has shown that any hyperfine field experienced by nuclei other than those in substitutional sites is very much smaller than the unique hyperfine field. This is discussed further in section 3.4, but may be the result of the clustering of silver near lattice-defects in the heat. The results have shown that a large proportion of the silver impurity can occur in such low field sites even when the impurity concentration is as low as $3 \times 10^{-4}$ at %. The site distribution seems to depend more on the heat treatment of the alloy than on the concentration when the concentration is below $10^{-2}$ at %.

## 3.2 Sample preparation for alloys of $^{110}Ag^{m}$ in iron and nickel

### a) Preparation of alloys for conventional nuclear orientation

For the nuclear orientation experiments the only limit on the impurity concentration is provided by the mass of the radioactive silver impurity required to give a sufficiently high count-rate, from most of the gamma transitions, for the axial anisotropies to be measured as a function of the lattice temperature. There is no restriction on the size or shape of the iron host as there is for the resonance experiment, so, for most of the samples a mass of between $10^{-1}$ and 1 gram of iron containing about 1 μCi of $^{110}Ag^{m}$ was used. The combination of the high vapour pressure and low solubility of silver made sample preparation by thermal diffusion difficult, but it was considered a more reliable method than ion implantation. The $^{110}Ag^{m}$ radioactivity was obtained in the form $AgNO_3$ in dilute nitric acid with a specific activity of 2mCi/mg. This specific activity enabled nuclear orientation samples containing $10^{-5}$ to $10^{-3}$ at % of stable and active silver to be prepared. A range of alloys was made by thermal diffusion of the silver from an electroplated layer of silver on the surface of the iron. The iron was heated to a temperature between 1200°C and 1600°C in a sealed quartz tube containing a small pressure

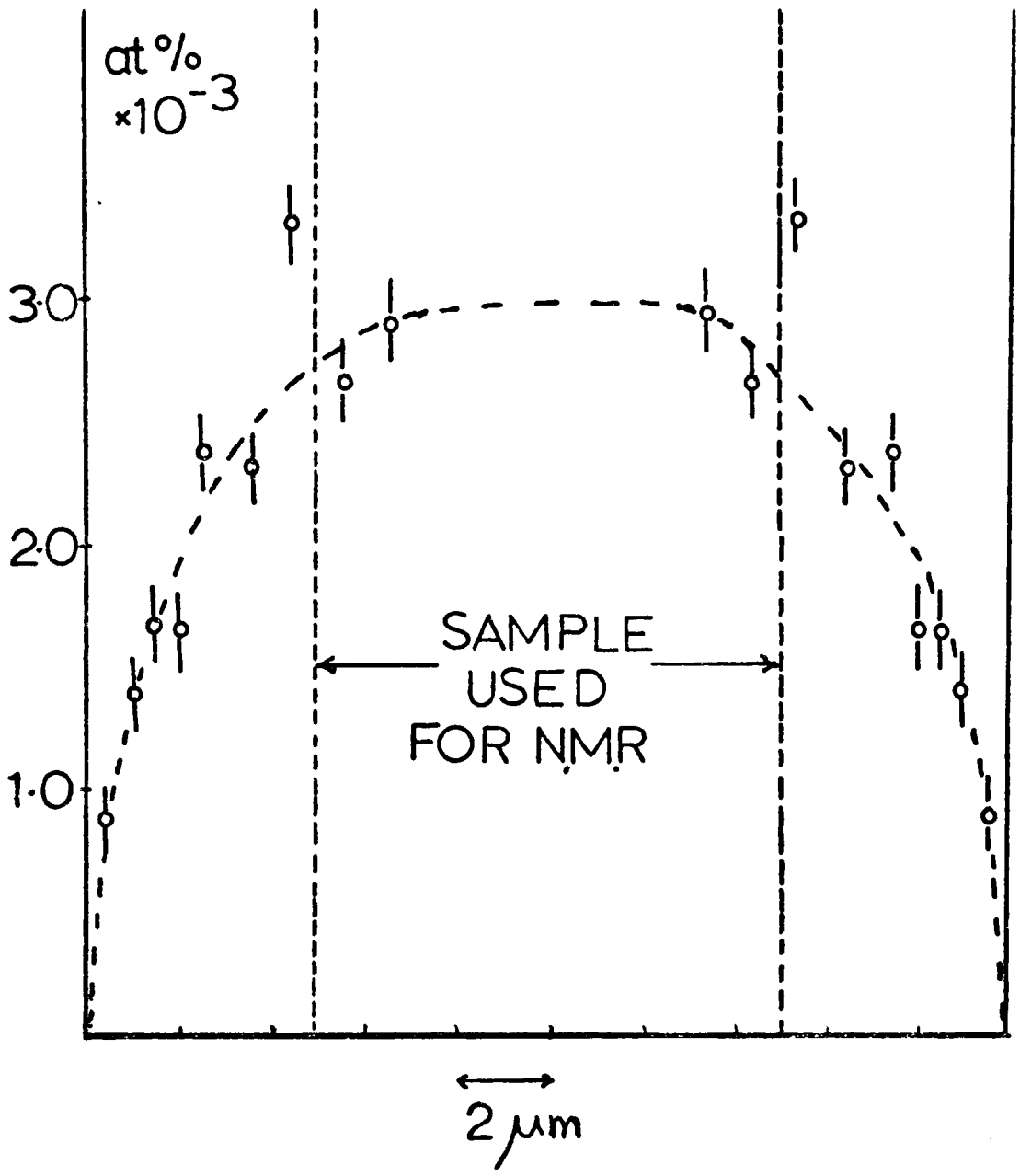
of hydrogen. The diffusion could be checked by monitoring the radioactivity of the sample as the surface of the iron was etched in dilute nitric acid. The etching also served to remove any silver still on the surface of the iron. A temperature of 1200°C for 20 hours was found to be sufficient to produce a uniform distribution of the silver impurity throughout an iron sample of thickness 0.5mm, but the measurement of the gamma ray anisotropies was required to determine the impurity site distribution. The largest gamma ray anisotropies were obtained from samples diffused at greater than 1400°C or melted and then rapidly cooled. All the nuclear orientation measurements for the analysis of the decay scheme were prepared on samples in this way, and gave gamma ray anisotropies within 5% of each other.

b) Preparation of thin foil samples for resonance

The samples prepared for the N.M.R./O.N. experiments do not have such a stringent requirement that all the impurity atoms should occupy lattice sites. In a dilute alloy the resonance will be observed only on such impurities; the influence of impurities in other sites is only to increase the statistical fluctuations of the gamma-ray anisotropy measurements. The priority for the resonance measurement is to obtain a sufficiently high count-rate from a foil, comparable in thickness to the R.F. skin depth.

Fig.3.1 shows the impurity silver concentration through a 20 μm iron foil after the silver impurity has been diffused from a surface layer for 10 hrs at 1200°C. The impurity concentration falls off near the surface, reflecting the very low concentration of silver in the vapour phase at the diffusion temperature of 1200°C. The foils were etched to a thickness of 10 μm to remove the surface layer and the resulting foil rolled to 3 μm, and soldered to the cold finger of the chrome alum salt pill. With the maximum impurity concentration obtainable of $3 \times 10^{-3}$ at %, 1 $cm^2$ of the foil gave a count rate of 200 c/s over the energy range from 600 to 1000 KeV.

FIG 3·1




Concentration of the silver impurity through a 20μm iron foil after diffusion for 1hr at 1200°C

on a 3 x 3 inch NaI detector at 8 cms. Such a wide energy window for the resonance detection single channel analyser was possible because all the intense gamma-transitions in that region show the same sign of the axial gamma-ray anisotropy. The ntt anisotropy in the window at $1/T = 50K^{-1}$ was -15%. This was slightly smaller than that expected from work on a more dilute sam ple but gave a sufficiently good signal/noise ratio to detect the resonance.

### 3.3 N.M.R./O.N. measurements in Fe and Ni

The initial orientation measurements to identify the range of search using the temperature dependence of the gamma-ray anisotropy of the 764 KeV transition gave a hyperfine field in Fe of 450 (20) kOe. Alternate counts with the frequency modulation of $\pm$400kHz on, and off, but maintaining a constant carrier wave amplitude, showed a nuclear resonance at

$$\nu_n = 203.75\ (1)\ \text{MHz}$$

in a polarising field of 2.20kOe. The resonance in this field and an increased polarising field of 4.4kOe are shown in Fig.3.2. The destruction of the gamma-ray anisotropy was small ($\sim$15 - 20%), probably because of the thickness of the iron foil compared with the 1 $\mu$m Skin depth.

The resonance frequency corrected for the applied field gives a hyperfine field of

$$H_{eff} = -447.2(2)\ \text{kOe}$$

using the value for the magnetic moment of 3.604(4) $\mu_n$, measured by Fuller and Cohen [108]. The resonance frequency in the increased polarising field, of 4.40 kOe, of 202.7(2) MHz confirms the negative sign of the hyperfine field.

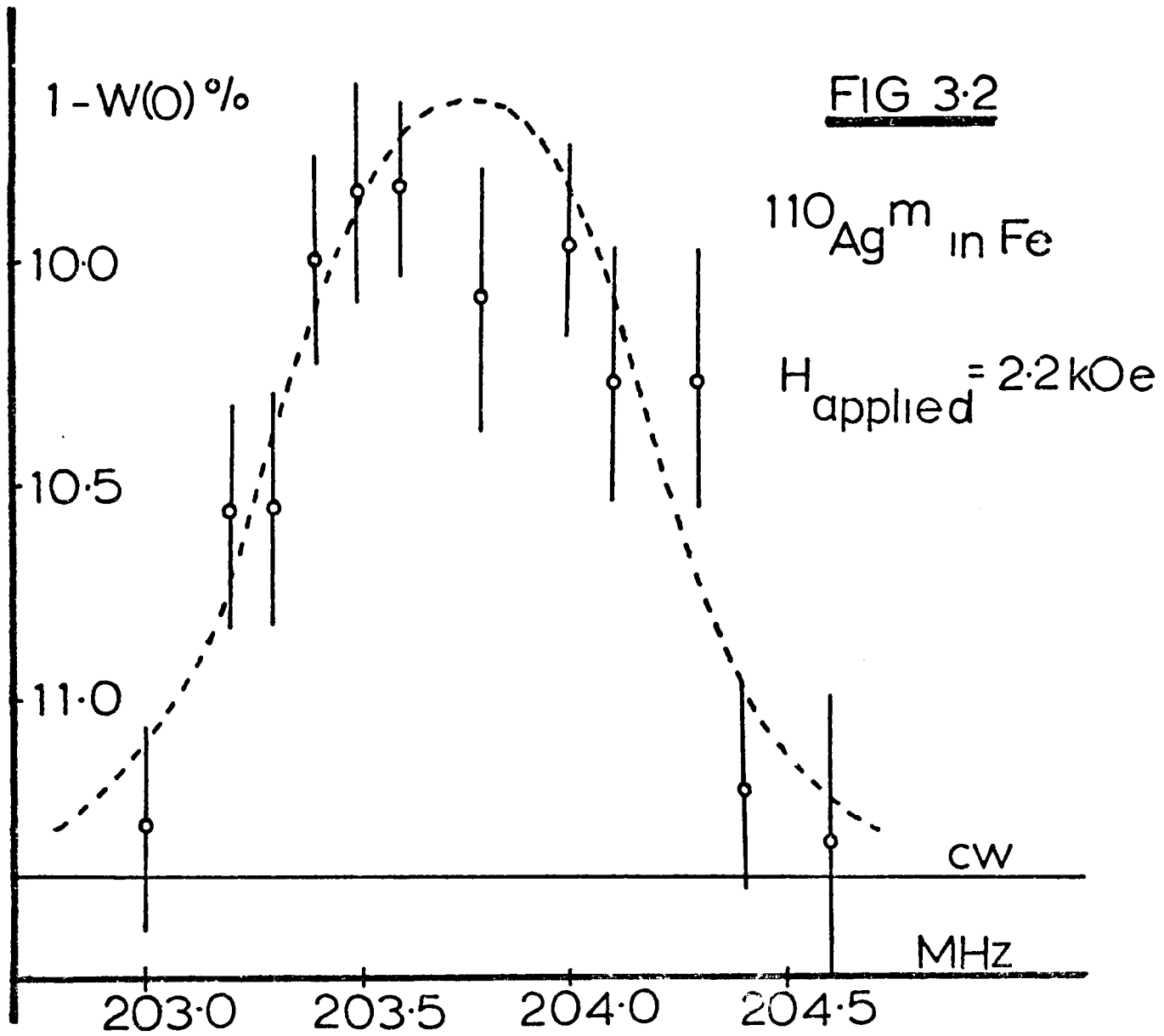



FIG 3·2

$^{110}Ag^{m}$ in Fe

$H_{applied}$ = 2·2 kOe

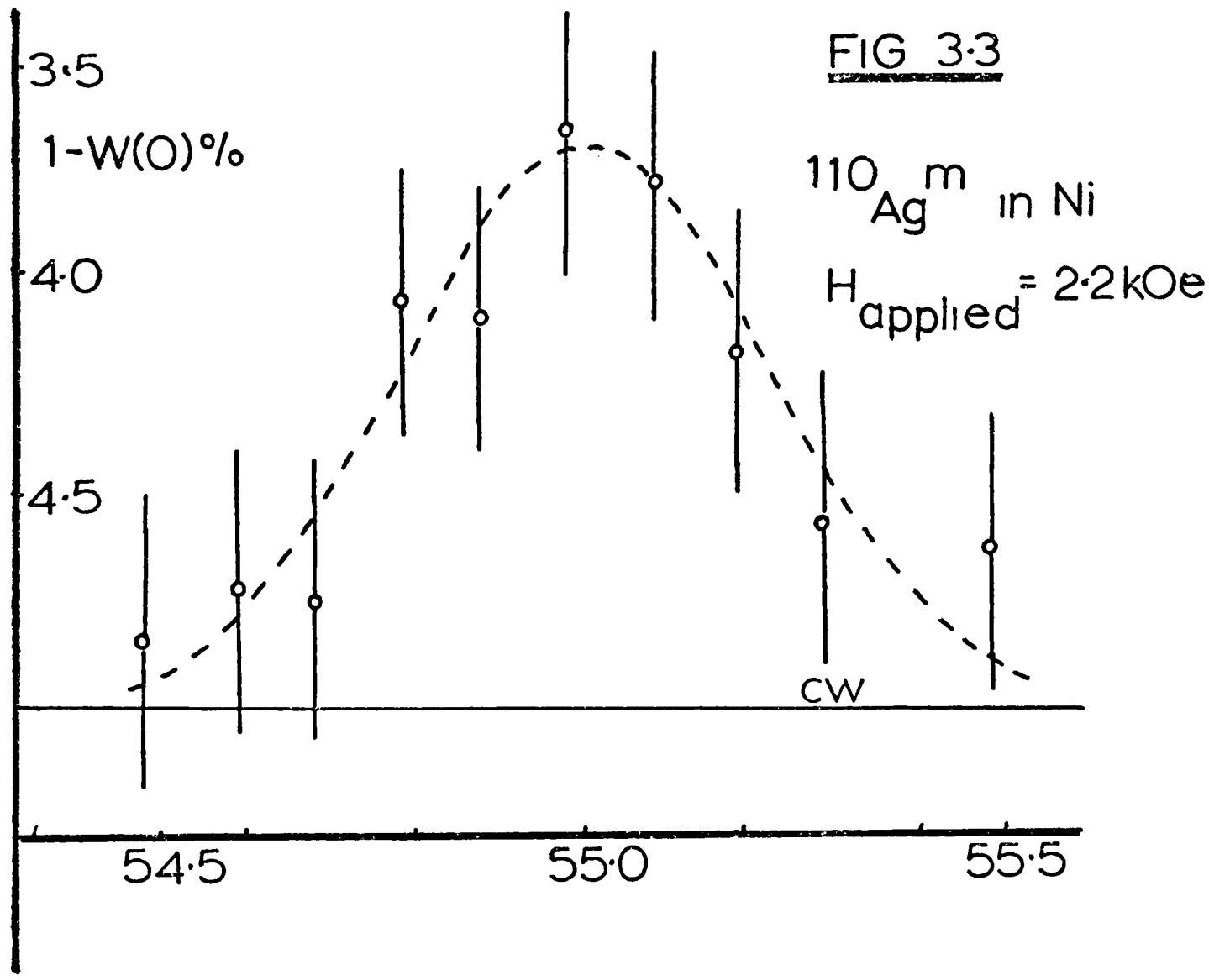



FIG 3·3

$^{110}Ag^{m}$ in Ni

$H_{applied}$ = 2·2 kOe

Using a similar sample of Ni $^{110}Ag^{m}$; but observing the 1385 keV and 1505 keV transitions, which have more favourable decay parameters and therefore large anisotropies; a nuclear resonance was detected at

$$\nu_n = 55.0(2) \text{ MHz}$$

in an applied field of 2.20kOe. The resonance is shown in Fig.3.3. The greater solubility of silver in nickel enabled a more active sample to be prepared, and the less intense, high energy, gamma transitions to be used to detect the resonance. An average axial anisotropy of +6% at $1/T = 40k^{-1}$ was observed in an energy window from 1200keV to 1600 keV. The corrected resonance frequency gives a hyperfine field of

$$H_{eff} = 122.4(4) \text{ kOe}$$

assuming a negative sign for the hyperfine field.

The measurements in iron and nickel are in surprising, and perhaps fortuitous, agreement with the saturation electronic magnetic moments of iron and nickel at $0^{\circ}K$. Using the values $2.2160(15)\mu_\beta$ and $0.6157(7)\mu_\beta$ for iron and nickel respectively [44], the expected field in nickel would be 122.05 (20) kOe. This variation of the hyperfine field with the saturation magnetisation of the host is discussed further in comparison with similar measurements in gold and iridium impurities elsewhere in this thesis.

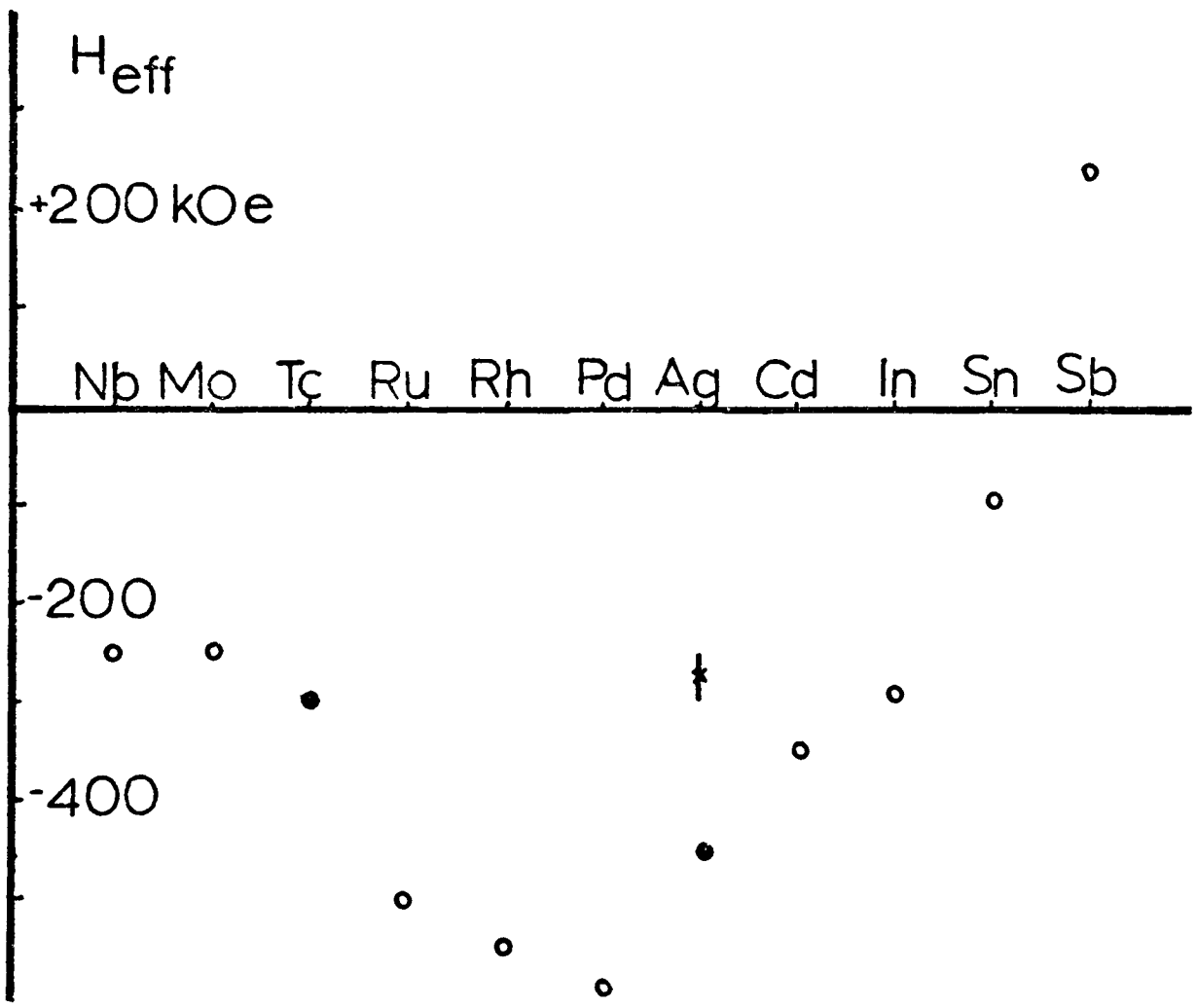
The measured hyperfine field for Fe $^{110}Ag^{m}$ of 447.2(2) kOe, while being in good agreement with the orientation measurements, differs considerably from the published results of Shirley and Westenbarger [ 41 ], and Knott et al [ 45] on $^{110}Ag^{m}$, and Craknell and Wilson [ 46 ] on $^{109}Ag^{m}$. The more recent work of Fox and Stone [ 47 ] has shown the $^{109}Ag^{m}$ discrepancy to be associated with spin lattice relaxation during the 40 sec lifetime of this isotope. The complex $^{110}Ag^{m}$ gamma-ray spectrum made analysis of the NaI detector study of Westenbarger very difficult. The value of

Table 3.1 N.M.R./O.N. measurements on $^{110}Ag^{m}$

| Host | Applied field $H_a$ kOe | Resonance frequency MHz | linewidth MHz | FM (MHz) |
|---|---|---|---|---|
| Fe | 2.20 | 203.75(10) | 1.00(10) | 0.40 |
| Fe | 4.40 | 202.70(20) | 1.10(10) | 0.40 |
| | | $H_{eff}$ = -447.2(2) kOe | | |
| Ni | 2.20 | 55.0(2) | 0.50(20) | 0.20 |
| | | $H_{eff}$ = 122.4 (4) kOe | | |

$H_{eff}$ = 250(6) kOe reported in reference [45] is from an implanted source, and may be reduced because of the known low solubility of silver in iron. Our result is in very good agreement with the predicted value of -400kOe calculated on the basis of conduction-electron-polarisation, which is expected to be the dominant hyperfine field producing mechanism for silver. The higher value is more consistent with the systematics of the hyperfine fields at neighbo uring impurity elements in the periodic table, than the previous low values. Fig.3.4.

FIG 3·4




Hyperfine fields of impurities in iron

- This work
- × Previous measurements on Fe Ag

## 3.4 Comparison of the nuclear orientation results on several alloys

With an accurate knowledge of the hyperfine field of $^{110}Ag^{m}$ in iron from the resonance, the nuclear orientation results from various alloys can be used to study the site distribution of the silver impurity. Two gamma-rays were used for this study; the 764 keV gamma-ray, because its decay parameters are well known, and the 1384KeV gamma-ray because of the large anisotropies shown at the temperatures used. It has already been mentioned that some alloys showed smaller nuclear orientation anisotropies than alloys quenched from a very high temperature. The temperature dependence of the gamma-ray anisotropies from these poor samples can be used to study the relative sizes of the hyperfine fields from the various impurity sites. The simplest possible model assumes that any impurity nuclei, not in substitutional lattice sites, will experience a very small hyperfine field, associated with the core polarisation proportional to the conduction electron magnetisation at the impurity site. On the basis of such a model, the gamma-ray anisotropy will only arise from those impurities in lattice sites. If the factor (1-x) is defined as the number of impurities in lattice sites divided by the total number of active impurities, both the $Q_2U_2F_2$ and $Q_4U_4F_4$ factors will be reduced by the same factor (1-x). If the hyperfine field at non-substitutional sites is not negligible compared with the N.M.R./O.N. measurement, the temperature dependence of the gamma-ray anisotropies will deviate at low temperatures from the set of curves defined by values of (1-x). The results from three alloys are shown in Figs.3.5 and 3.6. In both figures the upper curve gives the best fit to data from two samples with concentrations of $1 \times 10^{-4}$ at % cooled quickly from 1400 and 1500°C. The lower curves, b) and c), are fits to the data from a sample diffused at 1200°c (c), and a melted sample, cooled over a period of 10 hours (b).

FIG 3·6

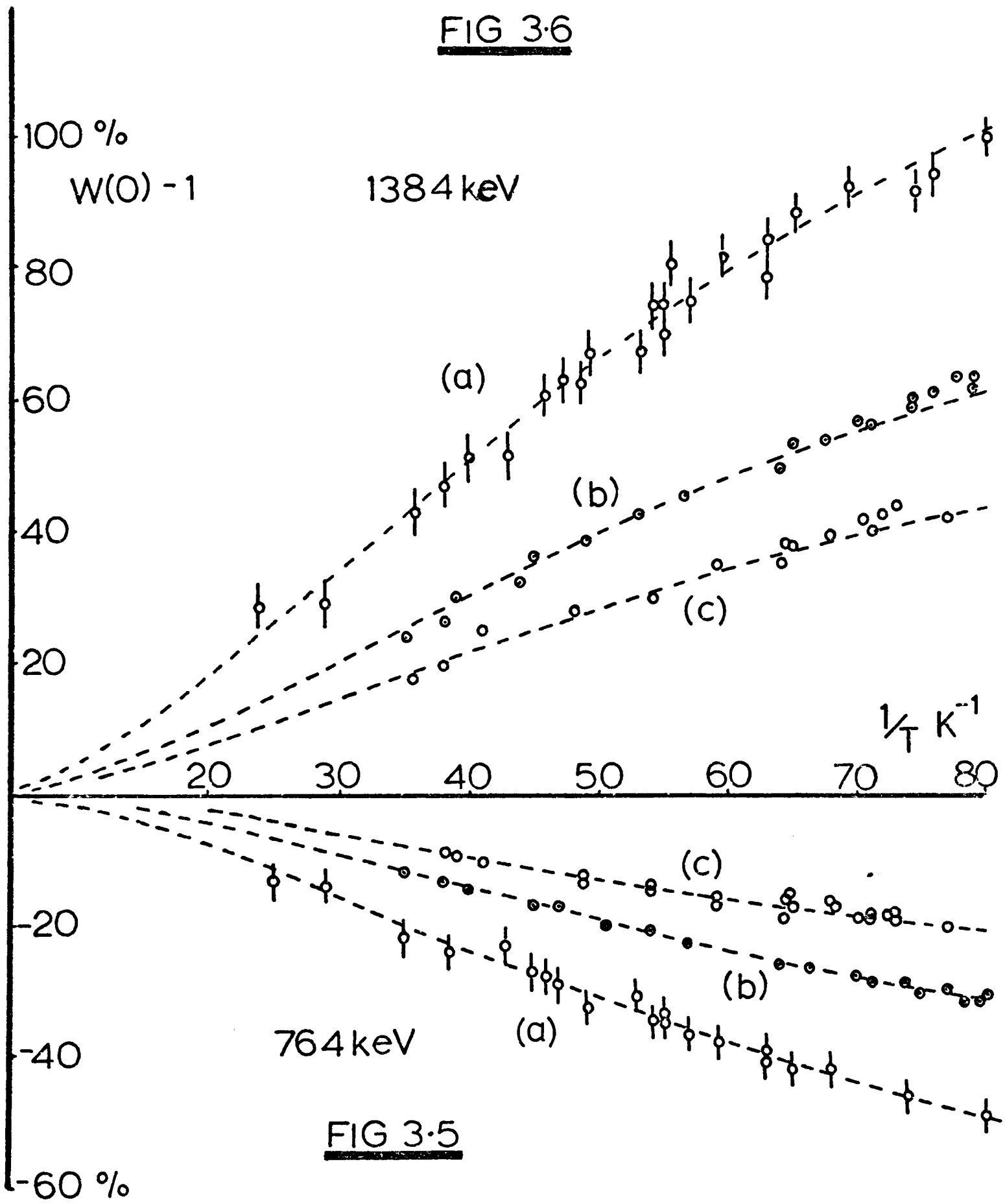



FIG 3·5

The comparison of gamma-ray anisotropies from alloys with different thermal histories

Both sets of data are fitted with the same values of $Q_2U_2F_2$ and $Q_4U_4F_4$, but with values of (1-x) of 0.588 and 0.431. The comparison of the data with the experimental results tends to suggest that the hyperfine field experienced by the non-substitutional impurity is small: an upper limit of about 50 kOe can be deduced from the deviation from the expected temperature dependence at $1/T = 80$.

In view of this result and the method of sample preparation, the most likely explanation for the distribution of sites would be that the silver impurity tends to form clusters in the iron lattice, probably at lattice defects and grain boundaries. The only way to distinguish between such behaviour and a possibly more stable interstitial site would be by channeling measurements, but the available concentrations would make such measurements very difficult.

### 3.5 Nuclear orientation measurements on $^{110}Ag^m$ in iron

The decay scheme and gamma-ray spectrum of $^{110}Ag^m$ are shown in Figs.3.7 and 3.8. The excited states of $^{110}Cd$ are fed from the 254 day $6^+$ parent state of $^{110}Ag^m$, 116 KeV above the $^{110}Ag$ ground state. The dominant beta decay transitions are the 84 KeV $6^+ \rightarrow 5^+$ transition and the 531 KeV $6^+ \rightarrow 6^+$ transition feeding the 2927 KeV and 2480KeV states of $^{110}Cd$. The decay of $^{110}Ag^m$ to $^{110}Cd$ has been studied by a number of investigations [ 48 ] [ 49 ] [ 50 ]. Extensive studies of the beta-rays and internal conversion electrons [ 51 ] [ 52 ] have resulted in a well established level scheme for $^{110}Cd$, showing that the excited states can be considered as a set of collective vibrational oscillations about a spherical equilibrium state. This is most clearly seen in the first excited state, of spin and parity $2^+$, and the set of $0^+$, $2^+$ and $4^+$ excited states representing a two phonon state. The measurements of the M1 and E2 transition probabilities is of importance for comparison with calculations on the vibrational model [ 53 ]

FIG 3·7 DECAY SCHEME OF $^{110}Ag^{m}$

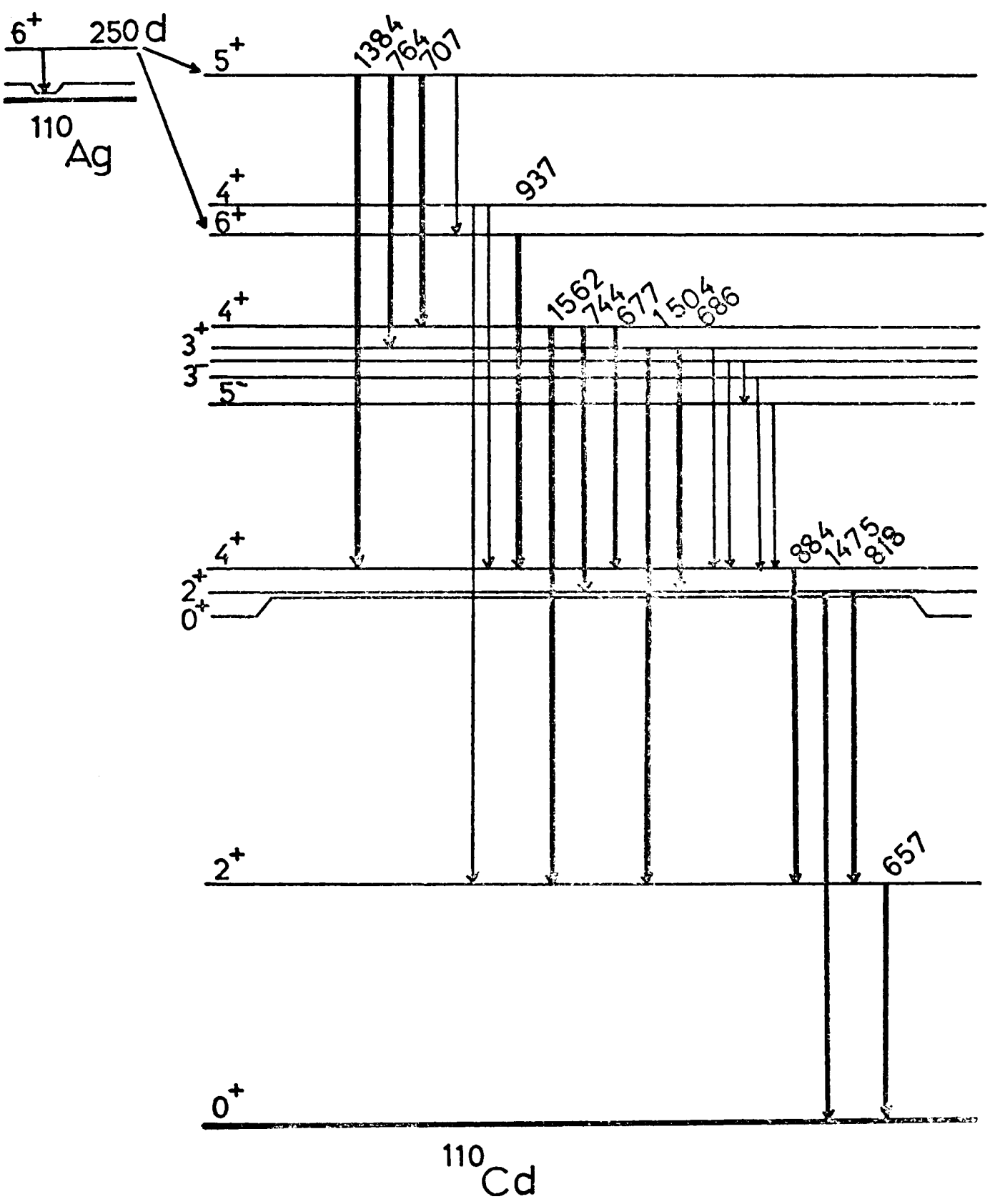
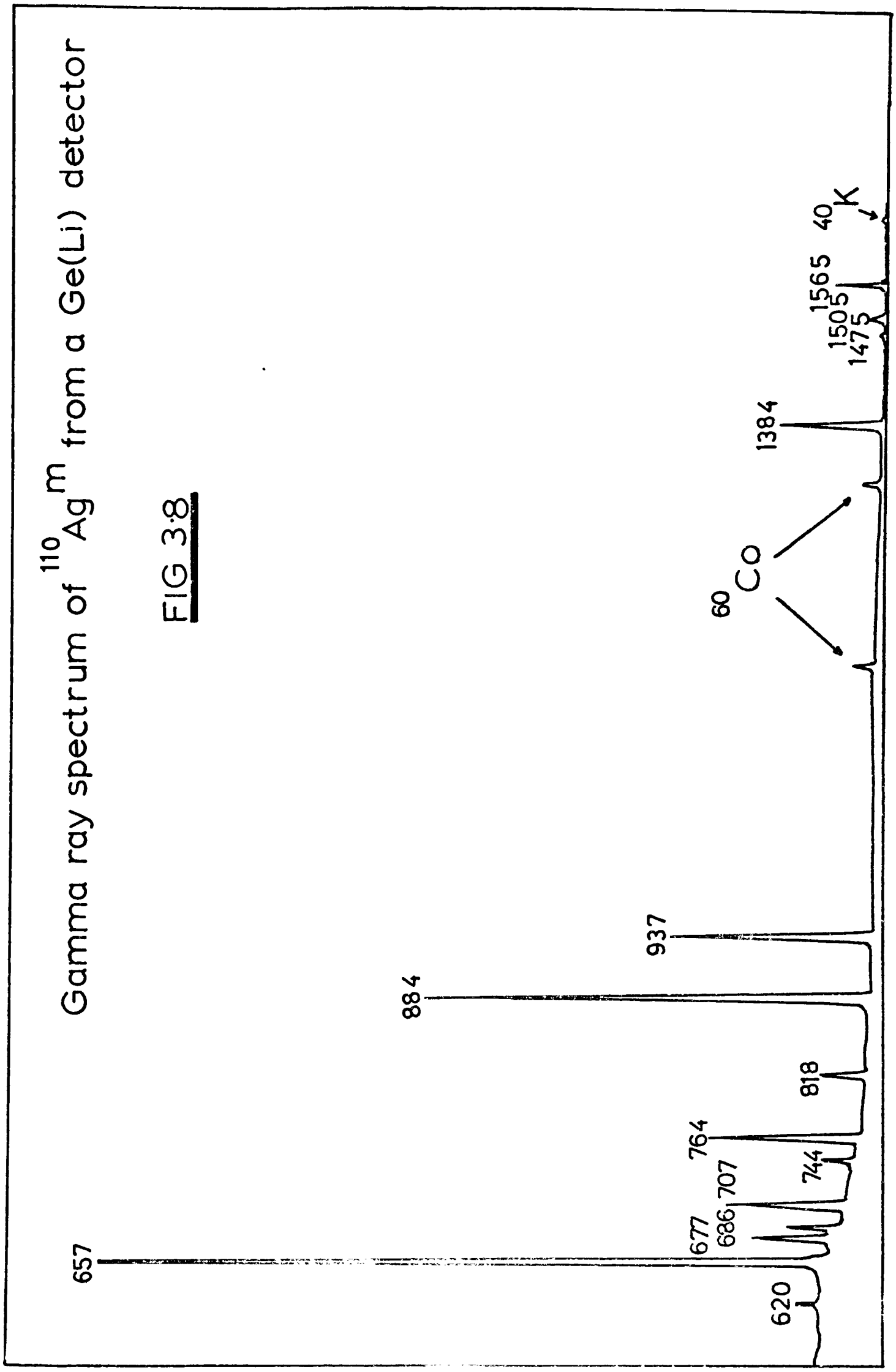


FIG 3.8


Gamma ray spectrum of $^{110}Ag^{m}$ from a Ge(Li) detector
657
620
677
686
707
744
764
818
884
937
$^{60}Co$
1384
1475
1505
1565
$^{40}K$

and the pairing-plus-quadrupole model proposed by Kumar and Baranger [ 54 ], and applied so far to the mass region $182 < A < 196$.

The Fermi; Gamow-Teller mixing of the $6^+ \rightarrow 6^+$, 531 KeV beta decay has been studied by Knott, Andrews, Cohen, Pipkin and Santry [ 45 ], using a coincidence measurement of the beta-ray asymmetry from oriented nuclei. This would provide a more direct measurement of the beta decay multipolarity, than the observation of the subsequent gamma transitions in this experiment, but the uncertainty involved in the sample preparation, and their inferred hyperfine field of $250 \pm 6$ kOe throws some doubt on their measurements. In this analysis the beta decays are observed only through the $U_K$ coefficients of subsequent gamma transitions, and appear to show a $\gamma_\beta = 1$ multipolarity only, within the limits of the experiment.

The analysis of all the gamma-ray anisotropy measurements was done using a least-squares fitting programme on the P.D.P.8L computer. The axial gamma-ray anisotropies are given by the expression

$$1 - W(0) = B_2 Q_2 U_2 F_2 + B_4 Q_4 U_4 F_4$$

Knowledge of the hyperfine field from the resonance experiment, and of the temperature of the impurity system from the $\underline{Fe}^{60}Co$ thermometer near the $^{110}Ag^m$ sample enables values of $B_2$ and $B_4$ to be calculated for each measurement of the gamma-ray anisotropies. The anisotropy is a function only of $B_2$ and $B_4$ with the parameters $Q_2U_2F_2$ and $Q_4U_4F_4$ merely constants of proportionality. The values of $1-W(0)$ will therefore lie on a plane in the space defined by $1-W(0)$, $B_2$ and $B_4$; with the differential gradients $Q_2U_2F_2$ and $Q_4U_4F_4$. The programme, given in appendix A, performs a least squares fit of the anisotropy data to such a plane with $Q_2U_2F_2$ and $Q_4U_4F_4$ as the free and independent parameters. The different temperature dependances of the $B_2$ and $B_4$ terms make the fit sensitive to both free parameters, but since the contribution to the anisotropy from the $B_4$ term is generally much smaller than that from the $B_2$ term, the accuracy

of the measurement of $Q_4U_4F_4$ is lower. With the large hyperfine field provided by the iron host and the temperature range from 1/T = 30 to 1/T = 130 $k^{-1}$, the available data enabled $Q_2U_2F_2$ to be measured to about $\pm$ 0.01, and $Q_4U_4F_4$ to about $\pm$ 0.08, with some variation reflecting the intensity of the observed transition. Each data point used in the fitting procedure was weighted by a factor representing the time of the counting period, since the rate at which the temperature changes is slower for the experiments using chrome alum; for the temperature range 1/T = 30 $k^{-1}$ to 1/T = 80$k^{-1}$; than the rate of warm-up of the C.M.N. cooled sample between 1/T = 70$k^{-1}$ and 1/T = 130 $k^{-1}$. In practice, of course, the orientation parameters $Q_2U_2F_2$ and $Q_4U_4F_4$ are not independent, since a given multipolarity mixing determines both parameters. When the results for these two parameters from the least-squares-fit were inconsistent, the data was fitted by an iterative procedure starting from the l.s.f. value of $Q_2U_2F_2$ including the additional constraint imposed on $Q_4U_4F_4$ by the mixing ratio associated with the value of $Q_2U_2F_2$. The use of an iterative procedure was needed because there is no analytical expression linking $U_2$ and $U_4$, and $F_2$ and $F_4$, for a given value of $\delta$(M1/E2).

All the major observed transitions were studied except the 449 KeV and the 620 KeV transitions where the low intensity and high background level from higher energy transitions made useful measurements impossible.

The 84 KeV β-decay and the 764 KeV gamma transition

The initial nuclear orientation measurements to identify the range of the search for the N.M.R. signal used the observation of the temperature dependence of the 764 KeV gamma transition. The gamma transition is a $5^+ \rightarrow 3^+$ transition of pure E2 multipolarity, and is fed entirely by the 84 KeV β-transition. The spins and parities of the initial and final states of the β decay suggest that it should be an allowed transition with a pure $\chi_\beta$ = 1

multipolarity. The log ft value for the 84 KeV transition of 5.4 tends to confirm this conclusion. Any contribution from the β-decay matrix elements giving $\gamma_\beta = 2$ would be associated with a 2nd forbidden transition which is very unlikely. If a pure $\gamma_\beta = 1$ multipolarity is assumed for this beta decay, all the decay coefficients are known for the 764 KeV gamma transition. The comparison of the experimental and theoretical values for $U_2F_2$ and $U_4F_4$ for the 764 transition are given below

| | experimental | theoretical ($\gamma_\beta = 1$) |
|---|---|---|
| $U_2F_2$ | - 0.397(5) | -0.403 |
| $U_4F_4$ | - 0.196(20) | -0.210 |

The values for both $U_2F_2$ and $U_4F_4$ are slightly smaller than the theoretical values. The most likely explanation is that, despite the care taken in the sample preparation, not all the silver impurity atoms are in substantial sites. If; as was shown in section 3.4; this distribution of sites can be represented by a constant factor, (1-x), on both $U_2F_2$ and $U_4F_4$, for all the gamma rays, the appropriate factor of 0.980 (5) can be included in the $U_{2,4}$ for the beta decay, and will have no further influence on the analysis. The experimental data and the calculated fit for the anisotropy as a function of the temperature are shown in Fig.3.9.

The 537 KeV β-decay and the 937 KeV gamma transition

This other major beta-decay provides a situation similar to that for the 84KeV decay. The observed gamma transition at 937 KeV is a $6^+ \rightarrow 4^+$ transition of pure E2 multipolarity, with well known values for $F_2$ and $F_4$. The initial state is fed by the 537 KeV β-decay and by the 447 KeV gamma transition following the 84 KeV β-decay. The relative intensities of these feeds is given in the Nuclear-data sheets as 30.8 and 3.51 per 100 decays of $^{110}Ag^m$ respectively. The beta decay is a $6^+ \rightarrow 6^+$ transition with a log ft

FIG 3·9

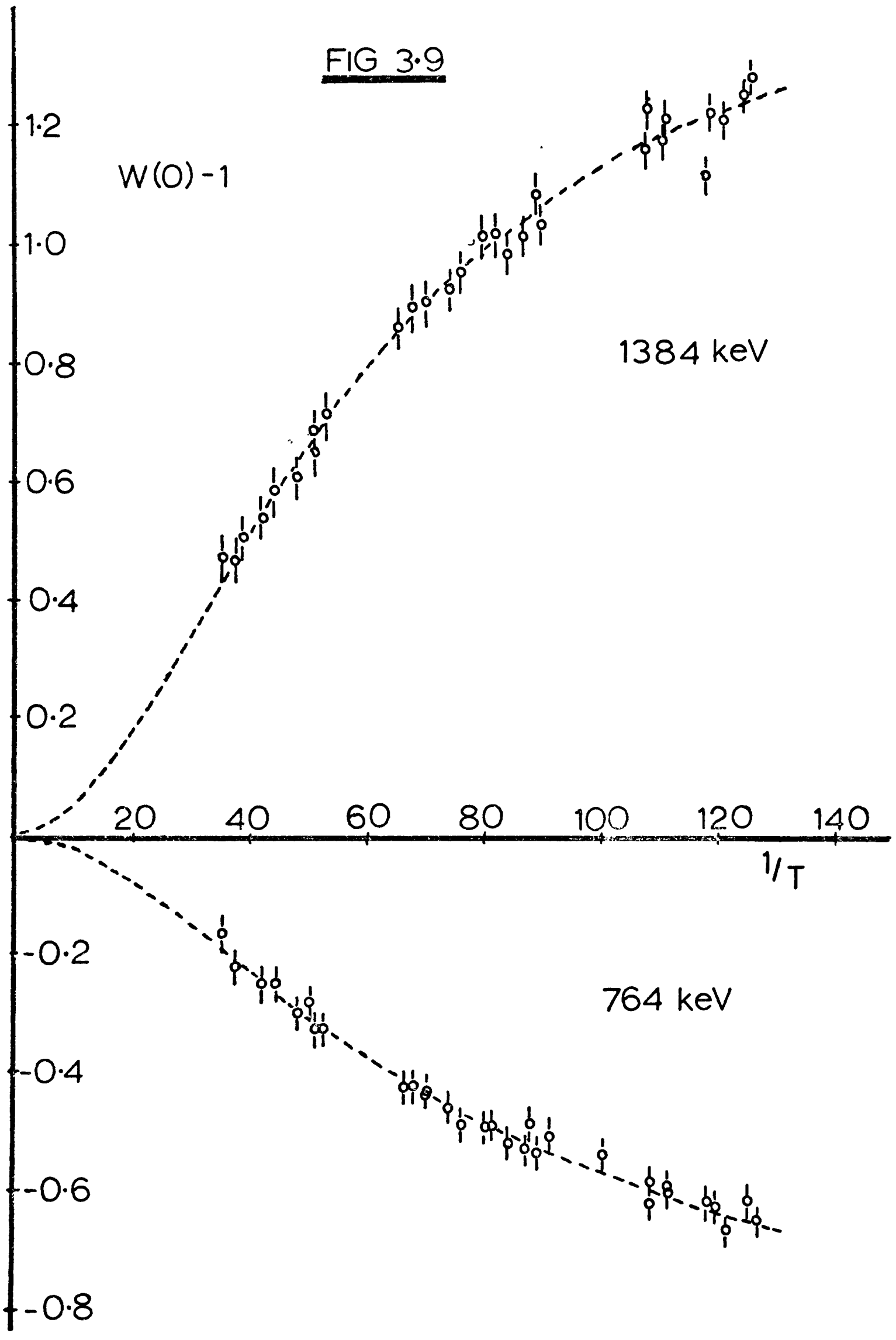
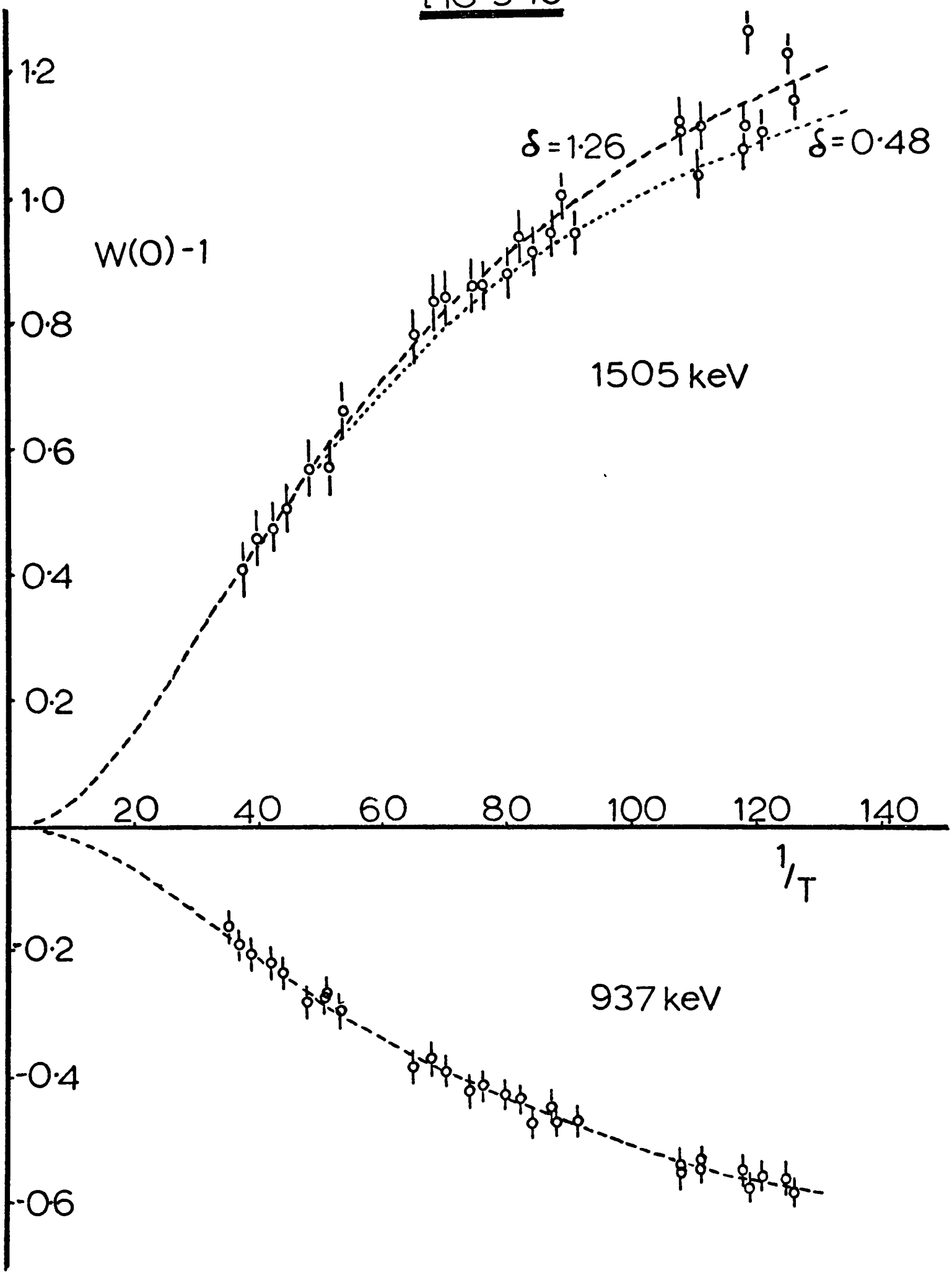

W(0) - 1
1·2
1·0
0·8
0·6
0·4
0·2
-0·2
-0·4
-0·6
-0·8
20
40
60
80
100
120
140
1/T
1384 keV
764 keV

FIG 3·10


1·2
1·0
0·8
0·6
0·4
0·2
W(0) - 1
δ = 1·26
δ = 0·48
1505 keV
20
40
60
80
100
120
140
1/T
-0·2
-0·4
-0·6
937 keV

value of 8.3. As an allowed transition the possible multipolarities are $\gamma_\beta = 0$ and $\gamma_\beta = 1$ with respective values of $U_2$ of 1.000 and 0.9286. The contribution to the $U_K$ coefficients from the 447 KeV gamma feed will depend on the multipolarity assumed for this $5^+ \rightarrow 6^+$ transition. The angular correlation measurements of Krane and Steffen give a value for $\delta(M1//M2)$ of - 0.45(20) for the mixing. Using this value the feed will give contributions of $U_2 = 0.887$ and $U_4 = 0.654$. With the appropriate weighting due to the relative intensities, the theoretical estimates of $U_2F_2$ and $U_4F_4$, for the 937 KeV gamma transition, are given below and compared with the experimental values

| | 937 KeV experimental | Theoretical $(\gamma_\beta = 0)^{537}$ | $(\gamma_\beta = 1)^{537}$ |
|---|---|---|---|
| $U_2F_2$ | - 0.365(5) | -0.398 | -0.372 |
| $U_4F_4$ | - 0.143(20) | -0.201 | -0.156 |

The experimental results fit very well with the theoretical values for $\gamma_\beta = 1$, when the factor of 0.98 is included for the non-unique site distribution. A multipolarity of $\gamma_\beta = 1$ for the 537 KeV beta decay is consistent with the log ft value for the transition. The data and the least-squares-fit are shown in Fig.3.10.

The 1384 KeV transition

The initial excited state of this transition is the $5^+$ level at 2.927 Mev. The level is fed entirely by the 84 kev beta-transition for which the decay parameters are now known. The $5^+ \rightarrow 4^+$ gamma transition will be of mixed M1 and E2 multipolarity with a variable value of $\delta$ which can be used to fit the experimental values of $U_2F_2$ and $U_4F_4$. The experimental values of $U_2F_2$ and $U_4F_4$, and the deduced values of $F_2$ and $F_4$ are compared below with the theoretical values for the quoted values of $\delta$.

| $U_2F_2$ | $F_2$(expt) | $F_2[\delta=-0.42]$ | $F_2[\delta=-0.50]$ |
|---|---|---|---|
| +0.900(10) | +0.955 (10) | +0.915 | +0.980 |

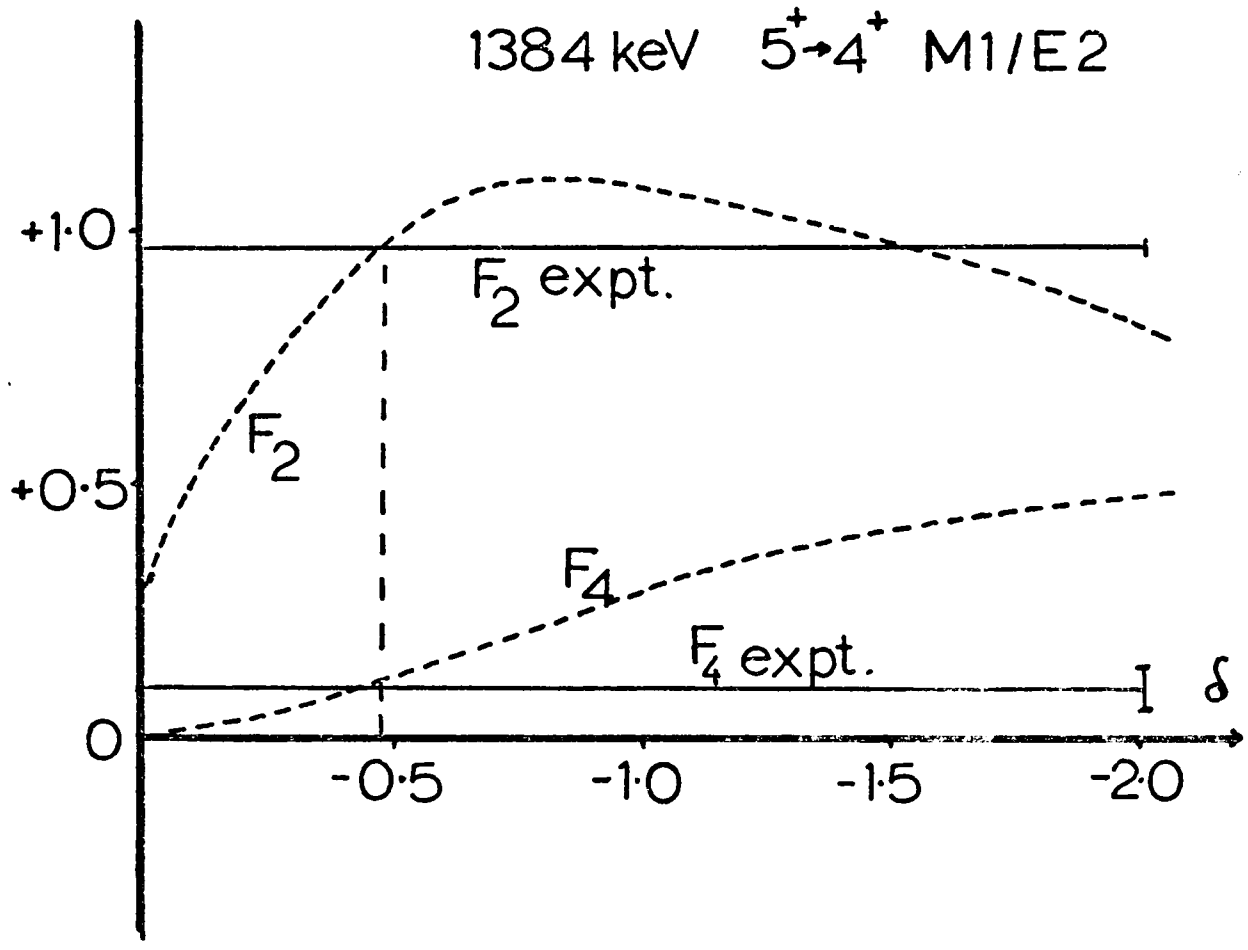
| $U_4F_4$ | $F_4$(expt) | $F_4[\delta=-0.42]$ | $F_4[\delta=-0.50]$ |
|---|---|---|---|
| +0.076(20) | +0.094(20) | +0.085 | +0.113 |

The experimental values of both $F_2$ and $F_4$ indicate a value of $\delta$ of -0.46(1). The sign of $\delta$ is clearly given by the sign of the gamma-ray anisotropy when the $F_2$ term is dominated by the coherent mixed $F_2$ parameter multiplied by $2\delta$. The sign convention used is that of Biedenharn and Rose [ 18 ]. All the results for these mixed transitions are summarised in Table 3.2. The experimental data are shown in Fig.3.9 with the calculated curve for a value of $\delta = -0.46$.

The 706 KeV transition

This is a very similar transition to the 1384 KeV tannsition, de-exciting the same $5^+$ state by a mixed M1/E2 transition. It is a lower intensity transition and does not provides such an accurate measurement of $\delta$. The analysis is identical to that for the 1384 KeV transition and is shown diagramatically in Fig.3.11. The best value of $\delta$ from the experimental value of $U_2F_2$ is $\delta = -0.58(2)$, with a consistent value of $\delta = -0.60(10)$ from the measurement of $U_4F_4$. The comparison of the measurements with the calculated fit is shown in Fig.3.12.

FIG 3·11


1384 keV 5+→4+ M1/E2
+1·0
+0·5
0
F2 expt.
F2
F4
F4 expt.
δ
-0·5
-1·0
-1·5
-2·0

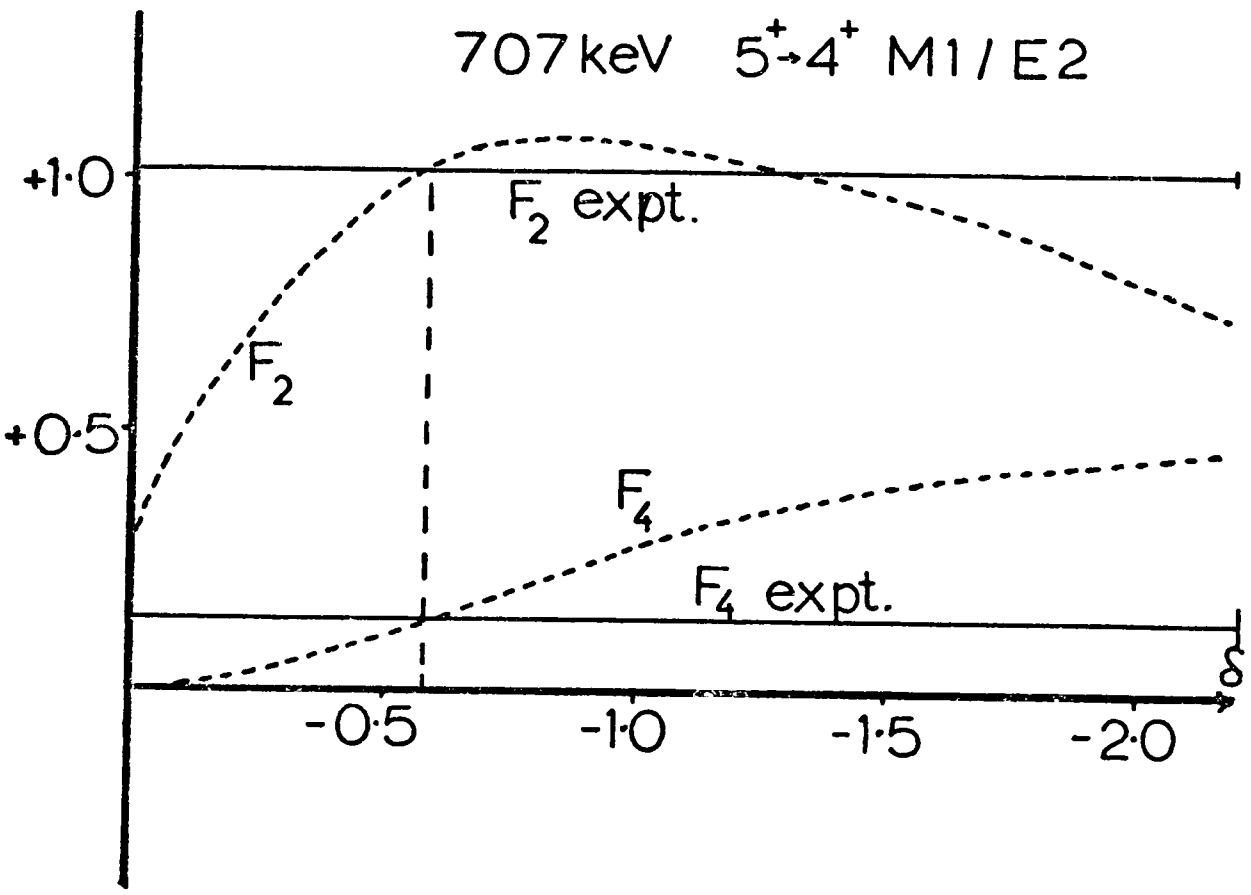
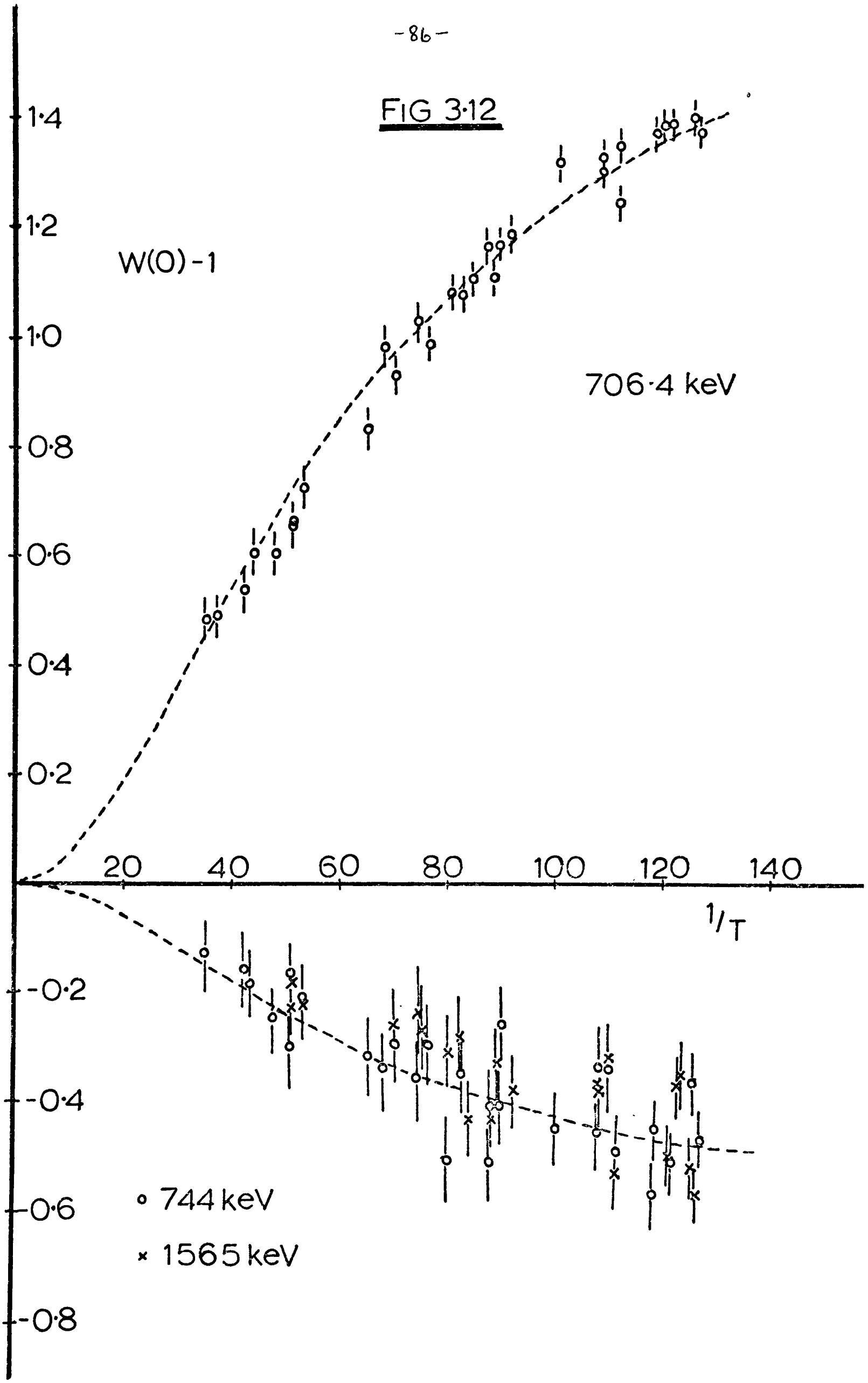

707 keV 5+→4+ M1/E2
+1·0
+0·5
F2 expt.
F2
F4
F4 expt.
δ
-0·5
-1·0
-1·5
-2·0

FIG 3·12


1·4
1·2
1·0
0·8
0·6
0·4
0·2
W(0) - 1
706·4 keV
20
40
60
80
100
120
140
1/T
-0·2
-0·4
-0·6
-0·8
o 744 keV
× 1565 keV

The 744 KeV and 1562 KeV transitions

Both of these transitions are fed entirely by the 707 KeV decay and are $4^+ \rightarrow 2^+$ transitions showing pure E2 multipolarity. Since the $F_2$ and $F_4$ coefficients are well known for a pure E2 transition, both of these gamma-rays provide a check on the mixing ratio deduced for the 707 KeV feed. The value of $\delta$ for the 707 KeV transition will change the $U_2$ and $U_4$ coefficients for these two gamma rays. Both the 744 KeV and the 1562 KeV transitions are shown together in Fig.3.12 with the calculated curve for the value of $\delta = -0.58$ for the 707 KeV gamma-ray. The agreement confirms the previous analysis.

The 677 Kev transition

This $4^+ \rightarrow 4^+$ transition, again fed entirely by the 707 KeV transition, shows a mixed M1 and E2 multipolarity. The decay parameters from the preceding transitions are now known accurately, and therefore the experimental values of $U_2F_2$ and $U_4F_4$ can be used to determine the value of $\delta$ for this transition. The experimental values of $U_2F_2$ and $U_4F_4$ with the declared values of $F_2$ and $F_4$ are given below

| $Q_2U_2F_2$ | $Q_4U_4F_4$ | $F_2$ | $F_4$ |
|---|---|---|---|
| -0.063(10) | -0.014(30) | -0.030(15) | -0.030(60) |

The values of $\delta$ suggested by these values are: $\delta = -0.44(5)$ from the value of $F_2$ and $\delta = -0.30(30)$ from the value of $F_4$. The small negative anisotropies shown by this gamma ray, and the low intensity make a more accurate determination very difficult. The data is shown in Fig.3.13.

FIG 3·13

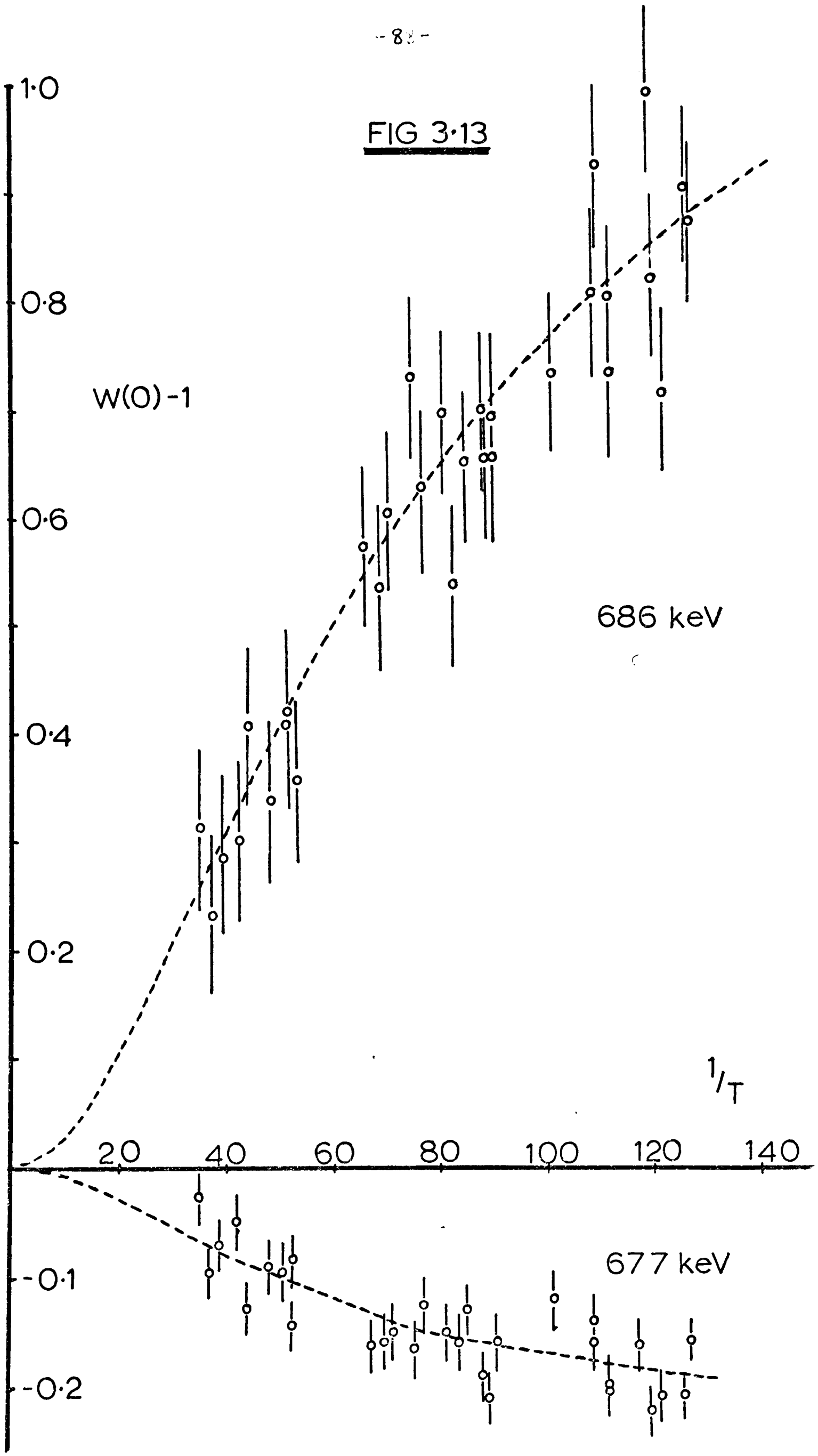
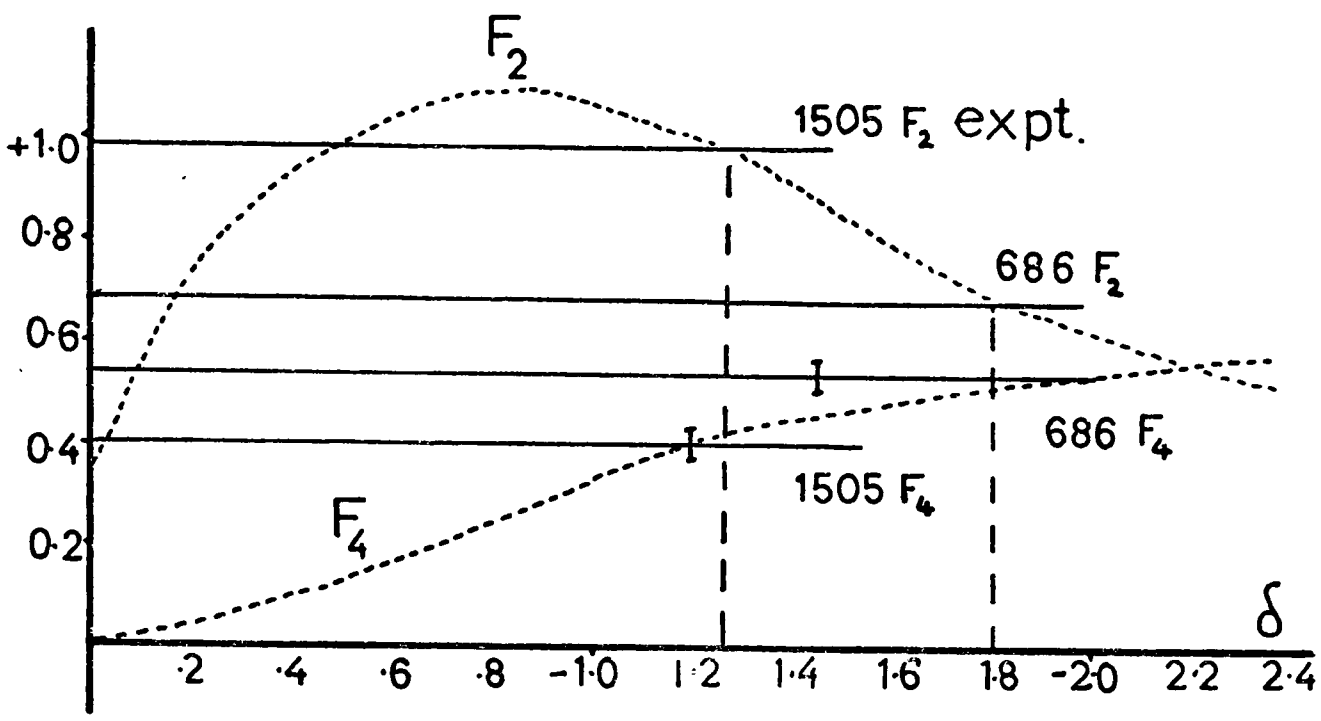
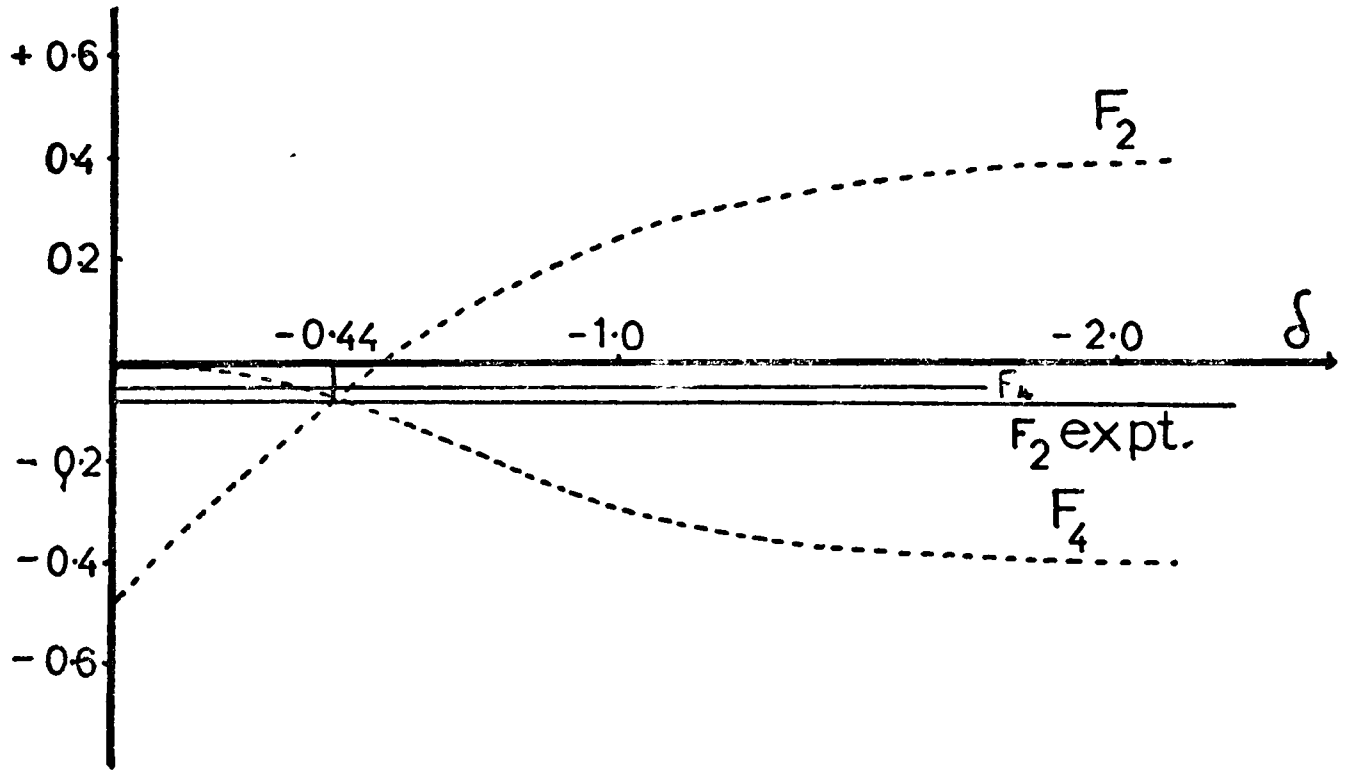


FIG 3·14

1505 keV and 686 keV $3^+$-$2^+$ M1/E2




677 keV



The 686 KeV transition

This transition occurs in the branch of the decay fed by the 764 KeV transition. The $3^+ \rightarrow 2^+$ transitions will again have a mixed M1 and E2 multipolarity which can be studied with the deduced values for $F_2$ and $F_4$ from the orientation measurements. The $U_2$ and $U_4$ coefficients from the previous transitions are again below

| $U_2Q_2$ | $U_4Q_4$ | $U_2F_2Q_2$(expt) | $U_4F_4Q_4$(expt) | $F_2$ | $F_4$ |
|---|---|---|---|---|---|
| + 0.761 | +0.373 | +0.515(10) | +0.206(30) | +0.68(2) | +0.54(5) |

The analysis in terms of the $\delta$ value for the mixing is shown diagramatically in Fig.3.15. The value of $\delta$ is well defined by the experimental value of $F_2$, with the $F_4$ value distinguishing between the two possible solutions. The best value of $\delta$ is - 1.80(5). The anistropy data is shown in Fig.3.13.

The 1505 KeV transition

The analysis if this $3^+ \rightarrow 2^+$ transition is identical to that for the 686 KeV transition and is shown in Fig.3.14 for the experimental values

$F_2 = +0.99(1)$ $F_4 = +0.40(20)$

The value of $F_2$ gives two possible solutions for $\delta$ of either $\delta = -0.48(3)$ or $\delta = -1.26(6)$. The value of $F_4$ give a solution of $\delta = -1.2(-0.5)$ suggesting the larger value of $\delta$ as the most likely solution. These solutions will be discussed further in the comparison with other measurements in section 3.6. The experimental data for this gamma-ray is shown in Fig.3.10.

The 884 and 1476 KeV transitions

The 884 KeV, $4^+ \rightarrow 2^+$ transition, is fed by the 937 KeV gamma, the 677 KeV, and the weak 620 KeV gamma transitions. The multipolarity is expected to be pure E2. The mixing ratios derived for the 677 KeV and the value of $\delta = -0.80 \pm 0.50$ given by Steffen for the 620 KeV transition can be used to calculate the decay coefficients associated with the mixed feed. The calculated values are compared with the experimental values below.

calculated $Q_2U_2F_2 = -0.345(18)$ $Q_4U_4F_4 = -0.120(10)$

experimental $Q_2U_2F_2 = -0.360(10)$ $Q_4U_4F_4 = -0.118(20)$

The agreement confirms the analysis of the preceding transitions and the identification of the 884 KeV gamma transition as pure E2.

A similar comparison can be made for the 1475 KeV transition but the low intensity of the transition makes the comparison less useful. This is also a pure E2, $4^+ \rightarrow 2^+$ transition with the observed results being consistent with this identification.

calculated $Q_2U_2F_2 = -0.319(15)$ $Q_4U_4F_4 = -0.078(10)$

experimental $Q_2U_2F_2 = -0.324(20)$ $Q_4U_4F_4 = -0.20(20)$

The 818 KeV transition

This $2^+ \rightarrow 2^+$ mixed M1/E2 transition shows small positive anisotropies indicating a mixed transition with a negative sign of $\delta$. The $F_2$ and $F_4$ coefficients can again be declared from the experimental results using the calculated values of $U_2 = -0.34$ and $U_4 = -0.06$ from the feeds. The combination of $F_2$ and $F_4$ gives a value of $\delta$ of

$$\delta = -1.36(10)$$

The experimental results fitted with this value of $\delta$ are shown in Fig.3.15.

FIG 3·15

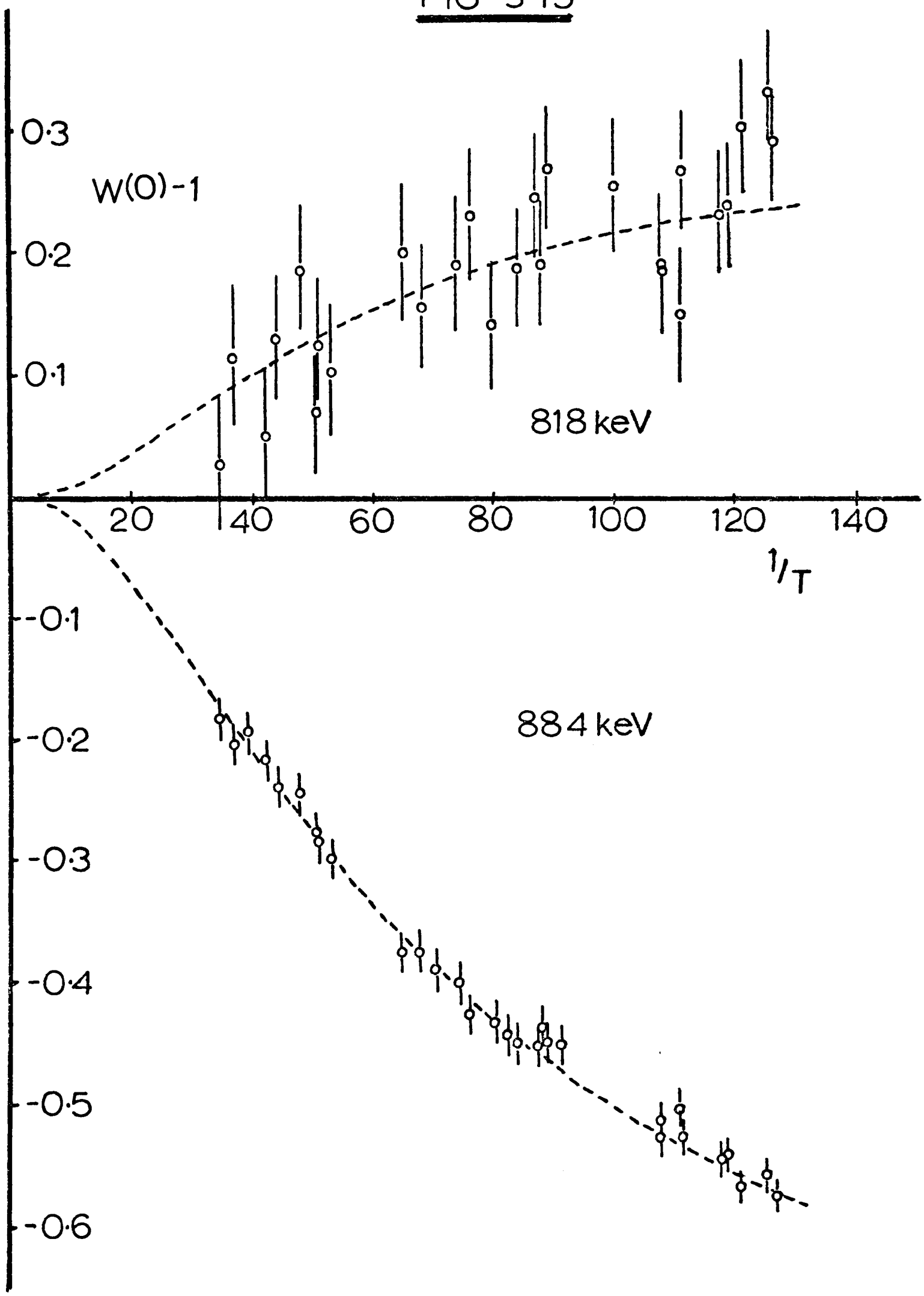

0·3
W(0)-1
0·2
0·1
818 keV
20
40
60
80
100
120
140
1/T
-0·1
884 keV
-0·2
-0·3
-0·4
-0·5
-0·6

Table 3.2

| γ-energy KeV | intensity | $J_i^\pi$ | $J_f^\pi$ | Multipolarity | $U_2F_2$ | $U_4F_4$ |
|---|---|---|---|---|---|---|
| 657 | | $2^+$ | $0^+$ | E2 | -0.320(10) | -0.10(5) |
| 677 | | $4^+$ | $4^+$ | M1/E2 | -0.066(10) | -0.016(30) |
| 687 | | $3^+$ | $2^+$ | M1/E2 | +0.540(10) | +0.240(30) |
| 707 | | $5^+$ | $4^+$ | M1/E2 | +0.965(10) | +0.114(30) |
| 744 | | $4^+$ | $2^+$ | E2 | -0.320(15) | -0.073(30) |
| 764 | | $5^+$ | $3^+$ | E2 | -0.395(5) | -0.195(20) |
| 818 | | $2^+$ | $2^+$ | M1/E2 | +0.181(10) | +0.015(20) |
| 884 | | $4^+$ | $2^+$ | E2 | -0.361(10) | -0.139(30) |
| 937 | | $6^+$ | $4^+$ | E2 | -0.365(5) | -0.143(20) |
| 1384 | | $5^+$ | $4^+$ | M1//2 | +0.900(10) | +0.076(20) |
| 1476 | | $2^+$ | $0^+$ | E2 | -0.319(15) | -0.078(10) |
| 1505 | | $3^+$ | $2^+$ | M1/E2 | +0.795(10) | +0.175(30) |
| 1562 | | $4^+$ | $2^+$ | E2 | -0.320(15) | -0.073(30) |

The 657 KeV transition

The ground state $2^+ \rightarrow 0^+$ transition is a pure E2 decay. The comparison of the experimental and calculated values for $U_2F_2$ and $U_4F_4$ provides a useful check on the consistency of the analysis. Fig.3.16 shows the experimental gamma-ray anisotropies with the least-squares-fit and the temperature dependence expected from the calculated decay coefficients. A comparison of the observed and calculated decay parameters is given below.

| | | |
|---|---|---|
| calculated | $Q_2U_2F_2 = -0.325(20)$ | $Q_4U_4F_4 = -0.080(10)$ |
| experimental | $Q_2U_2F_2 = -0.306(10)$ | $Q_4U_4F_4 = -0.088(10)$ |

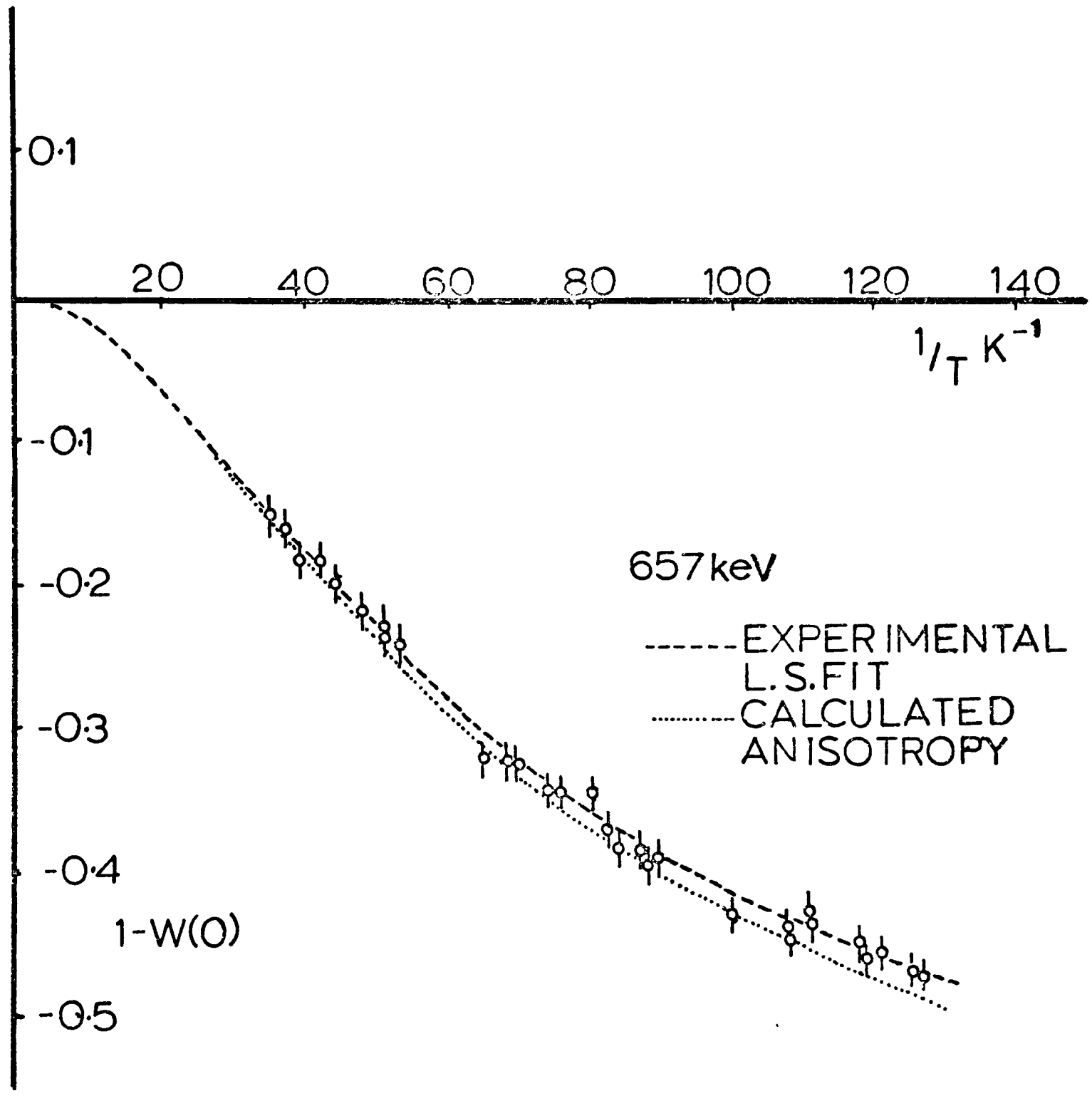
The full list of all the observed gamma-rays, intensities and orientation parameters is given in Table 3.2. In section 3.6 the values of $\delta$ calculated for all the mixed M1/E2 transitions is compared with previous measurements, and the results discussed in terms of the vibrational structure of $^{110}$Cd in section 3.7.

## 3.6 Comparison of the M1/E2 mixing ratios with other experimental results

Similar measurements of the multipolarities of gamma transitions can be made by several techniques. The techniques of $\gamma$-$\gamma$ angular correlation; coulomb excitation, k-conversion coefficient measurement and nuclear orientation will all provide measurements of $\delta$(M1/E2).

Previous measurements on the excited states of $^{110}$Cd with NaI detectors using the nuclear orientation technique [ 57 ] and the angular correlation technique [ 48 ] have been restricted by the poor resolution and the complex gamma-ray spectrum. The K-conversion coefficients for the Z of 48 and the typical energies of the gamma-rays involved in this decay are not strongly dependent on the relative amounts of the M1 and E2 multipolarities, and therefore such measurements do not provide a

FIG 3·16


0·1
20
40
60
80
100
120
140
1/T K⁻¹
-0·1
-0·2
-0·3
-0·4
1-W(0)
-0·5
657keV
EXPERIMENTAL
L.S.FIT
CALCULATED
ANISOTROPY

very accurate determination of δ. The measurements of Maraguez, Reyes-Suter and Suter [ 52 ] are consistent with the more accurate measurements outlined here. The mixing ratio of the 818 KeV gamma transition has been measured by coulomb excitation by Milner, McGowan and Stelson [ 56 ] gives a value of δ = -1.5 which is in agreement with this measurement and the γ-γ angular-correlation measurement of Krane and Steffen [ 55 ].

The most complete series of measurements on this decay scheme, so far reported, has been these γ-γ angular correlation measurements of Krane and Steffen. Their results are shown for comparison in Table 3.3. The measurements all show good agreement except for the 1505 KeV transition. The nuclear orientation measurement of the $F_2$ decay parameter gave two possible solutions, the higher value being chosen as more likely on the basis of the measurement of the $F_4$ parameter. The measurements of Krane and Steffen give a value in agreement with the lower of the two possibilities for δ. The curve, b), in Fig.3.10 shows the calculated gamma ray anisotropies for the lower value of δ = 0.48.

The small discrepancy between the two quoted values for δ (1384) may be due to a combination of random and systematic errors. The value of δ = -0.37(3) from the γ-γ angular correlation measurements would give much smaller anisotropies in the nuclear orientation experiment than has been observed.

very accurate determination of δ. The measurements of Morangues, Reyes-Suter and Suter [ 52 ] are consistent with the more accurate measurements outlined here. The mixing ratio of the 818 KeV gamma transition has been measured by coulomb excitation by Milner, McGowan and Stelson [ 56 ] gives a value of δ = -1.5 which is in agreement with this measurement and the γ-γ angular-correlation measurement of Krane and Steffen [ 55 ].

The most complete series of measurements on this decay scheme, so far reported, has been these γ-γ angular correlation measurements of Krane and Steffen. Their results are shown for comparison in Table 3.3. The measurements all show good agreement except for the 1505 KeV transition. The nuclear orientation measurement of the $F_2$ decay parameter gave two possible solutions, the higher value being chosen as more likely on the basis of the measurement of the $F_4$ parameter. The measurements of Krane and Steffen give a value in agreement with the lower of the two possibilities for δ. The curve, b), in Fig.3.10 shows the calculated gamma ray anisotropies for the lower value of δ = 0.48.

The small discrepancy between the two quoted values for δ (1384) may be due to a combination of random and systematic errors. The value of δ = -0.37(3) from the γ-γ angular correlation measurements would give much smaller anisotropies in the nuclear orientation experiment than has been observed.

Table 3.3 Measurements of δ for M1/E2 transitions in $^{110}Cd$

| γ - energy KeV | This work δ | correlation [a] | Coulomb excitation [b] | K-conversion coefficients [c] |
|---|---|---|---|---|
| 677 | - 0.44(5) | -0.25(20) | | 0.0 → ∞ |
| 687 | - 1.80(5) | $-1.1^{+0.8}_{-0.4}$ | | 0.0 → 10 |
| 707 | - 0.58(2) | -1.0 ± 0.3 | | < 0.8 |
| 818 | - 1.36(10) | -1.20(15) | - 1.5 | < 5 |
| 1384 | - 0.46(1) | -0.37(3) | | 0.0 → ∞ |
| 1505 | -1.26 (6) | -0.55(10) | | 0.0 → ∞ |
| | [-0.48(3)]* | | | |

a) K.S.Krane and R.M.Steffen Phys Rev C2 724 1970

b) W.T.Milner, F.K.McGowan, P.H.Stelson, R.L.Robinson and R.O.Sayer Nucl Phys A129 687 1969

c) J.A.Moragues, P.Reyes-Suter and T.Suter Nucl Phys A99 652 1967

## 3.7 The excited state structure in $^{110}Cd$

The excited state levels, and the spins and parities of particularly the lower lying levels in $^{110}Cd$ are typical of a "vibrational" nucleus, but the observation of appreciable M1 admixture in the transitions from the two phonon $2^+$ state to the one phonon $2^+$ excited state at 818 KeV is not in agreement with the predictions of a harmonic vibration model. Several models have been proposed for anharmonic effects in the structure of vibrational nuclei, but the most successful theory is that proposed by Kumar and Baranger on the basis of a pairing-plus-quadrupole model. This has been particularly successful in explaining experimental measurements of M1/E2 mixing in the mass region $182 < A < 196$, and a similar approach for the mass region around A = 110 may well be appropriate. As has been pointed out by Krane and Steffen, transitions between the higher energy excited states in $^{110}Cd$, which will be less accurately represented by a vibrational model, do not generally show larger M1 admixtures. All the transitions for which the spins and parities allow $\Delta l=1$ and $\pi_i = \pi_f$, show large admixtures of M1 character, which, particularly in the case of 818KeV transition, requires a modification of the simple harmonic oscillator model for these states. No specific calculations for mass 110 have been performed on the pairing-plus-quadrupole model, but the existence of accurate measurements from this experiment and the work of Steffen et al will now provide a basis for comparison with future theoretical estimates.

## Chapter 3(a) Nuclear orientation of $^{109}Cd$ and $^{109}Ag^{m}$ in nickel

### 3.8 Introduction

Although the experiment does not fall within the general theme of this thesis, it is included here because of the close ties with the previous experiments on $^{110}Ag^{m}$, and as another example of a system that cannot be studied by nuclear orientation alone. The large nuclear orientation effects for this impurity arise mainly from the polarisation of the 40 sec metastable state of $^{109}Ag^{m}$ which is populated by the decay of $^{109}Cd$. The hyperfine interactions of $^{109}Cd$ and $^{109}Ag^{m}$ are of opposite sign, so the initial population distribution of the magnetic substates of $^{109}Ag^{m}$ differs considerably from the thermal equilibrium value. The lifetime of this state is comparable with the typical spin lattice relaxation times for the impurity in a ferromagnetic host in the temperature range $1/T = 10\ K^{-1}$ to $100\ K^{-1}$ so the re-distribution of the populations of the magnetic substates will give a temperature dependence to the gamma-ray anisotropy, intermediate between that expected for $^{109}Cd$ and $^{109}Ag^{m}$, in thermal equilibrium with the lattice. When the hyperfine fields are known, a system like this provides a sensitive measurement of the nuclear spin-lattice relaxation times.

Measurements on an implanted sample of $^{109}Cd$ in iron by R.A.Fox showed an anomalous temperature dependence of the gamma-ray anisotropy of the 88KeV transition, de-exciting the metastable state $^{109}Ag^{m}$. Using the now known hyperfine field of silver in iron, the observed anisotropies have been analysed to give a value of $T_1T$ for silver in iron, and have shown that the temperature dependence of the relaxation time follows the low temperature form

$$\frac{1}{T_1} = \left(\frac{h\nu}{2C_K k}\right) \coth\left(\frac{h\nu}{2kT}\right)$$

The interest in the experiment discussed in this chapter is in the comparison of the value of $C_K$ deduced for the nickel host with that found for silver in iron by Fox and Stone. This is discussed after the description of the experiment in section 3.10. The analysis of the gamma-anisotropy measurements depends on the knowledge of the hyperfine field of silver in nickel from the N.M.R./O.N. experiment of $^{110}Ag^m$ in nickel.

## 3.9 Nuclear orientation measurements

The measurements of the 88KeV gamma-ray anisotropy from $^{109}Ag^m$ in nickel also show an anomalous temperature dependence. It must be pointed out, in the context of remarks in earlier sections of this chapter, that the samples used were prepared by ion implantation to overcome the problem of the insolubility of cadmium in nickel. Two samples were prepared, the results from one being shown in Fig.3.17.

The short lifetime and the decay rate of the $^{109}Ag^m$ state give a concentration of less than $10^{-10}$ for this state in the nickel lattice. The dominant spin-spin interaction for dilute impurities in the Suhl-Nakamura interaction, but its effects are negligible below an impurity concentration of $10^{-6}$. The analysis of the relaxation effects must therefore be done without the assumption of a spin temperature. The theory of Spanjaard and Hartmann-Boutron assumes independent relaxations of the different nuclei through their interaction with the conduction electrons

$$\mathcal{H} = \Gamma \, \underline{I}.\underline{S} \; \delta(\underline{R} - \underline{r})$$

The time dependance of the populations of the 40 sec state is then given by the solutions of the Master equation

$$\frac{dP_m}{dt} = -[W_{m,m-1} + W_{m,m+1}] P_m + W_{m+1,m} P_{m+1} + W_{m-1,m} P_{m-1}$$

where

$$W_{m,\,m+1} = \frac{1}{T_1'} \left| \left\langle m+1 \left| \frac{I^+}{2} \right| m \right\rangle \right|^2; \quad W_{m,m-1} = \frac{1}{T_1''} \left| \left\langle m-1 \left| \frac{I^-}{2} \right| m \right\rangle \right|^2$$

The $\gamma$-ray anisotropy is given by

$$W(\theta) = \frac{1}{\tau} \int_0^\infty dt \exp(-t/\tau) \sum_{K \text{ even}} B_K(t) F_K P_K \cos(\theta)$$

where $B_K = \sqrt{2I+1} \sum_m P_m \langle m \mid T_K^0 \mid m \rangle$

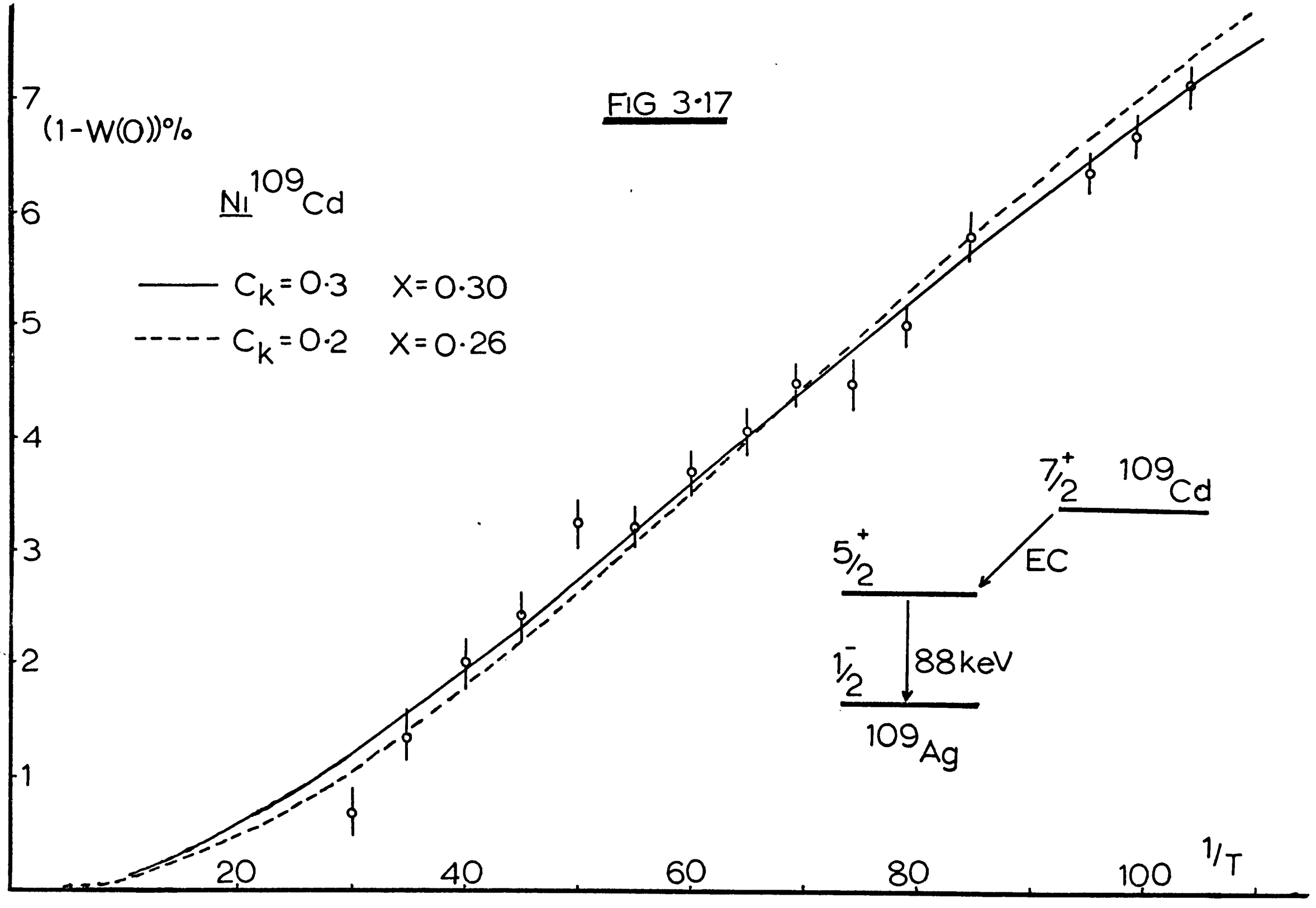
With a knowledge of the hyperfine field of Ag in nickel from the resonance of $^{110}Ag^m$ the results were fitted using numerical solutions of the above equations for various values of $C_K$.

It was found to be impossible to reproduce the observed temperature dependence for a single value of $C_K$ assuming all the nuclei experienced the full hyperfine field. A second parameter was introduced to include the possibility of a proportion of nuclei experiencing a very small hyperfine field.

$$X = \frac{N_o \text{ in high field sites}}{\text{Total No. impurities}}$$

A two parameter fit using $C_K$ and X produced a best fit to the data for $C_K = 0.3 \pm 0.1$; $X = 0.30 \pm 0.01$. The second sample gave similar results for $C_K$ but a larger value for X representing the different history and implantation dose.

FIG 3·17


(1-W(0))%
7
6
5
4
3
2
1
Ni 109Cd
Ck = 0·3 X = 0·30
Ck = 0·2 X = 0·26
20
40
60
80
100
1/T
7/2+ 109Cd
EC
5/2+
1/2-
88keV
109Ag

| | $C_K$ | X |
|---|---|---|
| Sample 1 | 0.3 ± 0.1 | 0.30 ± 0.01 |
| Sample 2 | 0.3 ± 0.1 | 0.34 ± 0.01 |
| annealed sample | - | ⟨0.03 |

One sample was annealed at 500°C for 1 hour. The 88KeV gamma showed less than 0.5% anisotropy over the temperature range from $1/T = 20K^{-1}$ to $1/T = 80k^{-1}$. This justifies the assumption of zero hyperfine field for a large proportion of the $^{109}Cd$ nuclei. The comparison with the results in iron where the assumption was made that all the nuclei experienced the full hyperfine field is similar to that for other implanted samples, such as Fe Yb and Ni Yb [ 115 ]. The difficulty in producing a uniform site distribution in nickel may be due to the larger amount of damage created during the implantation, than in an iron lattice, because of the f.c.c. structure of nickel.

### 3.10 Discussion of the relaxation measurement

The result obtained for $C_K$ shows a more rapid relaxation for the $^{109}Ag^m$ nucleus in nickel than that in iron. This is surprising if the relaxation mechanism is predominantly an interaction of the form A.I.s. with the conduction electrons. The Korringa constant for such a situation is proportional to the density of states at the Fermi surface, and inversely proportional to the square of the Zeeman splitting energy of the nuclear magnetic substates. With the smaller hyperfine field of silver in nickel, one would expect a Korringa constant in nickel about a factor of ten larger than in iron. A similar ratio of the spin-lattice relaxation times to that shown in this experiment has been observed for Manganese, and cobalt in the two hosts. Spanjaard has suggested [ 116 ] that the observed ratio may be explained if a virtual magnon

mechanism is assumed for the relaxation process. The lower saturation magnetisation of the nickel host will be associated with a smaller energy gap at the lower end of the magnon dispersion curve. On the basis of such a mechanism the relaxation times in nickel would be expected to be shorter than for an equivalent Zeeman splitting in iron by a factor of 12, (from the ratio $(2.216/0.62)^2$). The smaller Zeeman splitting of the nuclear substates of $^{109}Ag^{m}$ in nickel will however give a factor of $\sim 1/10$ between the values of $C_K$ in iron and nickel, therefore the observed relaxation times in iron and nickel would be expected to be similar. This is in agreement with the results obtained for $C_K$ of 0.48 in iron, and 0.30 in nickel, but more data on other systems is required before any definite conclusions can be reached.

# CHAPTER 4

# THEORETICAL MODELS FOR THE INTERACTION OF IMPURITIES WITH THE FERROMAGNETIC HOST ELECTRONS

4.1 The hyperfine interactions of impurities in the ferromagnetic hosts represent a combination of several terms from different interaction mechanisms. One of the main interests of the work in this thesis has been to use the N.M.R. and nuclear orientation techniques to investigate the magnitudes of the various components of the observed interactions. This chapter is devoted to a brief summary of the theories that have been proposed to explain the interactions of impurities with the polarised conduction electrons of the host lattice, with particular reference to the formation of localised magnetic moments on the impurity sites.

The complete Hamiltonian representing the hyperfine interaction experienced by an impurity nucleus is given by

$$\mathcal{H}_T = \mathcal{H}_c + \mathcal{H}_{OD} + \mathcal{H}_{S.D.} + \mathcal{H}_Q + \mathcal{H}_{ext}$$

The latter term, $\mathcal{H}_{ext}$, represents the interaction of the nucleus with the external magnetic field, the demagnetising field, and the Lorentz field. The dominant hyperfine interaction in the cubic ferromagnetic hosts is the Fermi-contact hyperfine interaction, $\mathcal{H}_c$, with the polarised s and $p_{\frac{1}{2}}$ electrons of the impurity

$$\mathcal{H}_c = 2\beta\left(\frac{\mu}{I}\right)\left\langle r_o^{-3}\right\rangle (\underline{I}.\underline{S})$$

Numerical factors and relativistic effects are absorbed into the effective value for $\left\langle r_o^{-3}\right\rangle$ for the contact interaction.

The orbital dipolar interaction represents the interaction between the nuclear spin and the orbital angular momentum of the impurity electronic states

$$\mathcal{H}_{O.D.} = 2\beta\left(\frac{\mu}{I}\right)\left\langle r_1^{-3}\right\rangle (\underline{L}.\underline{I}.)$$

The two remaining terms are the spin dipolar and electric quadrupole interactions

$$\mathcal{H}_{S.D} = 2\beta\left(\frac{\mu}{I}\right)\left\langle r^{-3}\right\rangle [L(L+1)(\underline{I}.\underline{S}) - \tfrac{3}{2}(\underline{L}.\underline{I})(\underline{L}.\underline{S}) - \tfrac{3}{2}(\underline{L}.\underline{S})(\underline{L}.\underline{I})]$$

$$\mathcal{H}_{Q} = \frac{e^2 Qq}{4I(2I-1)} [3I_z^2 - I(I+1)]$$

The cubic symmetry of the iron, nickel and f.c.c. cobalt host lattices tends to quench the orbital angular momentum of the impurity and to give zero electric field gradient at lattice sites, therefore, a finite contribution from these last three terms can only be associated with an interaction breaking the cubic symmetry about the impurity site. This theoretical discussion is particularly concerned with the formation of a localised magnetic moment on the impurity, and the unquenching of the orbital angular momentum through the action of the spin-orbit interaction.

The theoretical discussion can conveniently be split into three parts. The interaction of the host conduction electrons with the impurity arises through the screening of the electric charge of the ionised impurity atom and the mixing of the impurity wavefunctions with those of the host lattice. The direct calculation of the electron wavefunctions associated with the impurity state would require an extension of the unrestricted Hartree-Fock calculation method used for the many-electron aspects of the undisturbed atoms, and is impracticable with present techniques. The interactions of the impurity with the conduction electrons can however be represented using simplified impurity models. The first section deals with the formation of a virtual bound state on the impurity using a simple free electron model for the conduction electrons proposed by Friedel [58] and the model used by Wolff [10], with more realistic wavefunctions.

The second section is concerned with the formation of a localised spin magnetic moment on the impurity. The splitting of the virtual bound state on the impurity, from the exchange interaction in the ferromagnetic lattice, may push one substate across the Fermi-level. The unequal populations of the spin ↑ and spin ↓ states will then give a net spin magnetisation localised about the impurity site.

The final section considers the influence of the spin-orbit interaction of the impurity atomic orbitals on the quenched orbital angular momentum, when a net spin magnetisation exists in the virtual bound state associated with the impurity. The orbital dipolar, spin dipolar, and electric quadrupole hyperfine interactions become non-zero when the spin-orbit interaction perturbation produces a localised orbital magnetic moment.

## 4.2 The formation of a virtual bound state on an impurity

When an impurity atom is introduced into a metallic host lattice, the excess nuclear charge, determined by the difference in valency of the impurity and host, will locally displace the mobile electrons in the host conduction band until the excess nuclear charge Z is perfectly screened. A number of models have been proposed to provide a description of the electronic states associated with the screening of this charge. The conductionbands of the ferromagnetic metals, iron, cobalt and nickel, contain electrons of 3d and 4s character with a high density of states associated with the narrow d-band. For transition metal impurities the interaction of the impurity electrons with the d-band of the host metal can be described by the models of Friedel [58], Woolf [10], and Anderson [59].

Two alternative approaches to the problem are shown by these models. The model proposed by Anderson considers a localised level representing a d state of the impurity in a sea of mobile electrons. The one electron Hamiltonian includes the energies of the d-state, and the Bloch states of the conduction electrons, and off-diagonal matrix elements coupling the two. This coupling between the Bloch states and the localised d state broadens the latter, producing a virtual level localised at the impurity site.

The alternative approach originating in the work of Friedel and elaborated by Woolf and Clogston [ 9 ] considers the effect of the free conduction electrons scattering from a potential due to the single impurity ion. A virtual level arises as a maximum in the impurity scattering cross section as a function of the energy of the incoming Block wave. This model is the more appropriate for the case of transition metal impurities in iron, cobalt and nickel because of the strong coupling between the impurity d states and the conduction electrons, and is therefore discussed in more detail.

## The Friedel, Woolf, Clogston models

In the model proposed by Friedel the wavefunctions of the free plane wave conduction electrons, scattered by a localised potential, V, at the impurity site are analysed in spherical harmonics. The condition of self consistency requires that the total charge screened by the scattered electrons below the Fermi surface must be equal to the excess charge, Z, of the impurity with respect to the valency of the host. The screened charge per unit K, the wave vector of the Block waves, in a sphere of radius R is given by the difference in the integral $\int_0^R \psi_\lambda^2 \, dr$ between the solutions of Schroedingers equation for $V = V_{imp}$ and $V = 0$. The scattering potential, Vp, is chosen such that the summation over k gives the total charge displaced by Vp below the Fermi energy $E_F$ as

equal to Z.

$$Z = \frac{2}{\pi} \sum_{l} (2l + 1)\, \eta_l (E_F)$$

This condition, where $\eta_l$ is the phase shift produced by the potential Vp on $\Psi_l$ must always be satisfied. A spherically symmetric potential at the impurity, not quite strong enough to produce a bound state of orbital angular momentum l, will produce an anomalously large amplitude of the l-th spherical component of the conduction band states, localised at the impurity site, corresponding to an excess charge density, approximately equal to that of the l-th bound state (with degeneracy 2l+1). This corresponds to a resonance in the scattering of the conduction band electrons, peaked at energy $E_o$, representing a virtual bound state of width $\Delta E$. Friedel gives an expression for the width of the resonance associated with the scattering, showing that this width decreases with increasing l as $1/(2l+1)$. For a d-state of l=2 typical values for the energies involved give a width of order 1-2eV at the Fermi level of 7ev for copper.

In the studies of Woolf and Clogston the wavefunctions of the scattered Block waves are expanded in terms of the Wannier functions as used by Slater and Koster in thei r papers [60,62] on impurity states in crystals. The assumption is made that the scattering potential V gives only diagonal matrix elements between Wannier functions, within a single band. Using a Hamiltonian containing the effect of the unperturbed lattice and the potential $V_o$, the Schroedinger equation is solved by Clogston using the set of Green's functions

$$G_{ME}(r_i - r_o) = \frac{1}{N} \sum_{K} \frac{e^{ik.(r_i - r_o)}}{E_{MK} - E}$$

where $E_{MK}$ are the solutions with V = 0.

The solutions are given by Clogston in terms of the phase shift $\gamma(E)$ of the unperturbed Bloch waves

$$\gamma(E) = \tan^{-1}\left(\frac{\pi \Omega \rho(E)}{F(E)-1/V_0}\right) \qquad \Omega \text{ is the atomic volume}$$

The form of $\gamma(E)$ is shown in Fig.4.1 and represents a virtual bound state of width $\Delta E$ as discussed by Friedel. The energy of the virtual bound state is given by the maxima in the wavefunction amplitude

$$U_m(R_0) = e^{ik.R_0} / \left\{ [1-V_{mm} F_m(E)] + i\pi V_{mm} \rho_m(E) \right\}$$

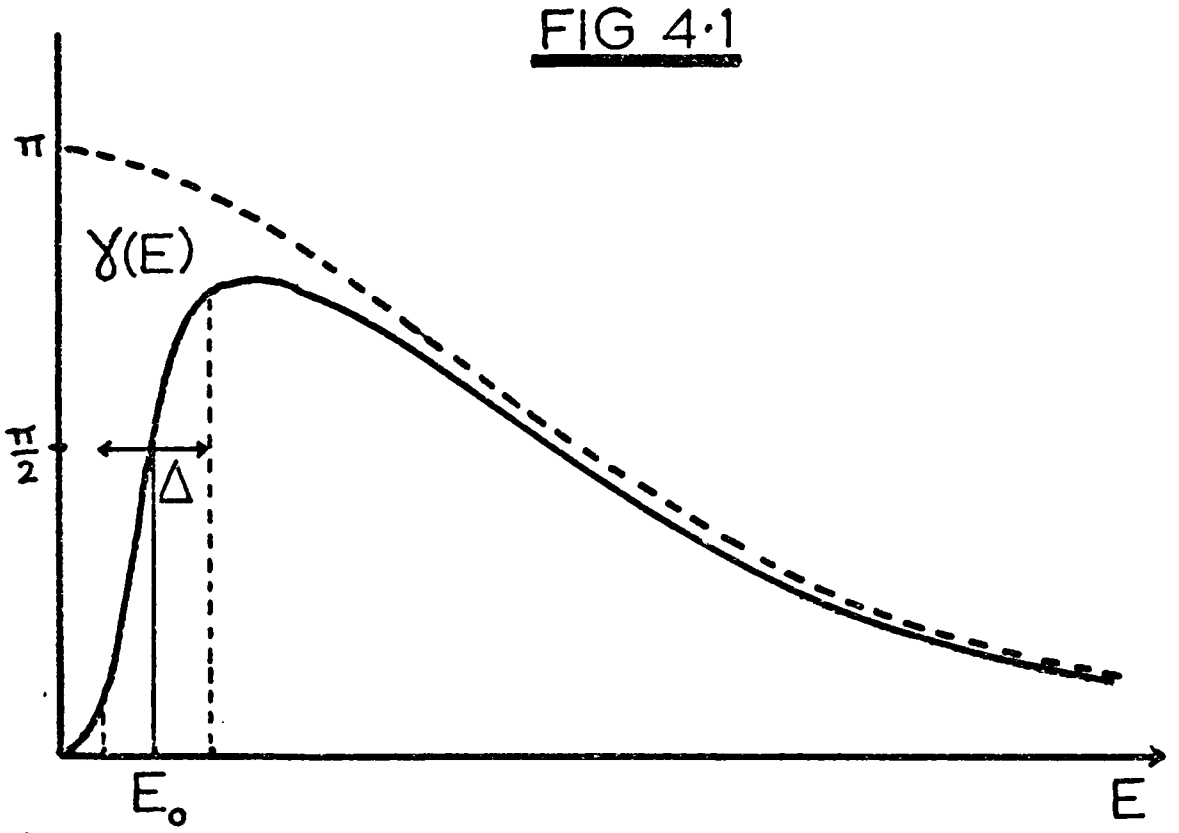
$\rho_m(E)$ is the density of states in the band m, and F(E) is the principal part of the integral

$$F_m(E) = P \int \frac{\rho_m(E)\, dE}{(E-\epsilon)}$$

The maxima occur at energies for which the factor [1-V.F(E)] is zero. These values are given by the intersections of the line (1/V) with F(E). Fig. 4.2b shows F(E) and the density of states as a function of E.

The roots [1-V.F(E)] = 0, with a negative derivative, gives the energy $E_0$ of the scattering resonance. If $E_0$ lies outside the band, $\rho(E) = 0$, and $U_m(R_0) \rightarrow \infty$ as $E \rightarrow E_0$, implying the existence of a bound state of the impurity atom at $E_0$. If $E_0$ lies within the band, $U_m(R)$ merely shows a resonance corresponding to a virtual bevel.

FIG 4·1




The phase shift for a real bound state------
and virtual bound state at energy $E_0$——




The change in the number of states below an energy E for three different values of V.

## 4.3 The Formation of a local spin magnetic moment

The virtual bound state formed on an impurity in a ferromagnetic host will be split by the exchange interaction. The most important matrix element of the exchange interaction corresponds to the interaction $U_{nd\uparrow\, nd\downarrow}$ postulated by Anderson

$$U = \int |\phi_d(r_1)|^2 |\phi_d(r_2)|^2 \, e^2 |r_1 - r_2|^{-1} \, d\tau_1 \, d\tau_2$$

When the virtual bound state is narrow and close to the Fermi surface, a part of one sub-level may be forced above the Fermi surface producing a net spin polarisation at the impurity. The formation of such a localised moment will depend sensitively on the energy and width of the virtual state.

The effect of the exchange interaction can be represented by spin dependent potentials, $\delta V\uparrow$ and $\delta V\downarrow$, on the impurity. The general theory of Woolf gives simultaneous solutions for $\delta V\uparrow$ and $\delta V\downarrow$ for given values of $E_F - E_o$, showing that when $(E_F - E_o)$ is small, the stable solutions give $\delta V\uparrow \neq -\delta V\downarrow$, with a consequent spin polarisation. The condition given by Woolf for the existence of a localised moment is given below

$$\frac{(\Delta E)^2 + (E_F - E_o)^2}{(\Delta E)^2} < \left| \pi V^2 \, (\Delta E) \, F'^2 \right|$$

where $F' \simeq \dfrac{F(E) - 1/V}{(E - E_o)}$

This requires the existence of a narrow virtual level lying close to the Fermi surface.

More specific calculations are made easier in cobalt and nickel hosts than in iron by the fact that the band structure of nickel and cobalt has the spin down part of the 3d band overlapping the Fermi surface, while the other, spin up, half is completely full, and below $E_F$ in energy.

The variation of the local spin moment on the first and third series of transition metal impurities in iron, cobalt and nickel has been studied by Campbell and Gomes [63] and Demangeat and Gautier [64]. The general trend of the local moments of the 3d transition elements has been reproduced by Campbell and Gomes using a model treating the 3d conduction band as five-fold degenerate, consisting of five equal and independent subbands. Fig. 4.2 shows a comparison of the experimental results with the predictions of this model. The sudden reversal of the magnetic moment is due to the emptying of a bound state containing 5d spin-up electrons, which moves above the Fermi level when the excess impurity charge, $|Z_{imp}|$, becomes greater than $Z_c$, the excess charge required to produce a sufficiently deep scattering potential.

The situation for the 5d series of transition elementimpurities has not been so extensively studied. The calculations of Demangeat and Gautier have used the method of Slater and Koster [60] for a self consistent calculation of the impurity scattering potential, and the electron density, on the impurity site, and the nearest neighbours. In their calculation, the crystal field splitting of the 3d conduction band is included. In the cubic symmetry of the substitutional impurity site, the5-fold degenerate d states are split into a 2 fold degenerate $\Gamma_3$ state and a triply degenerate $\Gamma_5$ state. The separation of the $\Gamma_3$ and $\Gamma_5$ states is considered large compared with the energy width of the virtual bound states formed. The localised spin polarisation due to the formation of virtual bound states of $\Gamma_5$ character were calculated for 3d and 5d impurities for a range of values of $Z_{imp}$ from $Z = -1$ to $Z = -5$. The trend of the results for the 5d impurities is shown in Fig.4.2. For the case of iridium, which has $Z = -1$ in nickel, and is of particular interest in this work, two types of solution are found. Both are possible without a more detailed knowledge of the position and width of

the virtual bound d states relative to the Fermi surface. A virtual bound state of $\Gamma_5$ character would give a local moment of + 1.9$\mu_B$ on the iridium impurity, by an interaction analogous to that of Cobalt in a nickel host (also having $Z_{imp} = -1$) where the charge screening is provided by the part of the nickel d band with a large value of the density of states at the Fermi surface, thus spin down, giving an impurity moment of order

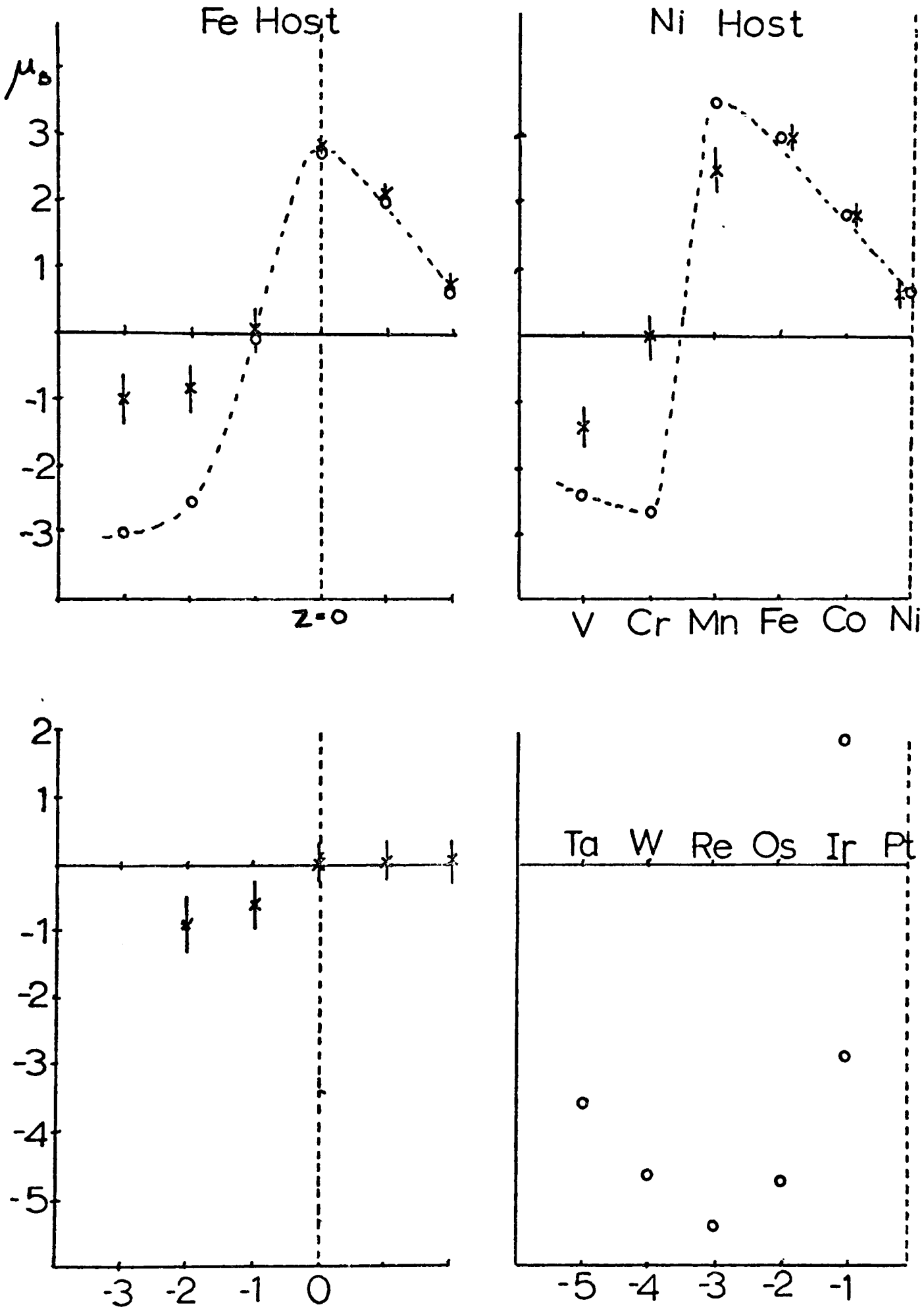
$$\mu_{imp} \approx \mu_{host} - 2\mu_B$$

The alternative solution gives a reversal of the magnetic moment due to the pushing of a $\Gamma_5$ bound state across the fermi level and with a loss of the spin-up electrons. This gives a moment of $\sim -2.8\mu_B$.

This is a zero-temperature description, but if the temperature is increased, the screening conditions will change slightly because of the effect of the thermal broadening of the Fermi level, and the occupation of the narrow bound state when it is close to the Fermi energy. This will have the effect of giving an anomalous temperature dependence to the impurity hyperfine field, when the bound state is very near the Fermi level. Such an effect is observed for the case of manganese in iron [ 65], and has been discussed by Campbell [ 66 ] in terms of a stable high temperature state with a local moment of $-0.5\mu_B$ and a stable low temperature state with a moment of $+0.5\mu_B$. The measurements of Collins and Low [ 67 ] using neutron scattering measurements are shown in Fig.4.2 for comparison with the theoretical predictions. The agreement is good for the 3d impurities, but all the 5d impurities in iron showed very small moments at the temperature of 290°K of the measurements.

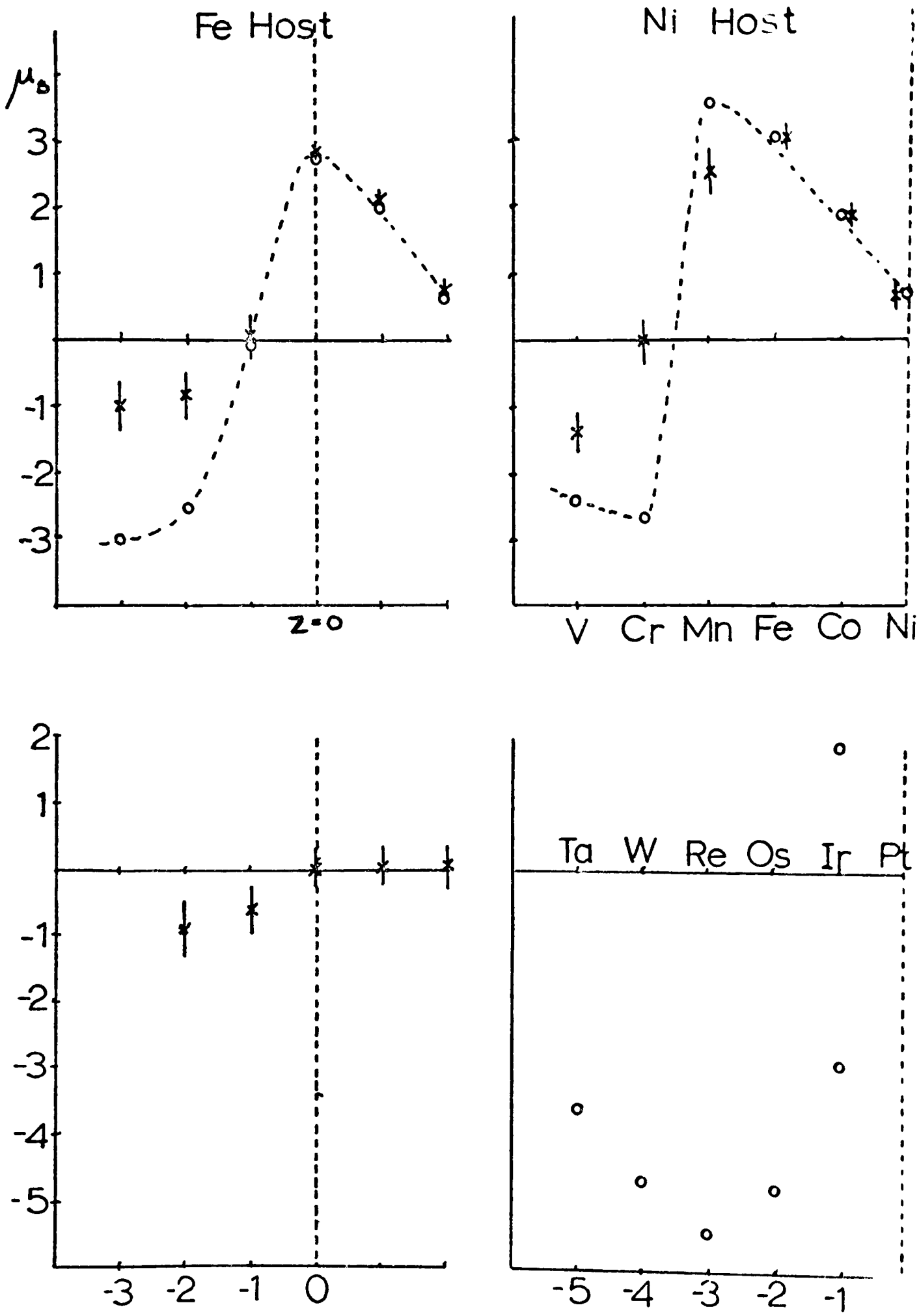
The calculations of Campbell and Gomes and Demangeat and Gautier do not include the effects of s-d hybridisation or the spin-orbit interaction on the localised d states. The s-d hybridisation in the host

FIG 4·2




Calculated values(63)(64) and experimental measurements(67) of the localised moments on the 1st and 3rd transition series impurities

FIG 4·2




Calculated values(63)(64) and experimental measurements(67) of the localised moments on the 1st and 3rd transition series impurities.

metal will tend to broaden the virtual bound states [ 68] but will be less important for small values of $|z|$ because of the more localised states [ 69].

## 4.4 The Orbital angular momentum of impurities

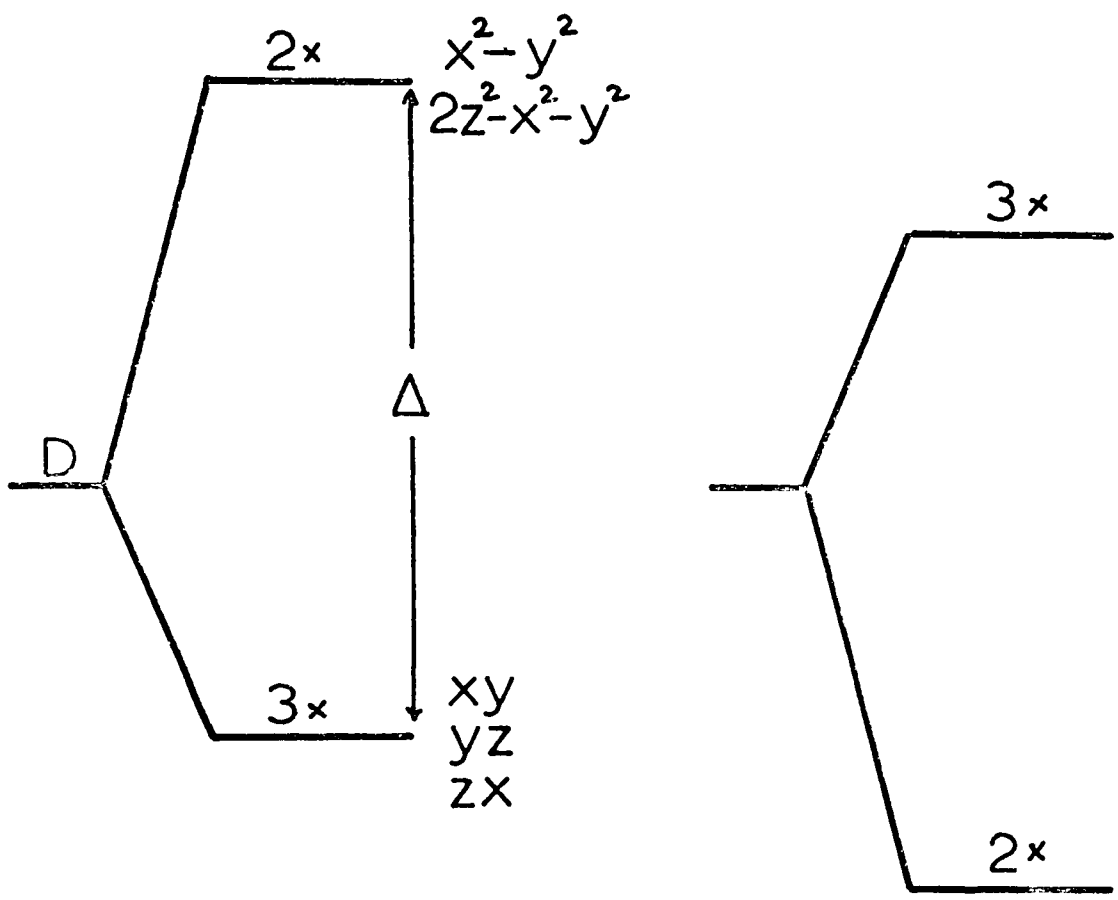
The orbital angular momentum associated with the d states of the impurity in a cubic environment tends to be quenched by the crystal field. The crystalline Stark effect described by Van Vleck [ 70 ] will remove the degeneracy of the $L_s$ wavefunctions, with the translational symmetry requirements of the lattice, as well as the rotational symmetry of the crystal space group, ensuring the removal of any degeneracy which may exist under the point group alone. The real wavefunctionscan be written as linear combinations of the $L_s$ substates, in terms of the radial function f(r) and the angular dependence in Cartesian coordinates. The wavefunctions form the $\Gamma_3$ and $\Gamma_5$ representations of the cubic symmetry group, and show zero values for the diagonal matrix elements of the orbital magnetic moment.

$$\left.\begin{aligned} r^2 C_{2,0} &= \tfrac{1}{2}(2z^2-x^2-y^2) \\ \tfrac{1}{2} r^2(C_{2,2} - C_{2,-2}) &= \sqrt{\tfrac{3}{2}}\,(x^2-y^2) \end{aligned}\right\} \quad \Gamma_3$$

$$\left.\begin{aligned} -\tfrac{i}{2} r^2(C_{2,2} - C_{2,-2}) &= \sqrt{3}\,xy \\ \tfrac{i}{2} r^2(C_{2,1} + C_{2,-1}) &= \sqrt{3}\,yz \\ -\tfrac{1}{2} r^2(C_{2,1} - C_{2,-1}) &= \sqrt{3}\,zx \end{aligned}\right\} \quad \Gamma_5 \qquad [70]$$

For a single d electron the two-fold degenerate state forming the representation $\Gamma_3$ has a higher energy than the three-fold degenerate

FIG 4·3




Crystal field splitting of 5-fold degenerate d-states in cubic symmetry

state, giving an energy splitting, typically in the range 5000-15,000 $cm^{-1}$. For a $d^9$ state, like that of iridium in a nickel host the splitting is inverted, since the electrostatic energy in the crystal field has the opposite sign for the positive 'hole' in the d shell.

In the absence of the spin-orbit interaction, the magnetic moment associated with the quenched d states of the impurity will be entirely due to the unequal numbers of spin up and spin down electrons, and will have a g value of 2. The deviation of the electronic g value from the spin only value, due to the influence of the spin orbit interaction, has been considered by Brooks [71] and Fletcher [72] in their studies of the magnetic anisotropy of ferromagnetic cubic crystals. The spin-orbt interaction is introduced as a small perturbation on the quenched wavefunctions, with three assumptions; a) the matrix elements of the interaction between Bloch functions are approximately the same as between the corresponding free atom wave functions, b) the perturbation is small compared with the effect of the crystal field and the exchange forces, and c) the interaction does not alter the Fermi distribution of occupied states. Following the work of Brooks and Fletcher the wavefunctions can be expanded in powers of the spin-orbit perturbation $\xi . L_g . S_g$ and the quenched wavefunctions $\Psi_o$

$$|\Psi\rangle = |\Psi_o\rangle - \frac{\xi}{2\Delta}\sum_k \langle K|1_g|\Psi_o\rangle |K\rangle + \frac{\xi^2}{4\Delta^2}\sum_K \sum_n \langle K|1_g|n\rangle\langle n|1_g|\Psi_o\rangle|K\rangle$$

$$- \frac{1}{2}\frac{\xi^2}{4\Delta^2}\langle\Psi_o|1_g^2|\Psi_o\rangle|\Psi_o\rangle$$

where $\Delta$ is the crystal field splitting, $S_g = \frac{1}{2}$, and $|K\rangle$ are the Bloch functions with wavevector K.

The orbital angular momentum is given by the expectation value of $L_z$ between the perturbed states.

## 4.5 The Hyperfine interactions

The importance of the effect of the spin-orbit interaction for the hyperfine interaction experienced by the impurity nucleus is that, for incomplete quenching of the orbital angular momentum, the orbital dipolar, spin dipolar, and electric quadrupole terms in the hyperfine interaction will have non-zero values. The contribution to the hyperfine interaction due to the orbital dipolar term is proportional to the expectation value $\langle\Psi|l_z|\Psi\rangle$ at the impurity site, and the contributions of the spin-dipolar and electric quadrupole terms are proportional to $\langle\Psi|l_z^2 - \frac{1}{3}l(l+1)|\Psi\rangle$. A completely quenched orbital angular momentum in cubic symmetry will give $\langle|l_z|\rangle$ and $\langle|l_z^2 - \frac{1}{3}l(l+1)|\rangle$ both equal to zero.

The orbital dipolar hyperfine interaction associated with an orbital moment localised on the impurity atom can be written [13]

$$\mathcal{H}_{O.D.} = \mp 2\beta\left(\frac{\mu}{I}\right)\langle r_1^{-3}\rangle \eta \langle|l_z|\rangle I_z$$

where $\eta$ represents the number of units of $|e|$ contributoing to the localised moment and the $\mp$ signs refer to electrons and holes respectively. $\langle r_1^{-3}\rangle$ is the expectation value of $r^{-3}$ for the distribution of the orbital angular momentum associated with the impurity. The value of $\langle|l_z|\rangle$ is calculated by both Brooks and Williams [73] using wavefunctions representing the quenched orbital angular momentum states of an impurity atom, giving

$$\langle|l_z|\rangle = -\frac{\delta}{3\Delta}l(l+1)$$

The appropriate forms of the hyperfine interaction Hamiltonians for the spin-dipolar and electric quadrupole interactions are given below. The magnetic spin-dipolar term:

$$\mathcal{H}_{S.D.} = -2\beta\left(\frac{\mu}{I}\right)\langle r_s^{-3}\rangle_\eta \langle 1\|\alpha\|1\rangle \langle|3l_s^2 - l(l+1)|\rangle\ I_s$$

The electric quadrupole term:

$$\mathcal{H}_Q(\text{real}) = \frac{e^2Q}{4I(2I-1)} \cdot 2\langle r_q^{-3}\rangle\langle 1\|\alpha\|l\rangle\eta\langle|3l_s^2 - l(l+1)|\rangle$$

$$\times \left\{3I_s^2 - I(I+1)\right\}$$

For a single electron the value of $\langle l\|\alpha\|l\rangle$ is given by Abragam and Bleaney as $-2/[(2l-1)(2l+3)]$. For the spin dipolar term $\langle r_s^{-3}\rangle$ represents the distribution of the electronic spins, but, in the Hamiltonian for the electric quadropole interaction, $\langle r_q^{-3}\rangle$ contains the Sternhermier antishielding parameter, describing the contribution to the effective field gradient from the electronic core states of the impurity [74]: $V_{zz} = V_{zz}^{\circ}(1-\gamma(r))$. The quantity $\gamma(r)$ is a function of the distance r from the nucleus to a charge e, and can become very large when r is greater than the atomic radius. In general, however $\gamma(r)$ will be a small correction for an electric field gradient originating from a charge distribution penetrating the closed shells of the impurity atom.

The calculations of Williams give the following expression for the expectation value $\langle|l_z^2|\rangle$ in the presence of a spin-orbit perturbation on the quenched orbital magnetic states. [73]

$$\langle|l_z^2|\rangle = \frac{1}{3}l(l+1) + \frac{\lambda^2}{4\Delta^2}\left\{3\langle\psi_o|l^4|\psi_o\rangle - \frac{1}{9}[l(l+1)]^2\right\}$$

The spin dipolar and electric quadrupole hyperfine interactions will therefore be non-zero only in second order in the perturbation $\lambda/\Delta$.

## 4.6 Conclusion

Using the nuclear orientation and N.M.R./O.N techniques, the existence of a localised magnetic moment on an impurity atom will only be detected by observation of the contributions to the hyperfine interaction from the orbital dipolar and the electric quadrupole interactions, associated with the unquenching of the orbital angular momentum through the spin-orbit interaction. The orbital dipolar term is non-zero in first order in the spin-orbit interaction perturbation, and in some cases can be expected to give a significant contribution to the total hyperfine interaction, comparable with the Fermi contact term. The second order spin dipolar term will not be detected, but, as is shown in the next chapter, the particular sensitivity of the N.M.R./O.N technique to small quadrupole splittings, makes the electric quadrupole term as easy to observe as the orbital magnetic dipolar term.

The strength of the spin-orbit interaction is a rapidly varying function of the atomic mass number. The interaction increases with approximately the fourth power of the atomic number, and will become important for nuclei of mass greater than 150. The experiments have concentrated on the interactions of heavy impurity elements. The following experiments using N.M.R./O.N on isotopes of gold and iridium were designed to measure the contributions, to the total hyperfine interaction, from the formation of localised orbital magnetic moments on the impurities. An appropriate breakdown of the hyperfine interaction for the analysis of the experimental results, can be summarised in terms of the effective magnetic fields and electric field gradient.

$$H_{\text{effective (total)}} = H_{\text{contact}} + H_{\text{non-contact}} + q$$

$H_{\text{contact}}$ is the s-electron contact hyperfine interaction from

core polarisation and conduction electron polarisation; $H_{non-contact}$ is the effective field produced by the orbital dipolar and spin dipolar interactions, and q is the effective "electric field gradient" associated with the nuclear electric quadrupole interaction. The experiments have enabled the relative sizes of some of these components to be measured; the results are interpreted in the terms of localised magnetic moments discussed in this chapter.

# CHAPTER 5

# THE MEASUREMENT OF MIXED M1/E2 HYPERFINE INTERACTIONS

## 5.1 Introduction

The effect of the addition of a small electric quadrupole interaction in the nuclear hyperfine Hamiltonian is discussed in this chapter in terms of the effect on nuclear orientation and N.M.R./O.N. measurements.

One possible source of a small electric quadrupole interaction in cubic ferromagnetic metals was outlined in chapter four. The mixed M1/E2 Hamiltonian is formulated in section 5.2 of this chapter, and the effect on conventional nuclear orientation experiments is considered in section 5.3. It is shown that electric quadrupole interactions of magnitude a few percent of the magnetic hyperfine splitting are difficult to detect in a conventional nuclear orientation experiment, and can lead to considerable errors in the derived value of the Zeeman splitting if the experiment is interpreted in terms of a pure magnetic dipole interaction. In section 5.4, the effect on the N.M.R./O.N. absorption spectrum is investigated, and it is shown that by this method electric quadrupole admixtures giving interaction energies of more than 0.1 percent of the Zeeman splitting can be clearly identified and measured.

## 5.2 The mixed E2/M1 hyperfine interaction

The existence of a nuclear electric quadrupole interaction requires a finite electric field gradient at the nucleus. Such gradients can arise either from the arrangement of neighbouring ions, generally with shielding corrections associated with the electrons of the ion under consideration, or from the electrons of the particular ion itself associated with a non zero value of the expectation value of the operator $L_z^2 - \frac{1}{3} L(L+1)$ for the occupied electron states.

Of the ferromagnetic metal hosts, Fe, Co, Ni and Gd, only Gd, and Co in its hexagonal phase, will show crystal field induced quadrupole effects. For an impurity in a substitutional site and in the absence of mechanical strain, the crystal field effects of the cubic hosts will give no electric field gradient at the impurity nucleus. The influence of the exchange field on the electronic states of transition impurities has been considered in the previous chapter. The formation of an unquenched orbital moments through the spin-orbit interaction will give an electric quadrupole interaction co-axial with the bulk-magnetisation of the host. In the calculations in this chapter this coaxial condition is assumed. In the hexagonal hosts, since the electric field gradient may result partly from the crystal field, the magnitude will be, in general, anisotropic with respect to the crystal axes. In polycrystalline material the observed effects would represent an averaging over the effects of the electric field gradient at all directions in the crystal. The averaging depending in detail on the crystal structure. This averaging is not considered further as the impurities can be studied in single crystal samples, in which the relative orientation of the crystal axes to the magnetisation can be controlled and varied.

Whatever the origin of the electric field gradient, it may be represented by a second rank tensor, which can be diagonalised to involve only three terms $V_{xx}$, $V_{yy}$ and $V_{zz}$ where x, y and z define the principle axes of the field gradient. $V_{zz}$ is connected to the orbital angular momentum operator by the relation

$$V_{zz} = \sum_i -2e \quad \langle r_i^{-3} \rangle \langle l_i \| \alpha \| l_i \rangle \left\langle \left| 3\, l_{zi}^2 - l_i(l_i+1) \right| \right\rangle$$

The summation being over all contributing electrons.

For a nucleus of spin I and electric quadrupole moment $Q$ the nuclear electric quadrupole Hamiltonian can be written as

$$\mathcal{H}_Q = \frac{-3eQV_{zz}}{4I(2I-1)} \left\{ [I_z^2 - \frac{1}{3} I(I+1)] + \frac{\eta}{3} [I_x^2 - I_y^2] \right\}$$

In the situation under consideration the nuclear electric quadrupole Hamiltonian can be considered as a small perturbation on the magnetic Hamiltonian

$$\mathcal{H}_M = \frac{-\mu_N H_{eff} I_z}{I}$$

where $\mu_N$ is the nuclear magnetic dipole moment, and $H_{eff}$ is the effective magnetic field acting at the nucleus.

The energies of the nuclear magnetic substates are then given by the expression

$$E_{I_z} = \frac{\mu_N H_{eff} I_z}{I} + P[I_z^2 - \frac{1}{3} I(I+1)] \left\{ \frac{3\cos^2\theta - 1}{2} + \eta \frac{\sin^2\theta \cos 2\phi}{2} \right\}$$

where $P = - \frac{3eQV_{zz}}{4I(2I-1)}$

The angles $\theta$ and $\phi$ define the direction of the magnetic field with respect to the principal axes of the electric field gradient. As mentioned previously, the simple case of $Z = z$ and $\theta = \phi = 0$ for the co-axial situation is considered. For the resonance experiment the energy separation of the magnetic substates is required. The energy spacings between adjacent $I_z$ levels then have 2I values distributed symmetrically about the central magnetic zeeman value

$$E_m = \frac{\mu_N H_{eff}}{I}$$

$$E_{M+Q} = \frac{\mu_N H_{eff}}{I} + P\,(2I_z + 1)$$

where $I_z$ varies from -I to + (I-1)

In subsequent sections, calculations of quadrupole effects are made in terms of P, since this is the parameter which appears in the simplest form in the Hamiltonian. Consideration of the sensitivity of the measurement and of its variation with the spin of the isotope chosen, is given in terms of P, and the more basic parameter $V_{zz}$.

## 5.2 Small Quadrupole Effects in Conventional Nuclear Orientation

In conventional nuclear orientation experiments the presence of two or more terms in the Hamiltonian is detected by measurement of the variation of the anisotropy as a function of temperature. In this section we investigate the sensitivity of such an experiment to the presence of a coaxial quadrupole hyperfine coupling small compared to the magnetic dipole coupling. This is done by calculating using standard methods [ 14 ], the anisotropy versus temperature curve for the combined Hamiltonian

$$\mathcal{H}_{M+Q} = \frac{\mu_N H_{eff}}{I} I_z + P[I_z^2 - \tfrac{1}{3}I(I+1)]$$

varying the parameter

$$X = \frac{P}{\left|\frac{\mu_M H_{eff}}{I}\right| + |P|}$$

and fitting each point on the curve so produced by a simple magnetic Hamiltonian

$$\mathcal{H}_M = \frac{\mu_N \bar{H}}{I} I_z$$

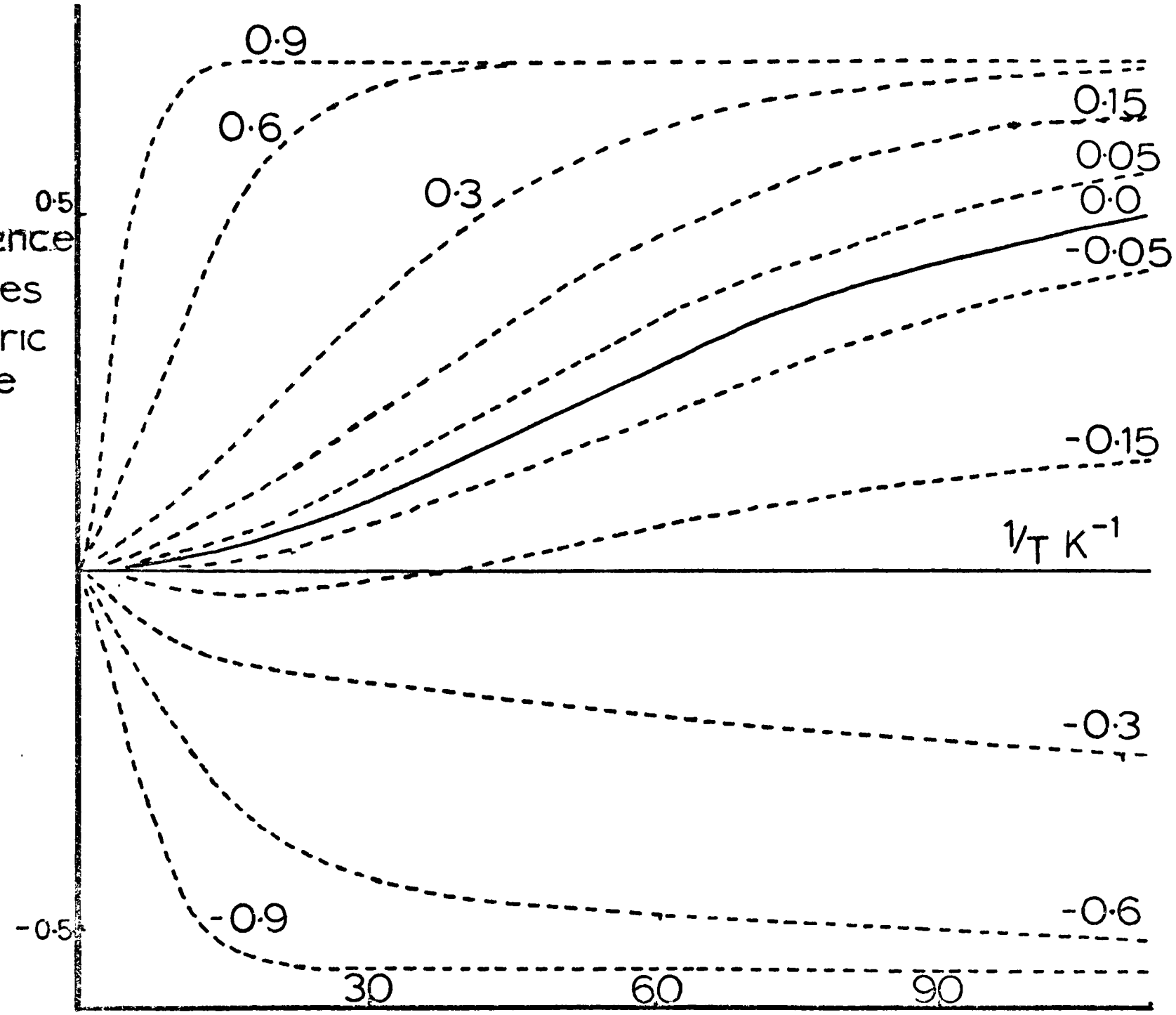
using the same nuclear decay scheme parameters throughout. The result

FIG 5·1

The temperature dependence of the gamma ray anisotropies for various ratios of the electric quadrupole and magnetic dipole hyperfine interactions

$U_2F_2 = 0{\cdot}50$

$$X = \frac{P}{|P|+\mu H}$$



is a temperature dependent $\left(\frac{}{H}\right)$ since the mean energy spacing of the nuclear $I_g$ levels with appreciable populations changes with temperature as the upper $I_g$ levels are depopulated. The asymptotic value of $\bar{H}$ so defined is therefore, for small, X,

$$\bar{H}_{\text{limit } T \to 0} = H_{eff}\,[1+(2I-1)X] \qquad (4)$$

when only the two lowest energy $I_g$ states have appreciable populations.

Figures 1 and 3 show $\bar{H}$ plotted as a function of $\mu_N H_{eff}/IkT$ for nuclear spins 2 and 4 and various values of X. The first noteworthy fact is that for small values of X, $\bar{H}$ is almost constant over wide ranges of temperature. Since the rapid changes of $\bar{H}$ occur at high temperatures where nuclear orientation anisotropies are small and less accurately measurable, the results of an experiment with such a mixed Hamiltonian are very likely to be regarded as well fitted by a simple Zeeman Hamiltonian, and the value of H to be quoted as $H_{eff}$. In many cases the maximum discrepancy between the anisotropies appropriate to the true Hamiltonian and the simple magnetic one with an average value of $\bar{H}$ is less than 1% at any temperature. Thus only the most precise measurements of the temperature dependence of the anisotropy would reveal the existence of any quadrupole component for the range of X shown. The ratio $\bar{H}_{average}/H_{eff}$ for various I and X is given in table 1. If (somewhat arbitrarily) we take the largest X shown in the figures as that for which a discrepancy from the simplest magnetic Hamiltonian might be detected, then the degree of insensitivity of conventional nuclear orientation to small quadrupole admixtures is such that the deviation of $\bar{H}_{average}/H_{eff}$ from unity is of order $\pm$ 25% for all nuclear spins.

To give some quantitative idea of the quadrupole splittings involved we may rewrite equation 4 for small P as

FIG 5·2

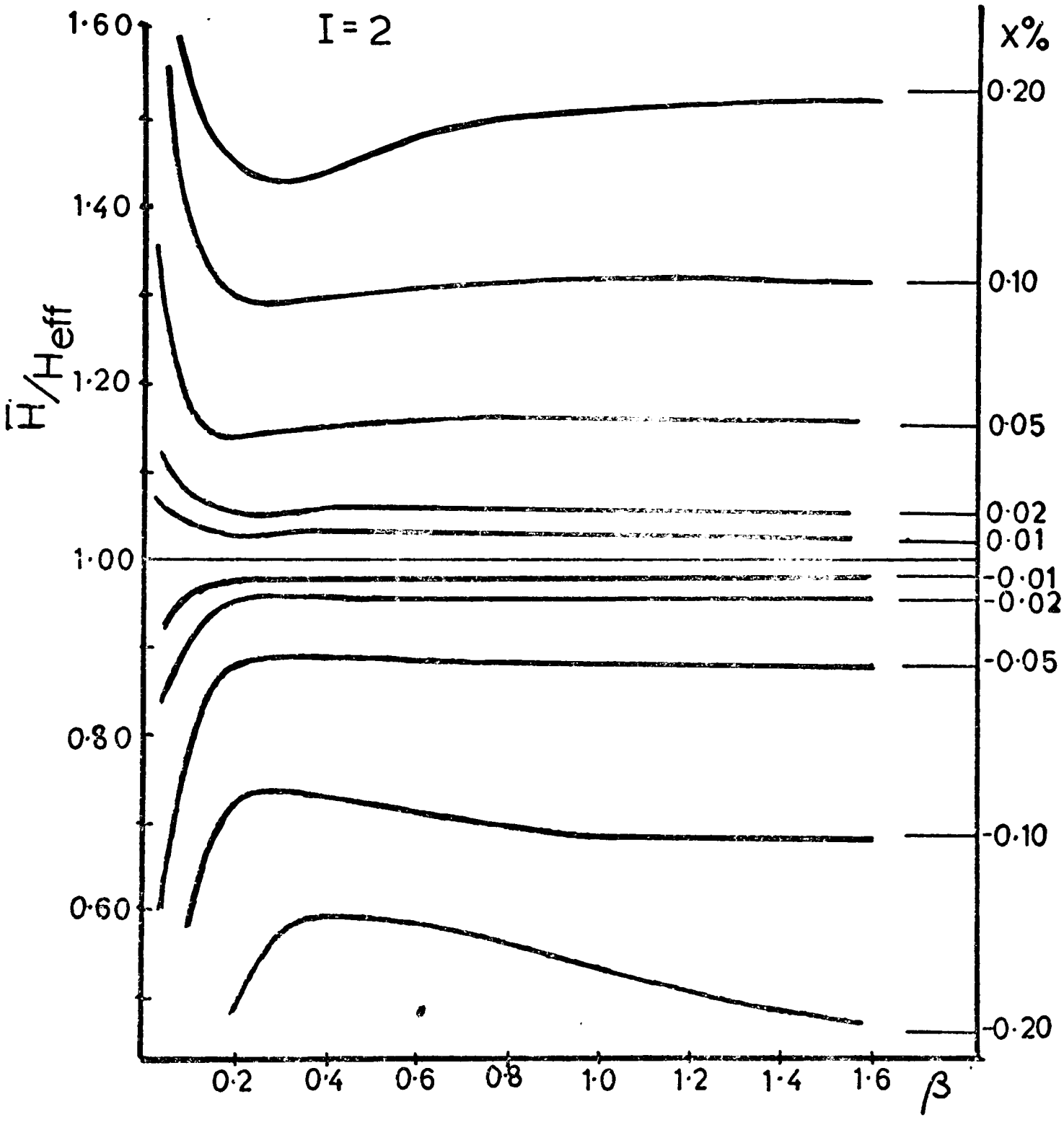
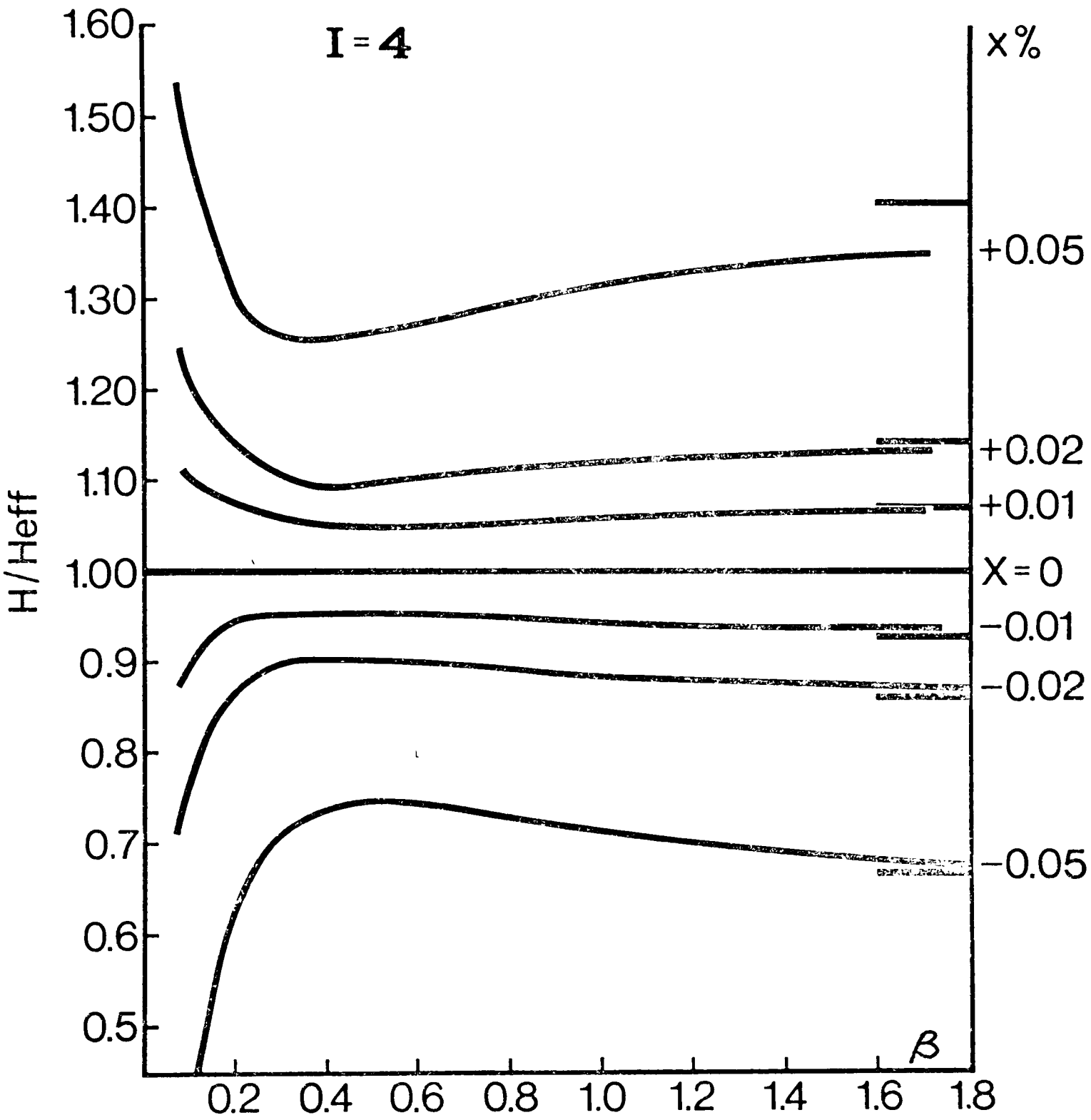

I = 2
X%
0·20
0·10
0·05
0·02
0·01
-0·01
-0·02
-0·05
-0·10
-0·20
1·60
1·40
1·20
1·00
0·80
0·60
$\bar{H}/H_{eff}$
0·2
0·4
0·6
0·8
1·0
1·2
1·4
1·6
β

FIG 5·3


I = 4
X %
+0.05
+0.02
+0.01
X = 0
−0.01
−0.02
−0.05
H/Heff
β
1.60
1.50
1.40
1.30
1.20
1.10
1.00
0.9
0.8
0.7
0.6
0.5
0.2
0.4
0.6
0.8
1.0
1.2
1.4
1.6
1.8

## Table 5.1

Table of the mean apparent values of the hyperfine interaction, $\bar{H}_{eff}$, compared with the magnetic hyperfine field, $H_{hf}$, as a function of X and the nuclear spin I

| X | $\bar{H}_{eff}/H_{hf}$; I | | |
|---|---|---|---|
| % | 1 | 2 | 4 |
| -10 | 0.885 | 0.727 | - |
| - 5 | 0.945 | 0.870 | 0.743 |
| - 2 | 0.979 | 0.950 | 0.896 |
| - 1 | 0.990 | 0.975 | 0.946 |
| 0 | 1.000 | 1.000 | 1.000 |
| 1 | 1.010 | 1.025 | 1.054 |
| 2 | 1.021 | 1.050 | 1.104 |
| 5 | 1.055 | 1.130 | 1.257 |
| 10 | 1.115 | 1.273 | - |

$$\frac{\bar{H}_{lim}}{H_{eff}} \approx 1 + \frac{I(2I-1)P}{\mu_N H_{eff}} = 1 + \frac{3eQV_{zz}}{4\mu_N H_{eff}} \qquad (5)$$

Equation 5 shows that the minimum detectable value of P is of order 25% of the Zeeman splitting for I = 1, falling to 4% for I = 4. These P values correspond to electric quadrupole couplings $eQV_{zz}$ of order 10% of the magnetic dipole coupling $\mu_N H_{eff}$ for all spin values.

We can also see from eqn.5 that since $V_{zz}$ and $H_{eff}$ are isotope independent, to first order, the deviation of $\bar{H}$ from $H_{eff}$ for a given $V_{zz}$ is, as we would expect, minimised by use of the isotope with the smallest $Q/\mu_N$ ratioavailable in a given impurity/host system, even though the quadrupole term is not experimentally detected.

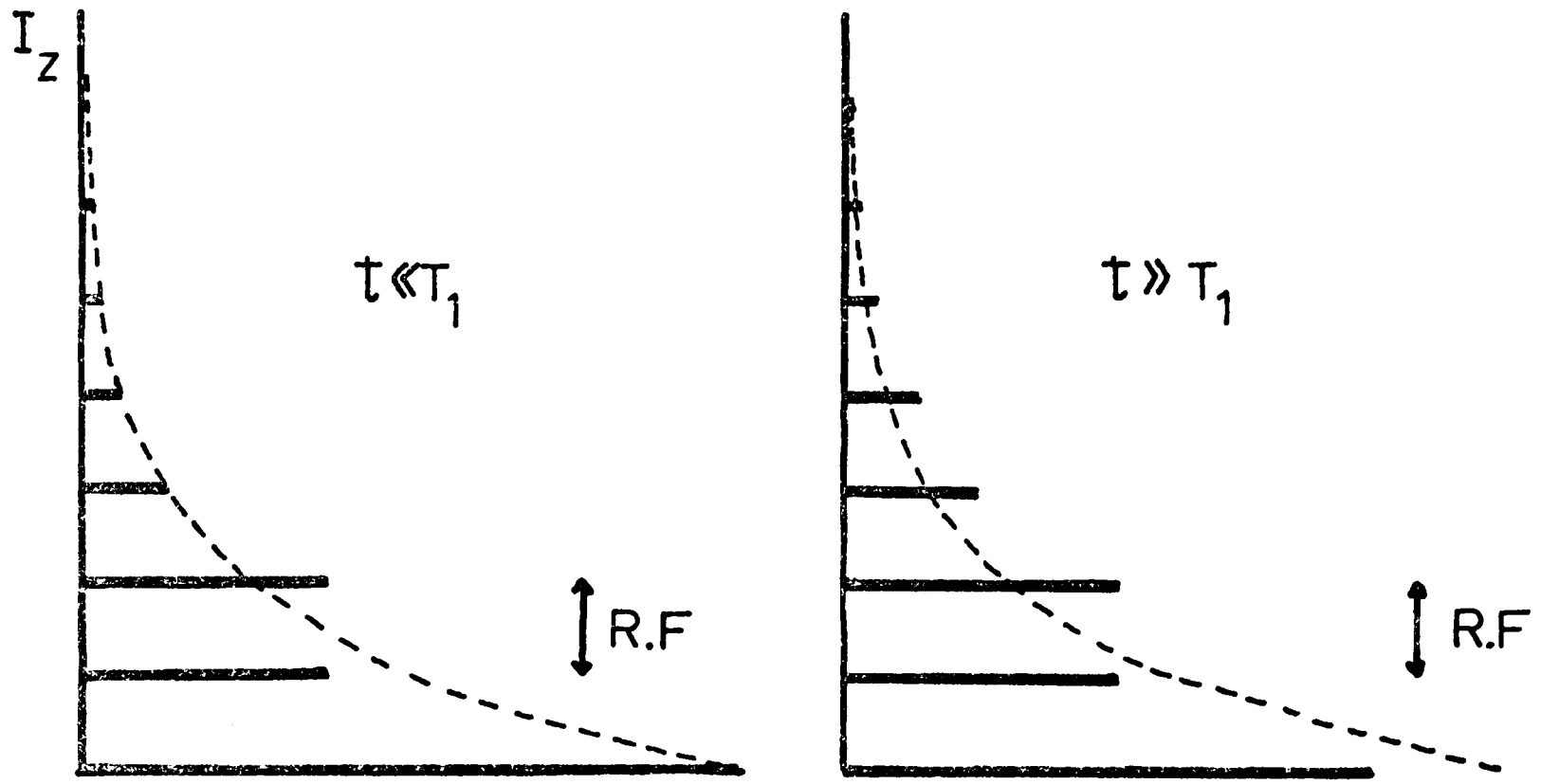
## 5.3 The Effect of a Quadrupole Splitting upon the N.M.R./O.N. resonance line

For a purely magnetic Hamiltonian, the magnetic substates are equally spaced in energy, therefore on resonance, R.F. induced transitions between all adjacent substates tend to equalise the populations, with a consequent reduction in the $\gamma$ emission anisotropy. In ferromagnetic hosts this is modified by the inhomogeneity in the hyperfine field, as shown in Ch.2, giving a resonance line of width of order 0.5% of the total splitting.

The effect of a small quadrupole effect is to split the resonance line into 2I component lines representing transitions between each pair of magnetic substates. It is then necessary to consider the effects of resonance of each pair of substates separately. The change in anisotropy involved in resonance of each of these transitions must be calculated using the orientation parameters $B_K$ [15]. Only the first two non-zero parameters, $B_2$ and $B_4$, are of importance.

The observed destruction of the gamma anisotropy for an r.f. field at resonance with the energy splitting of a chosen pair of magnetic substates has been considered in two limiting cases: a) the effect observed with no

FIG 5·4




POPULATION DISTRIBUTION OF SUBSTATES FOR SPIN 4, SHOWING RESONANCE OF $I_z = 3-2$ SUBSTATE TRANSITION, COMPARED WITH THE EQm BOLTZMANN DISTRIBUTION; FOR $t \ll T_1$ AND $t \gg T_1$

spin-lattice relaxation subsequent to the application of the r.f. field; and b) the effect after a Boltzmanndistribution has been re-established by spin-lattice relaxation for the populations of substates not directly influenced by the r.f. field. In both cases the r.f. field is assumed strong enough to saturate the resonance, i.e. equalise the populations of the substates directly involved.

a) The first case involves calculating the change observed in the orientation parameters $B_2$ and $B_4$ when the population of the substates, between which resonant absorption occurs, are equalised, with all other substate populations unaffected. Fig.5.1 shows that even a small electric quadrupole interaction can significantly change the thermal equilibrium values of the orientation parameters, therefore a mixed hamiltonian was used in the calculations. The resonance response is calculated in terms of the percentage change in the thermal equilibrium anisotropy, observed either on the axis of magnetisation, [1-W(0)], or in the equational plane. At the temperatures normally used, $30 < \frac{1}{T} < 80$, the $B_4$ term will provide only a small contribution to the thermal equilibrium anisotropy, but on resonance, the changes in $B_4$, when substate populations of adjacent magnetic states are equalised, are much greater than the changes in the $B_2$ term. For nuclei of spin greater than 3/2 it is important to include the $B_4$ term. Figs. 5.5 and 5.6 show the results for resonance of pairs of substates for spin 4 and spin 2 nuclei at three temperatures. The values of $\beta$ ( $\frac{\mu H}{IKT}$ ) correspond to temperatures of $\frac{1}{T} = 30$, 60 and 90 for the nuclei $^{192}$Ir (spin 4) and $^{198}$Au (spin 2) in the hyperfine fields of Ni and Fe respectively. The change in the anisotropy on resonance for the case where no relaxation occurs, $t \ll T$, is very small for all transitions except the ground state $I_4 \rightarrow I_3$ transition. In the limit of $\frac{1}{T} \rightarrow \infty$ the only transition observed will be the ground state transition since all other substates are completely depopulated. The resonance response will give a single resonance line shifted by (2I-1)P from the pure magnetic

situation.

b) The second case is the one applicable to impurities in ferromagnetic hosts where spin-lattice relaxation times are short compared with the counting periods for N.M.R./O.N. The r.f. field is again assumed to maintain equal populations in the pair of magnetic substates on resonance, but the spin-lattice interaction is allowed to re-establish a Boltzmann distribution, appropriate to the lattice temperature, for all other substates, relative to those experiencing resonant absorption. The changes in the populations of the resonated states disturbs the equilibrium of these populations with respect to their adjacent substates. The relaxation effect will re-distribute the populations of all the substates and can increase the proportion of the anisotropy destroyed on resonance by a factor of 10 for many of the substate resonances in high spin systems. Energy is absorbed by all substate transitions through the relaxation mechanism rather than by only the directly resonated transition.

Calculations of the effects expected have been done for spin 2 and 4 and are illustrated in Figs. 5.5 and 5.6. These show the comparison between the cases $T \ll T_1$ and $T \gg T_1$. The effect of relaxation in making more components of the resonance observable is clearly seen.

FIG 5·5

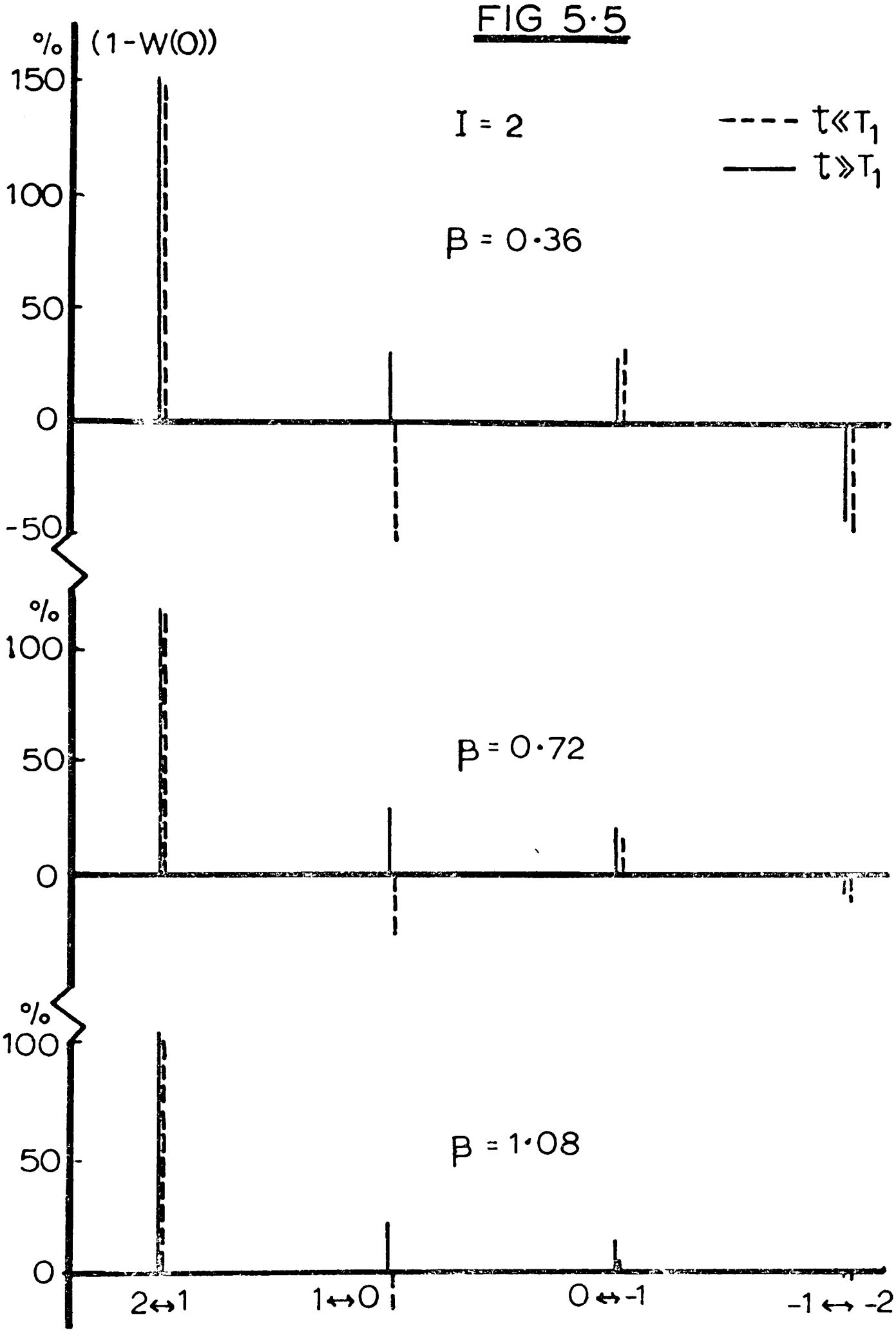
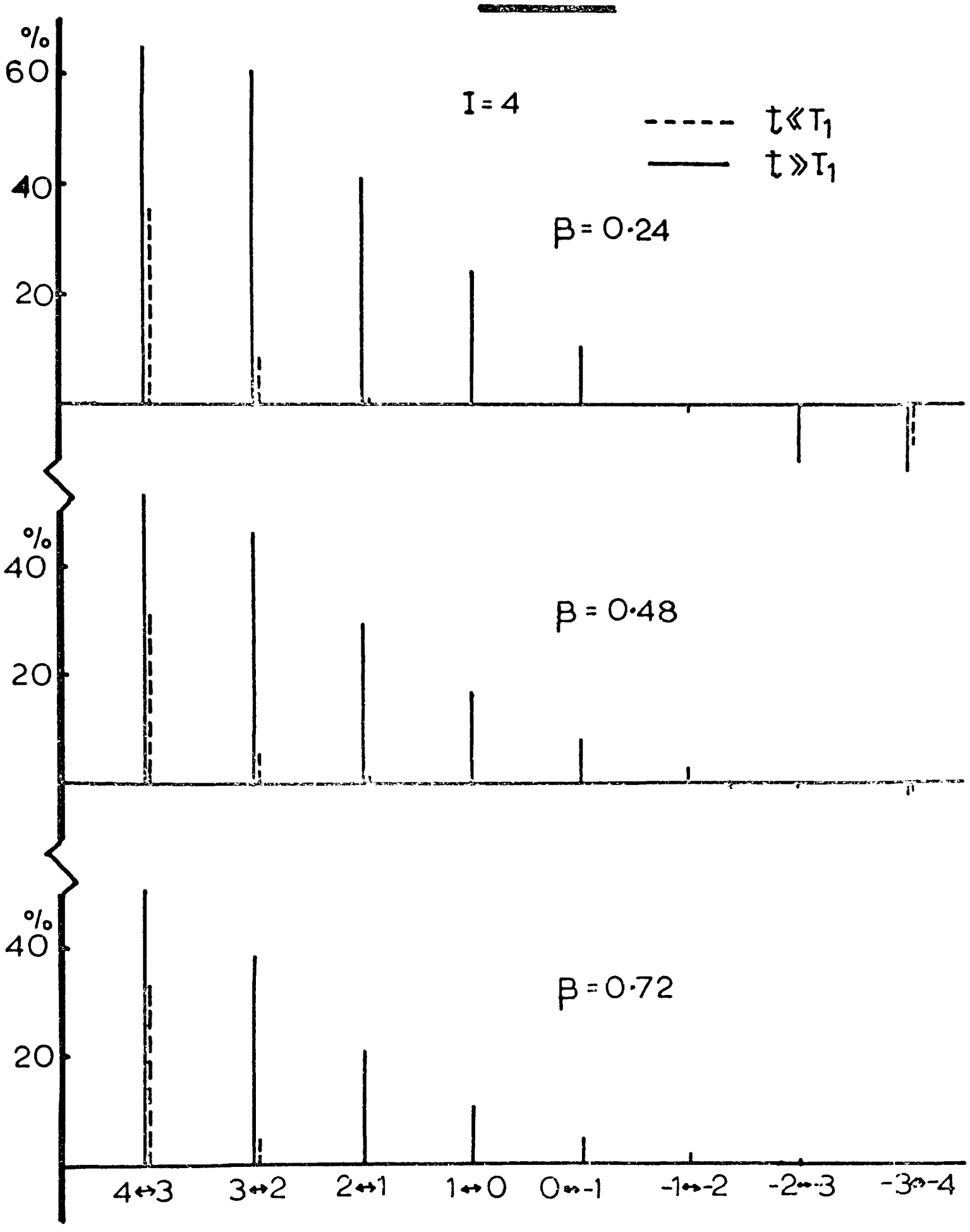

% (1-W(0))
150
100
50
0
-50
I = 2
---- t≪T1
—— t≫T1
β = 0·36
%
100
50
0
β = 0·72
%
100
50
0
β = 1·08
2↔1
1↔0
0↔-1
-1↔-2

FIG 5·6


%
60
40
20
I = 4
----- t « T1
—— t » T1
β = 0·24
%
40
20
β = 0·48
%
40
20
β = 0·72
4↔3
3↔2
2↔1
1↔0
0↔-1
-1↔-2
-2↔-3
-3↔-4

## 5.4 The effect of inhomogeneous broadening

It has been observed in all NMR/ON experiments in ferromagnetic metals that there is an inhomogeneous broadening of the resonance line due to random variations of the interactions at the impurity sites. For broadening of order 1 MHz, to observe resonance, the r.f. signal must be frequency modulated to produce resonant absorption in a finite number of nuclei. It is assumed that an r.f. field of frequency $\nu$ with modulation $\pm \Delta\nu$ will produce resonance in all substate transitions in the r ange of energy $\frac{1}{h}(\nu - \Delta\nu)$ to $\frac{1}{h}(\nu + \Delta\nu)$, leaving all others unaffected. This is justified since the predominant $T_2$ interaction for very dilute impurities in ferromagnetic hosts is the Suhl Nakamura interaction between transitions of equal energy, so that nuclei in different parts of the broadened line are not 'on speaking terms' with each other, but only with the lattice. The proportion of the anisotropy destroyed on the centre frequency of the resonance will depend on the ratio of the linewidth to the frequency modulations amplitude, but the total destruction can be calculated by an integration over the linewidth.

The effect of the inhomogeneous broadening of the resonance line, and the consequent frequency modulation required to observe the resonance, must be taken into account when the frequency splitting of the quadrupole effect on the resonance line is of the same magnitude, or less than, the inhomogeneous broadening. Using a Gaussian distribution for the distribution of effective magnetic fields about the mean value, the number of nuclei experiencing a resonant effect on one or more of the quadrupole split transitions can be calculated. The change in the anisotropy of the gamma emission from these nuclei can then be deduced. The NMR/ON effect is found by summing the anistropy changes from each set of nuclei experiencing different resonant transitions at each frequency. The frequency modulation may include several quadrupole split components of the magnetic resonance line.

For each $I_z$ level transition the fraction of the gaussian distribution involved is calculated for each frequency setting, and the total resonance effect obtained by summing over the 2I substate transitions. For the case where P is constant for all nuclei the above calculation performed for a series of values of the applied r.f. frequency will yield the NMR/ON line shape.

c. Results

In figs. 5.7 and 5.8 we show the resonance line shapes calculated for two values of P and for I = 2, 4. In all cases the curves correspond to the following Boltzmann factors between adjacent $I_z$ states

| | | Typical [1-WCO)] | $\frac{1}{T}$ |
|---|---|---|---|
| A Boltzmann factor | 0.8 | 1% | 10 |
| B " " | 0.5 | 7% | 30 |
| C " " | 0.1 | 30% | 100 |

(the variation of Boltzmann factor with $I_z$ caused by the quadrupole term is small for the values of P chosen). The ordinate is the percentage destruction of the equilibrium anisotropy corresponding to the appropriate Boltzmann factor. This allows clear appreciation of the variation of lineshape with temperature, but masks the fact that the equilibrium anisotropies, and hence the observability of the resonance effects, also vary strongly with temperature. The equilibrium anisotropies are therefore given for each curve. This point is exemplified by curve A, I = 2, which suggests a well resolved and detachable structure, but for the fact that the changes of count rate on resonance would be of order a few tenths percent.

Using this technique the quadrupole splitting is detected as the result of observing the contribution to the lineshape, of two or more components of the multiplet structure. Which particular components are

FIG 5·7

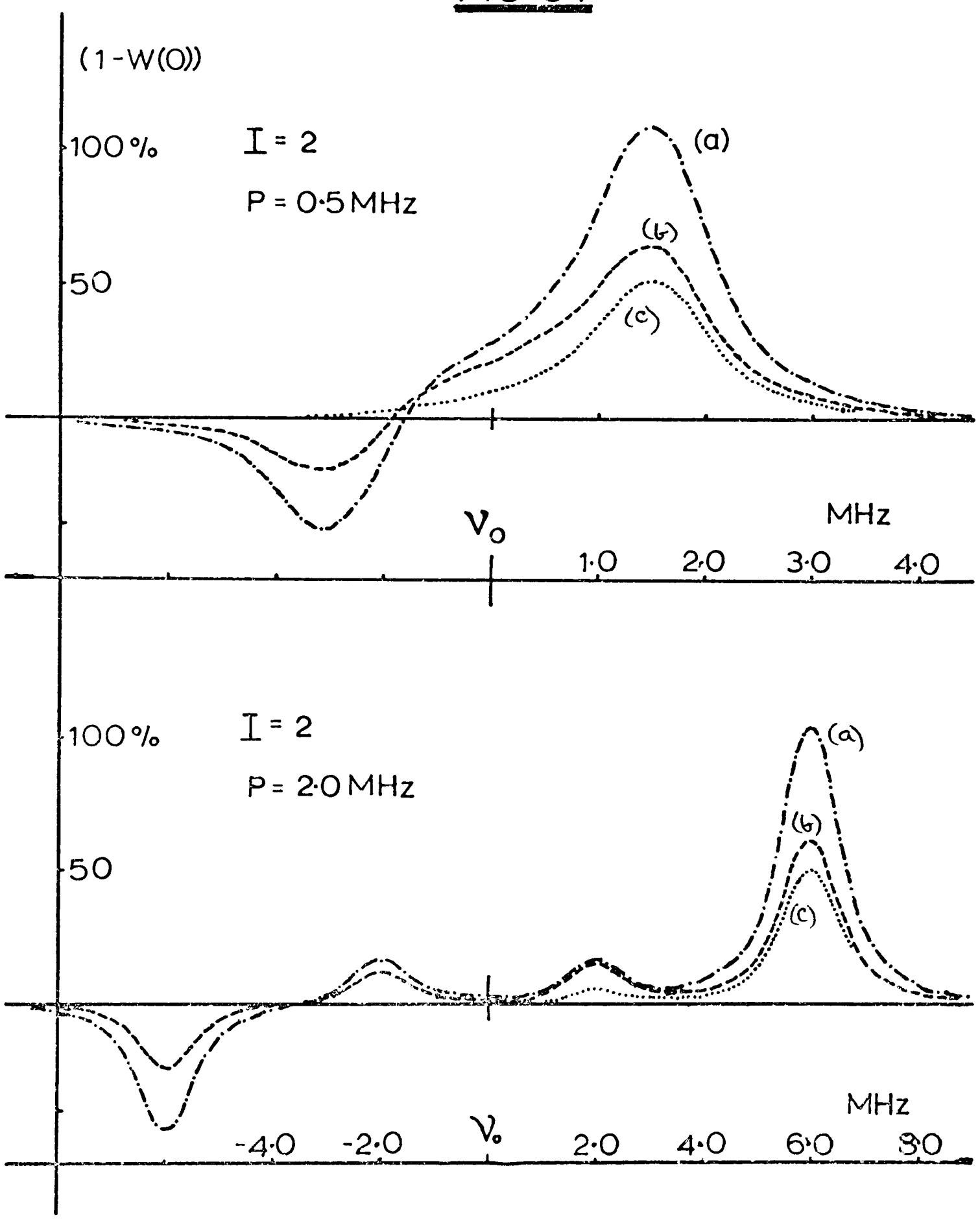
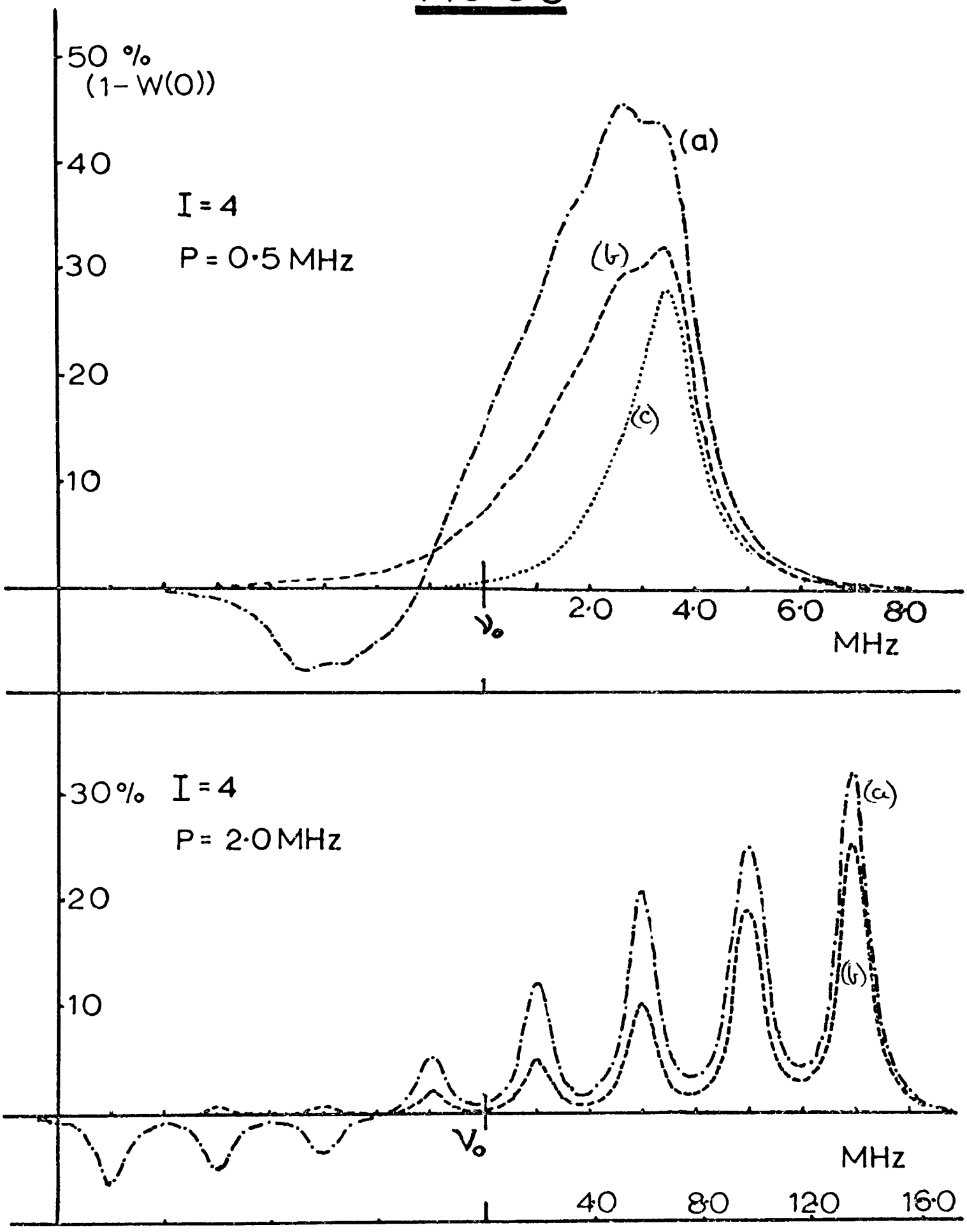

(1-W(0))
100%
50
I = 2
P = 0·5 MHz
(a)
(b)
(c)
$\nu_0$
MHz
1·0
2·0
3·0
4·0
100%
50
I = 2
P = 2·0 MHz
(a)
(b)
(c)
MHz
-4·0
-2·0
$\nu_0$
2·0
4·0
6·0
8·0

FIG 5·8


50 %
(1- W(0))
40
30
20
10
I = 4
P = 0·5 MHz
(a)
(b)
(c)
$\nu_0$
2·0
4·0
6·0
8·0
MHz
30%
I = 4
P = 2·0 MHz
20
10
(a)
(b)
$\nu_0$
MHz
40
80
120
160

involved depends upon the nuclear spin and the temperature of the system but the difference of the component energies is 2NP where N is an integer which can take on values from 1 to (2I-1), that is, an integer of order I. The components are detected provided their separation is comparable with their inhomogeneous broadening.

The inhomogeneous broadening mechanism in these systems is not well understood, but experimental results show that the line-width (FWHM) in all systems is 1.0 $\pm$ 0.5% of the resonant frequency. This leads to the empirical criterion for resolution

$$2IP_{min} \sim 0.01 \frac{\mu_N H_{eff}}{I}$$

or, substituting for P and rearranging

$$(eQV_{zz})_{min} = 0.01 \frac{\mu_N H_{eff}}{I} \cdot \frac{2}{3} [2I-1] \qquad (7)$$

From these relations the minimum detectable value of P is of order 0.5% of the Zeeman splitting for I = 1, falling to 0.1% for I = 4. The corresponding ratios for the electric quadrupole coupling $eQV_{zz}$ to the magnetic dipole coupling $\mu_N H_{eff}$ are of order 0.1% decreasing slowly with increasing nuclear spin.

Thus the NMR/ON technique allows detection and measurement of electric quadrupole admixtures which are two orders of magnitude smaller than the smallest detectable by conventional nuclear orientation.

From inspection of the above equation we can see that for a given host/impurity system the most sensitive measure of $V_{zz}$ is yielded by the isotope for which the ratio $\mu_N(2I-1)/QI$ is smallest. However this result is little more than a guide.

For systems of high spin where a resonance effect can be observed from many substate transitions, fig.5.8 shows that the peak of the

resonance effect observed an oriented nuclei will change in frequency as the temperature of the host lattice is changed. At very low temperatures the peak will shift to a frequency (2I-1)P off the frequency associated with the pure Zeeman splitting, whereas at higher temperatures the contribution to the resonance effect from the other substate transitions will broaden the resonance line and give the peak of the resonance signal at a frequency nearer the magnetic splitting frequency. It may be possible to use this effect to detect the existence of a small quadrupole splitting, although it has the disadvantage that the resonance must be observed at temperatures where the thermal equilibrium gamma-ray anisotropies are very small. For the spin 4 system shown in Fig.5.8 the shift in the resonance peak between lattice temperatures of $\frac{1}{T} = 10K^{-1}$, and $\frac{1}{T} = 100\ K^{-1}$ is about 1 MHz for P = 0.5 MHz, but the linewidth observed in the NMR/ON experiment varies fro m 1.5MHz to 4.0MHz. The measurement of the resonance by the perturbation of the gamma-ray anisotropy at a temperature of $\frac{1}{T} = 10K^{-1}$ would however require very long counting periods and a stable temperature in a region not easily studied with the available adiabatic demagnetisation techniques.

## 5.5 The effect of incomplete resonance saturation on the observed NMR/ON lineshape for a small quadrupole splitting

For many systems, the assumption of complete saturation of the nuclear resonance is not justified, either because of relaxation mechanisms comparable with the RF perturbation throughout the sample, or because the attenuation of the RF power in the metal hosts limits the range of the RF field to produce saturation of the resonance in only a proportion of the impurity nuclei. Since the observed lineshape for the nuclear resonance depends on contributions from several substate transitions the measurement of an electric quadrupole splitting from the lineshape requires a knowledge of the relative magnitudes of the changes in anisotropy associated with such transitions. The induced transition probability for each substate transition is given by

$$W_{ij} = \frac{\pi H_1^2}{2\hbar} |\mu_{ij}|^2 f(w)$$

where f(w) is the shape function associated with the applied frequency and the resonance frequency $\omega$ . For a linearly polarised RF field in the plane perpendicular to the axis of magnitvsation the matrix element for the induded transition rate $|\mu_{ij}|$ is given by [29]

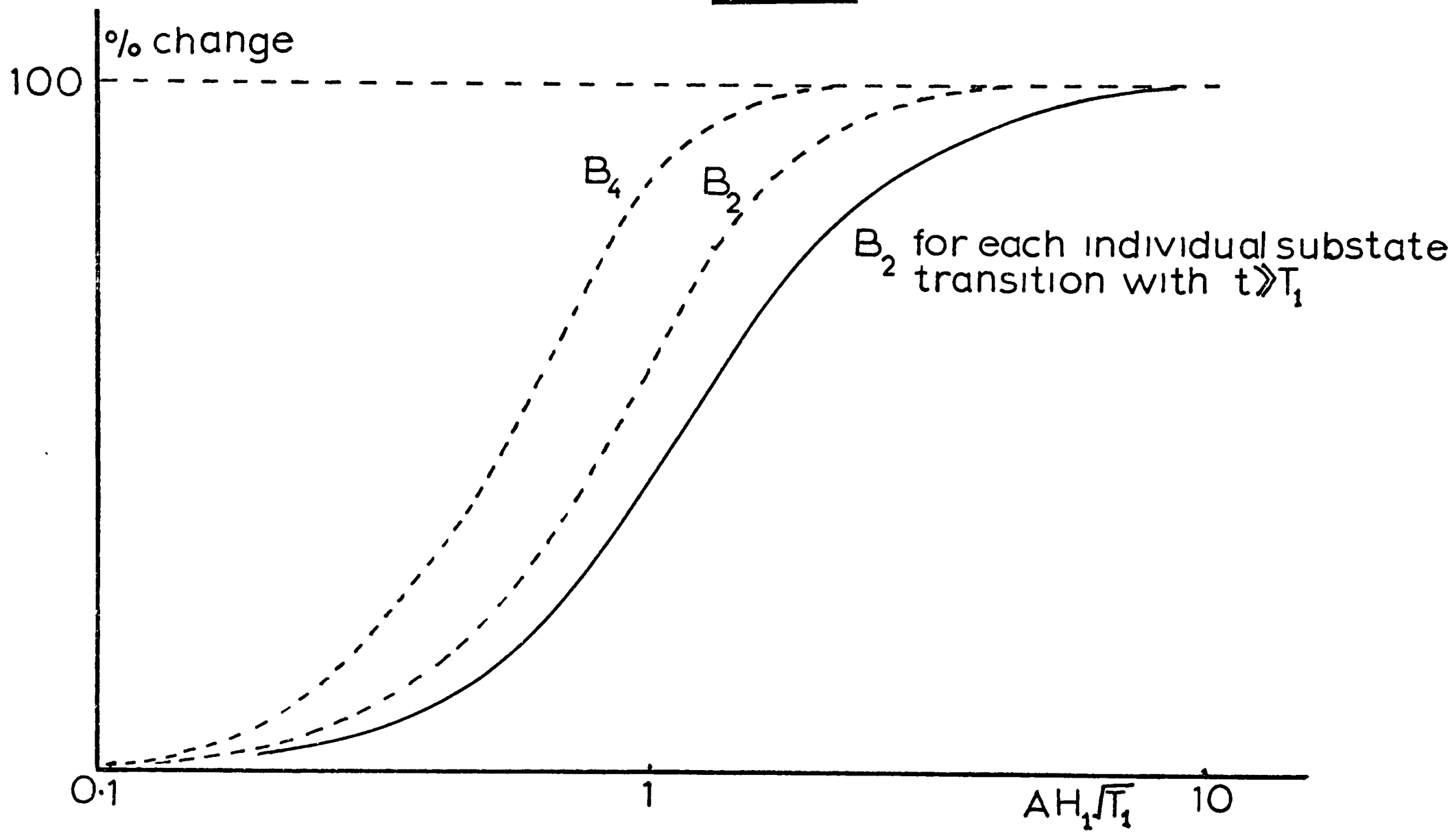
$$|\mu_{ij}| = [\underline{I[I+1]-M(M+1)}]^{\frac{1}{2}}$$

For a spin I = 4 the induced transition rates will be in the ratios 8 : 14 : 18 : 20: 20 : 18 : 14 : 8. For a small electric quadrupole splitting relative to the magnetic interaction, the relaxation processes will produce an identical magnitude for the relaxation interaction for each of the substate transitions. For such a situation where $W_{ij}^{RF}/W_{ij}^{REL}$ is the same for each substate transition the factors $[I(I+1)-M(M+1)]/(2I+1)^2$

cancel and the degree of saturation of each of the 2I components of the resonance line will be the same. The computer calculations have shown that the changes in the gamma-ray anisotropies associated with a given degree of saturation of each substate resonance are proportional to the changes with complete saturation even in the situation of $t \gg T_1$ where other substate populations are also affected.

This means that for small quadrupole splittings where P is of the same order of magnitude or the inhomogeneous broadening, the asymmetry of the nuclear magnetic resonance line will not change with the degree of saturation of the resonance. However, the saturation of each component of a quadrupole split resonance line when $t \gg T_1$ will require a larger RF field than is required for a pure magnetic interaction, as the power is only absorbed directly by one or two of the substate transitions rather than by all the transitions. For a spin of 4 the calculations have shown that the RF amplitude required to produce 90% saturation in the resonance change in the gamma-ray anisotropy is a factor of $\sim 3$ greater for each component in the resonance line than that required for an unsplit resonance line. This is shown in Fig.5.9. In this case the saturation curves of $B_2$ and $B_4$ are very similar.

FIG 5·9


% change
100
$B_4$
$B_2$
$B_2$ for each individual substate transition with $t \gg T_1$
0·1
1
$AH_1\sqrt{T_1}$
10

## 5.6 Conclusions

The results presented in this chapter shows that a small co-axial electric quadrupole interaction can lead to a considerable error in the interpretation of conventional nuclear orientation experiments if they are interpreted only with a pure magnetic hyperfine hamiltonian. The NMR/ON technique however, is well suited to detecting small electric quadrupole interactions giving splittings to the nuclear resonance line of down to one part in $10^3$ of the magnetic interaction. The measurement of such contributions may constitute a new line of investigation into the electronic interactions of impurity atoms with the ferromagnetic host lattice and conduction electrons. The results of measurements of electric quadrupole interactions can be compared with the measurements of the orbital dipolar contribution to the magnetic hyperfine interaction from unquenched local magnetic moments as discussed in the last chapter.

# CHAPTER 6

# NUCLEAR MAGNETIC RESONANCE OF GOLD IMPURITIES IN IRON COBALT AND NICKEL

## 6.1 Introduction

The experiments described in this chapter are designed to measure the contributions to the hyperfine interactions of gold isotopes as dilute impurities in the ferromagnetic lattices. The accurate measurement of the hyperfine anomaly of two isotopes of the same element provides a method of separating the contributions to the total magnetic hyperfine interaction from the s-electron Fermi contact interaction and the orbital dipolar interaction, the origin of which was discussed in chapter 4. The nuclear magnetic resonance technique is also sensitive to any electric quadruple interaction associated with the localised orbital magnetic moment on the impurity. This chapter can be conveniently subdivided into four sections. A brief description of the origin of the hyperfine anomaly is followed by a discussion of the N.M.R./O.N. results on the two isotopes $^{199}$Au and $^{198}$Au in iron. The measurements of Fox and Stone [20] showed an apparent discrepancy between the hyperfine anomaly measured for these two isotopes in an iron lattice and that deduced from atomic beam measurements. The more accurate measurements described here distinguish between a true effect of the magnetic hyperfine interaction on the hyperfine anomaly and the effect of an electric quadruple interaction. The comparison of the hyperfine anomaly results and the limit set on the electric quadrupole interaction is discussed in terms of the models considered in chapter four for the effect of a localised orbital moment. The third and fourth sections deal with the N.M.R./O.N. measurements in cobalt and nickel hosts. The results provide the first accurate measurement of the hyperfine interaction of gold isotopes in these hosts and the first observation of nuclear magnetic resonance of dilute impurities in a cobalt host lattice. The measurements

in the cobalt host are analysed in the same way as the results in an iron host in terms of a localised gold orbital moment. The smaller effective magnetic hyperfine field in nickel gives very small orientation effects with a consequent loss of sensitivity for the nuclear magnetic resonance. The observed resonance for $\underline{Ni}^{198}Au$ gives the magnitude of the total hyperfine interaction but does not allow a separation of the components to be made.

## 6.2 The hyperfine Anomaly

The term hyperfine anomaly is used to describe the difference between the ratio of the magnetic dipole moments of two nuclei and the ratio of the interaction energies with the magnetic field provided by a hyperfine interaction. The anomaly is defined by the form

$$\frac{\nu_1}{\nu_2} = \frac{g_1}{g_2}\,[\,1 + {}^1\Delta^2]$$

where $\nu_{1,2}$ are the magnetic resonance frequencies in the hyperfine field and $g_1$ and $g_2$ are the nuclear g factors measured in a uniform magnetic field. The hyperfine anomaly is the result of the non-uniform distribution of the nuclear magnetism throughout the nucleus and the variation of the effective hyperfine field over the finite size of the nucleus. The hyperfine interaction energy is given by the general form

$$W = \int \mu(r)\, H_{eff}(r)\, d\tau$$

This may often differ from the value $\mu_N \cdot H_{eff}(0)$ for a point dipole. If the interaction energy W is written as

$$W = W_{point}\,(1 + \varepsilon)$$

the observed ratio of $W_1/W_2$ for two isotopes in the same hyperfine field will give an hyperfine anomaly equal to

$${}^1\Delta^2 = (\varepsilon_1 - \varepsilon_2)/(1 + \varepsilon_2) \approx \varepsilon_1 - \varepsilon_2$$

The effect of the distribution of the nuclear magnetism is most clearly seen on the Fermi-contact hyperfine interaction of a single impaired s-electron in the state $m_s = +1/2$. The principal quantum number does not influence the calculation, since in first order the radial distri bution of the electron density over the nuclear volume is sensitive only to the angular momentum quantum number, L. The finite size of the nucleus and the consequent finite charge distribution makes the electric potential inside the nucleus non-coulomb, and results in a change in the electronic interaction relative to that of a 'point' charge distribution. This is shown in Fig.8.1a. The work of Bohr and Weisskopf [75] and Eisinger and Jaccarino [76] on the effect on the hyperfine interaction associated with spin and orbital nuclear magnetism, moments, shwws that for a uniform distribution of nuclear magnetism, the radial variation of the s-electron density, coupled with the distribution of magnetism, reduces the magnitude of the hyperfine interaction relative to that of a point magnetic dipole, by the amount $\epsilon$, where

$$\epsilon = \left\langle 1 - \frac{|\Psi(r)|^2}{|\Psi(0)|^2} \right\rangle \approx \frac{2R_e}{a_o} \left\langle \frac{R^2}{R_e^2} \right\rangle_{av}$$

The typical order of magnitude of this effect for Z = 50 is only $\sim 10^{-3}$ to $10^{-2}$, but very much larger anomalies have been observed as a result of the difference in action of the hyperfine field on the nuclear orbital and nuclear spin magnetic moments. The distribution of nuclear magnetism associated with an unpaired proton spin will follow the radial variation of the proton density, whereas the magnetism associated with the orbital angular momentum will give a contribution to the hyperfine interaction depending on the average value of $H_{eff}$ through the proton orbit. The general expressions given by Bohr and Weiskopf are

$$W_s = -\mu_N \left\langle g_s \vec{B}(r).\vec{S} \right\rangle_{I,I}$$

$$W_L = -\mu_N \langle \epsilon_1 B_{orr}(r) L_s \rangle_{J,I}$$

The value of $\varepsilon$ is given by the sum of the spin and orbital components

$$\varepsilon = -\frac{ZR_e}{a_o} \left\langle \frac{R^2}{R_e^2} \right\rangle_{av} [a_s (1+\xi) + 0.62\, a_L] \qquad \alpha_s + \alpha_L = 1$$

The values of $a_s$ and $a_2$ can be calculated for a chosen nuclear model on the basis of the definitions [78]

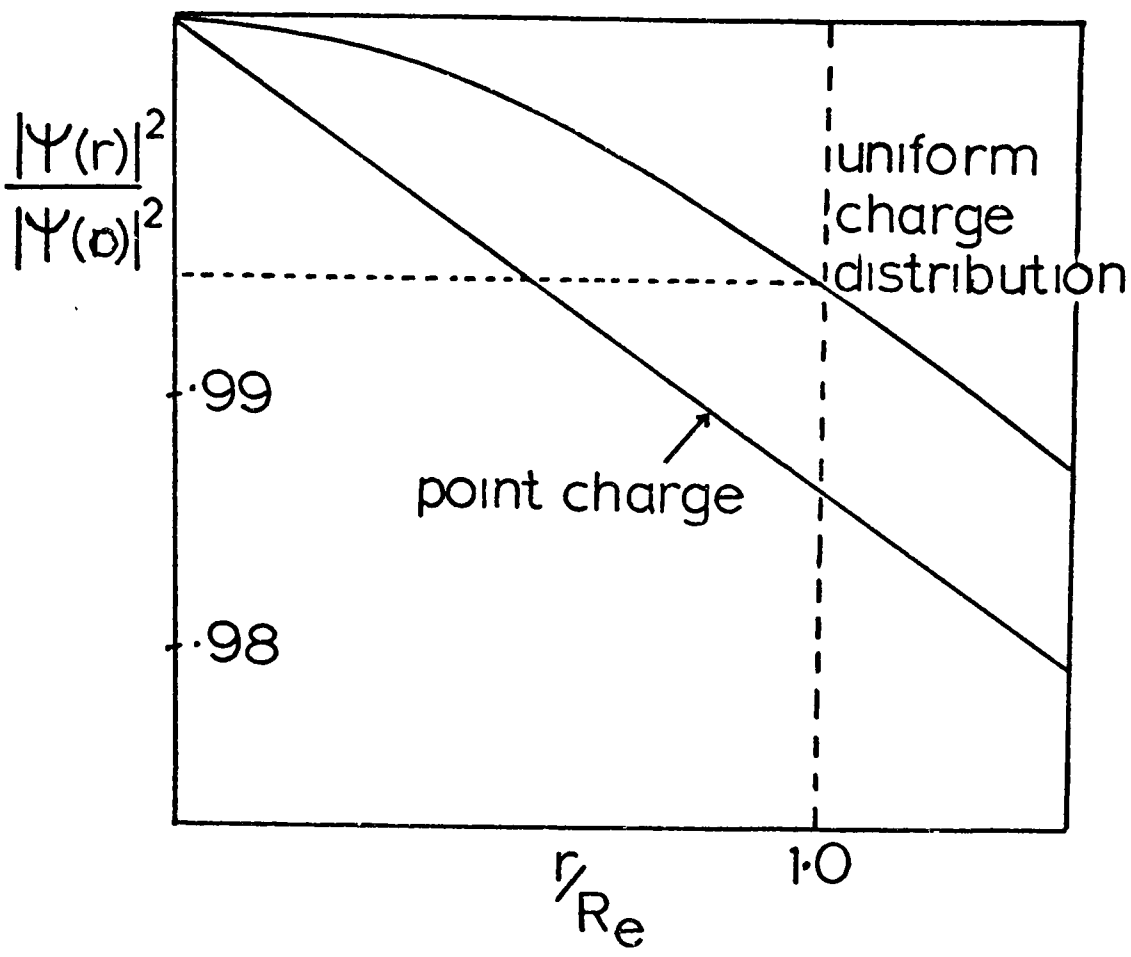
$$a_s = \frac{\langle \epsilon_s S_s \rangle_{I,I}}{\epsilon_I^I} \qquad a_2 = \frac{\langle \epsilon_s L_s \rangle_{I,I}}{\epsilon_I^I}$$

Fig.6.1b shows the values of $a_s$ and $a_2$ for a single proton state for $p_{\frac{1}{2}}$ and $d_{3/2}$ nuclei. For both these states the spin and orbital magnetic moments nearly cancel; leaving th e value of $\xi_s + \xi_L$ as a larger proportionof the net magnetic moment. The effect is largest for heavy nuclei since $\varepsilon$ increases as $Z^2$, and the relativistic correction factor

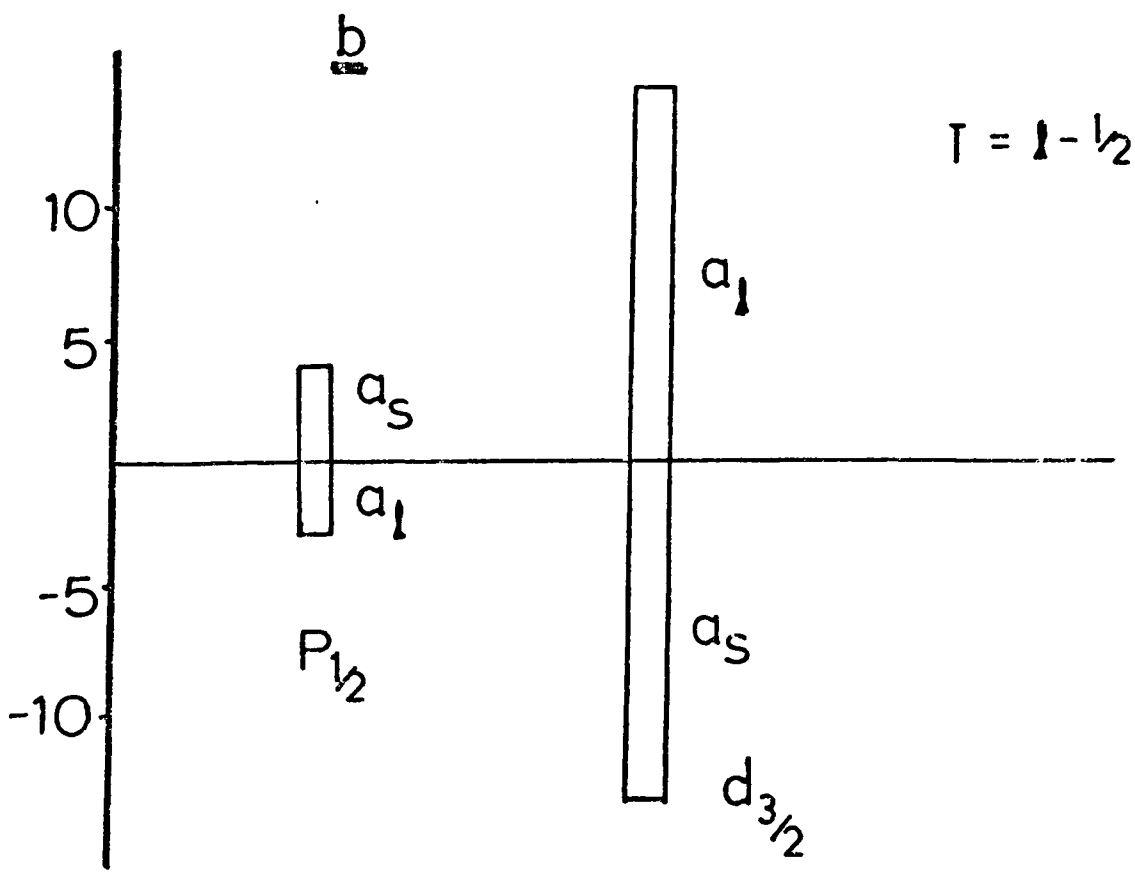
$$\left(\frac{a_o}{2Z R_e}\right)^{2(1-\rho)} \qquad \rho = \left(1 - \frac{Z^2 e^4}{\hbar^2 c^2}\right)^{\frac{1}{2}}$$

becomes important for large Z. Such a factor also provides a contribution to the hyperfine anomaly from relativistic $p_{\frac{1}{2}}$ electron interactions which can become very large for A greater than 200. This is particularly relevant for an atom with a single $p_{\frac{1}{2}}$ electron (or hole) outside a closed shell, although the problem is very complicated in compounds and solids where more than one electron can frequently contribute. It is not clear how the $p_{\frac{1}{2}}$ contribution to the hyperfine anomaly can be extracted in magnetic solids, where an appreciable net polarisation can occur in p shells.

FIG 6·1




Variation of the S-electron density over the nuclear volume (15)




Spin and orbital contributions to the magnetic moment for $p_{1/2}$ and $d_{3/2}$ nuclei

The hyperfine anomaly is associated only with the Fermi-contact hyperfine interaction. The orbital dipolar and spin dipolar hyperfine interactions give a uniform effective magnetic field over the nuclear volume with no hyperfine anomaly. The comparison of an observed hyperfine anomaly associated with a hyperfine interaction of unknown origin with the hyperfine anomaly due to a pure s-electron contact interaction will show the proportion of the unknown hyperfine interaction due to an orbital dipolar interaction

$$\frac{\nu_1}{\nu_2} = \frac{\mu_1}{\mu_2}\left[1 + {}^{1}\Delta^{2}_{obs}\right] = \frac{\mu_1}{\mu_2}\left[1 + \frac{H_o}{H_{eff}}\,{}^{1}\Delta^{2}_{c}\right]$$

$$\frac{H_o}{H_{eff}} = \frac{{}^{1}\Delta^{2}_{obs}}{{}^{1}\Delta^{2}_{c}}$$

The practicality of using this technique to separate the components in the magnetic hyperfine interaction in ferromagnetic host has been demonstrated by Fox and Stone [20] using the N.M.R./O.N. technique on the mass 199 and 198 isotopes of gold, and by Perlow et al [78] using the Mossbauer technique on $^{193}$Ir in iron and nickel.

Both the mass 199 and 198 isotopes of gold have a ground state nuclear structure containing an unpaired $(2d_{3/2})$ proton. The 199 Au isotope has a nuclear structure containing a $(2d_{3/2})^3$ proton state and $(2f_{5/2})^2$ neutron state [17]. The spin and parity of $3/2^+$ arises only from the proton state. The $^{198}$Au isotope has an unpaired $(3p_{\frac{1}{2}})^1$ neutron giving with the $d_{3/2}$ proton, a spin and parity of $2^-$ to the ground state. The unpaired $d_{3/2}$ proton in $^{199}$Au will produce spin and orbital contributions to the nuclear magnetic moment of opposite sign and similar magnitude. The small measured magnetic moment of $^{199}$Au of $0.27_{\mu N}$ [82] results from the near cancellation of the spin and orbital contributions, and the similarity to the Schmidt value of $+0.13\mu_N$ provides evidence of the

closeness of the ground state configuration to $(2d_{3/2})^3_{3/2}$. The different radial distribution of magnetism associated with the two components and the near cancellation of the two components to the magnetic moment combine to produce a magnification of the value of $\xi$ relative to the magnetic moment. The same effect applies to the $^{198}$Au isotope but the additional contribution to the magnetic moment from the unpaired neutron reduces the difference between the effect of the distribution of magnetism and that of a point dipole.

The hyperfine anomaly between isotopes of gold can be conveniently measured in an atomic beam experiment. The ground state of the gold atom has a configuration $5d^{10}6s^1$. In the atomic beam experiment the gold nucleus will experience the hyperfine interaction due to the single electron in a 6s orbital. The hyperfine anomaly will therefore correspond to that associated with a pure s-electron Fermi contact interaction. A summary of the atomic beam measurements is presented in Table 6.1.

## Table 6.1

| Isotope | $I^{\pi}$ | $\mu$ | $\Delta_c$ | | |
|---|---|---|---|---|---|
| $^{196}_{79}Au$ | $2^-$ | 0.5823 | $^{196}\Delta^{197}$ | 8.0% | [ 83 ] |
| $^{197}_{79}Au$ | $\frac{3}{2}^+$ | +0.1449 | | | |
| $^{198}_{79}Au$ | $2^-$ | 0.5842 | $^{197}\Delta^{198}$ | 8.5% | [ 82 ] |
| $^{199}_{79}Au$ | $\frac{3}{2}^+$ | +0.2673 | $^{198}\Delta^{199}$ | 4.5%* | |

* Deduced from the other values $^{197}\Delta^{198}_{c}$ and $^{197}\Delta^{199}_{c}$

## N.M.R./O.N. measurements of $^{199}Au$ in iron

In general, in a cubic ferromagnetic lattice, the dominant contribution to the magnetic hyperfine interaction will be the Fermi-contact interaction associated with core polarisation of s-electrons or conduction electron polarisation. It was shown in chapter 4 that appreciable contributions from the spin dipolar and orbital dipolar interactions can occur in association with an unquenched orbital moment on the impurity atom. Although gold is not a transition element, the interaction of the outer 5d and 6s shell electrons with the 3d and 4s electrons of the conduction band of iron can be expected to produce effects, similar to those for transition metal impurities. The spin-orbit interaction may produce an unquenched 5d, or possibly 6p, orbital moment on the gold atom, both of which would give rise to orbital and spin dipolar magnetic interactions and an electric quadrupole interaction. The aim of the experiments was to use the measurement of the hyperfine anomaly to investigate such magnetic interactions.

The accurate measurement of the ratio of the hyperfine splittings of the two gold isotopes by N.M.R./O.N., and thus the determination of the hyperfine anomaly, is complicated by the effect of the probable electric quadrupole interaction. It was shown in chapter five that the effect of a small electric quadrupole interaction on the N.M.R./O.N. frequency response is to shift the peak of the resonance response. In the limit of very low temperature, when the substate population distribution allows only one extreme component of the quadrupole split resonance line to be seen, the frequency shift is equal to (2L-1) P.

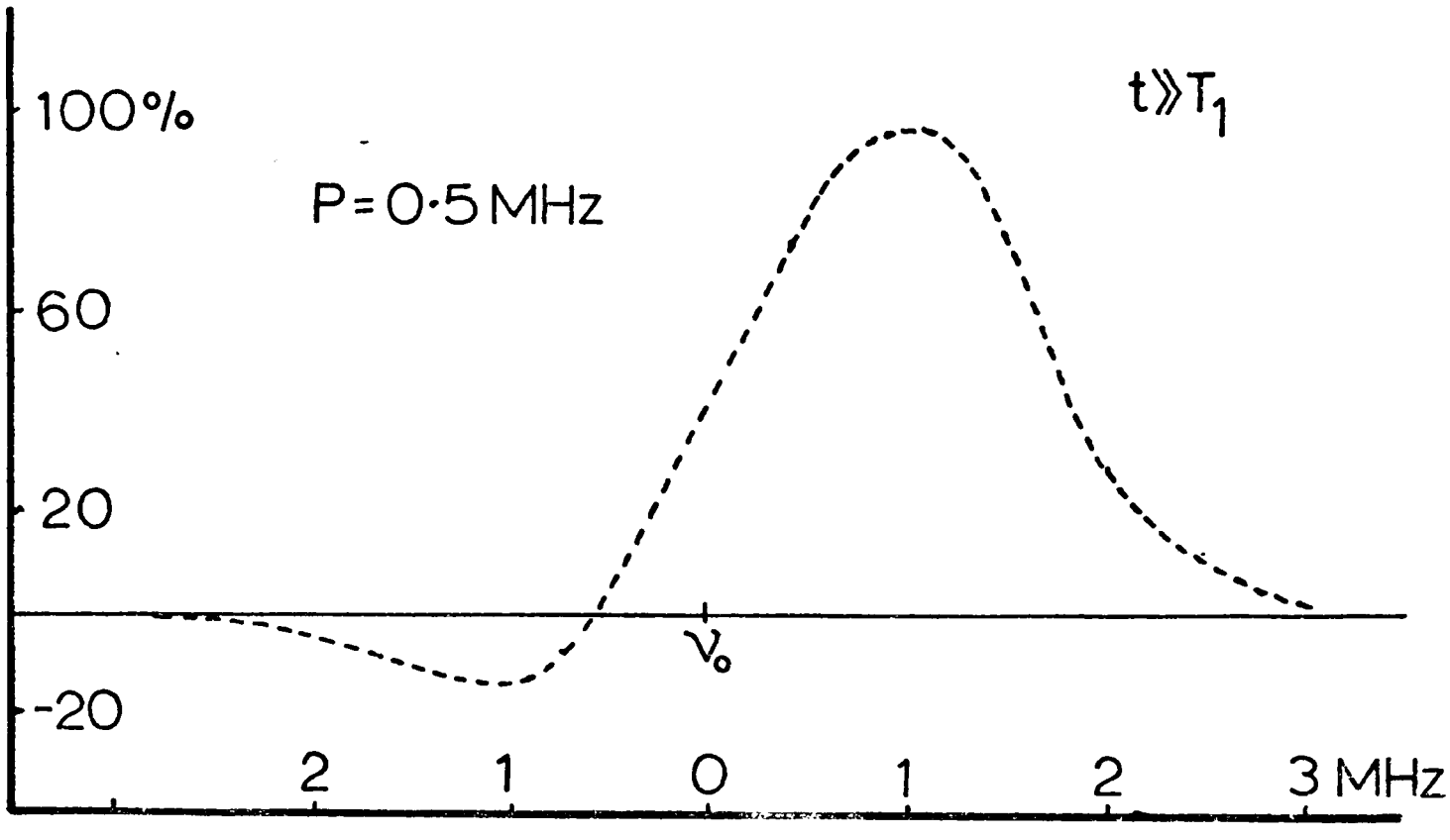
The orbital dipolar hyperfine interaction enters as a first order term in the influence of the spin-orbit interaction perturbation, but is observed only through the difference in the hyperfine anomaly in the iron lattice from the pure s-electron anomaly. Since the hyperfine anomaly for

for $^{198}$Au and $^{199}$Au isotopes is only $\sim 5\%$, the change in the ratio of nuclear magnetic resonance frequencies associated with a 10% orbital dipolar contribution to the total magnetic interaction would be of the order of 0.5%. The electric quadrupole interaction will have a direct influence on the magnetic resonance spectrum, and, although proportional only to a second order term in the spin-orbit perturbation, could produce an apparent change in the ratio of resonance frequencies comparable with the influence of the orbital dipolar magnetic contribution. In the limit of very low temperature and $P \ll \frac{\mu_N H}{I_N}$, the ratio of apparent resonance frequencies can be written in the form

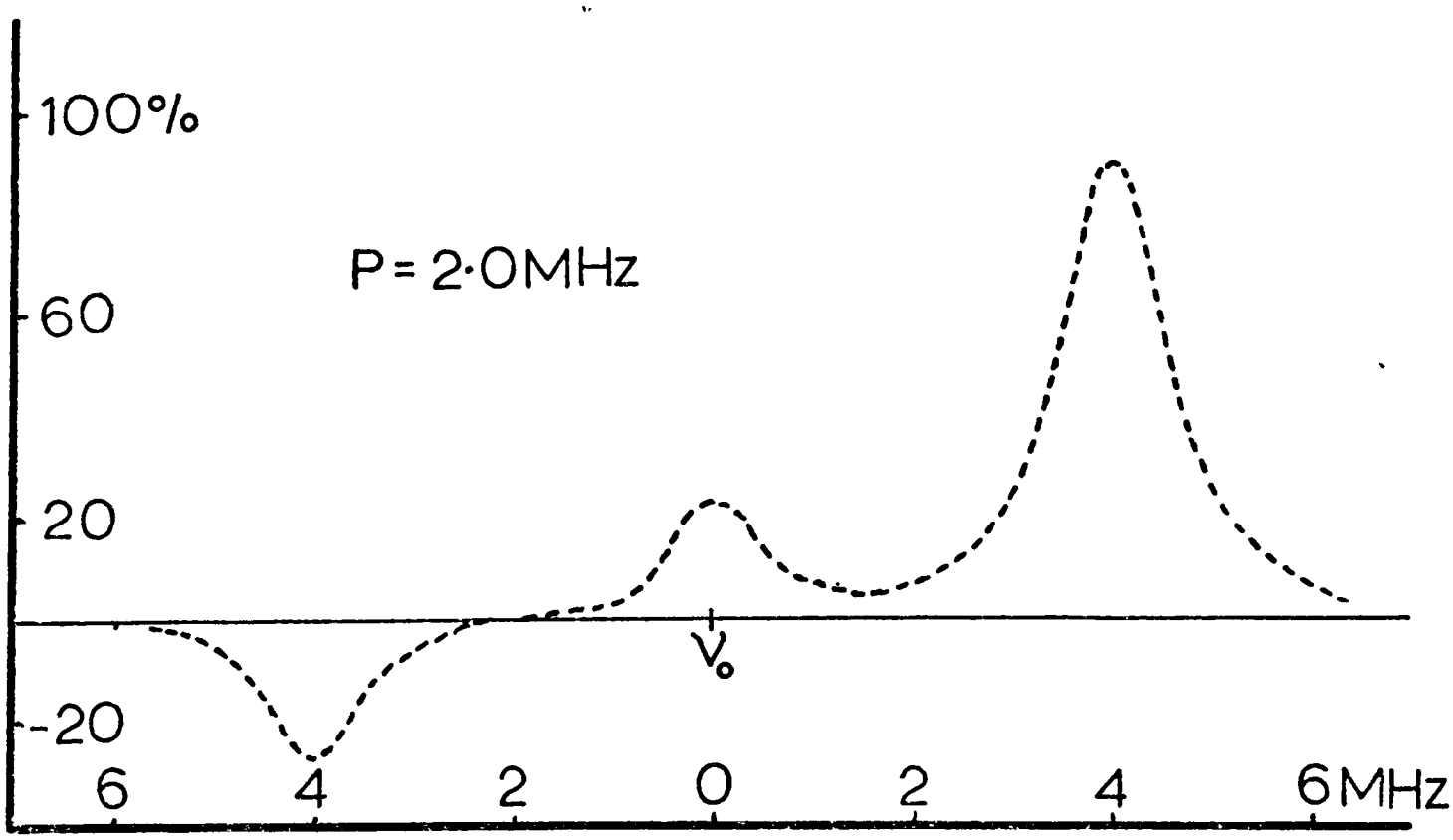
$$\frac{\nu_1}{\nu_2} = \frac{g_1}{g_2}\left[1 + {}^1\Delta^2_{Fe}\right] + \frac{e^2 q}{4 g_2 H_{eff}}\left[\frac{Q_1}{I_1} - \frac{Q_2}{I_2}\right]$$

For an accurate description of the hyperfine interaction these two influences on the ratio $\nu_1/\nu_2$ must be separated. The study of the detailed frequency dependence of the N.M.R./O.N. response provides a method of independently measuring the magnitude of P for each isotope. The spin of 3/2 of the $^{199}$Au ground state means that an electric quadrupole interaction will split the nuclear resonance line into three components representing the transitions $M_z = \frac{3}{2} \rightarrow \frac{1}{2}$ , $\frac{1}{2} \rightarrow -\frac{1}{2}$ , $-\frac{1}{2} \rightarrow -\frac{3}{2}$ . The degree of nuclear orientation at the temperature used for the nuclear resonance experiment allows all the substate transitions to be observed. The sensitivity of the N.M.R./O.N. experiment to a small electric quadrupole interaction is greater for the spin 3/2 ground state of $^{199}$Au than the spin 2 ground state of $^{198}$Au because of the factor of $1/[4I(2I-1]$ in the definition of P. Fig.6.2 shows the computed resonance spectra for Fe $^{199}$Au with values of P of 2.0MHz and 0.5MHz at a temperature of $1/T = 60K^{-1}$. The change in sign of the axial anisotropy change on resonance for the $-\frac{1}{2} \rightarrow -\frac{3}{2}$ substate transition gives a good indication of the existence of an electric

FIG 6·2




Computed N.M.R.O.N. curves for $^{199}$Fe Au



quadrupole splitting. The computed curves are for the situation when $t \gg T_1$, allowing the thermal equilibrium population distribution to be re-established between substates not directly influenced by the R.F. field. This is important for the $-\frac{1}{2} \rightarrow \frac{1}{2}$ substate transition, since, in the absence of relaxation, changes in the ratio of population between the $M_2 = \pm 1/2$ states will produce no change in the observed gamma ray anisotropy. The indirect influence through the spin lattice relaxation, will produce a change in the $B_2$ orientation parameter. The low spin of 3/2 means that there is no contribution to the gamma ray anisotropy from the $B_4$ term. In the presence of a sufficiently large electric quadrupole splitting such that only one substate transition is resonated at a time, the change in the gamma-ray anisotropy associated with the resonance of the $\frac{3}{2} \rightarrow \frac{1}{2}$ transition can be greater than 100%. This is because the anisotropy will change sign when the combined population of the $\pm \frac{1}{2}$ substates is greater than that of the $\pm \frac{3}{2}$ substates.

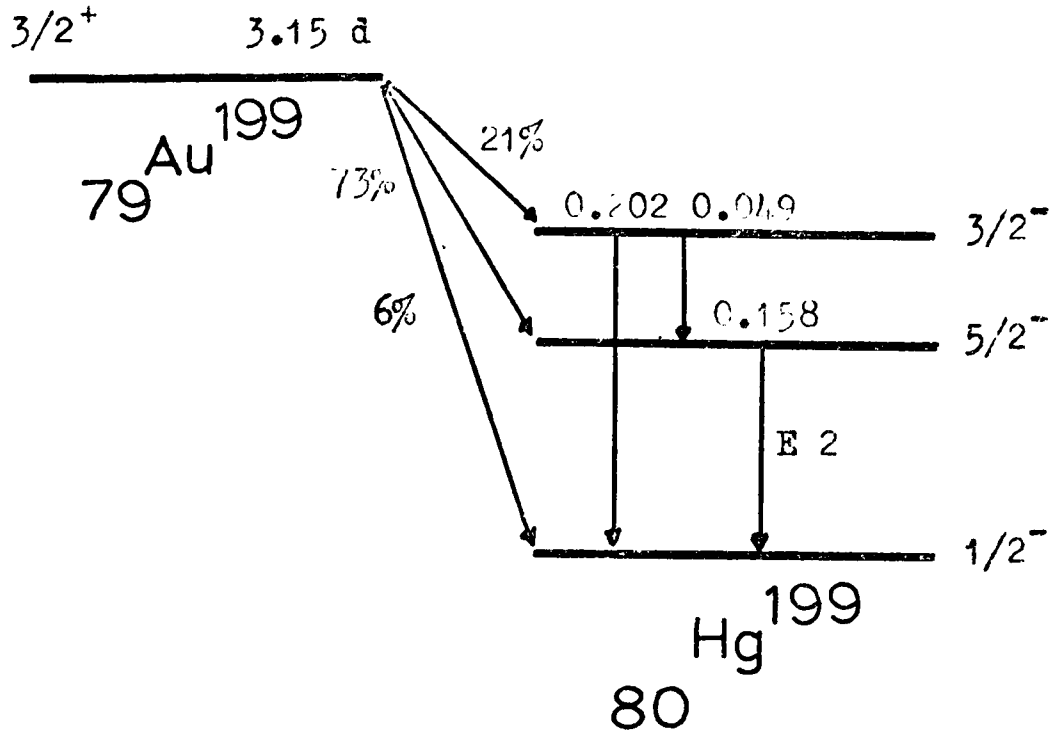
The initial experiments of Fox and Stone on the nuclear magnetic resonance of $^{199}Au$ and $^{198}Au$ in iron showed a maximum resonance response for each isotope at 168.0 ± 0.3 MHz and 260.0 ± 0.2 MHz respectively. This indicates an apparent hyperfine anomaly of 5.5 ± 0.2% in the iron hyperfine field, but the signal/noise ratio was not good enough to investigate the origin of this effect. This experiment, with considerably improved sensitivity was designed to detect the possible effect of the electric quadrupole interaction and improve the accuracy of the measurement.

The gold 199 activity was obtained as a solution of $AuCl_2^+$ in 4M HCl. The half-life of this isotope is 3.2 days. The initial specific activity of the solution of 10 mCi/mg enabled resonance samples containing less than $10^{-1}$ at % of gold to be produced with a sufficiently high gamma-ray count rate for the first six days. The samples were prepared by thermal diffusion from a layer of active gold, electroplated onto the iron surface from the $AuCl_2$ solution. A diffusion time of 10 hrs. at 850°C was found sufficient to produce a uniform distribution of the activity throughout the 1 μm thick foil.

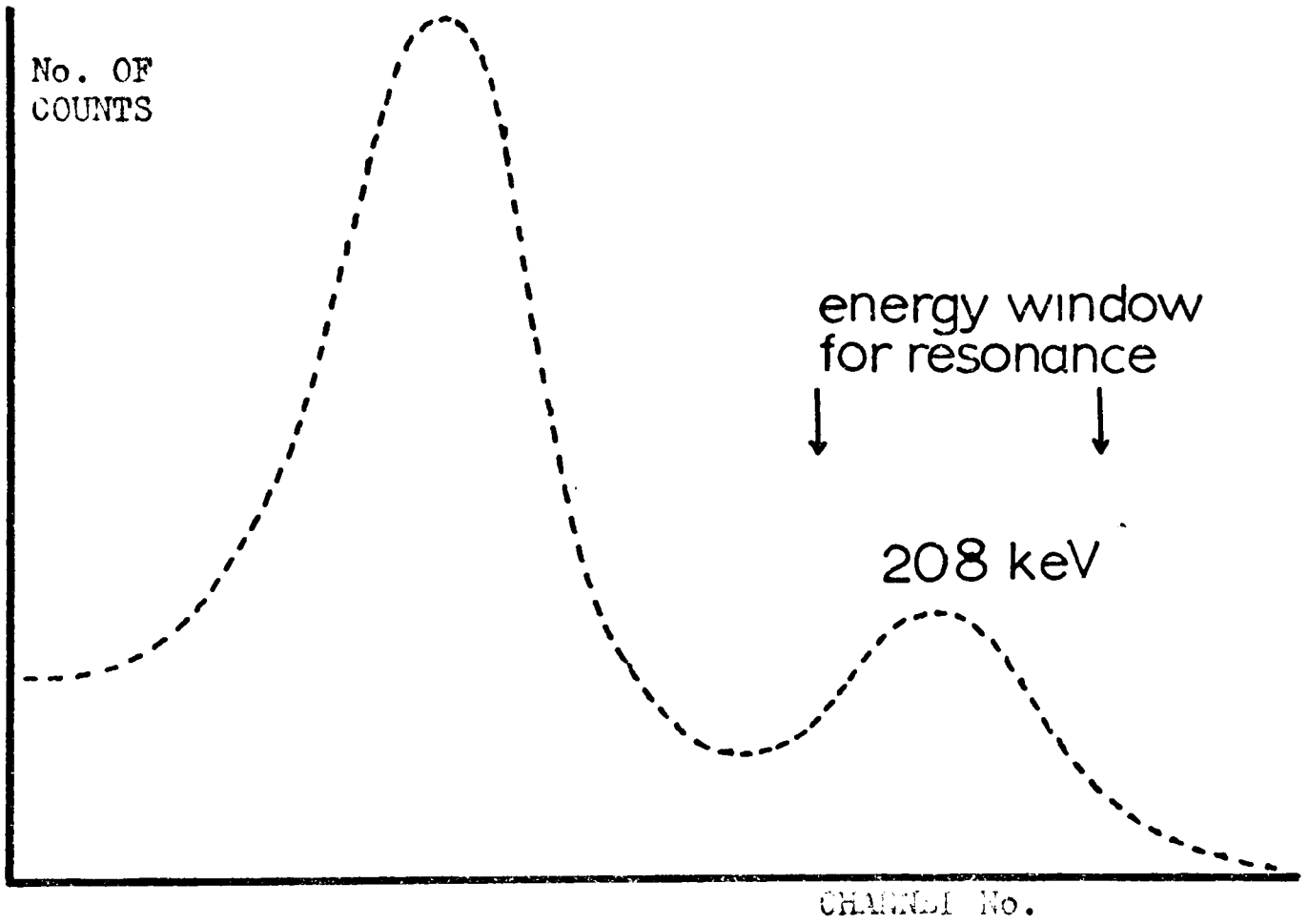
The decay scheme of $^{199}Au$ is shown in Fig.6.3. The 158 KeV and 208 KeV gamma transitions are the strongest, and are just resolved by a NaI detector. The decay coefficients give axial anisotropies of opposite sign on the two peaks. At a temperature of $\frac{1}{T} = 70\ K^{-1}$ the 158 KeV and 208 KeV peaks show anisotropies of - 4% and +9% respectively. A single channel analyser window over the 208 KeV peak gives a better signal/noise ratio for resonance, despite the lower intensity, because the degraded radiation under the 158 KeV peak shows the opposite sign of anisotropy to the peak, considerably reducing the net anisotropy.

The nuclear resonance was observed as the difference in the 208 KeV gamma ray anisotropy shown by the thermal equilibrium population distribution and that observed when the R.F. carrier wave is modulated over a frequency range of ±400KHz. The frequency range of the experiment was extended to ±5 MHz either side of the resonance peak to include the possibility of an electric quadrupole splitting giving a value of P up to 2.5 MHz. The result of the N.M.R./O.N. experiments is shown in Fig.6.4. This shows a single resonance line with no obvious asymmetry and no frequency region showing a consistent resonance effect of opposite sign. The comparison

FIG 6·3




DECAY SCHEME OF $^{199}Au$




GAMMA RAY SPECTRUM OF $^{199}Au$ FROM A NaI. DETECTOR SHOWING THE ENERGY WINDOW USED FOR THE RESONANCE EXPERIMENT

with the calculated effect using a value of P = 0.5 MHz gives an indication of the sensitivity of the technique. The experimental result enables an upper limit of $P \leqslant 0.3$ MHz to be put on the magnitude of the electric quadrupole splitting. Evidence that the electric quadrupole splitting is not so large that all but one component of the resonance line lay within our region of search is provided by the Mossbauer measurements [86] where no large quadrupole splitting was seen. The centre frequency for the magnetic interaction is 167.45 (10) MHz in an applied polarising field of 1.7 kOe. This measurement, corrected for the applied field, can be used with the measurement of Fox and Stone for $^{198}$Au in iron to give the hyperfine anomaly in iron. The limit set on P from the N.M.R./O.N. measurement of $^{199}$Au in iron suggests that the value for $^{198}$Au in iron will be less than 0.15 MHz, assuming similar electric quadrupole moments. This justifies the use of the centre frequency found by Fox et al for the resonance of Fe$^{198}$Au.

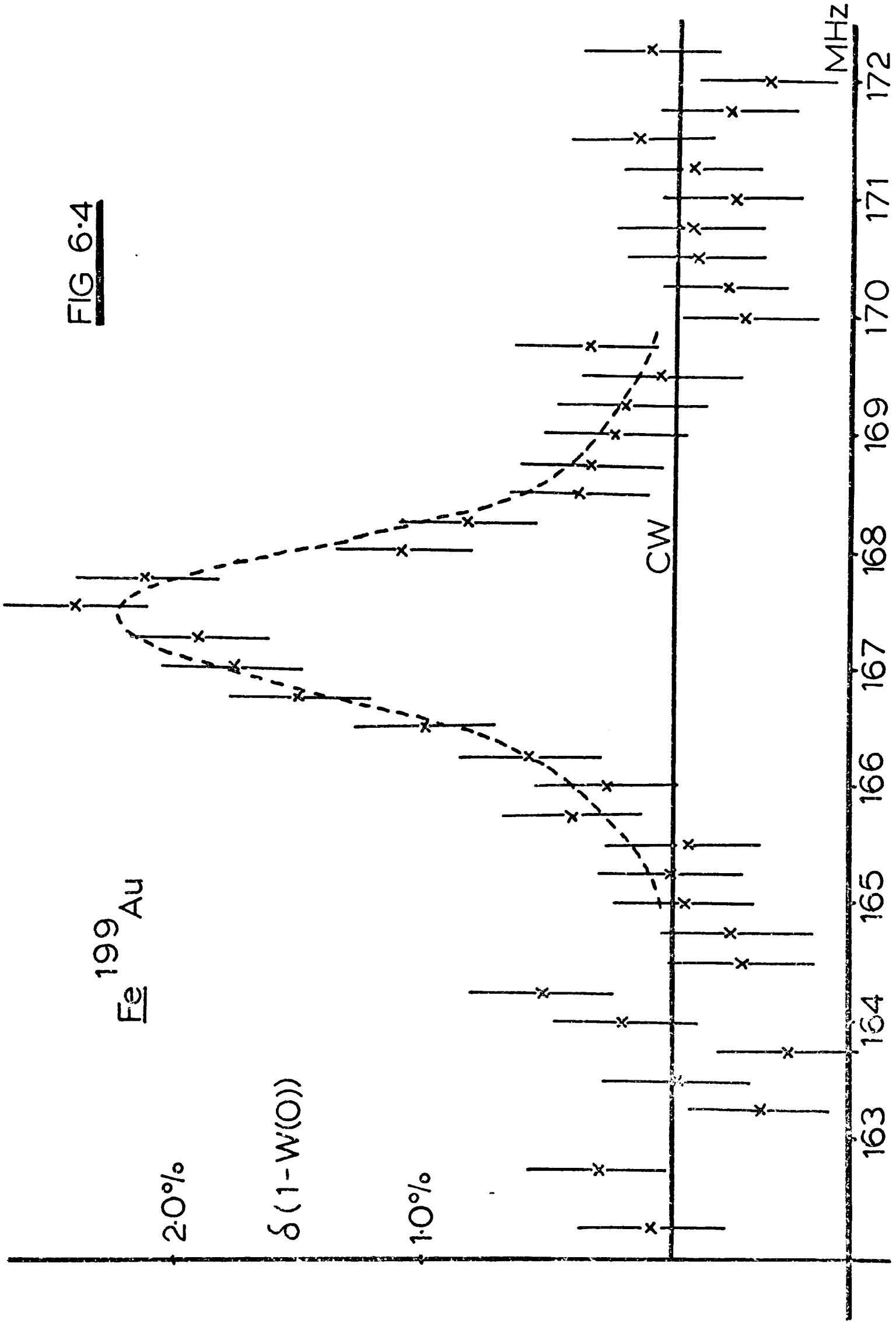
The value of $^{198}\Delta_c^{199}$ deduced from the experiments of Van der Bout et al is $-4.503 \pm 0.2\%$. The error arises almost entirely from the direct measurements of the magnetic moments, and therefore cancels out to a large extent in the comparison of this contact hyperfine anomaly with that measured in iron. The ratio of the hyperfine interaction splitting for the two nuclei in the field produced by the unpaired 6s electron of the gold atom is

$$\frac{a^{198}}{a^{199}} = 1.56535 \quad \frac{g^{198}}{g^{199}} = 1.63915(200)$$

The ratio of the resonance frequencies in iron is

$$\frac{\nu_1^{198}}{\nu_2^{199}} = 1.55217\ (100)$$

FIG 6·4


$^{199}$Au
Fe
2·0%
δ(1-W(0))
1·0%
CW
MHz
163
164
165
166
167
168
169
170
171
172

The hyperfine anomaly in the hyperfine field in the iron host is then $^{198}\Delta^{199}_{Fe} = -5.31(20)$. This indidates a Fermi-contact hyperfine field of -1453 KOe and an orbital dipolar hyperfine field of +220 ± 30 KOe, where the signs of the fields are relative to the external applied magnetic field. A complete summary of the results is shown in table 6.2.

The origin of such orbital dipolar contributions to the hyperfine field was discussed in chapter four. In the case of a gold impurity, a localised magnetic moment may arise through the action of the spin-orbit interaction on a virtual bound state of either 6p or 5d character. The calculations of Williams [84] have shown that the sign of the orbital dipolar field associated with a state of 5d character will be +ve where as a 6p state will have negative polarisation with respect to the 3d electrons and would therefore give a negative orbital hyperfine interaction. Since the spin-dipolar interaction is only of second order in the spin-orbit interaction perturbation it is neglected in comparison with the orbital dipolar term in the analysis of the experimental results.

The sig n of the observed orbital dipolar hyperfine field suggests that it is associated with a virtual state of 5d character. Using the results obtained in chapter four the orbital dipolar magnetic hyperfine field for a 5d electron is given by

$$H_D = \pm 2\beta \left\langle r_{5d}^{-3} \right\rangle_{\ell} \frac{2\xi}{\Delta} \cdot \eta$$

$\eta$ is a factor representing the number of electrons contributing to the unquenched orbital moment. This relationship must be considered in the light of the constraint imposed by the observed upper limit on the electric quadrupole interaction. The interpretation of the electric quadrupole Hamiltonian presented in chapter four is considered in detail in chapter seven, the result only bei ng used here.

$$q = -\left\langle r_q^{-3} \right\rangle \frac{17}{7} \frac{\zeta^2}{\Delta^2} \eta$$

The experimental result gives a limit for P which provides a limit on the value of eqQ for $^{199}$Au in iron.

$$eqQ \lesssim 8 \times 10^{-21} \text{ ergs.}$$

The quadrupole moment of $^{199}$Au has not been measured, but an adequate estimate can be made by comparison with the measured quadrupole moment of $^{197}$Au of 0.58b. The values of $\left\langle r_{5d}^{-3} \right\rangle_l$ and $\left\langle r_{5d}^{-3} \right\rangle_q$ present a problem. The value of $\left\langle r_{5d}^{-3} \right\rangle_q$ contains the Sternheimer antishielding parameter and can be expected to differ from $\left\langle r_{5d}^{-3} \right\rangle_l$ by a corresponding factor. Because the 5d wavefunctions penetrate the gold core the factor will not be as large as for an external crystal-field electric field gradient. The magnitude of $\left\langle r_{5d}^{-3} \right\rangle_l$ is difficult to estimate because of the uncertainty in the detailed shape of the 5d wavefunctions on the gold atom. A value of 10 a.u has been calculated by Clogston for the 5d orbitals of platinum but gives only a rough guide to the order of magnitude to be expected [85].

A rough estimate of $\zeta/\Delta$ can be made if the assumption is made that $\left\langle r^{-3} \right\rangle_l / \left\langle r^{-3} \right\rangle_q \simeq 1$. The orbital dipolar and electric quadrupole estimates then lead to the two expressions

$$\frac{\zeta^2}{\Delta^2} \left\langle r^{-3} \right\rangle \eta \lesssim 4.5 \times 10^{-2} \text{ a.u} \qquad \frac{\zeta}{\Delta} \eta \left\langle r^{-3} \right\rangle = 8 \times 10^{-1} \text{ a.u}$$

$$\text{Then } \frac{\zeta}{\Delta} \gtrsim 0.5 \times 10^{-1}$$

Due to the uncertainty in the estimate of $\left\langle r^{-3} \right\rangle_{5d}$ it is more realistic to give a limit for $\eta \left\langle r^{-3} \right\rangle_l$ of $\gtrsim 10^{26}$ cm$^{-3}$ than to give $\eta$ alone. The order of magnitude for the unquenched orbital moment calculated by Fox and Stone from the previous experiments was $\sim 0.1\ \mu_B$, but with the results from this more recent experiment, the probable values of $\left\langle r^{-3} \right\rangle_l$

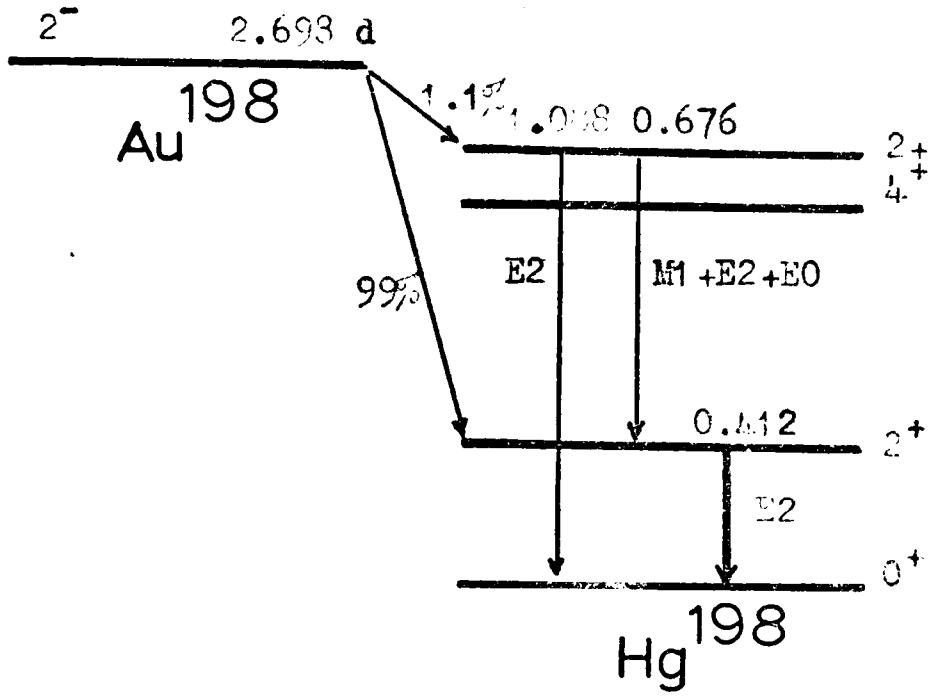
and $\xi_0/\Delta$ suggest that this may be an underestimate. The value of $\langle r^{-3} \rangle_1$ appropriate for the 5d orbitals of gold in an iron lattice may be considerably different from the value for atomic platinum because of the large value of Z = +3. The gold atom may tend to have a triply ionised electronic structure, with the excess charge shielded by the less localised 5d orbitals of a virtual bound state. The value of $\langle r^{-3} \rangle_1$ varies strongly with the degree of ionisation, therefore a mean value over all the 5d orbitals will be difficult to calculate.

## 6.3 N.M.R./O.N. of $^{199}$Au and $^{198}$Au in Cubic Cobalt

As a continuation of the measurements in the iron host, the same two isotopes of gold have been studied in cubic cobalt and nickel hosts. This has the two-fold purpose of investigating the contributions to the hyperfine interaction and of studying, in more detail than has previously been possible, the variation of the components of the magnetic interactinn as the saturation magnetic moment of the host lattice changes.

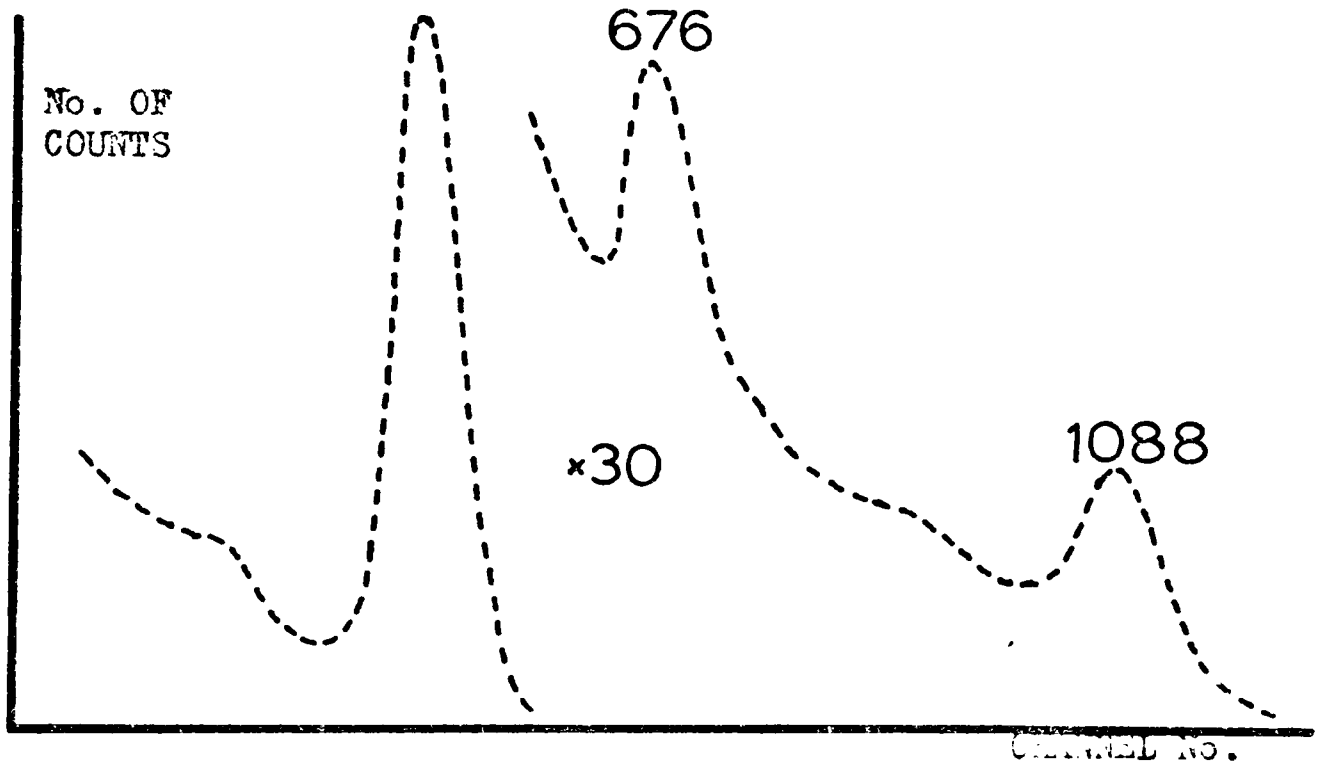
The measurements of Grant, Kaplan, Keller and Shirley [ 86 ] using the Mossbauer technique on $^{197}$Au, and Shirley et al [ 87 ] using the nuclear orientation of $^{198}$Au, give results for the total hyperfine field for gold in cobalt of -990(120) and -780(80) KOe respectively. Both these measurements used a cobalt, host, given a heat treatment to produce a predominantly cubic lattice structure. The major difficulty in the determination of the hyperfine field from nuclear orientation measurements in cobalt is the large magnetic field required to saturate the magnetisation of the polycrystalline cobalt host. A preliminary nuclear orientation experiment using a dilute impurity of $^{198}$Au, to get an improved estimate of the hyperfine field, showed a variation with the applied field up to 12 KOe. The decay scheme and gamma-ray spectrum of $^{198}$Au are shown in

# FIG 6·5




DECAY SCHEME OF $^{198}$Au

412



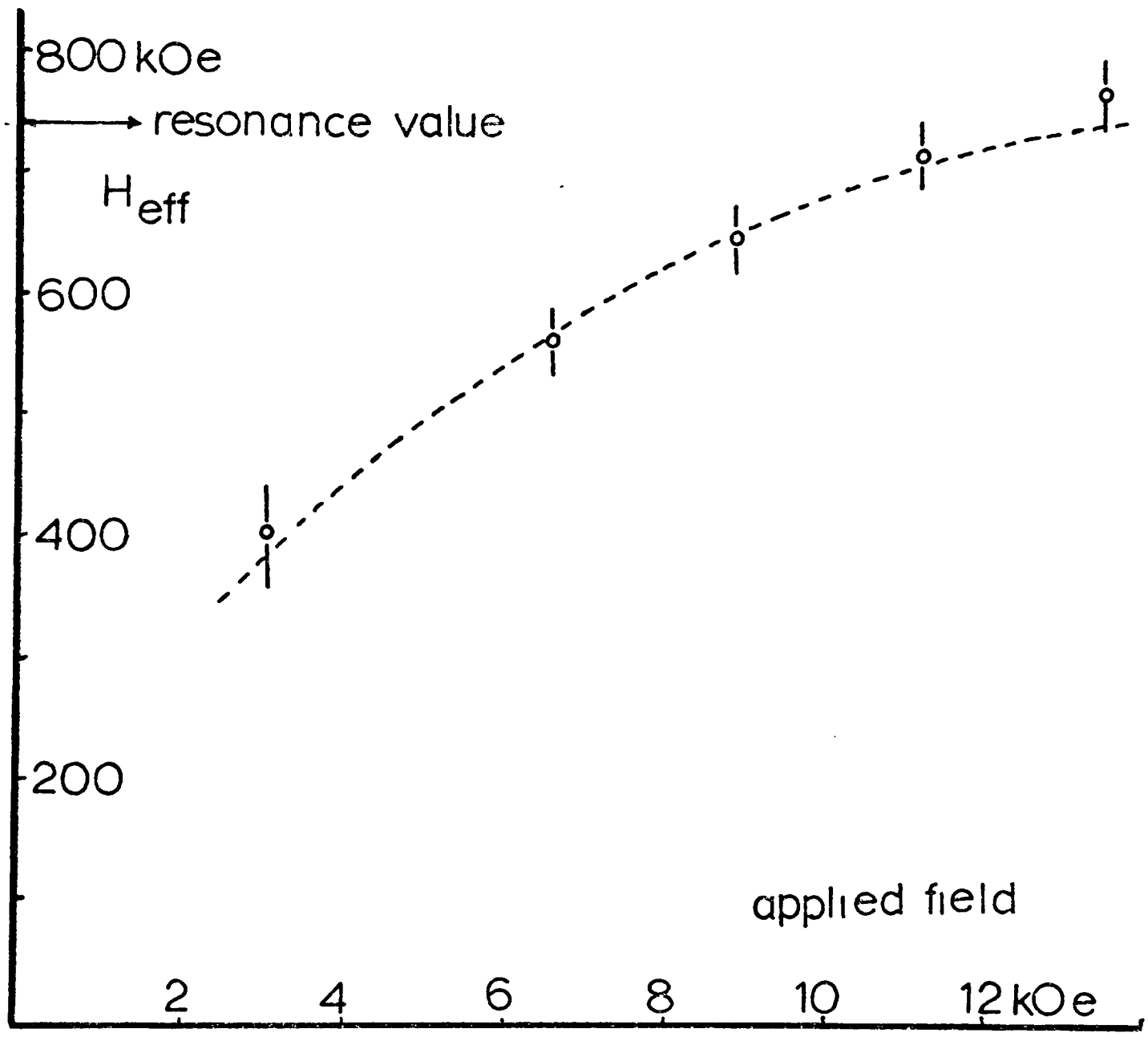

GAMMA RAY SPECTRUM OF $^{198}$Au FROM A NaI. DETECTOR SHOWING THE 412keV PEAK USED FOR THE RESONANCE DETECTION AND THE WEAK HIGH ENERGY TRANSITIONS.

Fig.6.5. The 412 KeV gamma shows large orientation anisotropies and was used to investigate the apparent hyperfine field as a function of the applied field. The results are shown in Fig.6.6 and show that for 95% saturation of the host magnetism, a field of greater than 12kOe is required. For the resonance experiment a compromise must be reached between the attenuation of the gamma ray anisotropy, through incomplete saturation of the magnetisation, and the reduced enhancement factor for the R.F. field associated with a large external magnetic field.

The samples for the resonance experiment were produced by thermal diffusion of the active gold into 1 μm cobalt foils from an electroplated layer of gold on the surface. The diffusion temperature of 900°C for 10 hrs also served to anneal the cobalt foil, producing almost complete transformation to the cubic phase [88]. The $^{198}Au$ was obtained by neutron irradiation of stable $^{197}Au$. A small quantity of order 1 mg was irradiated at a flux of $10^{12}$ n/sec/cm$^2$ for one day; the active gold being dissolved in aqua regia and the solution boiled to dryness. The residue was taken up in 3M HCl from which the active gold was plated onto the sample. The sample preparation for the samples containing $^{199}Au$ was very similar, except that the active gold was already in a 4M HCl solution.

Although the incomplete saturation of the host magnetisation in small applied fields is a serious handicap in the interpretation of nuclear orientation measurements, the nuclear magnetic resonance position will not be influenced in a direct way by the distribution of quantisation axes. The change in the gamma ray anisotropy observed on resonance is heavily weighted by the $P_2$ and $P_4$ factors for those nuclei aligned parallel to the external field. These nuclei will see the full projection of the external field along the axis of the hyperfine interaction, and will experience a resonance at the frequency

FIG 6·6




The apparent hyperfine field as a function of the applied polarising field for $^{198}Au$ in polycrystalline cobalt

$$\nu_n = \mu \frac{(H_{eff} - H_{applied})}{Ik}$$

The variation of the resonance frequency with increasing applied field will then be linear, with a slope $\mu/I$ . The nuclear magnetic resonance of $Co^{198}Au$ at two applied field values of 2.2kOe and 8.9kOe are shown in Fig.6.7. The linearity of the variation of the resonance frequency as a function of the applied field is shown in Fig.6.8. The experimental results are compared with a line of slope corresponding to the known magnetic moment and spin of $^{198}Au$. Extrapolation to zero applied field gives the magnetic resonance frequency.

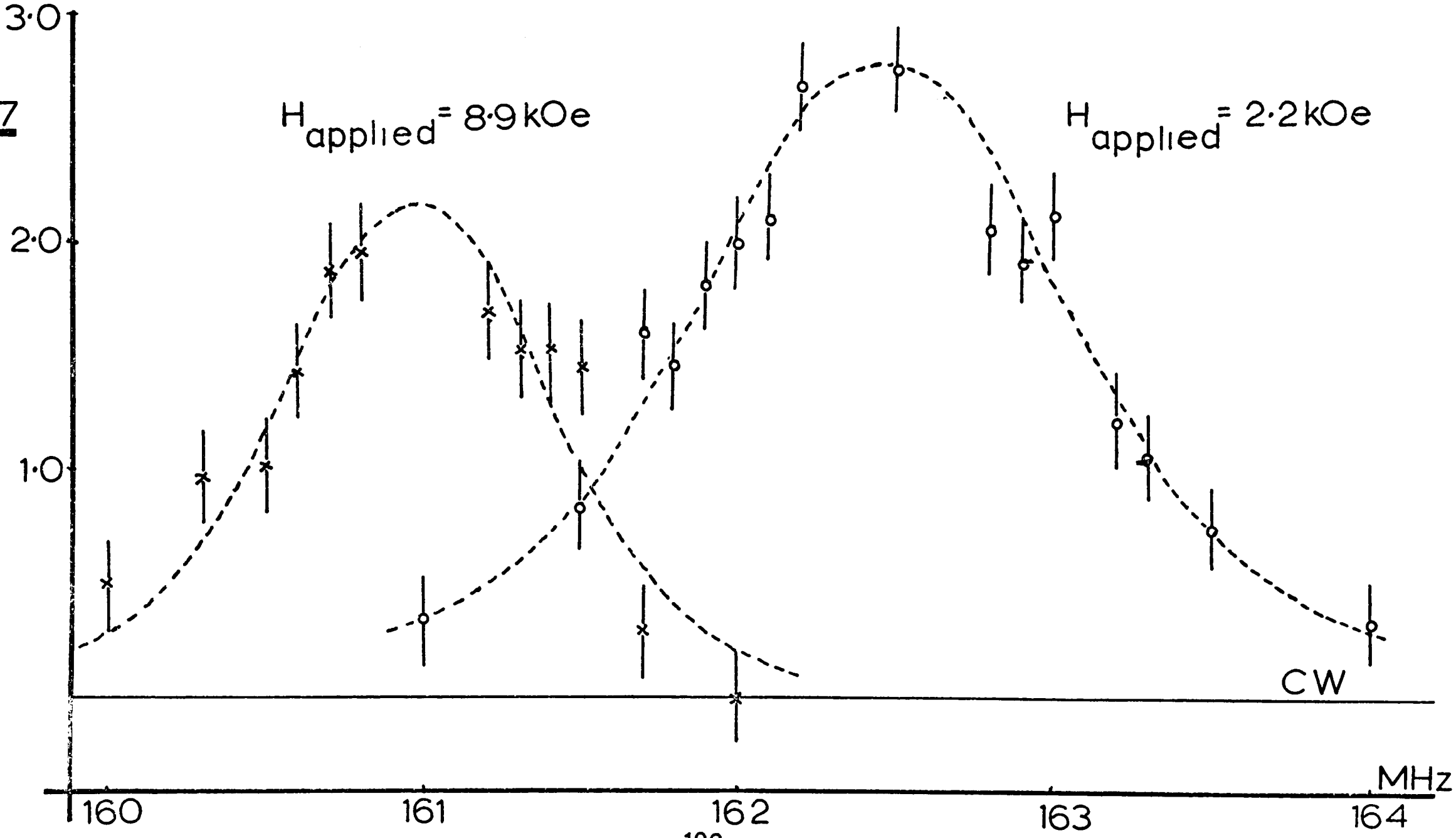
$$\nu^{Co}_{198} = 162.95\ (5)\ MHz.$$

To investigate any asymmetries is the resonance response, the frequency modulation amplitude was reduced to 300kHz. This has the effect of reducing the observed width of the resonance, and therefore increasing the sensitivity to small electric quadrupole splittings. The resonance is shown in Fig.6.7a. Any electric quadrupole splitting was too small to be observed, with the natural linewidth due to inhomogeneous broadening of 0.50% in good agreement with the systematic variation discussed in chapter 1.

The resonance of $\underline{Co}^{199}Au$ is shown in Fig.6.9. The smaller gamma-ray anisotropies shown by the $^{199}Au$ gamma rays do not give such a good signal/noise ratio at the temperatures available with chrome alum. The resonance centre frequency, corrected for the applied field, is at the frequency. 104.4(1)MHz.

The two resonance frequencies for $^{198}Au$ and $^{199}Au$ in cobalt can be used to compare the hyperfine anomaly in a cobalt host with the pure s-contact anomaly. The value of $^{198}\Delta^{199}$ in cobalt is found to be -4.8(2); smaller than that in the iron hyperfine field, but still larger than the pure s-electron anomaly of -4.5(2). The non-contact hyperfine field shown

FIG 6·7




Nuclear magnetic resonance of $^{198}Au$ in cubic cobalt

FIG 6 7(a)

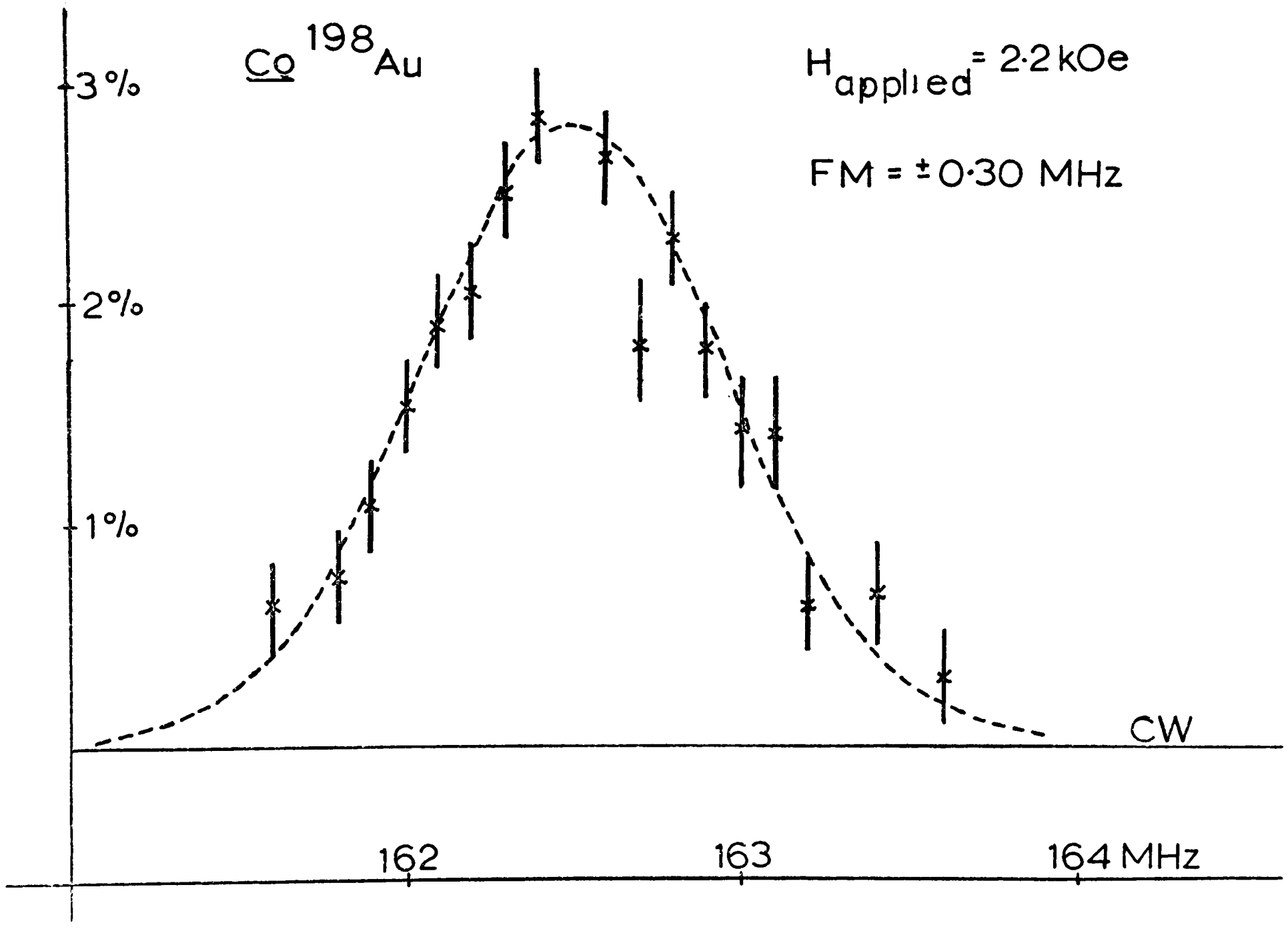


FIG 6·8

Variation of the resonance frequency of $\underline{Co}^{198}Au$ with the applied field

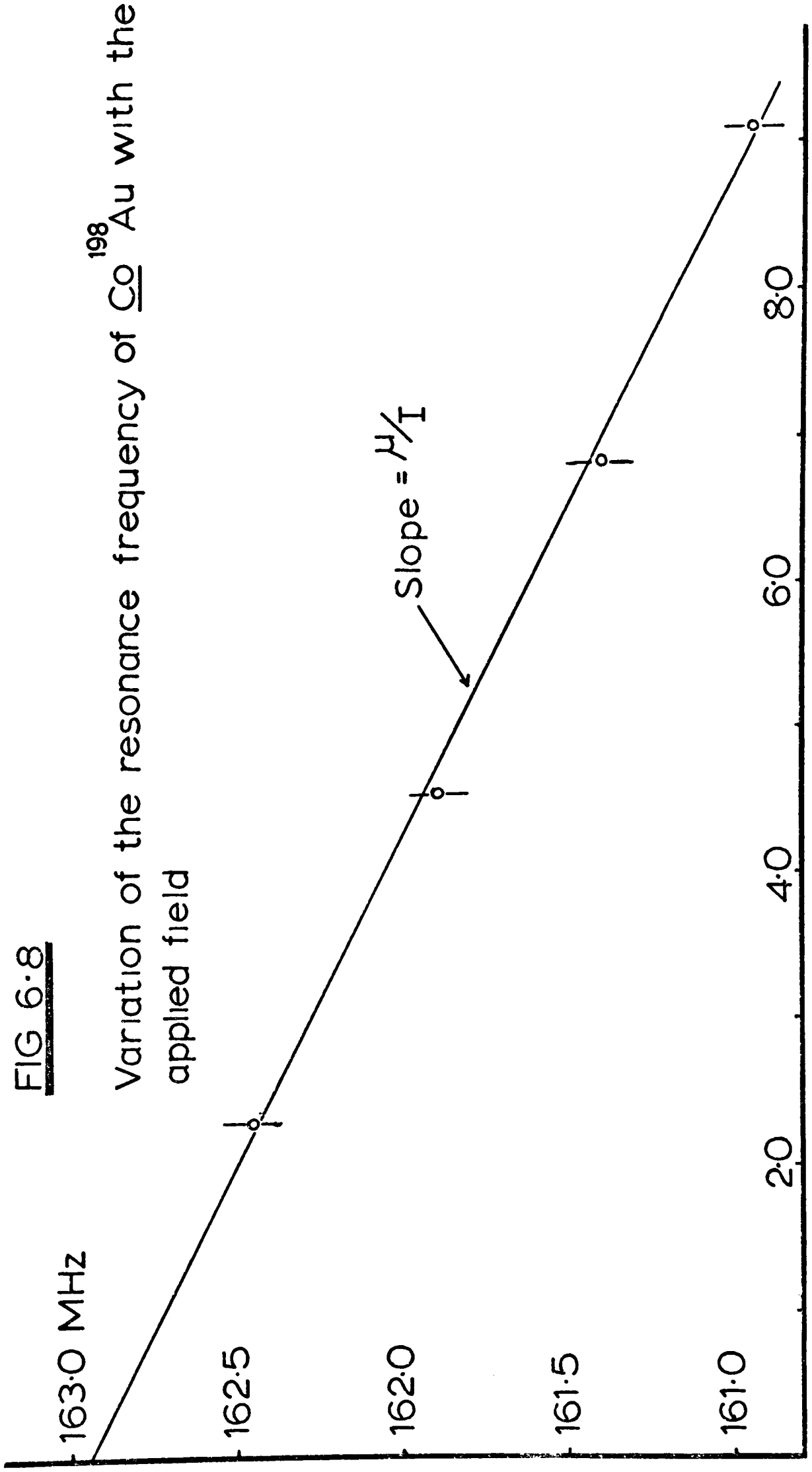
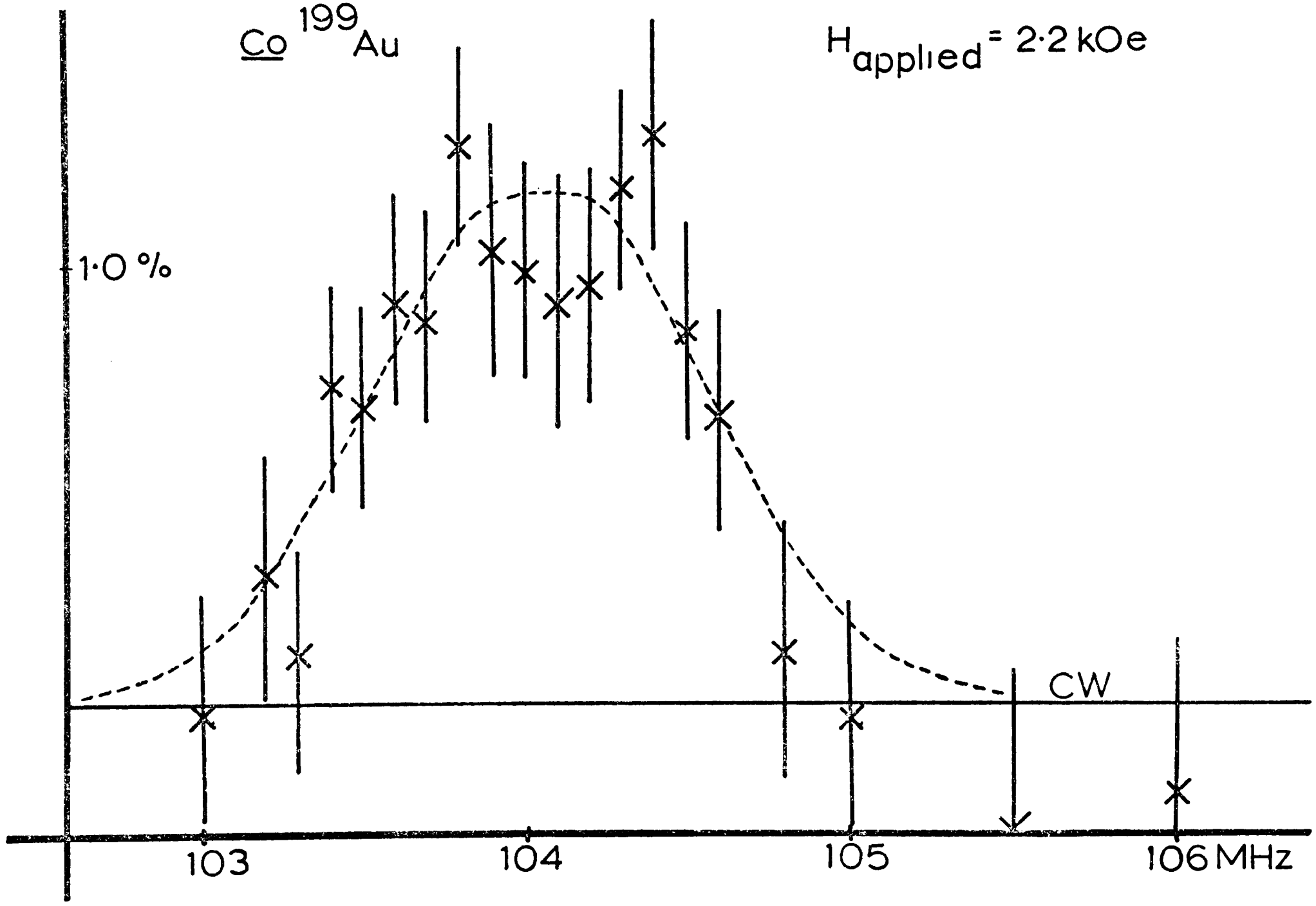


FIG 6·9



by this result is +60(30)kOe, representing 8% of the total interaction. The full analysis of the measurements is shown in Table 6.2.

A similar comparison, of the orbital dipolar field and the limit on the electric quadrupole interaction, to that for the iron host measurements would suggest the order of magnitudes:

$$\frac{\omega_Q}{\Delta} \lesssim 0.2 \qquad \eta \sim 0.1$$

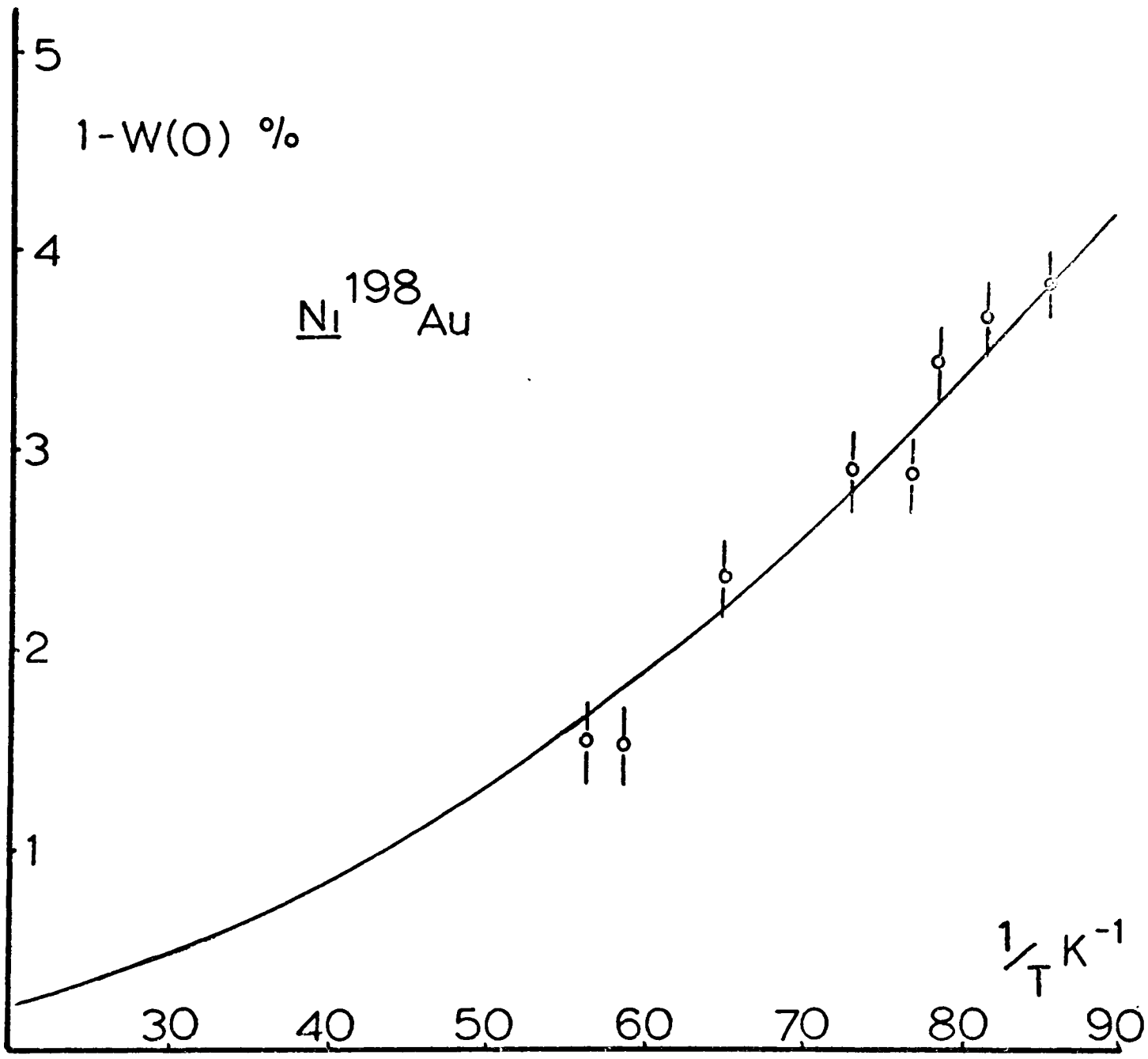
with the poor approximations for $\langle r^{-3} \rangle_1$ and $\langle r^{-3} \rangle_Q$ discussed before. These values are again in agreement with the order of magnitude expected, but a detailed analysis would require a better knowledge of the gold wavefunctions in the cobalt lattice.

## 6.4 N.M.R./O.N. of $Ni^{198}Au$

The smaller hyperfine field on gold in the nickel host reduces the sensitivity of the conventional nuclear orientation experiment. For the temperature range available from adiabatic demagnetisation of Chrome Alum, the anisotropy of the 412KeV gamma-ray of $^{198}Au$ is only of the order of 1 to 4%. Previous measurements of the hyperfine interaction have produced results of -340(60)kOe [86], 420(120) kOe [89] and -180 kOe [90]. The results of a preliminary nuclear orientation experiment are shown in Fig.6.11. The best fit indicates a hyperfine field of 360(20)kOe, indicating a frequency range of 70-90 MHz for the resonance experiment.

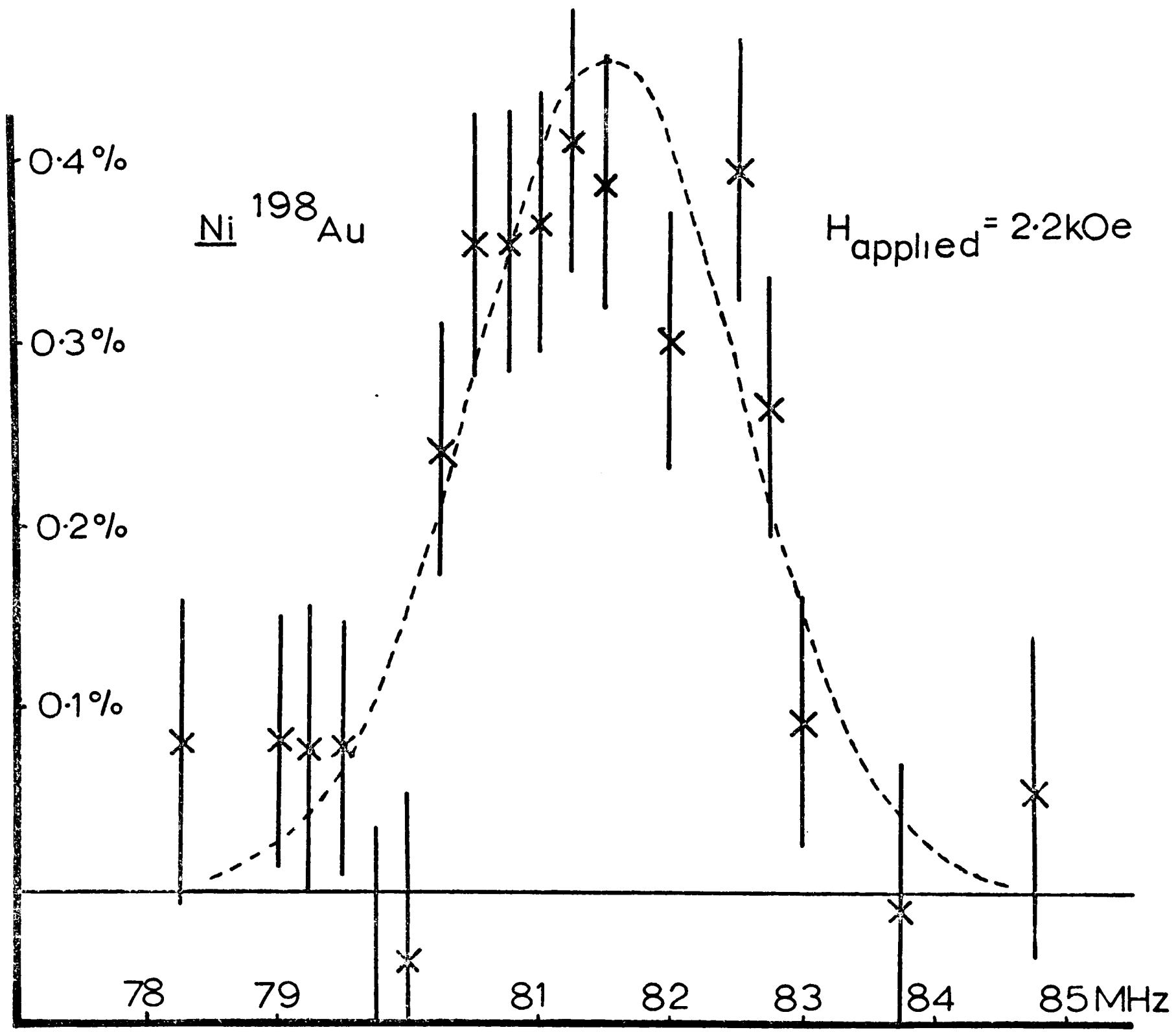
The resonance samples were prepared as for iron and cobalt, using 1μm polycrystaline nickel foils. The resonance is shown in Fig.6.12 and indicates a hyperfine field, corrected for the applied field, of -365.2(8)kOe. The observed inhomogeneous line-width of 2.5 MHz represents a much greater porportion of the hyperfine interaction energy than for any other resonance

FIG 6·10




Nuclear orientation measurements on $^{198}$Au in nickel fitted with the temperature variation for a hyperfine field of 360kOe

FIG 6·11



differing by a factor of three from the systematic behaviour of the linewidths observed for other impurities in nickel. The gold impurity concentration in the sample was 0.3 at % greater than that used for other samples because of the higher countrate required by the smaller gamma ray anisotropies. Thus concentration is getting near the solubility limit of about 1 at % and may produce additional inhomogeneous broadening due to interactions with gold neighbours. The poor signal/noise ratio makes it impossible to distinguish between a broadening associated with the higher gold concentration and a possible broadening from an unresolved quadrupole splitting. A value of P = 0.7 MHz would be sufficient to produce an apparent linewidth similar to that observed.

The increased linewidth reduces the accuracy of the measurement to such an extent that a comparison with a similar resonance of Ni $^{199}$Au would not give a useful estimate of the hyperfine anomaly. The smaller gamma-ray anisotropies shown by $^{199}$Au would also require a lower temperature than is obtainable with chrome alum to give sufficient sensitivity to observe the nuclear resonance.

Table 6.2

| Isotope | Host | $\nu_n$(MHz) | P(MH$_s$) | $^{198}\Delta^{199}$ | $H_{eff}$ | $H_c$ | $H_{O.D}$ |
|---|---|---|---|---|---|---|---|
| $^{199}$Au | Fe | 167.7(1) | $\lesssim$0.3 | | -1233(1) | -1453(30) | +220(30) |
| $^{198}$Au | Fe | 260.3(1) | $\lesssim$0.15 | -5.3(2) | -1169(1) | -1389(30) | +220(30) |
| $^{199}$Au | Co | 104.4(1) | $\lesssim$0.3 | | - 769(1) | -829(30) | + 60(30) |
| $^{198}$Au | Co | 162.95(5) | $\lesssim$0.15 | -4.8(2) | - 732(1) | -792(30) | + 60(30) |
| $^{198}$Au | Ni | 81.5(2) | $\lesssim$0.7 | | -365.2(8) | | |

## 6.5 The variation of $H_{eff}$ with the saturation moment of the Host

The greater accuracy of the resonant hyperfine field measurements in the three hosts makes possible a comparison with some of the simple theories so far proposed for the variation of the hyperfine field of an impurity with the saturation magnetic moment of the host lattice. Campbell [ 40 ] has extended the model for the conduction-electron-polarisation contact interaction, proposed by Daniel and Friedel [ 7 ] for s-p type impurities in iron, cobalt and nickel hosts, to explain the systematic variation of the hyperfine field of the 4P elements, silver to Xenon. A similar model should be appropriate for the elements in the 6s, 6p region of the periodic table. In addition to the Daniel and Friedel polarisation mechanism, Shirley has suggested an s-p and s-d mixed term [ 91 ] in the conduction electron wavefunctions. The model proposed by Campbell [ 92 ] considers this mixing $\alpha$, as proportional to the host moment $\mu_h$. Using wavefunctions of the form

$$\Psi = (1 - \tfrac{1}{2}\alpha^2)\,\Psi_s + \alpha\Psi_p$$

the contact magnetic hyperfine interaction is proportional to the s-electron density of states at the nucleus

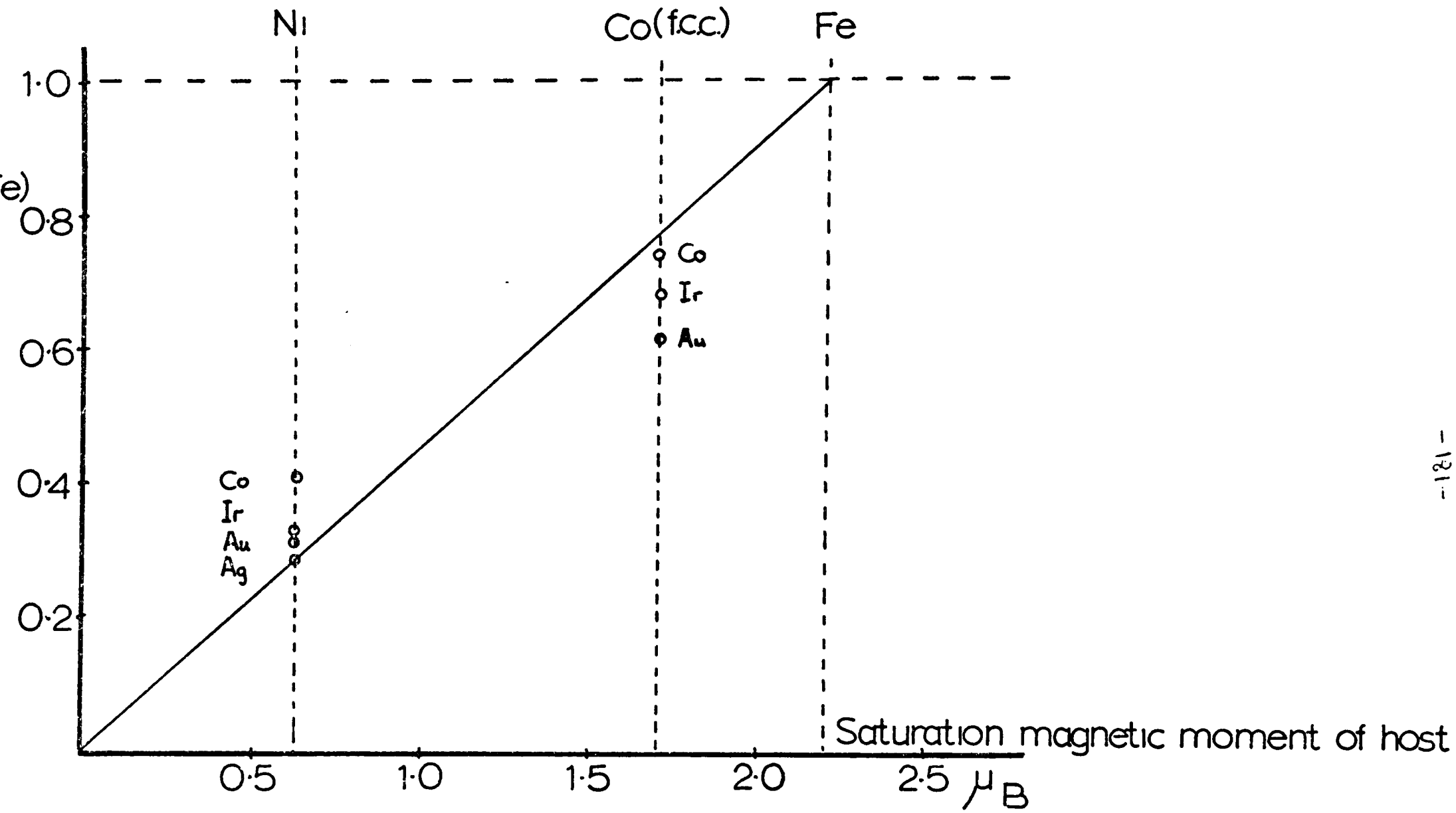
$$H_{eff} \propto |\Psi(0)|^2 = (1 - \alpha^2)\,|\Psi_s(0)|^2$$

If the core polarisation component in the hyperfine interaction is assumed to be proportional to $\mu_h$, a variation of the hyperfine field of an impurity with $\mu_h$ will then have the form

$$H_{imp} = \alpha\,\mu_h + \beta\,\mu_h^2$$

For many of the 4p type impurities, a variation of this form gives a better representation of the experimental results than the first order linear relationship.

FIG 6·12




Variation of the hyperfine fields of Ag, Au, Ir, and Co in the three cubic ferromagnetic hosts

As can be seen in Fig.6.13, such a relationship does not fit the results for gold in these three hosts. Any simple variation with the saturation moment of the host would not be expected to hold in great detail, but the results show that other factors such as the lattice spacing, and the detailed density of states of the conduction band may have a major part to play in the magnitude of the hyperfine interaction. The localised orbital moment on the gold impurity, while providing a contribution of 10% to the net hyperfine field does not appear to account for more than a small proportion of the deviation from a simple variation with $\mu_h$. It maybe of interest to see whether the hyperfine field shows a continuous variation with $\mu_h$ by alloying iron and cobalt and iron and nickel, although the local constitution of the alloys may not be regular enough for a single resonance line to be observed.

Similar results for silver, cobalt and iridium impurities are included in Fig.6.13 for comparison. The silver measurements are unique in following an apparently simple variation with $\mu_h$, but the ratio of the fields in iron and nickel may be fortuitious. A measurement in a cobalt host would be of interest, but, as for iron, the low solubility makes sample preparation very difficult.

## 6.6 Conclusions

The importance of the N.M.R./O.N. technique for the investigation of the detailed origin of the hyperfine interactions of very dilute impurities in ferromagnetic hosts is shown by the results obtained on the isotopes $^{198}Au$ and $^{199}Au$. The comparison of the orbital dipolar magnetic interaction found from the hyperfine anomaly measurements, and the limit set on the electric quadrupole splitting provides a useful indication of the electronic interactions of the impurity with the host conduction electrons. The particular cases of gold in iron and cobalt are difficult to treat theoretically because of the sensitivity of the calculations to the position of a virtual bound d-state relative to the fermi energy. The comparison of the experimental results in the magnitudes of the orbital dipolar field and electric quadrupole interaction, with the estimated values of $\zeta/\Delta$ from the spin orbit coupling parameter for 5d electrons [80] and the crystal field splitting of the $\alpha$ bands, is complicated by the uncertainty in the correct values to use for $\langle r_{5d}^{-3} \rangle_q$ and $\langle r_{5d}^{-3} \rangle_q$. The values deduced for $\zeta/\Delta$ have an uncertainty only from the ratio $\langle r_{5d}^{-3} \rangle_q / \langle r_{5d}^{-3} \rangle_1$ and agree in order of magnitude with estimated values from 0.1 to 0.5, but the magnitude of the unquenched orbital moment depends very much on the value of $\langle r_{5d}^{-3} \rangle_1$ used. A systematic study of the variation of the localised moments on impurities in the 5d series may lead to a better understanding of the electronic interactions.

# CHAPTER7

# NUCLEAR MAGNETIC RESONANCE STUDIES ON IRIDIUM IMPURITIES

## 7.1 Introduction

The hyperfine interaction of iridium isotopes in the ferromagnetic metals presents a similar situation to that of the gold isotopes. The reasons for continuing the investigation with iridium impurities are ones of convenience in both the experimental and theoretical aspects of the study. The band structure of ferromagnetic nickel and cobalt, where one spin subband of the conduction band is completely full, below the fermi level makes calculations of the shielding of the impurity excess charge easier than in iron, where both spin subbands overlap the Fermi surface. the impurity excess charge, Z, of -1 for iridium in nickel is also simpler to treat theoretically than the charge of Z, = +3 for gold in iron [ 63 ]. The work of Demangeat and Gautier [ 64 ] and Williams [ 73 ] has demonstrated the possibility of the formation of a virtual bound d -state associated with the screening of the z = -1 excess impurity charge on iridium. The large mass of the iridium impurity will also be associated with a strong spin-orbit interaction, as in gold, which will compete with the crystal field quenching of the orbital angular momentum, with the consequent additional contributions to the hyperfine interaction.

All the isotopes of iridium contain a single $2d_{3/2}$ proton, and will show large hyperfine anomalies when this provides the major contribution to the nuclear magnetic moment [ 78 ]. The isotope with an even number of paired neutrons, where this is the case, are most easily studied using the stable isotopes $^{191}Ir$ and $^{193}Ir$. The Mossbauer technique provides a method of measuring the hyperfine anomaly between the predominantly $2ds/_2$ proton ground state of $^{193}Ir$ and the first excited state of completely different magnetic character. The measurements

comparing the hyperfine anomaly in $IrF_6$ and Fe Ir have shown differences similar to those found by NMR/ON on gold, indicating a large contribution to the orbital dipolar hyperfine interaction in an iron host [ 81 ].

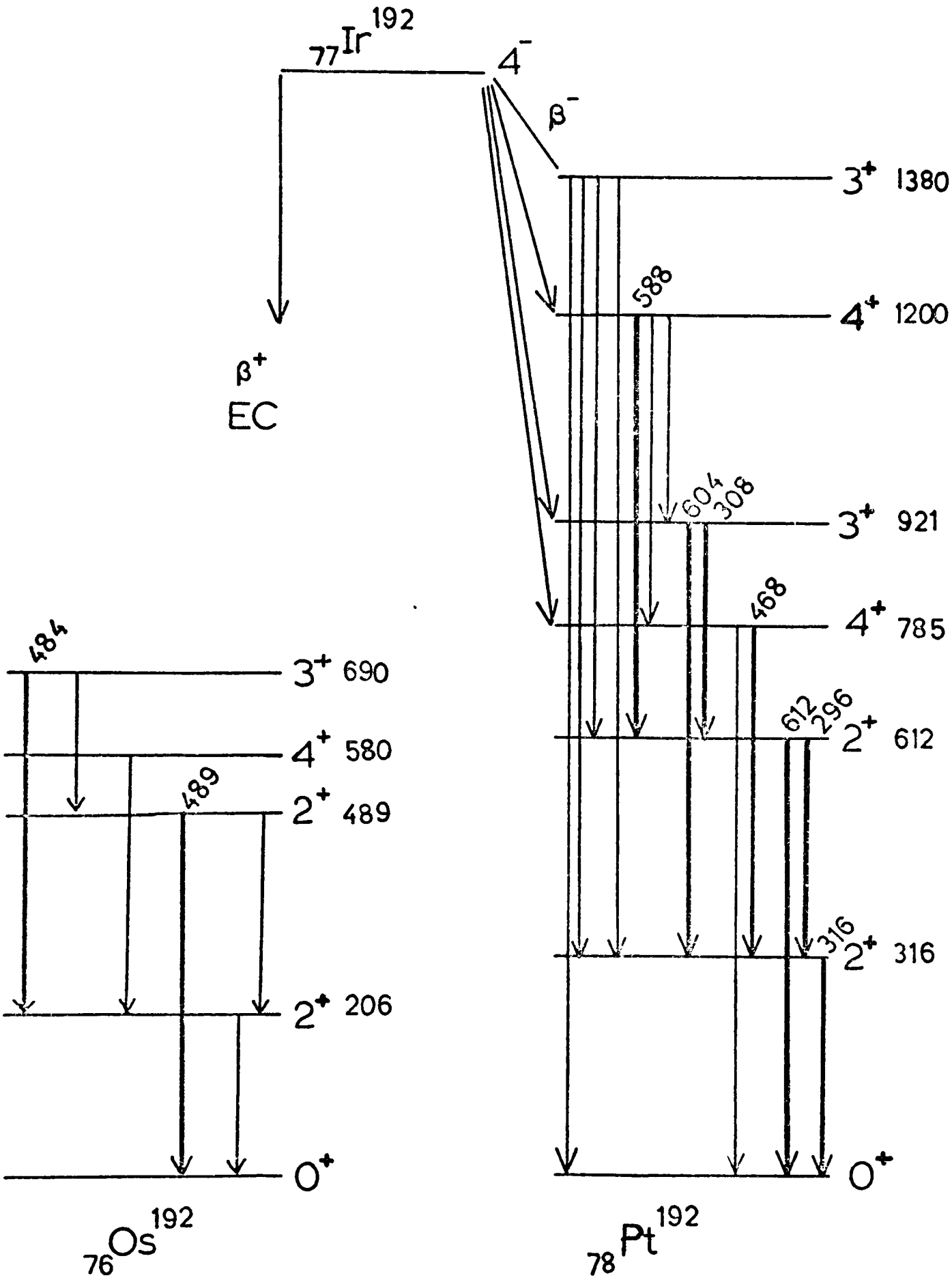
The nuclear orientation and NMR/ON experiments on iridium impurities in the ferromagnetic hosts were designed to measure the magnitude of the hyperfine interaction and the contributions from localised magnetic moment. A possible approach would be to measure the hyperfine anomaly between $^{192}$Ir and $^{194}$Ir, but the difficulty in obtaining a value for this anomaly from a pure s-electron hyperfine field means that the Mossbauer experiment is more convenient for such a measurement. The NMR/ON technique is however very sensitive to a small electric field gradient particularly in the case of iridium, since the nuclear electric quadrupole moments are large.

The 78 day isotope, $^{192}$Ir, was chosen for the nuclear orientation experiments since it shows large degrees of orientation with large gamma-ray anisotropies in all three ferromagnetic hosts. The experiments have concentrated on alloys with nickel and cobalt because more theoretical work has been done on those systems, and the metallurgy of the alloys of iridium with nickel and cobalt is better understood than that for iridium-iron alloys [ 93 ]. The measurements of the hyperfine interaction of iridium in iron have shown some large discrepancies between the resonance value and values obtained by integral techniques, due possibly to a poor solubility, and is discussed in chapter 8.

The decay scheme of $^{192}$Ir is shown in Fig.7.1. For the nuclear orientation experiments, the complex gamma-ray spectrum can be resolved using Ge(Li) detectors, but for the resonance experiments a 3" x 3" NaI detector was used. The 300KeV and 470KeV peaks on the NaI spectrum give axial gamma-ray anisotropies of 6% and 12% respectively at a temperature of 14 mK conveniently obtained by the adiabatic demagnetisation of chrome

FIG 7-1

DECAY SCHEME OF $^{192}Ir$



potassium alum, for $^{192}$Ir in the hyperfine field provided by a nickel host. In this chapter, a description of the sample preparations is followed by the NMR/ON results for $^{192}$Ir in nickel and the comparison with other techniques. The results of the resonance measurements in a cubic cobalt host are presented in section 7.5, and a general discussion of the magnetic hyperfine interaction in section 7.6.

## 7.2 Sample preparation

The production of dilute substitutional alloys by thermal diffusion depends on an adequate solubility for the impurity at the temperature of diffusion. The previous experiences of Cameron et al [ 94 ], and Reid, Shott and Stone [ 95 ] with the diffusion of iridium into iron hosts have shown that the alloys produced by thermal diffusion of the iridium below 1100$^{o}$C tend to show a non-unique hyperfine interaction at all the iridium nuclei. Recent measurements have suggested that even iridium-iron alloys produced at higher temperatures do not show a simple hyperfine interaction. The discrepancy between the nuclear orientation measurement s of Reid et al and the recently reported measurement of the hyperfine field of iridium in iron by NMR/ON is discussed in chapter eight [ ]. The solubility of iridium in nickel appears to be much higher than in iron, with a value of 1 at % at 1000$^{o}$C reported by Hanson [ 42 ]. No evidence of the poor alloy reproducibility, as for Fe Ir, has been reported, suggesting that iridium forms a well-behaved substitutional alloy with nickel. Because of this more reliable behaviour of NiIr systems, the NMR/ON measurement of the hyperfine interaction has been used to analyse the nuclear orientation measurements of $^{192}$Ir in nickel for the multipolarities of the beta and gamma transitions. These results are presented in chapter eight with a comparison with other measurements by different techniques and previous measurements from FeIr alloys.

The iridium radioactivity was obtained in the form $IrCl_6$ in solution in 4M HCL, with a specific activity of 2 → 12 mCi/mg, enabling samples to be produced for the resonance experiments containing 10 → 20 μCi of $^{192}Ir$, while maintaining an impurity concentration of less than $10^{-1}$ at %. Polycrystalline samples of NiIr were prepared by thermal diffusion from a surface deposit of $IrCl_6$ at 1000°C in an atmosphere of hydrogen for 10 → 20 hrs. The deposit of $IrCl_6$ was obtained by evaporating to dryness a few drops of the solution in 4M HCl on the surface of the nickel foil. At 1000°C the hydrogen reduces the salt to metallic iridium, which is then free to diffuse into the nickel host. Vacuum deposited polycrystalline nickel foils of thickness 1 μm were used for ease of handling and resonance sensitivity. The diffusion time and temperature were found sufficient to diffuse the iridium uniformly throughout the foil.

An approximate estimate of the magnitude of the magnetic hyperfine interaction was made from the temperature dependencies of the anisotropies shown by the 468 KeV gamma-ray, which has a well known gamma transition multipolarity, and measured decay parameters for the preceeding beta transition from the experiments of Reid et al. These preliminary orientation measurements suggested a region of search for the resonance around 150 MHz. Observing the anisotropy of the 468 KeV gamma-ray as a function of frequency, the polycrystatine samples showed a small broad resonance at about 166 MHz, but the poor degree of the destruction of the anisotropy on the resonance and broad line made an accurate measurement very difficult.

One possible reason for the unexpected width of the resonance and the small resonance destruction of the anisotropy could have been an anisotropic electric quadrupole interaction in the polycrystalline host. For this reason, several samples for resanance were prepared in single crystals of nickel. Using a single crystal host reduces the inhomogeneous broadening

of the resonance line [ 96 ], and enables the hyperfine interaction to be studied as a function of the angle of the crystal orientation with respect to the external polarising field. A nickel single crystal was cut into 1 mm thick slices with the faces of the slices normal to a [110] axis. The plane of the surface will then contain a [100], [110] and a [111] crystallographic axis. The slices used were circular discs of diameter 0.5 cms. The axis of magnetisation could be changed with respect to the crystal symmetry by rotating the slices with respect to the polarising field, while maintaining a sufficiently small and constant demagnetising field in the samples. The surface was prepared by electropolishing in 5.5% $H_2SO_4$ and the crystals oriented by X-ray diffraction.

The RF skin depth requires that for the resonance experiment, the iridium impurity should lie in a thin surface layer of depth $\sim$ 1 μm. This was achieved by controlled diffusion of the iridium from the surface deposit of $IrCl_6$. The solution of the diffusion rate equation, from Fick's law,

$$\frac{dn}{dt} = -D\frac{d^2n}{dx^2}$$

with the boundary conditions imposed by the initial impurity distribution, can be written in terms of a concentration distribution at time t of the form;

$$n(x) = Ae^{-X/\sqrt{Dt}}$$

The diffusion constant, D, is a rapidly varying function of the temperature. The diffusion rate in the single crystal was found to be very much slower than that in polycrystalline material, presumably because of the absence of the rapid diffusion in grain boundaries. The iridium concentration distribution as a function of the depth from the crystal

Spectrum of $^{192}Ir$ from a NaI detector showing energy windows used for resonance detection

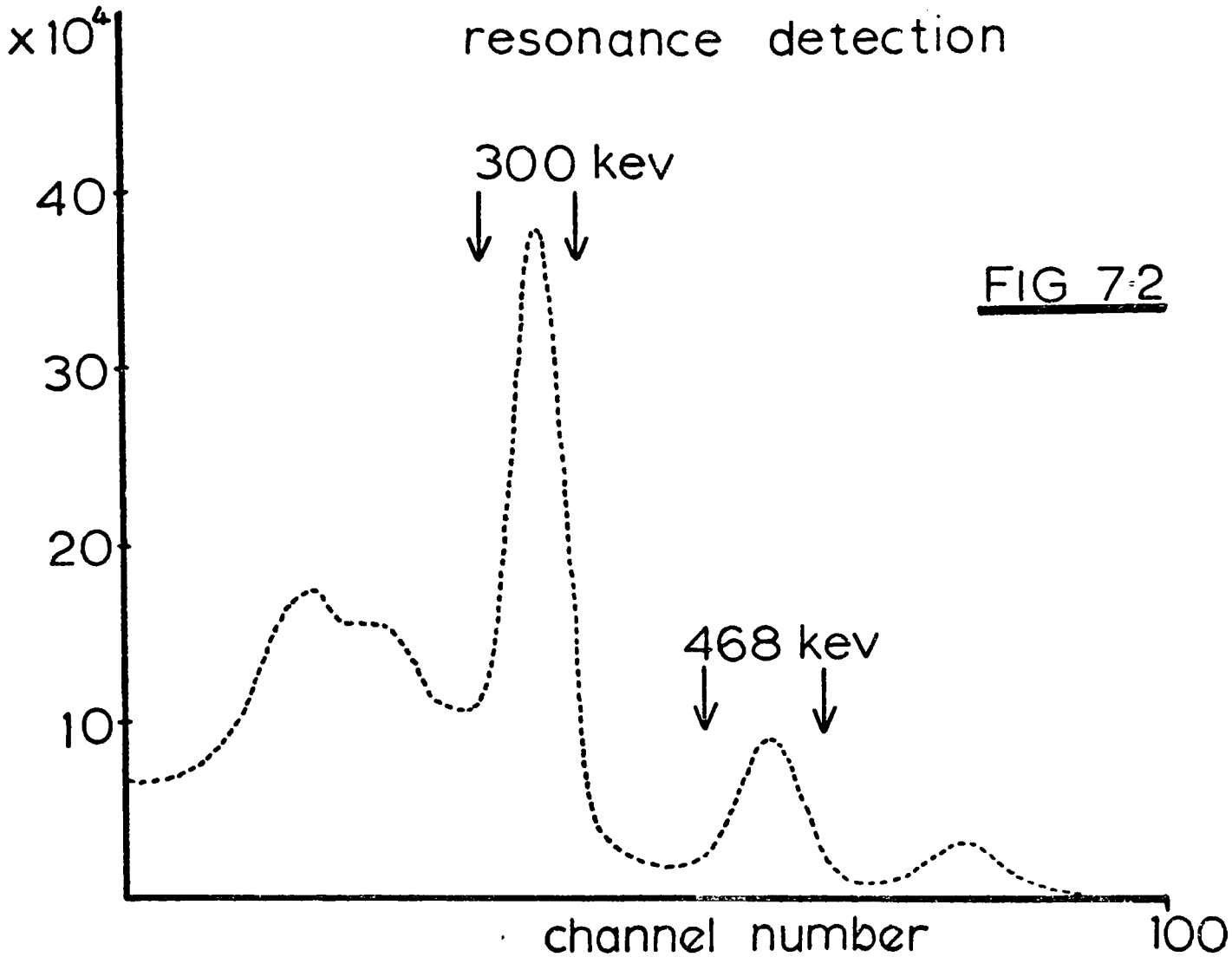



FIG 7·2

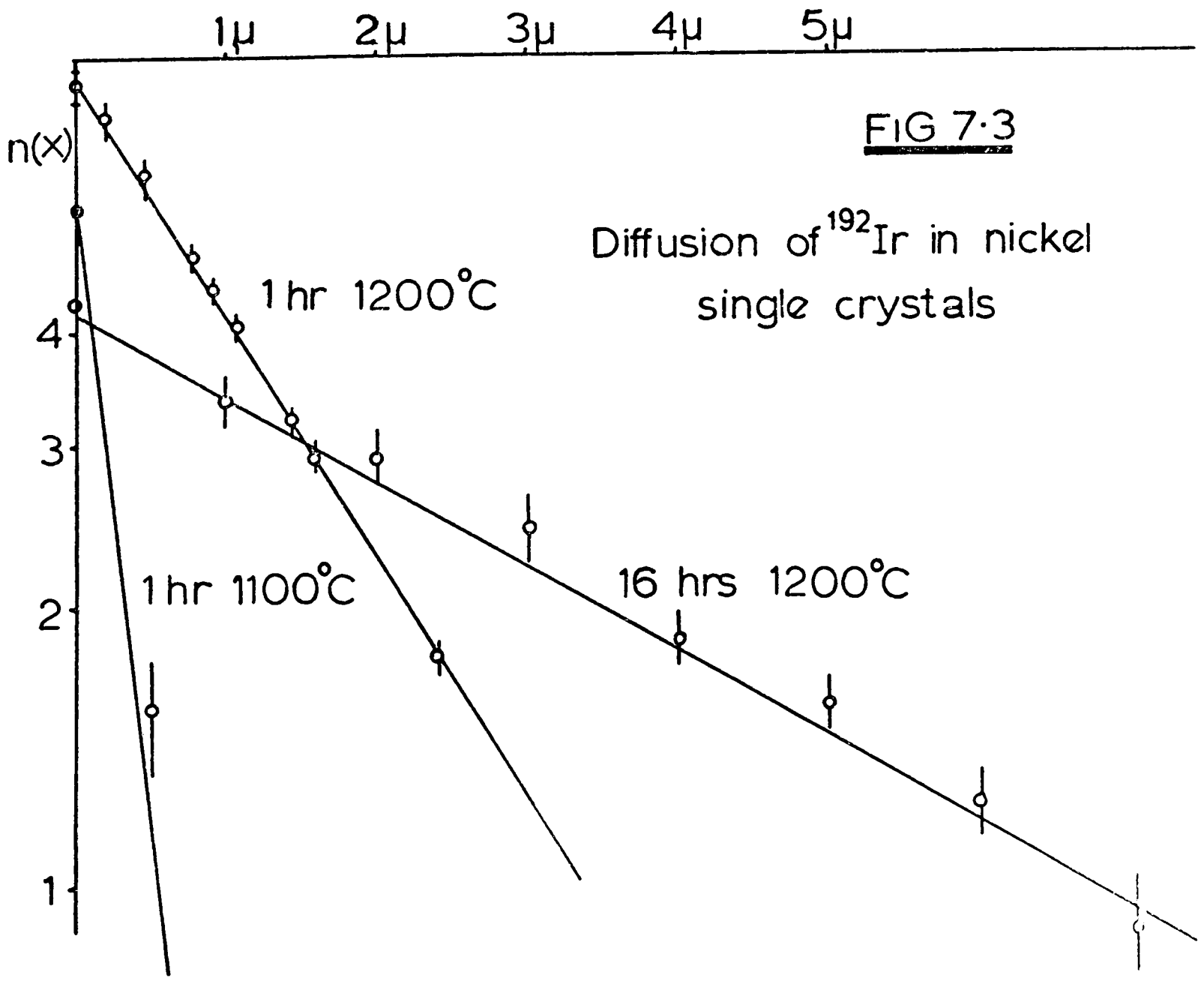



FIG 7·3

Diffusion of $^{192}Ir$ in nickel single crystals

surface could be conveniently measured by monitoring the radioactivity of the sample as the surface was electropolished away at a known rate. The distribution is shown in Fig.7.2 for several diffusion times and temperatures. The skin depth at 150 MHz will be of the order of 1 μm, therefore samples in which a large proportion of the impurity was within 1 μm of the surface were used. The best conditions seemed to be 1 hr at 1200°C producing a distribution of 'half depth' of 1.1 μm.

## 7.3 NMR/ON measurements on $Ni^{192}Ir$

Because of their higher efficiency, Na.I detectors were used for the resonance experiments. The spectrum is shown in Fig.7.3 with the energy windows set by the single channel analysers. Both the 300 KeV and the 468 KeV peak were monitored as a function of the RF frequency, and the resonance effect measured as the percentage change in the anisotropy between alternate FM and carrier wave counts for both peaks. Three samples of varying concentration, but similar impurity distribution depths of order 1 μm, were studied, all giving very similar results. The resonance responses as a function of frequency for two crystalline directions are shown in Figs.7.4 and 7.5, with an RF power level of 0.4V. In both cases the asymmetric resonance line is characteristic of the predicted NMR/ON line, split by a small quadrupole interaction. The data shown are from the 468 KeV gamma-ray peak, but the 300 keV peak gave identical results, (Fig.7.7) but with slightly worse statistical errors because of the smaller thermal equilibrium anisotropies. Data was also taken from an equatorial counter, with the resonance observed as a decrease in the count-rate. If the electric quadrupole interaction produces a splitting of the nuclear resonance line such that only one transition is observed at a time, the comparison of the axial and equatorial resonance effects can be used to determine which transition is being observed, because of the different relative sizes of the changes in $B_2$ and $B_4$; but, in this case, the splitting

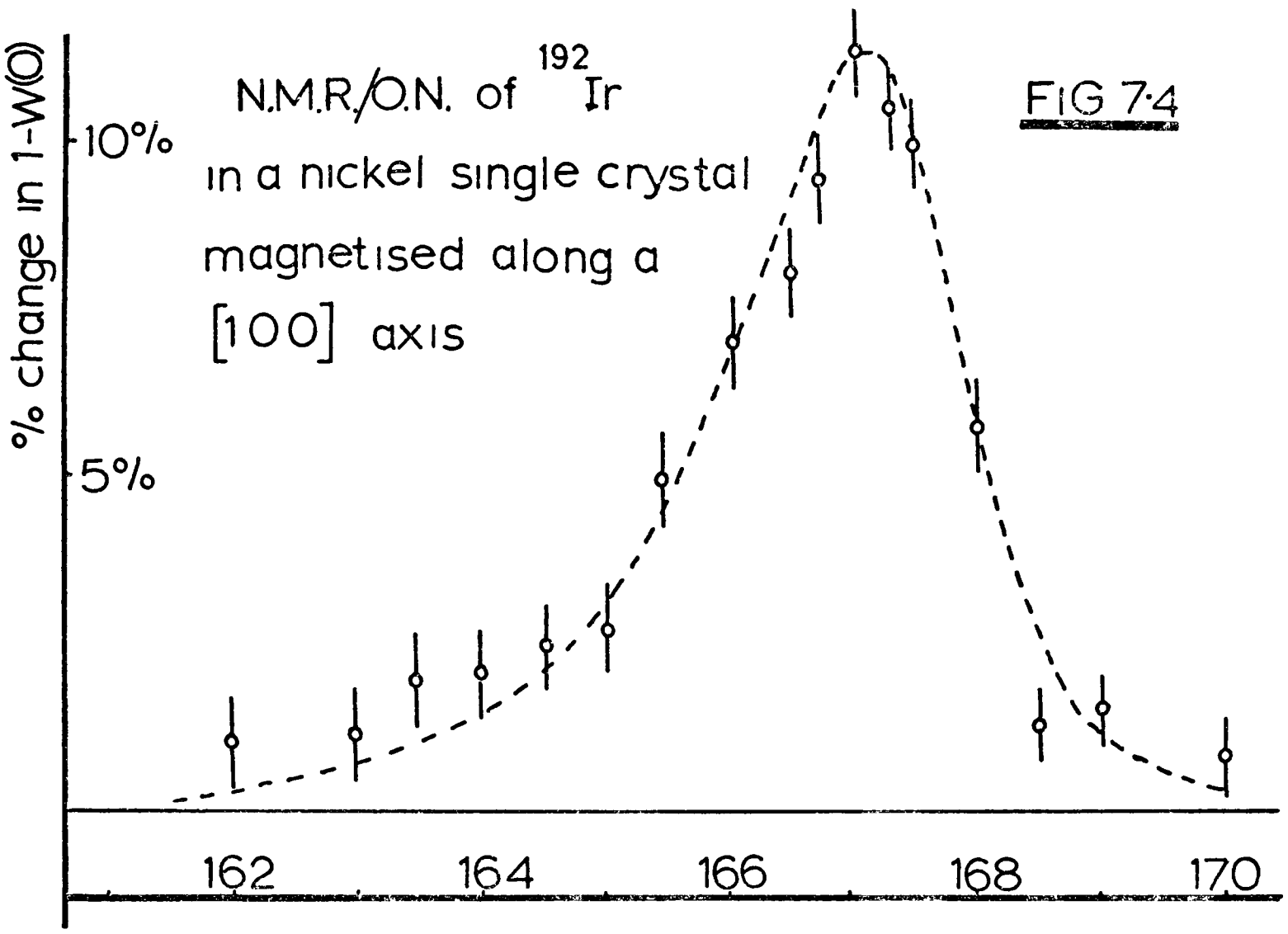

% change in 1-W(0)
10%
5%
N.M.R./O.N. of $^{192}$Ir
in a nickel single crystal
magnetised along a
[100] axis
162
164
166
168
170

FIG 7·4

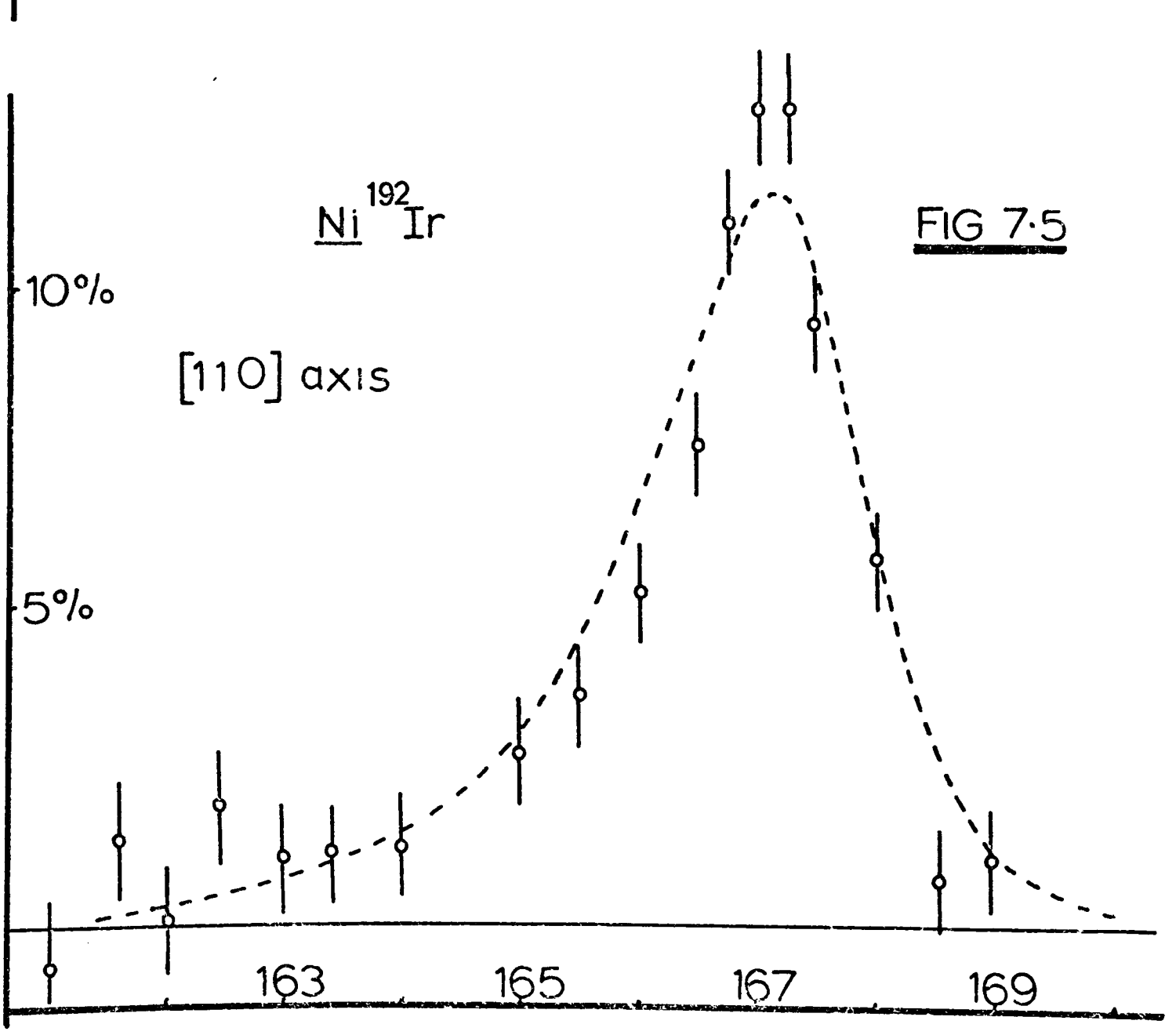

Ni $^{192}$Ir
10%
5%
[110] axis
163
165
167
169

FIG 7·5

is comparable with the inhomogeneous broadening and the amplitude of the frequency modulation, and an averaged ratio of $\frac{\Delta W(\pi/2)}{\Delta W(0)} = 0.48$ was obtained.

The experimental results can be accurately reproduced by the computed response at 14 mK for a value of P of 0.30 ± 0.05 MHz, with an inhomogeneous linewidth of 0.90 ± 0.10 MHz. The linewidth can be estimated from the high frequency end of the resonance line where only one magnetic substate transition provides a large contribution to the resonance effect. The best fit to the resonance curve gives a value for $\nu_0$, representing the magnetic interaction, of 165.45 ± 0.10 MHz. This fit, and the curves for other values of P are shown in Fig.7.6. The maximum destruction of the anisotropy with a frequency modulation of ± 400 kHz varied from 12% to 18% of the thermal equilibrium anisotropy for the three samples used representing about 30-40% of the nuclei reaching saturation. This is smaller than that calculated for the complete saturation of the resonance of all the impurity nuclei, but can be explained by an RF skin depth of order 0.5 μm with the RF power level used. With the estimated relaxation time, this would only saturate the resonance of nuclei within about 0.8 μm from the surface, the other nuclei giving a smaller resonance effect.

The importance of the spin-lattice relaxation mechanisms on the observed nuclear magnetic resonance effect when the resonance line is split by a small electric quadrupole interaction was shown in chapter five. For the greatest sensitivity to the electric quadrupole splitting the anisotropy changes should be observed after a time, t, long compared with the relaxation time. The relaxation time of $^{192}$Ir in nickel at 14 mK was estimated as less than 20s from the time taken for the re-establishment of the full thermal equilibrium anisotropy when the frequency modulation is switched off. This is consistent with the measurement of 2.2 ± 0.2 secs at 30 mK by Eska et al [97]. The resonance measurements on the single crystal samples

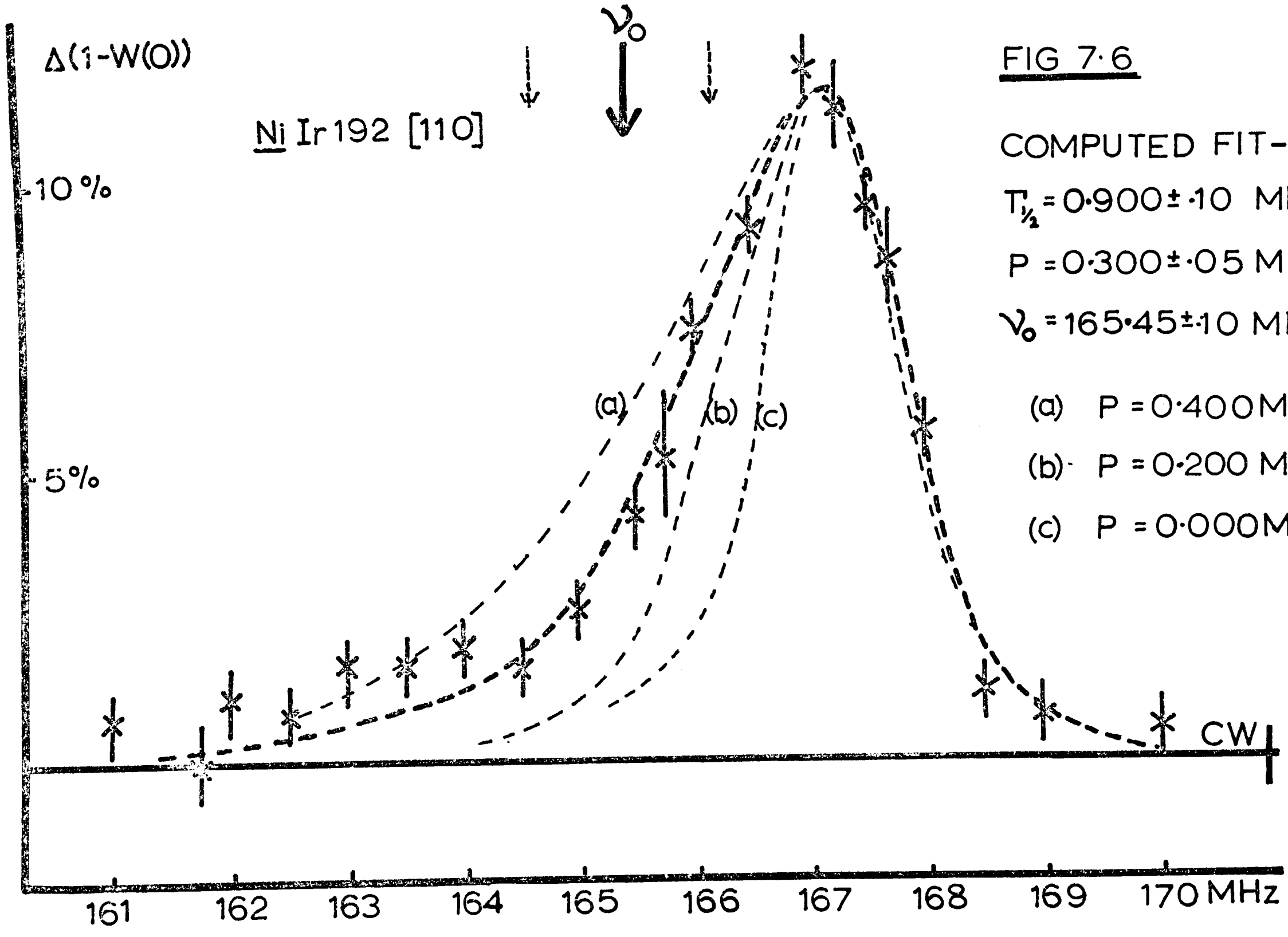



FIG 7·6

COMPUTED FIT---

$T_{1/2}$ = 0·900 ± ·10 MHz

P = 0·300 ± ·05 MHz

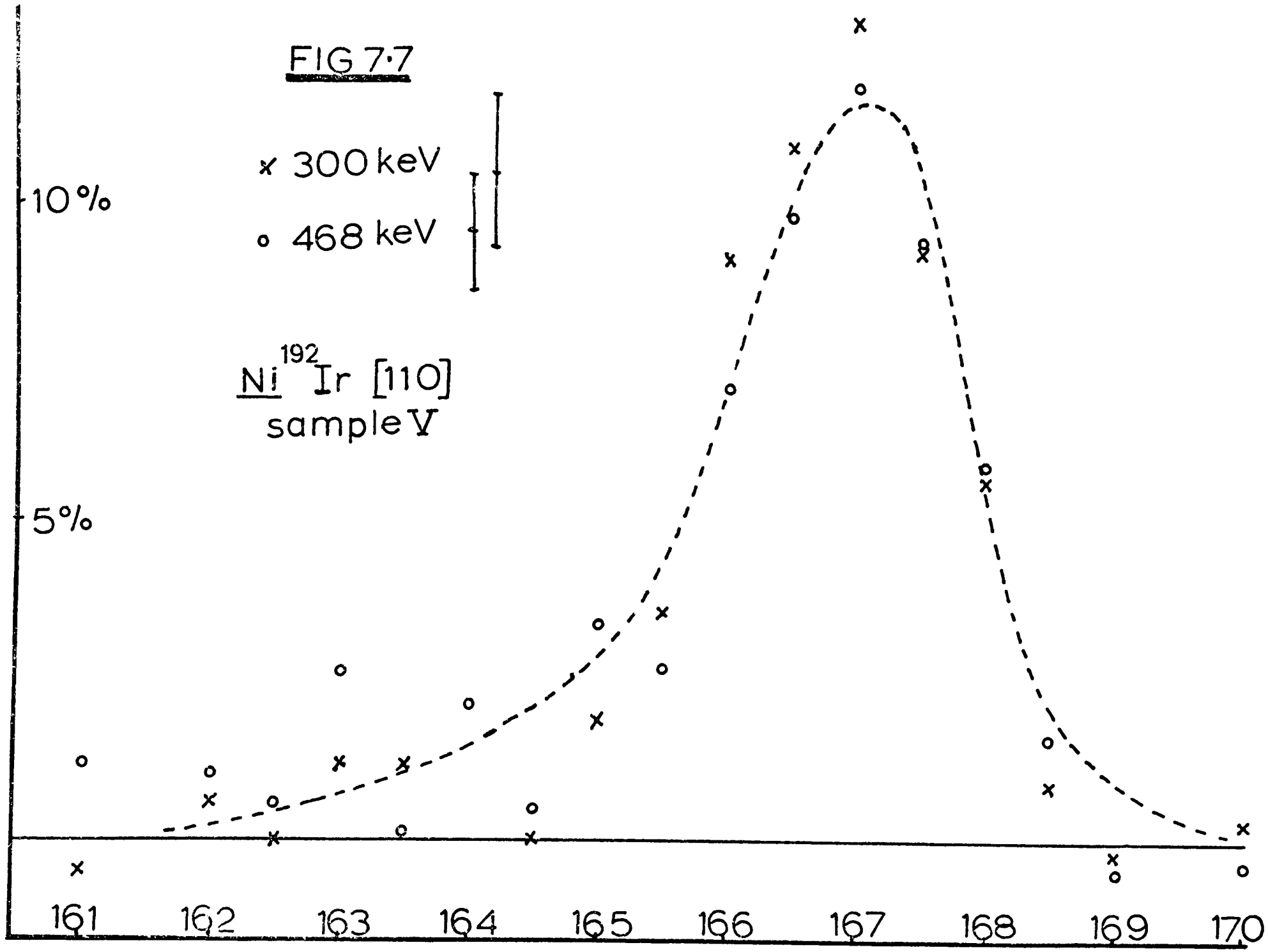
$\nu_0$ = 165·45 ± ·10 MHz

(a) P = 0·400 MHz

(b) P = 0·200 MHz

(c) P = 0·000 MHz

FIG 7·7


× 300 keV
o 468 keV
Ni 192 Ir [110]
sample V
10%
5%
161
162
163
164
165
166
167
168
169
170

were made using a 600 sec counting period, with a 30 sec "dead time" when the frequency modulation was switched on or off, to allow for relaxation effects. The computed fit to the resonance data assumed complete relaxation.

The three crystals orientations studied [100] [110] and [111] all gave identical results within the statistical fluctuations. More complete data was taken for the [100] and [110] crystallographic axes of magnetisation, but the data for the [111] axis gave similar measurements at the selection of frequencies studied. To accumulate a sufficient number of counts for a measurement of the difference between a frequency modulated and a pure carrier wave irradiation required a total counting period of 40 minutes at each frequency. In a typical experiment the temperature of 12.5 → 16 mK was maintained for 4 hours, allowing measurements to be made at about 6 frequencies. The apparent isotropic variation of the electric quadrupole splitting with the orientation of the host lattice is consistent with the nuclear electric quadrupole hamiltonian associated with the formation of a localised orbital moment on the iridium impurity. The local magnetic moment will always be co-axial with the host magnetisation, and when the spin-orbit interaction is only a small perturbation on the crystal field splitting, the magnitude of the localised moment, and the associated electric quadrupole and orbital dipolar hyperfine interactions, will be constant. [ ]

7.4 Summary and analysis of the measurements of the contributions to the hyperfine interaction in nickel, from an unquenched orbital magnetic moment

The Mossbauer measurements on $^{193}Ir$ by Wagner et al [ 81 ], following the work of Perlow [ 98 ], have shown the existence of a non-contact magnetic hyperfine interaction on iridium in nickel. The measurements were made by comparing the hyperfine anomaly between the ground state and the excited state at 73 KeV in the hyperfine field of nickel, with that measured in $IrF_6$ in its antiferromagnetic phase. The concentration of iridium in the alloys used was up to 3 at.% In the nickel host the hyperfine field was observed to decrease with the iridium concentration by 21 kOe per at %, the results quoted being extrapolated to zero concentration. For a non-uniform alloy such a variation could produce an asymmetry in the nuclear magnetic resonance line, but for the concentration of $10^{-2}$ at % of iridium the magnitude of the shift will be negligible [less than 100kHz]. The effect on the shape of the resonance must be kept in mind when considering the interpretation of the NMR/ON results as it may tend to give an overestimate of P.

The more recent experiments of Wagner have also shown a very small electric quadrupole interaction representing a similar value of $e^2qQ$ to that found in this NMR/ON experiment. This provides a useful check on the consistency of the measurements with the Mossbauer and NMR/ON techniques. While these experiments were being done, similar measurements, using the spin echo NMR technique on $^{191}Ir$ and $^{193}Ir$ in iron and nickel, by Aiga and Itoh in Osaka [ 99 ] also showed an electric quadrupole splitting of the NMR line. A summary of all the measurements is presented in table 7.1. The principle of the spin echo measurements differs from the other techniques in that the impurities observed lie in the ferromagnetic domain walls. There are obvious differences between the three sets of measurements, although all give the same order of magnitude for $e^2qQ/h$. It is too early to say

Table 7.1 Comparison of measurements on Iridium impurities

| Technique | isotope | host | concentration | $\frac{eQ}{4}$ (ergs) |
|---|---|---|---|---|
| N.M.R./O.N. | $^{192}Ir$ | Ni single crystal | $10^{-2}$ at % | $1.80(50) \times 10^{-20}$ |
| Mossbauer [81] | $^{193}Ir$ | Ni polycrystal | $1\frac{1}{2}$ at % | $0.82(17) \times 10^{-20}$ |
| | | Fe polycrystal | 1 at % | $0.90(17) \times 10^{-20}$ |
| N.M.R. [97] | $^{193}Ir$ | Ni | 0.3 at % | $0.50(10) \times 10^{-20}$ |
| Spin echo | $^{191}Ir$ | domain walls | | |
| | | Fe domain walls | 0.3 at % | $0.65\ (10) \times 10^{-20}$ |

where the differences may arise, although it may be associated with the different concentrations of the alloys used.

The comparison of the NMR/ON measurements on $^{192}Ir$ with the measurements on the stable isotopes requires an estimate of the ratio of the nuclear quadruple moments. The quadrupole moment of the mass 192 isotope has not been measured, but both the magnitude and the ratio of the moments of the 191 and 193 isotopes are known. The measurements give values for $Q^{191}$ and $Q^{193}$ of order 1.5b with a ratio of $Q^{191}/Q^{193} = 0.92\ (9)$ [100]. The addition of an extra neutron to the $(1i_{13/2})$ shell of the 191 nucleus will have little effect on the quadrupole moment since the major contribution will be from the nuclear core and the unfilled $2d_{3/2}$ proton shell [101]. For the purpose of comparison the quadrupole moment of $^{192}Ir$ is assumed to be the same as the $^{191}Ir$ and $^{193}Ir$ isotopes.

Analysis of the NMR/ON measurements

The results shown in chapter four, for the hyperfine interactions associated with the formation of an unquenched orbital magnetic moment, can be used to obtain an estimate of the magnitude of the unquenched orbital magnetic moment required to give an electric quadrupole splitting of the size found by experiment; as for the gold measurements in chapter six. The Hamiltonian for the electric quadrupole interaction can be written in the form

$$\mathcal{H}_Q = \frac{e^2Q}{4I[2I-1]} .2 \langle r_q^{-3} \rangle \langle 1 \| \alpha \| 1 \rangle \langle | 3I_z^2 - 1\,(1+1) | \rangle \eta \left[ 3I_z^2 - I[I+1] \right]$$

From the results presented in chapter four [ ]

$$\langle | 3I_z^2 - 1(1+1) | \rangle = \frac{3\xi^2}{4\Delta^2} \left\{ 3 \langle \Psi_o | 1^4 | \Psi_o \rangle - \frac{1}{9} \left\{ 1\,(1+1) \right\}^2 \right\}$$

The term $\langle \Psi_o | 1^4 | \Psi_o \rangle$ can be represented by the summation $\dfrac{2 \sum_o^1 M_1^4}{[2l+1]}$

Table 7.2 : N.M.R./O.N. measurements on $^{192}Ir$

| host | resonance frequency (MHz) [2.2 kOe] | P(MHz) | $T_n$ |
|---|---|---|---|
| Ni | 165.45 (10) | 0.30(05) | 0.90(10) |
| peak response | 167.20)(10) | | |
| Co(cubic) | 349.4 (10) | $< 0.30$ | 2.20(20) |

which, for a d-state of $l = 2$ leads to the numerical factor 34/5.

To calculate the splitting of the NMR line it is most convenient to work with the interaction energy $e^2Qq$, where q is given by

$$q = -\langle r_q^{-3} \rangle \quad \frac{17}{7} \quad \frac{\xi^2}{\Delta^2} \qquad \text{for a value of } l = 2.$$

In the calculations performed by Aiga et al, a value of $\langle r_q^{-3} \rangle_{5d}$ of 10.5 a.u is taken from Wagner and Zhan [ 80 ]. Wagner and Zahn also give an estimate of $\xi/\Delta$ of order 0.1. The experimental result from the NMR/ON experiment gives a value for $e^2Q.q$ of

$$(^{192}\text{Ir})\ e^2q. = 7.2 \times 10^{-20} \text{ ergs.}$$

The non-contact magnetic hyperfine interaction on iridium in nickel from the results of Wagner is of the order of $+50 \pm 50$ KOe. The most obvious point in the comparison with similar measurements on the gold isotopes is that, even allowing for the larger nuclear quadrupole moment, the electric quadrupole interaction on iridium is larger compared with the orbital dipolar hyperfine fields than for the gold interactions. If one uses similar values for $\langle r_q^{-3} \rangle$ and $\langle r_l^{-3} \rangle$, and the value of 10.5 a.u, the comparison of the orbital dipolar and electric quadrupole interactions suggests a solution with $\xi/\Delta \sim 0.2$ and $\eta \sim 0.2$. This calculation is only a rough guide because of the uncertainty in the values of $\langle r_q^{-3} \rangle$ and $\langle r_l^{-3} \rangle$ as discussed in chapter six, but the results are similar to those expected from the best theoretical estimates [ 80 ]. The sign of both interactions is consistent with the formation of a small localised orbital magnetic moment of $\overset{+ve}{-}$ sign. The value of $\eta$ , indicates a moment magnitude of order 0.2 $\mu_B$ . The estimate of $\langle r^{-3} \rangle_l$ for the 5d orbitals by Wagner and Zahn and Mann [ 102 ] may give a more accurate representation for iridium in nickel, than the estimates for gold, since the valency difference between the host and the impurity is smaller than for gold in iron. The electronic orbitals localised on the iridium may therefore

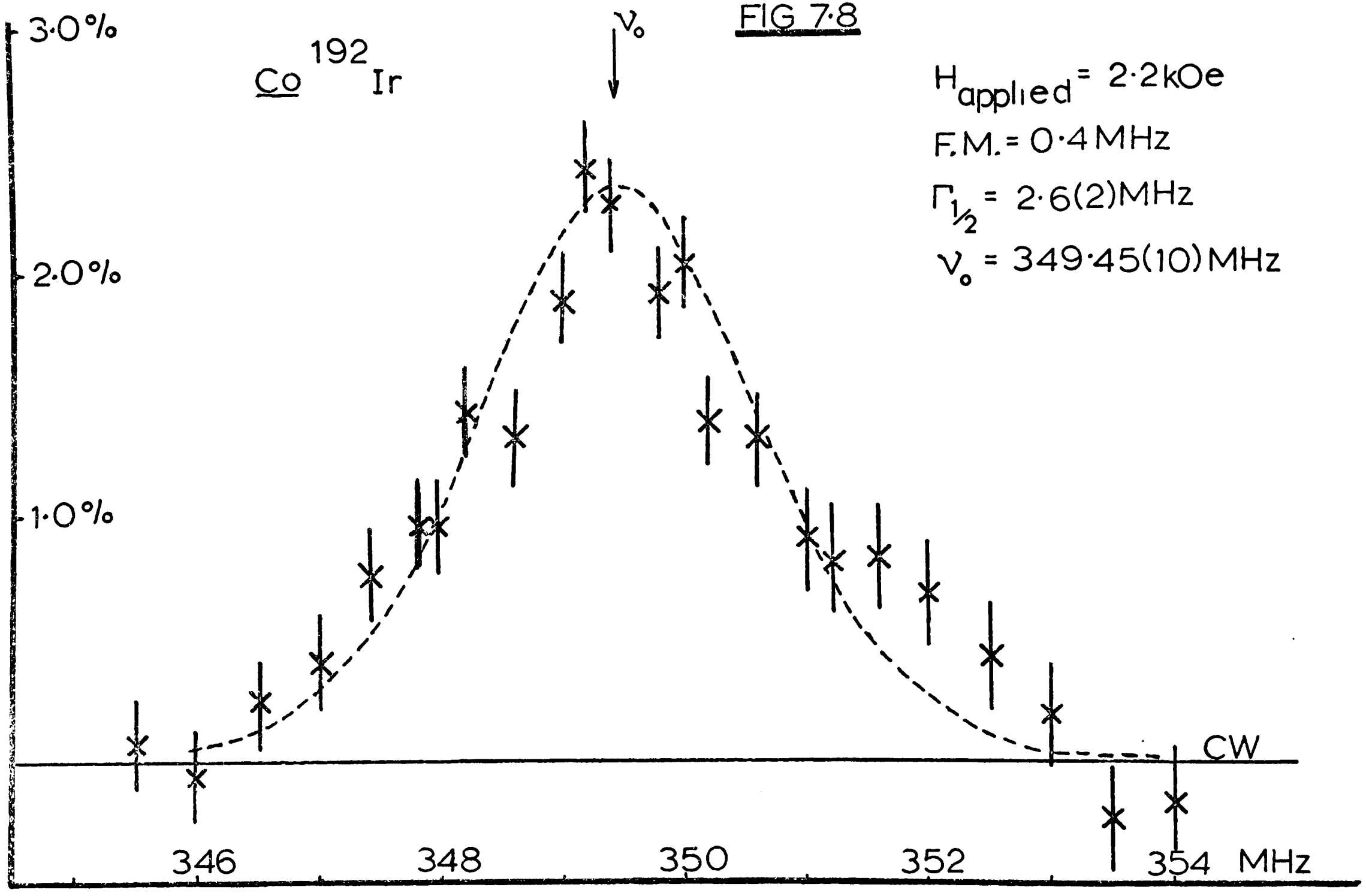
be more similar to the atomic configuration. The free atom Hartee-Fock calculations of Mann [102] give a value of $\langle r^{-3} \rangle_{5d}$ of 10.54 a.u. but the value derived for iridium in $K_2IrCl_6$ is 8.8 ± 0.8 a.u. [ 81 ]; smaller because of covalency effects.

## 7.5 The measurement of the hyperfine field of iridium in cubic cobalt, by NMR/ON

The mass 192 isotope was also used for the measurement of the hyperfine interaction in cubic cobalt. No previous measurement of the magnetic hyperfine field in cubic cobalt has been made, of the interaction in hexagonal cobalt has been measured using the Mossbauer technique on $^{193}Ir$ [ 81 ], giving a value for $H_{eff}$ of -1038(10)kOe and an electric quadrupole interaction equivalent to a value of P for 192 Ir of 1MHz. The strength of the hyperfine field in cubic cobalt is typically about 5% smaller than in the hexagonal phase, with the cubic phase having the advantage for resonance that there is no crystal field contribution to the electric field gradient at the nucleus. This will be the dominant mechanism for the large quadrupole splitting observed on the 193 isotope of iridium in hexagonal cobalt.

The NMR/ON measurements were made on samples containing less than $10^{-2}$ at % of iridium in foils of polycrystalline cobalt. It was not practical to prepare single crystal samples of cubic cobalt, because the stable form at room temperature is the hexagonal phase, with the phase change about 500°C. The iridium impurity was introduced by thermal diffusion, as in the nickel samples, with diffusion conditions of 1000°C for 20 hrs. The heat treatment and the long relaxation time for the re-establishment of the hexagonal phase at low temperatures ensured, as for the gold samples, that the structure of the foils was dominantly cubic. The NMR/ON results on two samples are shown in Fig.7.6. The resonance procedure was the same as for the nickel samples, but, because of the higher

FIG 7·8




$H_{applied}$ = 2·2kOe

F.M. = 0·4MHz

$\Gamma_{1/2}$ = 2·6(2)MHz

$\nu_o$ = 349·45(10)MHz

frequency, a lower RF power level had to be used (0.1V) to keep the RF heating at a sufficiently low level to give a useable counting time with the sample below 20 mK. The resonance shows no sign of any assymmetry due to an electric quadrupole splitting, but, as was shown in chapter five, the larger inhomogeneous resonance linewidth associated with the larger magnetic hyperfine interaction will tend to swamp out any assymmetry. An upper limit of $P < 0.3$ MHz can however be put on any quadrupole interaction from the lineshape and the ratio of the linewidth to the resonance frequency. The effect of an unresolved quadrupole splitting is to give an increased apparent linewidth as well as an assymmetry. The FWHM linewidths for $^{198}$Au in cobalt and $^{199}$Au in cobalt show percentage broadenings of 0.6% and 0.8% respectively. The FWHM linewidth for $^{192}$Ir in cobalt is 0.7% of the magnetic interaction again indicating a small value for P. The larger magnetic interaction, and consequent larger degree of orientation, will make the NMR/ON result less sensitive to small splittings than for $^{192}$Ir in nickel. The NMR/ON results are summarised in table 7.2.

The total integrated destruction of the anisotropy over the full resonance line shows that 70% of the nuclei reached saturation. The resonance frequency of 349.4(1)MHz is the highest we have observed with a single loop RF coil, and suggests that the technique is applicable over a very wide frequency range. Resonances up to 1200 MHz have been observed by Eska [97] with a similar arrangement in Munich, but we are at present restricted by the frequency range of the RF generator.

## 7.6 The magnetic hyperfine interaction on iridium, and the $^{192}$Ir g factor

Since the g-factor of $^{192}$Ir has not been directly measured, the results of experiments on the stable isotopes, $^{193}$Ir and $^{191}$Ir, must be used to estimate the magnitude of the hyperfine interaction. The contributions to the magnetic hyperfine interaction(from Mossbauer measurements of the hyperfine anomaly in $^{193}$Ir)are included in the tabulation below. The magnetic moment of $^{193}$Ir is well known, $^{193}\mu = 0.1583\ (6)_{\mu N}$.

Table 7.2

| Host | $H_{eff}$ (Total magnetic Interaction) | | | $H_c$ | $H_{O.D}$ |
|---|---|---|---|---|---|
| | (a) | (b) | (c) | (a) | |
| Fe | -1403(20) | -1395 (16) | 1478.5(5) | -1558(90) | +155(90) |
| Co(h.c.p) | -1038(10) | | | -1162(80) | +149(80) |
| Ni | - 468(8) | | 490.3(5) | - 520(50) | + 52(50) |

a) Wagner F.F. and Potzel, W. Hyperfine Interactions in Excited nuclei Vol.2 p.681. Ed.Goldring and Katish 1971.

b) Perlow, G.J. Henning, ., Olson, D. and Goodman, G.L. Phys.Rev.Lett. 23 680 (1969).

c) Aiga, M., Itoh, J., Saraswati, V., J.Phys.Soc.Japan 31, 1843, 1971.

There is an obvious discrepancy between the Mossbauer measurements, a) and b), and the NMR-spin Echo measurements, c). This is due to the -5.5% hyperfine anomaly between the $^{193}$Ir ground state and the first excited state. The influence of the hyperfine anomaly on the measured hyperfine field was discussed in chapter six. The large g-factor of the first excited state makes it more easy to use for the hyperfine field measurement in the Mossbauer experiment, while the NMR experiment will of course observe the nuclear ground state. The hyperfine anomaly measured by the Mossbauer technique agrees very w ell with that from the ratio, 1478.5(5)/1395(16), of the hyperfine fields.

The NMR/ON measurements on $^{192}$Ir can be used with the knowledge of the hyperfine field to estimate the nuclear g-factor of $^{192}$Ir. The value obtained will of course include the hyperfine anomaly between the $^{192}$Ir ground state and the $^{193}$Ir state. This will probably be of the same size as the 5% anomaly in $^{193}$Ir. For the measurements in nickel, the deduced g-factors are given below for the magnetic resonance frequency when the NMR/ON line is fitted for the electric quadrupole splitting of P = 0.30(5)MHz, and for the resoannce frequency if the NMR/ON line is considered without a quadrupole splitting.

a) $^{192}\mu$ = 1.779(1) $\mu_N$ b) $^{192}\mu$ = 1.797 (1) $\mu_N$

These estimates can be compared with the calculated moments on the basis of coupling between deformed proton and neutron orbitals. In the previous nuclear orientation measurements on this isotope a table of calculated values for $^{192}\mu$ was given for various proton and neutron configurations. [95]

Table 7.3

| proton assignment | neutron assignment | coupling rules obeyed? | $\mu$ | Deformation |
|---|---|---|---|---|
| $3/2^+$ [402] | $5/2^-$[503] | Yes | 1.36 | 2 |
| $3/2^+$ [402] | $5/2^-$[503] | Yes | 1.90 | -2 |
| $3/2^+$ [402] | $9/2^-$[505] | No | 1.38 | 2 |
| $1/2^+$ [400] | $9/2^-$[505] | Yes | 1.12 | 2 |
| $5/2^+$ [402] | $3/2^-$[512] | No | 2.18 | 2 |

On the basis of the previous estimate of $^{192}\mu$ = 1.41(6) $\mu_N$ a configuration of $3/2^+$[402]p; $5/2^-$[503] with a deformation of 2 was concluded, but these more recent measurements suggest a coupling of the $3/2^+$[402] proton to the 115th, $5/2^-$[503], neutron with a deformation of -2, giving a moment of 1.90$\mu_N$. This will be in good agreement with the experimental value if a hyperfine anomaly of order -5% exists.

It may be possible to make a more direct measurement of the magnetic moment by measuring the frequency shift in a very large applied magnetic field, but because of the small g-factor a field of 60 kOe will be required for sufficient accuracy. Such a measurement has not been possible yet because of instabilities in the superconducting magnetic system at such high fields.

## 7.7 Conclusion

These experiments have shown that the NMR/ON technique is sensitive to deviations from a simple Gaussian lineshape for the inhomogeneously broadened nuclear magnetic resonance. An important aspect of such a measurement is the establishment of an accurate baseline from the monitoring of the gamma-ray anisotropies when the RF carrier wave only is applied. The interpretation of the observed lineshape for $Ni^{192}Ir$ in terms of a small quadrupole splitting associated with an unquenched orbital magnetic moment on the iridium impurity, gives a value for the electric quadrupole interaction, larger, but comparable with other measurements on the stable isotopes of iridium. The NMR/ON technique has the advantage over other techniques that lower concentrations can be used, and the impurity can be studied in single crystal hosts. This latter fact has been used in this experiment to demonstrate the isotropic variation of the NMR response with the crystalline axis of magnetisation. The hyperfine interaction Hamiltonian deduced from these measurements is used in the next chapter to study the gamma decay multipolarities in the daughter nucleus $^{192}Pt$.

# CHAPTER 8

# NUCLEAR ORIENTATION MEASUREMENTS ON $^{192}Ir$

## 8.1 Introduction

Several authors have recently reported large discrepancies in the measurements of the magnetic hyperfine fields acting as impurities in the ferromagnetic hosts, iron and nickel. [ ][ ] A large and consistent discrepancy has been noticed, particularly, for dilute alloys containing iridum and osmium isotopes, between the techniques measuring an averaged hyperfine interaction, through an angular correlation or nuclear orientation method, and the techniques measuring the dominant well defined hyperfine interaction such as the mossbäuer technique or NMR/ON. The observed discrepancies make the interpretation of the measurements very difficult for the magnitude of the hyperfine interactions, and g factors, and the gamma-ray multipolarities from nuclear orientation measurements. In this chapter the combination of the NMR/ON measurements and conventional nuclear orientation measurements on $^{192}Ir$ in nickel hosts is compared with previous experiments [95] by nuclear orientations on $^{192}Ir$ in iron, and $\gamma - \gamma$ correlation measurements of the M1/E2 mixing ratios. The measurements of Reid et al [95] provided the temperature dependence of the gamma-ray anisotropies of $^{192}Ir$ in iron. These anisotropies were fitted for $U_2F_2$, $U_4F_4$ and the magnitude of the hyperfine interaction $\mu.H$. The results show considerable discrepancies in the E2/M1 mixing ratios on several gamma-rays with similar measurements from angular correlation experiments, and a large difference of 20% in the averaged hyperfine interaction compared with the recently reported value from NMR/ON. The similar discrepancies reported in the comparison of measurements using the ion-implemtation-perturbed-angular-correlation technique [IMPACT] and mossbauer measurements have tended to show that nickel represents a more reliable host lattice for the study of the third series transition elements than iron. The experiments discussed in this chapter tend to confirm this suspicion.

The gamma ray anisotropy measurements in nickel are interpreted in terms of the β and γ multipolarities of the decay modes as for the experiments on $^{110}Ag^{m}$, and the results compared with the angular correlation measurements. The interest in these measurements arises from the study of the deviations from a simple harmonic oscillator model for the excited states of $^{192}Pt$, similar to those observed for $^{110}Cd$. The mass region, $182 < A < 196$, has been studied in detail by Kumar and Baranger [54]. Their calculations on the basis of a pairing-plus-quadrupole force for quadrupole deformations, g-factors, and M1/E2 multipole mixing ratios, agree surprisingly well with recent experimental data [103]. The experimental results presented here resolve the discrepancy between the previous nuclear orientation measurements and γ-γ angular correlation measurements, and give further confirmation of the Kumar and Baranger model.

## 8.2 Comparison of measurements using various techniques

The simple interpretation of the results of experiments involving an integral measurement of the hyperfine interaction of impurities in ferromagnetic host requires the assumption that the internal magnetic field, $H_{eff}$, acting on the impurity nuclei satisfies the conditions.

1) The magnetic interaction $\mu_N \cdot H_{eff}$ is the dominant interaction.
2) It is the same for all impurity nuclei
3) It is parallel to $H_{ext}$ and is constant during the time period of the measurements.

Integral perturbed-angular-correlation (P.A.C.), ion-implantation-perturbed-angular-correlation, and nuclear orientation, all measure the hyperfine interaction averaged over all the impurity nuclei, and will give an unreliable result if any of the three conditions is not satisfied. The Mossbauer technique and all methods involving nuclear magnetic resonance

will identify the hyperfine field associated with a discrete lattice site occupied by a large proportion of the impurity atoms and will therefore give a true indication of the strength of the interaction for a reproducible system. The effect of a distribution of impurity sites will only be to reduce the signal strength for the NMR at the resonance condition.

The impurities of iridium and osmium have measured solubilities [ 81 ] of order 1% in iron and nickel lattices in the sense that a stable alloy can be produced with a macroscopic homogeneity. Systems showing a large proportion of interstitial impurity sites are usually associated with a known low solubility or strong chemical bonding, so the poor reproducibility of these alloys requires another explanation.

Two models have been proposed for the anomalous behaviour of iridium/iron alloys and osmium/iron alloys. The angular correlation measurements of King, Grabowski and Scharenberg [104] on alloys of iridium in iron, and iridium in nickel, showed inconsistent results in the iron based alloys, with an apparent reduction of order 20% in the hyperfine field compared with that expected from the nickel host data, and the known ratio of hyperfine fields between the two hosts from NMR measurements. Annealing the iron samples gave a further reduction in the averaged interaction depending on the heat treatment and the manner in which samples were cooled from the molten state. The examination of the polished and etched iron alloys by electron microscopy showed a 'microporosity' of the host lattice, more prominent in the samples giving a smaller hyperfine interaction. King et al have suggested that there may be a favourable lattice vacancy-impurity (Ir) pair formation, leading to the segregation of iridium impurities in the vicinity of pores (vacancy sinks), associated with a vacancy-drag effect. A similar mechanism has been suggested for alloys of Mn in copper by Wittenberger and Dayananda [105]. The dilute alloys of iridium in nickel show no change in the effective magnetic hyperfine interaction with annealing

suggesting that such a process does not occur in nickel.

The other possible explanation of the reduced values of $H_{eff}$ observed in iron alloys has been proposed by Ben-Zué et al [106]. On the purely empirical basis of fitting all the available from angular correlation measurements, on impurities implanted by recoil from Coulomb excitation, they propose that the excited nuclei experience a magnetic field that does not lie along the applied field direction, but rather lies along the generating vectors of a cone, making an angle $\theta$ with the applied field direction. They also considered fits with a distribution of angles for of the form $\exp(-\theta/\theta_m).\sin\theta$, where $\theta_m$ is a mean angle slightly larger than a single cone hypothesis.

A theoretical basis for such a distribution of the directions of the hyperfine fields has been proposed by Aharoni in terms of the magnetic saturation near impurity atoms. Neutron scattering experiments have frequently shown a reduction in the host magnetism in the vicinity of an impurity atom. Aharoni has shown [107] that the local saturation of the host magnetism in such a region can differ considerably from that of the bulk material, and that the local direction of the magnetisation will tend to lie at an angle $\theta$ to the applied field direction, with $\theta$ a function of the applied field, and the angle between a cubic axis and the applied field. For a system of tungsten impurities in a nickel lattice he gives an average value of $\theta$, in polycrystalline material, of $27^0$ for an applied field of 1000 Oe.

A conical distribution of the hyperfine fields will reduce the apparent magnitude of the observed hyperfine fields through the $P_2$ and $P_4$ legendre polynomials in the nuclear orientation experiments. These models are discussed in the interpretation of nuclear orientation data in an iron/iridium alloy in section 8.6.

The discrepancy in the integral, and resonance measurements of the hyperfine interactions will also produce systematic errors in the measurements

of M1/E2 mixing ratios measured by nuclear orientation. The measurements of such mixing ratios by $\gamma$-$\gamma$ angular correlation on liquid solutions will involve no perturbations associated with a distribution of hyperfine fields, and therefore provide a reliable comparison for the nuclear orientation experimental results.

## 8.3 Sample preparation

A significant factor in the interpretation of the results of the nuclear orientation data is the reproducibility of the results from various samples prepared in different ways. The experiments on $^{192}$Ir in nickel have used three types of samples: Polycrystalline samples in which the impurity is introduced by diffusion, Polycrystalline samples prepared by melting and alloying the nickel and iridium impurity to produce a uniform impurity distribution; and single crystal nickel samples, where the impurity is diffused from a surface deposit. There is not the same stringent requirement on the thickness of the sample as for the NMR/ON experiments, allowing a more dilute alloy to be used in the experiments. The concentration distribution in the single crystal samples was checked as for the resonance samples and was found to be consistent with the random distribution in a uniform medium. The knowledge of the hyperfine interactions from the resonance experiment enabled the anistropy vs temperature results to be analysed in terms of the single variable $U_2F_2Q_2$ linked with the associated value of $U_4U_4F_4$. Table 1 shows the summary of the sample preparations and deduced values of $U_2F_2Q_2$ for the 468 Kev gamma-ray. The 468 KeV gamma transition was chosen for the comparison of the nuclear orientation effects since it has a well known gamma decay multipolarity and follows a simple $4^-$ to $4^+$ $\beta$ decay. It is also well resolved from other transitions allowing a simplified analysis.

Table 8.1

| No. | Sample | preparation | concentration at % | $Q_2U_2F_2$(468KeV) |
|---|---|---|---|---|
| 1 | polycrystalline | Thermal diffusion 10 hrs 1000°C | $2 \times 10^{-3}$ | 0.350 ± 0.03 |
| 2 | polycrstalline | Thermal diffusion 20 hrs 1200°C | $1 \times 10^{-4}$ | 0.365 ± 0.02 |
| 3 | polycrystalline | melting 1500° 1 hr | $1 \times 10^{-4}$ | 0.360 ± 0.02 |
| 4 | single crystal [100] | Thermal diffusion 16 hrs 1200°C | $1 \times 10^{-2}$ | 0.345 ± 0.02 |
| 5 | single crystal [110] | Thermal diffusion 16 hrs 1200°C | $1 \times 10^{-2}$ | 0.375 ± 0.02 |

All the samples gave very similar results on all the gamma rays in applied fields of 5kOe and 8 kOe. The gamma-ray anisotropy measurements, shown in figs.8.3 to 8.7, represent an amalgamation of results from three samples. The theoretical fits are for the magnetic interaction, of 165.5MHz, and the electric quadrupole interaction of P = +0.300 MHz, with the correction for the applied magnetic field and the solid angle subtended by the Ge(Li) detection: $Q_2 = 0.955$, $Q_4 = 0.857$.

## 8.4 Gamma-ray spectroscopy

The gamma-ray spectrum of $^{192}$Ir was shown in Fig.7.1. The transitions studied are shown by the thicker lines. The close energy separation of the 296 KeV 308 KeV and 316 KeV peaks and the 588 KeV, 604 KeV and 612 KeV peaks required high resolution in the germanium detectors used for the experiment, in order to both resolve the peaks, and monitor the background level under each peak by extrapolating from higher energies. A background level was taken at energies immediately above each peak except for the 604 transition, where a window immediately below the peak in energy was used. This will provide an accurate estimate of the background since degraded radiation from the peak itself will show the same anisotropy as the peak at such similar energies. The spins and parities of the excited states used in the analysis of the nuclear orientation results are taken from Nuclear Data sheets and the Nuclear Data Table [108], [109]

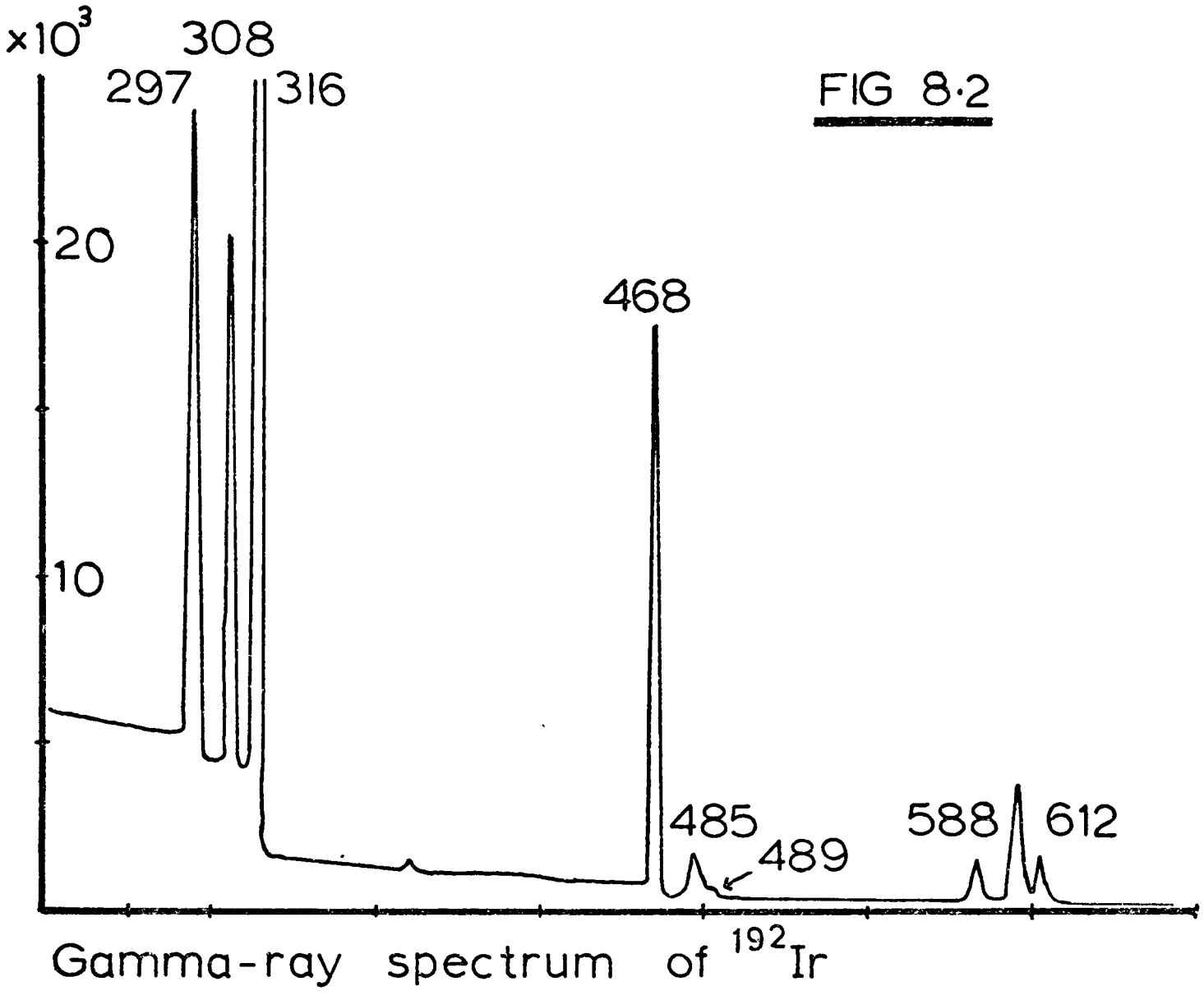
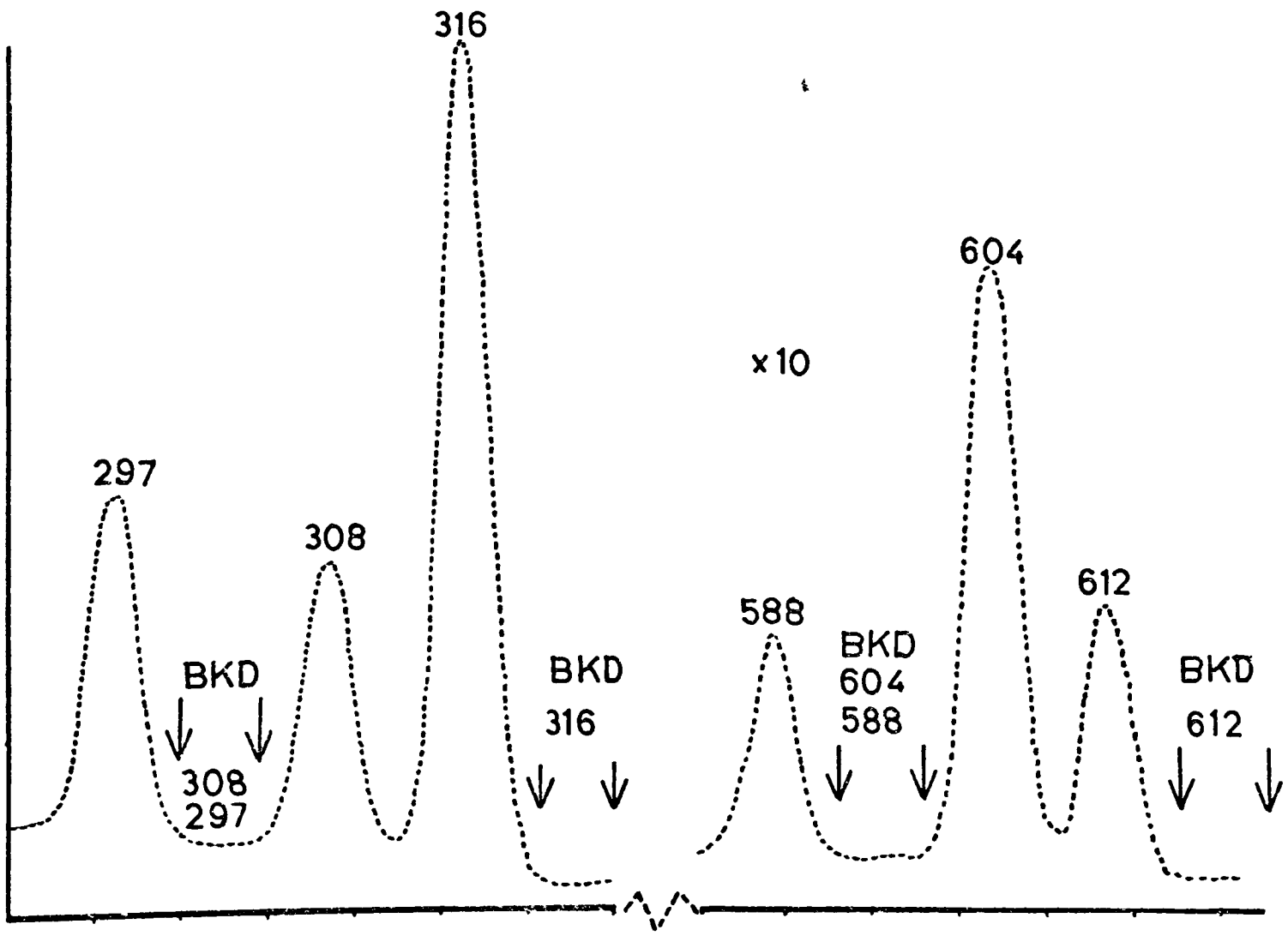



FIG 8·2

Gamma-ray spectrum of $^{192}Ir$



## 8.5 The interpretation of the nuclear orientation measurements of $Ni^{192}Ir$

### The 468 KeV gamma transition and the 669 KeV beta decay

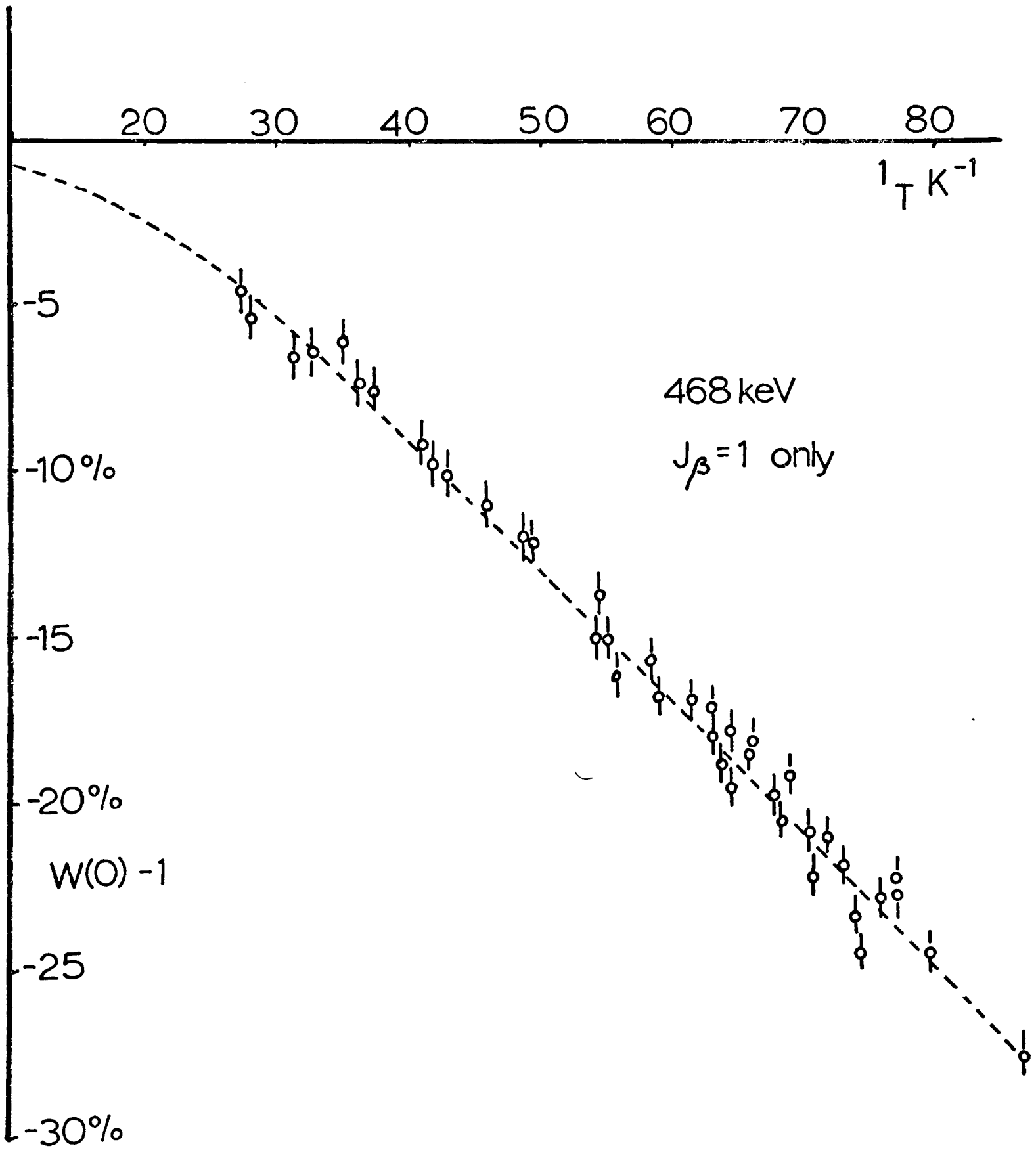
The 468 KeV gamma transition is fed predominantly from the 669 KeV β decay, with small contributions from the weak 136KeV and 417 KeV gamma transitions. These weak gamma decay feeds contribute less than 1% of the intensity of the 468 KeV transition, and give a negligible perturbation to the decay parameters for the 468 KeV transition. Their effect is not included in the analysis of the results.

The 669 KeV beta decay is a $4^-$ to a $4^+$ transition, and because of the parity change is therefore a first forbidden transition. Multipolarities of $\dot{\gamma}_\beta$ = 0, 1, and 2 are allowed, and can be expected to contribute to the nuclear orientation parameters for subsequent gamma transitions. The 468 KeV gamma transition is a pure E2, $4^+$ to $2^+$, decay, with well defined $F_K$ coefficients. The analysis of the nuclear orientation measurements on this gamma-ray contains only the variables associated with the beta decay. The data has been analysed as in the $^{110}Ag^m$ experiment, with the known hyperfine Hamiltonian, with the variables $U_2F_1Q_2$ and $U_4F_4Q_4$ linked by the additional constraint imposed by the consistency of the results with a single value of the multipolarity mixing. For the beta decay, only observed through the $U_K$ coefficients, such a simple constraint does not exist when $\dot{\gamma}_\beta$ = 0, 1, and 2 multipolarities are all allowed. The independent values of $Q_2U_2F_2$ and $Q_4U_4F_4$, shown below, are however both consistent with a pure $\dot{\gamma}_\beta$ = 1 multipolarity in the beta decay. Any other solution would involve an admixture of both $\dot{\gamma}_\beta$ = 0 and $\dot{\gamma}_\beta$ = 2 multipolarities, the latter of which is unlikely for the reasons discussed below. Fig.8.4 shows the best fit to the 468 KeV orientation data in a nickel host with the values for $Q_2U_2F_2$ and $Q_4U_4F_4$.

| | EXPT | Theoretical values with $\gamma_\beta = 1$ only |
|---|---|---|
| $Q_2U_2F_2$ | - 0.363 (10) | - 0.360 |
| $Q_4U_4F_4$ | - 0.130 (50) | - 0.128 |

The spectrum shape measurements [110] and the theoretical predictions of the $\xi$ approximation [111], suggest that the $\gamma_\beta = 2$ $(B_{ij})$ matrix element will be small compared with the $\gamma_\beta = 0$ and $\gamma_\beta = 1$ matrix elements. The $\xi$ approximation is expected to hold when the factor $\xi$ $(= -\alpha Z/2\rho$, where $\rho$ is the nuclear radius) is greater than the beta decay energy. For thecase of the 669 KeV beta decay the ratio of $\xi/W_o$ is of the order of 10, well within the range of validity of this theory. The $\beta$-$\gamma$ angular correlation measurements of Bhattacherjee et al [112] on this decay also suggested that the decay was dominated by the $\gamma_\beta = 1$ matrix element. The measurements here allow only a limit of $< 10\%$ $\gamma_\beta = 2$ to be put on the decay multipolarity, but the results of previous measurements justify the assumption of a pure $\gamma_\beta = 1$ multipolarity in the analysis of subsequent gamma-ray anisotropies.

FIG 8·4


20
30
40
50
60
70
80
$\frac{1}{T}$ K$^{-1}$
-5
-10%
-15
-20%
W(0) -1
-25
-30%
468 keV
$J_\beta = 1$ only

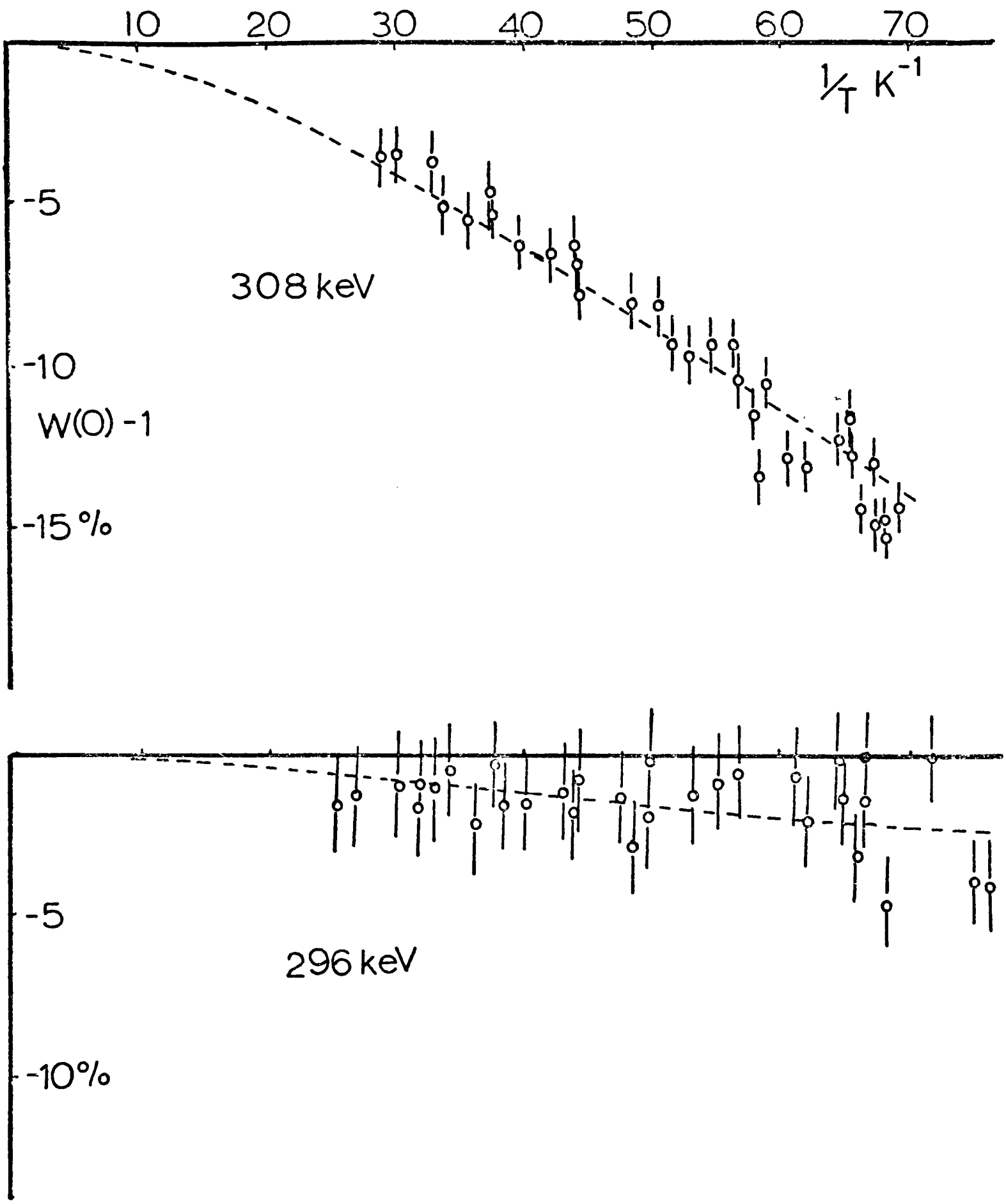
The 604 KeV and 308 KeV transitions

Both of these $3^+ \longrightarrow 2^+$ gamma transitions are of interest for measurements of the M1/E2 mix ing ratios because they feed the single phonon, $2^+$, and the two-phonon, $2^+$, excited states of $^{192}Pt$ respectively. The 604 KeV transition has been the subject of several experiments using the gamma-gamma angular correlation technique, giving values for $\delta$(M1/E2) ranging from + 1.9 to + 3.0. These values agree with the estimates on the basis of the Kumar and Baranger model, but differ considerably from the value of + 1.5 $\pm$ 0.1 from the previous nuclear orientation measurement. One of the aims of this series of experiments was to investigate this discrepancy.

These transitions are fed by the 536 KeV beta decay, with negligible contributions from the 4.37 and 281 KeV gamma rays feeds. The $4^+ \longrightarrow 3^+$ beta decay has been studied by Bhattacherjee et al, who proposed a cancellation among the normal $\gamma_\beta$ = 1 matrix elements and an important contribution from third forbidden components, on the basis of the energy dependence of the beta-gamma angular correlation anisotropies. More recent work of Senbert and Wilkinson has shown, however, that the large anisotropies that Bhattacherjee et al measured were probably associated with conversion electrons rather than the beta decay. The latter measurements, and the log ft value of 8.3 for this decay both suggest that the decay will have pure $\gamma_\beta$ = 1 multipolarity. The multipolarity of this decay is important in the analysis of the measurements on the 604KeV and 308KeV transitions since the nuclear orientation experiment is not sensitive independently to the $\beta$ and $\gamma$ mixing ratios. In the following analysis a pure $\gamma_\beta$ = 1 multipolarity is assumed; but the effect of admixtures of higher multipolarities, as suggested by Bhattacherjee, will be to increase the magnitude of the deduced values of $\delta$ for both the 604 and 308 KeV transitions.

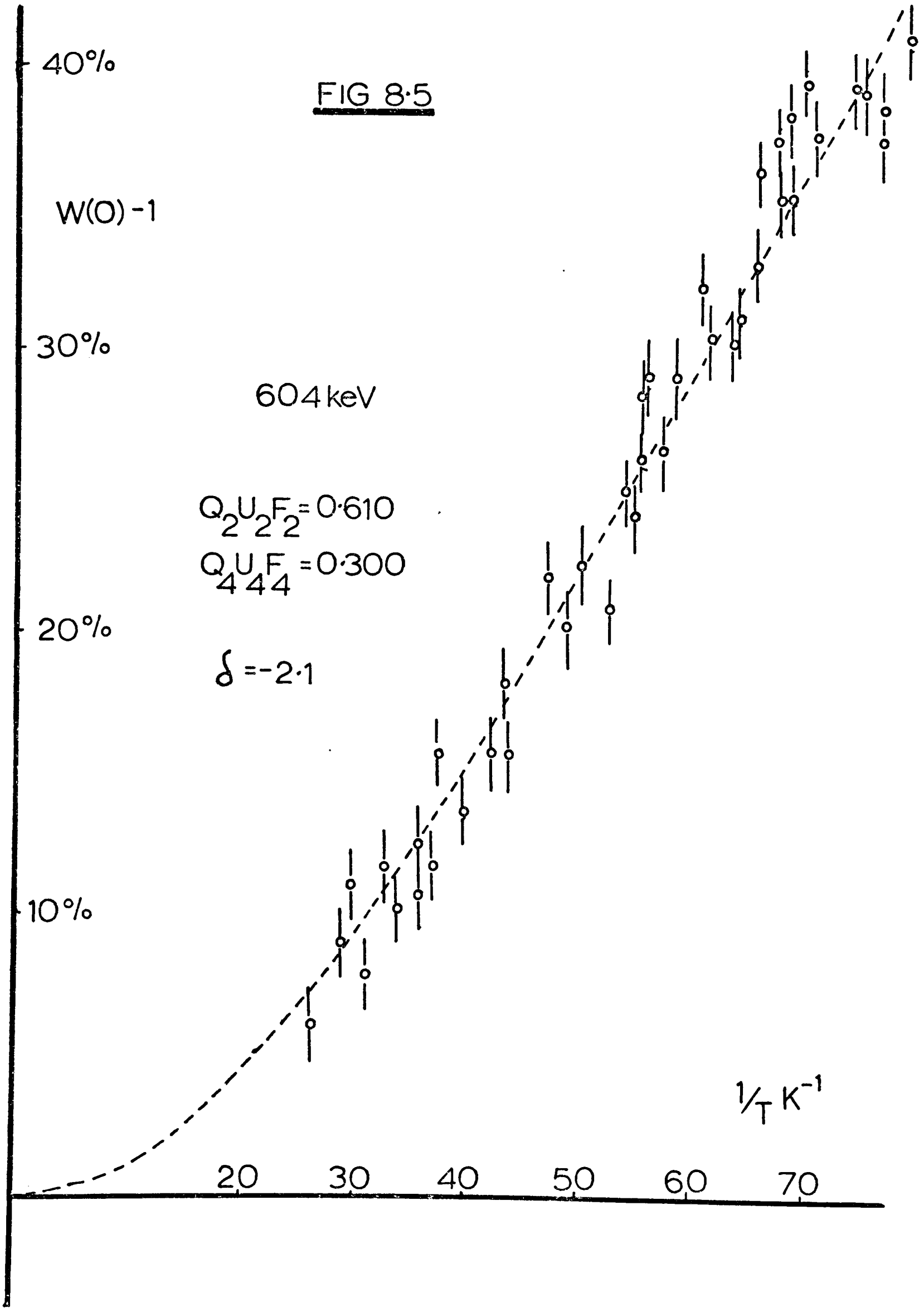
The best fit to the data from the 604 KeV transition is shown in Fig.8.5. The values of $Q_2U_2F_2$ and $Q_4U_4F_4$ are both consistent with a value

FIG 8·3




Nuclear orientation measurments on $^{192}_{Ni}Ir$

FIG 8·5


40%
W(0) -1
30%
604 keV
$Q_2U_2F_2$ = 0·610
$Q_4U_4F_4$ = 0·300
20%
δ = -2·1
10%
1/T K⁻¹
20
30
40
50
60
70

of $\delta$ (M1/E2) of + 2.1 $\pm$ 0.1. These values are discussed further in section 8.5, but this value for the 604 KeV transition is now in good agreement with other measurements. The value of +1.5$\pm$0.1, from the previous measurements by nuclear orientation in iron, would give gamma-ray anisotropies that are much too large (by a factor of 1.3) clearly not fitting the observed anisotropies.

The least squares fit to the anisotropy data from the 308 KeV gamma-ray is shown in Fig.8.4, with the experimental points. The constraint for $U_4 F_4$ is included in this fit. The value of $F_2$ deduced from this fit gives a mixing ratio of

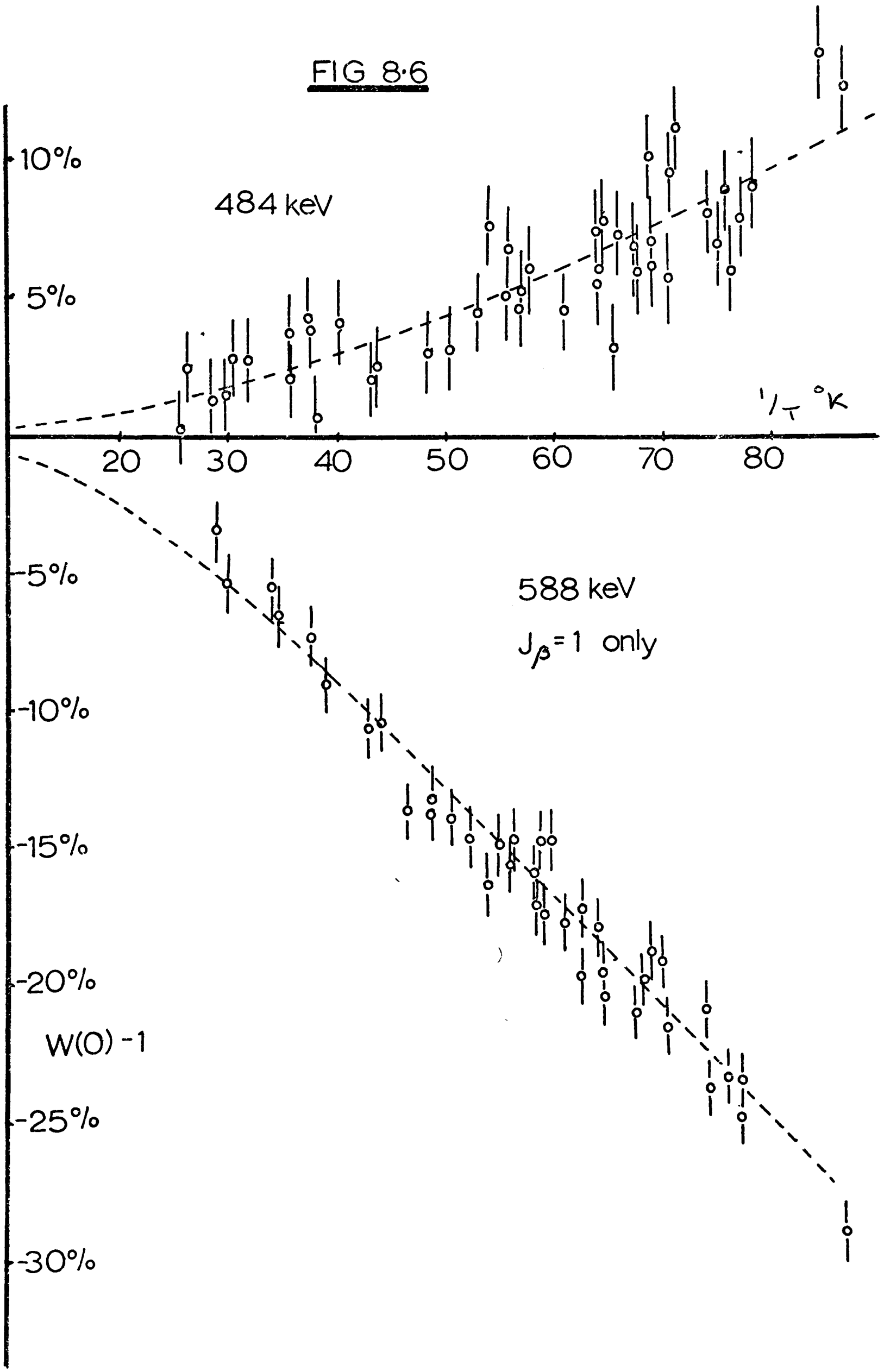
$$\delta^{308} = -8.0 \pm 0.8 \qquad F_2 = -0.345 \ (20)$$

The experimental values of $Q_2 U_2 F_2$ and $Q_4 U_4 F_4$ are given in table 8.2.

<u>The 588 KeV transition</u>

This transition is fed by the 252 KeV $\beta$ transition and has been analysed in terms of the beta decay multipolarities using the known $F_K$ coefficients of the E2, $4^+ \longrightarrow 2^+$, gamma transition. The analysis is very similar to that performed for the 468 KeV transition, giving the identical result that a pure $\gamma_\beta = 1$ beta decay multipolarity can explain the nuclear orientation results. The experimental data is shown in Fig.8.5 with the anisotropy vs. temperature curve for a pure $\gamma_\beta = 1$ beta decay.

FIG 8·6


10%
5%
484 keV
1/T °K
20
30
40
50
60
70
80
-5%
588 keV
$J_\beta = 1$ only
-10%
-15%
-20%
W(0) -1
-25%
-30%

The 297 KeV transition

This transition shows very small nuclear orientation anisotropies over the temperature range provided by the chrome alum salt demagnetisation. The analysis of the spectrum at this energy is complicated by the large temperature variation of the background level under this peak from the degraded radiation from higher energy gamma rays. The resolution of the Ge(Li) detector gives a peak width of only 2.5 channels at 300 KeV when the energy range from 250 KeV to 1500 KeV is accumulated into 1024 channels. Although the integral linearity of the multichannel analyser ts good to better than 1%; the energy window associated with each channel is only guaranteed to be constant to 10%. The variation in this differential linearity can produce significant errors when subtracting an equal number of channels of background from a narrow peak, particularly when the background level is comparable with the peak intensity and shows large anisotropies. This will explain why the data shows more than statistical fluctuations. The data shown in Fig.8.3 is consistent with a value of $\delta$(M1/E2) of $+10.0 \pm 2.0$ with the associated decay parameters

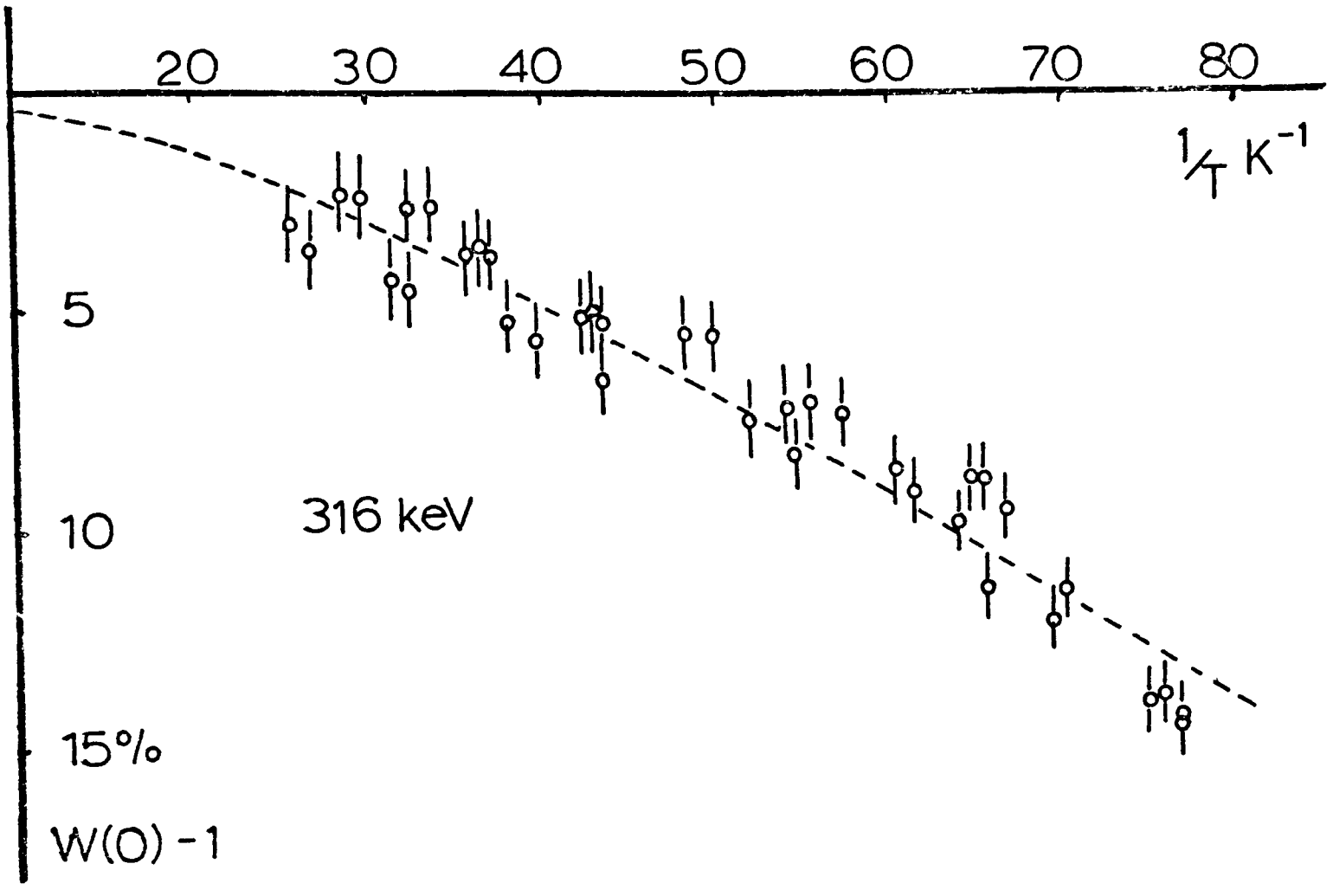
$$U_2F_2 = -0.05(2) \quad U_4F_4 = +0.08\ (4)$$

The 612 KeV and 316 KeV transitions

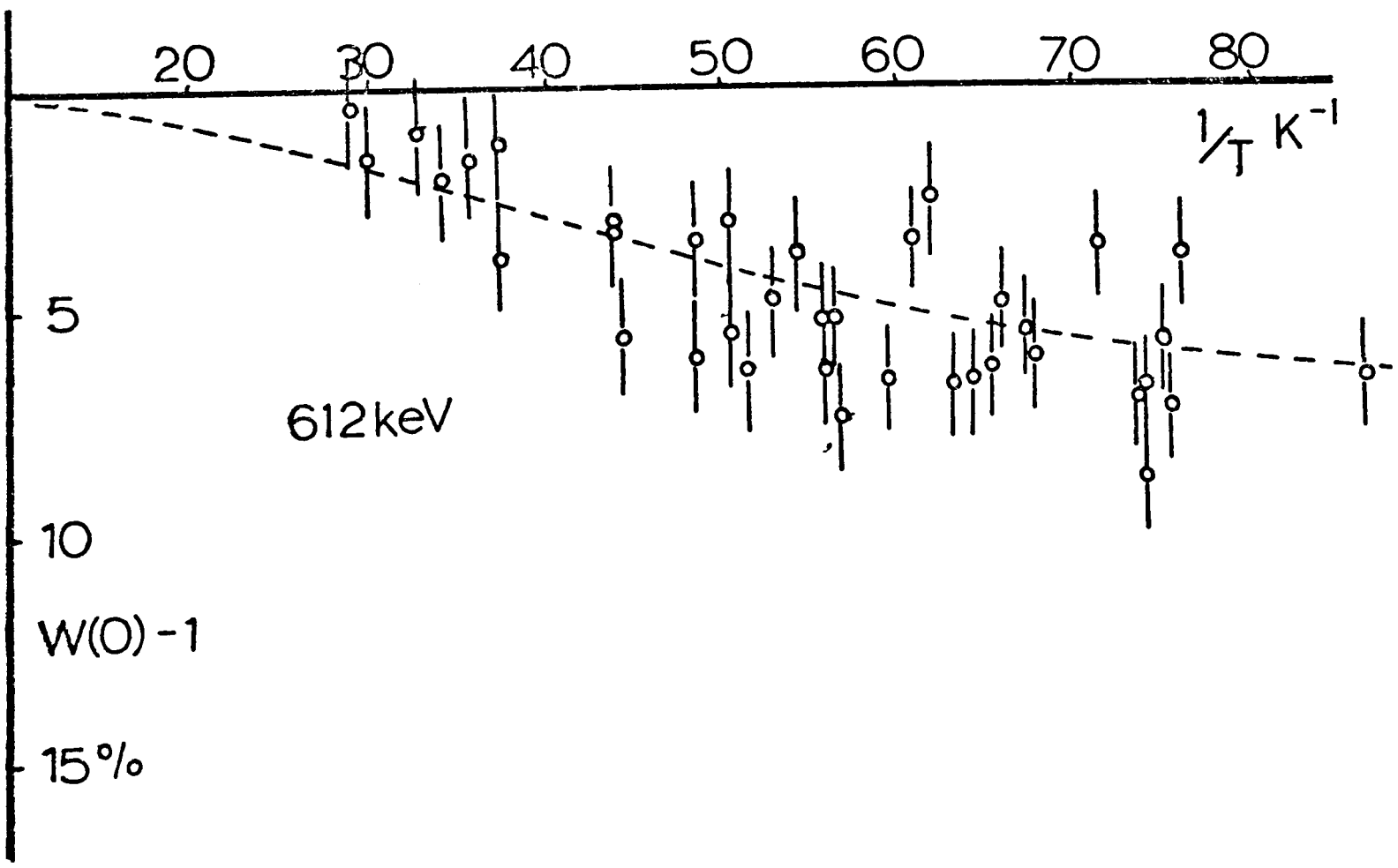
Both of these transitions have a pure E2 multipolarity, associated with the $2^+ \rightarrow 0^+$ transitions. The data from the nuclear orientation in nickel for these two gamma-rays is fitted with no free parameters; the $U_K$ coefficients are defined by the multipolarities already found for the previous gamma transitions, and the $F_K$ coefficients are known.

The details of the feeds to these transitions have been discussed in detail by Reid et al [95], only a brief summary being included in Table 8.2.

FIG 8·7




Fit to orientation data with no free parameters



The comparison of the experimental data with the calculated anisotropies is shown in Fig.8.6. The good agreement of the calculated anisotropies with the data confirms the general internal consistency of the analysis for the 588, 308 and 604 transitions, but, because the first is a pure E2, and the two latter transitions are predominantly E2 in character, the anisotropies of the 316 KeV and 612 KeV gamma-rays are not sensitive to changes in the values of $\delta$. This is because the $U_K$ coefficients do not contain a mixed term in $\delta$, and therefore for values of $\delta$ greater than 3, will be heavily weighted by $\delta^2$ towards the value for $U_K(E2)$.

The 484 transition in $^{192}$Os

This is the strongest transition in the $^{192}$Os branch of the decay and is fed directly by the $4^+ \rightarrow 3^+$ beta decay. The gamma transition itself is a $3^+ \rightarrow 2^+$ transition of E2/M1 character although the angular correlation results have tended to show predominantly E2 character. The larger log (ft) value for the beta decay compared with those to the $^{192}$Pt branch indicates the possibility of an admixture of the higher multipolarities associated with third forbidden transitions in the $\beta$ decay. The assumption of pure $\gamma_\beta = 1$ for the $\beta$ decay is therefore not as well justified as for the $4^-$ to $3^+$ $\beta$ decay in the $^{192}$Pt branch. The positive sign of the anisotropies shown by this gamma-ray indicates a mixed transition with a +ve sign for $\delta$. Allowing for the uncertainty in the $\beta$ decay feed decay coefficients the most probable value suggested by the data is in the range.

$$\delta = +8.0 \pm 0.5 \text{ for } \gamma_\beta = 1$$

to $$\delta = +7.0 \pm 0.5 \quad \text{for } \Delta^2\left(\gamma_{\beta=1} / \gamma_{\beta=2}\right) = 1$$

Table 8.2

| gamma-ray energy KeV | | experimental values for the orientation parameters $Q_2U_2F_2$ | $Q_4U_4F_4$ | Feeds |
|---|---|---|---|---|
| 296 | $2^+ \rightarrow 2^+$ | -0.050(20) | +0.080(40) | 12% (588), 88% (308) |
| 308 | $3^+ \rightarrow 2^+$ | -0.295(20) | +0.430(50) | 536KeV β decay $\delta_\beta$ = 1 only |
| 316* | $2^+ \rightarrow 0^+$ | -0.205 | -0.038 | 34.4% (296), 56.7% (468), 8.9% (604) |
| 468 | $4^+ \rightarrow 2^+$ | -0.363(10) | -0.130(30) | 669KeV β, $\delta_\beta$ = 1 only |
| 485 | $3^+ \rightarrow 2^+$ | +0.095(15) | +0.350(40) | $^{192}$Os branch $\delta_\beta$ = 1 only |
| 588 | $4^+ \rightarrow 2^+$ | -0.363(10) | -0.130(30) | 252 KeV β decay $\delta_\beta$ = 1 only |
| 604 | $3^+ \rightarrow 2^+$ | +0.610(10) | +0.300(30) | 536 KeV β $\delta_\beta$ = 1 only |
| 612* | $2^+ \rightarrow 0^+$ | -0.132 | +0.327 | 12% (588), 88% (308) |

* calculated values from multipolarity assignments of preceding gamma transitions

## 8.6 Comparison with other measurements and theoretical estimates

The nuclei in the mass range $180 < A < 200$ lie in a transition region where the equilibrium nuclear structure changes from one showing large deformations to the spherical structure near the doubly magic $^{208}Pb$. The transition from deformed to spherical nuclear shape is a gradual one with a slow change in the properties of these nuclei. An important aspect of the study of nuclei in this range has been the theoretical and experimental study of the excited states and the gamma transitions between them. In general, the gamma transitions between the lower excited states of heavy even-even nuclei are of a collective nature, with the electric quadrupole (E2) matrix element dominant over any magnetic dipole matrix element, in any gamma decay allowed by the angular momentum selection rules. The measurement of M1 admixtures into such gamma decays, between excited states, has shown however, that the states cannot be represented by a simple harmonic oscillator model. As mentioned in chapter three, the most successful model in explaining the observed M1 admixtures and quadrupole moments in these nuclei has been the pairing-plus-quadrupole model proposed by Kumar and Baranger. A detailed description of this model is beyond the scope of this thesis, but the basis of the calculations is the addition of residual pairing and quadrupole interactions to spherically symmetric independent particle wavefunctions. The variables are the proton and neutron pairing force strengths, estimated from odd-even mass differences, and the quadrupole force strengths. The magnitudes and signs of E2 and M1 transition matrix elements have been calculated by Kumar [103] in terms of matrix elements of the Bohr-Mottelson [114] multipole operators. The results of these calculations for the observed transitions in the decay of $^{192}Ir$ are shown in the last column of Table 8.3. Also included in table 8.3 are the measurements of $\delta$ from angular correlation measurements, K-conversion measurements and the previous nuclear orientation experiment of $Fe(^{192}Ir)$, although these measurement are suspect because the wrong hyperfine interaction was used.

Table 8.3 Comparison of measurements of the M1/E2 mixing ratios in $^{192}$Pt with theoretical estimates

| gamma energy KeV | Nuclear orientation | | γ-γ correlation | | | β-γ | K-conversion | Theory |
|---|---|---|---|---|---|---|---|---|
| | This work | Reid et al | (a) | (b) | (c) | (d) | (e) | (f) Kumar & Baranger |
| 296 | $-10.0 \pm 2.0$ | $+15^{+10}_{-5}$ | -9.0 to -11.0 | $-9.1^{+2.7}_{-1.7}$ | | | | -14.8 |
| 308 | $-8.0 \pm 0.8$* | $-7.3 \pm 0.2$ | -6.5 to -8.3 | $-9.9 \pm 1.0$ | $-6.3^{+0.5}_{-0.6}$ | | | - 9.2 |
| 468 | | | | | | | | |
| 484 | $+8.0 \pm 0.5$* | | | $+10.9^{+2.1}_{-1.5}$ | | | | + 4.8 |
| 588 | | | | | | | | |
| 604 | $2.1 \pm 0.1$* | +1.5-0.1 | +1.9 to 2.4 | $+2.1^{+0.3}_{-0.2}$ | $+2.5 \pm 0.2$ | $+3.0^{+1.2}_{-0.9}$ | $\delta = 1.57 \pm 0.08$ | +2.2 |
| 612 | | | | | | | | |

* assuming $\gamma_\beta = 1$ for the preceding β decay.

a) W.D.Hamilton and K.E.Davis Nucl Phys 122A 165 1969

b) Z.W.Grabowski Phys Rev 183 1019 1969

c) R.Berand, I.Berkes, R.Chiry, R.Harontunian, M.Levy, G.Morguier, G.Marest Phys Rev.C1 303 1970

d) J.W.Senbert and R.G.Wilkinson Phys Rev C Vol.2 721 1970

e) J.B.Willet and G.T.Emery International conference on Radioactivity in Nuclear spectroscopy (to be published)

f) Values from the pariing-plus-quadrupole model of Kumar and Baranger quoted by Grabowski

in the analysis.

The two transitions of greatest interest are the 604 KeV transition and the 297 KeV transition. The 604 KeV transition has been studied extensively by $\gamma-\gamma$ angular correlation and $\beta-\gamma$ angular correlation. The measurements all fall in the range 1.9 to 3.0 with a weighted mean of about 2.2. The orientation measurements on $^{192}$Ir in nickel described here give a value of $\delta = +2.1 \pm 0.1$ in very good agreement with the correlation measurements and the prediction of $\delta = +2.2$ on the Kumar and Baranger model. The value of $+1.5 \pm 0.1$ from the nuclear orientation measurements on $^{192}$Ir in iron is explained by the incorrect estimate for the hyperfine interaction and the poor alloy structure.

The results for the , $2^+ \rightarrow 2^+$, 296 KeV gamma-ray are generally smaller than the prediction of Kumar, but the very small nuclear orientation effects, and the problems involved in the gamma-ray spectroscopy make a more accurate experiment by nuclear orientation very difficult.

The measurements on the other $3^+ \rightarrow 2^+$ transition in $^{192}$Pt at 308 KeV are very near the model predictions, and consistent with the latest nuclear orientation measurements and $\gamma-\gamma$ correlation results.

Only two measurements of the mixing ratios of the 484 KeV transition in $^{192}$Os have been made. The result from this experiment of +8.0(0.5) is consistent with the value of $+10.9^{+2.1}_{-1.5}$ found by Grabowski et al, but both measurements are considerably higher than the predicted value of +4.8, although the sign of $\delta$ is in agreement with this prediction.

## 8.7 The Hyperfine interaction of $^{192}$Ir in iron

The nuclear orientation measurements on $^{192}$Ir in a nickel host give values for the decay parameters of all the gamma-rays, which can then be used to study the distribution of hyperfine fields shown by the nuclear orientation measurements in an iron host. The two models discussed in section 8.2 will give different temperature dependencies to the observed gamma-ray anisotropies, and, by comparing the anisotropies with the predictions of these models, some light may be thrown on the problems of nuclear orientation with such alloys.

The sample used in the nuclear orientation measurements of Reid et al was a 1% iridium/iron alloy, annealed at 1100°C after irradiation. With such a high concentration of iridium, a microscopic inhomogeneity may easily arise through such a mechanism as that proposed by Crabowski. A simple model for such an alloy would be to assume, as for the silver/iron alloys, that only a fixed proportion, X, of the impurity atoms experience the full hyperfine field on substitutional sites, with the remainder seeing only a very small field. This simple model does not, however, produce the observed temperature dependence for all the gamma transitions in iron, when the same factor, of X = 0.88, attenuates both the $Q_2U_2F_2$ and $Q_4U_4F_4$ terms. A detailed analysis on such a model would seem to require a continuous distribution of hyperfine fields about a mean value of 1150 kOe, compared with the NMR measurement of 140kOe. The shape of the temperature dependence of the observed anisotropies is not sensitive to the form of this distribution, but a unique field at all the impurity nuclei does not produce an adequate representation of the results.

The alternative approach, following the lead of Ben-Zvi et al, would be to consider the hyperfine fields at the iridium nuclei to be distributed along a range of conical generators making an angle $\theta$ with the applied field direction with a mean value of $\theta$ of $\theta_m$. The attenuation in the nuclear orientation effects then arises from the deviation of $P_2$ and $P_4$ from their values of 1.000 when $\theta = 0$. The angular dependence of these two parameters shows that the value of $P_4$ will fall off three times as rapidly as the $P_2$ value. The independent least squares fits for $Q_2U_2F_2$ and $Q_4U_4F_4$ with the $\underline{Fe}^{192}Ir$ data on the 468 KeV, 316KeV and 588 KeV gamma rays indicate that the attenuation of $U_2F_2$ is of the order of 0.82 (3) and the attenuation on $U_4F_4$ of the order of 0.92(5); not consistent with any unique value of $\theta_m$. These results suggest that such a model is not appropriate for iridium/iron alloys at the applied field of 5kOe.

The best description of the iron alloy from this analysis would therefore appear to involve a continuous distribution of hyperfine field from the nuclear magnetic resonance value of 1408 KOe [97] downwards, with a mean value around 1150kOe, probably associated with clustering of the iridium impurity, with an associated reduction in the magnitude of the hyperfine interaction. This clearly demonstrates the dangers of using alloys showing a non-substitutional distribution of impurities in hyperfine interaction and gamma-ray mixing ratio measurements.

## Appendix A

## Least squares fitting for $Q_2U_2F_2$ and $Q_4U_4F_4$ to gamma-ray anisotropy data with a known hyperfine interaction

The basis of this technique, described briefly in chapter three, and used for the analysis of the nuclear orientation measurements on $^{110}Ag^m$ and $^{192}Ir$, is the extension of the standard least squares fitting technique for the establishment of the plane, in the space defined by W(O), $B_2$ and $B_4$, about which the experimental measurements are distributed. This plane will show differential gradients, $W(O)/B_2$, and $W(O)/B_4$, equal to the appropriate values of $Q_2U_2F_2$ and $Q_4U_4F_4$. The programme used, minimises the value of the sum of the squares of the deviations of the experimental points from such planes, using the experimental values of W(O), and computed values for $B_2$ and $B_4$ calculated by an auxilary subroutine for each temperature measurement, and the known hyperfine interaction. Each point is weighted by a factor representing the length of time for which the spectrum was accumulated, to include the fact that the accuracy of each measurement is proportional to the square root of the number of counts in each peak. The temperature measurements from the $^{60}Co$ in iron thermometer all give a similar accuracy in 1/T over the range $1/T = 30K^{-1}$ to $1/T = 140K^{-1}$, therefore no additional weighting is included as a function of the temperature. Outside this range of temperature the accuracy of the measurements from the Fe $^{60}Co$ thermometer is reduced, because of saturation of the orientation at low temperatures, and the samll gamma-ray anisotropies at the higher temperatures.

The least squares fitting procedure involves the calculation of the following summations over all the measurements (i)

$$a = \sum_i W(0)_i \, B2_i \, m_i \; ; \quad b = \sum_i W(0)_i \, B_{4i} \, m_i \; ; \quad c = \sum_i B2_i^2 \, m_i \; ;$$

$$d = \sum B4_i^2 \, m_i \; ; \quad e = \sum_i B2_i \, B4_i \, m_i \; ; \quad f = \sum_i W(0)_i^2 \, m_i ;$$

$$g = \sum_i B2_i \, m_i \; ; \quad h = \sum_i B4_i \, m_i \; ; \quad j = \sum_i m_i$$

where $m_i$ is the weighting factor for each measurement. The values of $Q_2U_2F_2$ and $Q_4U_4F_4$ are then given by the expressions

$$Q_2U_2F_2 = \frac{(ad - be)}{(cd - e^2)} \qquad Q_4U_4F_4 = \frac{(bc - ae)}{(cd - e^3)}$$

The errors are calculated from t he scatter of the experimental points about the best fit plane, not from the standard deviation calculated from the gamma ray count-rate. This method includes the errors in 1/T and allows for the larger errors involved when a large background level is subtracted from the peak. The errors on $Q_2U_2F_2$ and $Q_4U_4F_4$ are calculated independently; for each variable the best fit value of the other is assumed and the error calculated on the basis of all the scatter of the data points giving an uncertainly to the one variable. This method does of course not allow for errors associated with co-operative deviations of $Q_2U_2F_2$ and $Q_4U_4F_4$ from the L.s.f. values, in the sense that a reduction in $Q_2U_2F_2$ and an increase in $Q_4U_4F_4$ can give similar anisotropies, but for a large temperature range the fit is sensitive to $Q_2U_2F_2$ and $Q_4U_4F_4$ independently. The errors estimated were always consistent with the constraint imposed between $Q_2U_2F_2$ and $Q_4U_4F_4$ by a single value of $\delta$, for mixed transitions. One standard deviation on the two variables is given by the following expressions.

$$\sigma_{Q_2U_2F_2} = \frac{i\sqrt{|f-K|}}{g(N-1)} \quad ; \sigma_{Q_4U_4F_4} = i\frac{\sqrt{|f-K|}}{h(N-1)}$$

where $K = [2(Q_4U_4F_4)b + 2(\Delta_2U_2F_2)a - 2(Q_2U_2F_2)(Q_4U_4F_4)e$

$$- (Q_2U_2F_2)^2\, c - (Q_4U_4F_4)^2\, d]$$

The basis of the programme in Focal language is given below.

```
ERASE ALL
C- SK FOCAL

01.01 TYPE ! "WEGHTED LEAST SQUARES FIT FOR J2F2 AND J4F4 " !
01.02 ERASE
01.05 * ; ASK N
01.12 TYPE ! "        W                                B2                        B4
01.20 FOR A=1,1,N; DO 2.00
01.21 SET AA=(ZX*YY-ZY*XY)/(XX*YY-XY↑2)
01.30 SET BB=(ZY*XX-ZX*XY)/(XX*YY-XY↑2)
01.40 SET SZ=(2*BB*ZY+2*AA*ZX-2*AA*BB*XY-AA↑2*XX-BB↑2*YY)
01.42 SET SS=FABS(ZZ-SZ)
01.45 SET SS=FSQT(SS)/(N-1)
01.50 SET SA=(SS*MM)/XB
01.55 SET SB=(SS*MM)/YB
01.70 GOTO 3.15
02.01 CALCULATE SIGMA X↑2,XY,Y↑2,Z↑2,ZX,ZY,,ZX,ZY
02.10 ASK W(A),B2(A),B4(A),T(A),
02.11 TYPE Z,  W(A),"     "B2(A),"      "B4(A),"      "T(A), !
02.15 SET ZX=ZX+(W(A)*B2(A)*T(A))
02.20 SET ZY=ZY+(W(A)*B4(A)*T(A))
02.25 SET XX=XX+(B2(A)↑2*T(A))
02.30 SET YY=YY+(B4(A)↑2*T(A))
02.35 SET XY=XY+(B2(A)*B4(A)*T(A))
02.40 SET ZZ=ZZ+(W(A)↑2*T(A))
02.45 SET XB=XB+(B2(A)*T(A))
02.50 SET YB=YB+(B4(A)*T(A))
02.55 SET MM=MM+(T(A))


03.01 COMMENT- PRINT RESULTS
03.15 TYPE !"J2F2      "AA,"+/-"SA
03.20 TYPE !"J4F4      "BB,"+/-"SB
03.22 FOR A=1,1,N; DO 4.00
04.10 SET E=AA*B2(A)+BB*B4(A)
04.20 TYPE !"BEST FIT TO DATA  "E,"     "A
03.30 *; QUIT
*
```

References

1. Khutsishvili G.R. Sov Phys J.E.T.P. 2 744 1956.
2. Samoilov B.N., Stephanov I.D., and Skylarevskii V.V. Sov.Phys J.E.T.P. 9 448 1383 1959
3. Bloembergen N. and Temmer G.R. Phys Rev 89 883 1953
4. Matthias E. and Holliday R.J. Phys Rev Letters 17 897 1966.
5. Fermi E. Z.Phys 60 320 1930.
6. Watson R.E. and Freeman A.J. Phys Rev 123 2027 1961.
7. Daniel E., and Friedel J., J. Phys Chem Solids 24 1601 1963.
8. Campbell I.A., J Phys C 2 1338 1969.
9. Clogston A.M. Phys Rev 125 439 1962
10. Woolf P.A. Phys Rev 124 1030 1961
11. Kanamori, J. Appl Phys 36 929 1965
12. Shirley, D.A., Rosenblum S.S., and Matthias E., Phys Rev 170 363 1968
13. Abragam A., and Bleaney, B., Electron Paramagnetic resonance of Transition ions' Clarendon Press 1970.
14. Blin-Stoyle R.J. and Grace M.A. Handbuch der Physik 42 555 1958
15. Gray T.P and Matchler G.R. Proc Roy Soc A 68 340 1955
16. Perentz M., and Rosenzweig N. Argonne Nat.Lab Rept A.N.L.-5324 1955
17. Enge H. 'Introduction to nuclear Physics' Addison Wesley 1966
18. Biedenharn L.C. and Rose M.E. Revs Mod Phys 25 729 1953
19. Brink D.M. and Rose H.J. Revs Mod Phys 39 306 1967
20. Fox R.A. and Stone M.J. Phys Letters 29A 341 1969
21. Abragam A. 'The Principles of Nuclear Magnetism' Clarendon Press 1961
22. Barclay J.A., Thesis, Lawrence Radiation Laboratory, Berkeley UCRL 18986 1969
23. Ref 22 and Matthias E, Olsen B., Shirley, D.A., Steffen R.M., and Templeton J.E. Phys Rev A.4 1626 1971.

24. Hartmann-Boutron F and Spanjaard D., Compt.Rend 268B 1260 1969.

25. The calculation of the total anisotropy destruction requires an accurate knowledge of the inhomogeneous linewidth. The resonances shown in Fig.2.6 show 81 ± 3% destruction, and more than 90% has been reported by P.T.Callaghan - Private communication.

26. Spanjaard D., and Hartmann-Boutron, F., Solid State Commun., 8 323 1970

27. Barclay J.A. and Gabriel H., J. Low Temp Phys 4 459 1971

28. Gabriel H., Phys Rev 181 506 1969

29. Abragam A., 'The Principles of Nuclear Magnetism' Clarendon Press 1961

30. Slichter C.P., 'Principles of magnetic resonance' Harper and Row

31. Mendosa, E., Experimental Cryophysics (Hoare, Jackson and Kruti eds) London Butterworths p.192 1961

32. Hall, H. Rev Mod Phys 8 358 1936

33. Yates M.J.L. in Perturbed angular correlations, ed. by E.Karlsson, E.Matthias, and K.Siegbahn (North-Holland Publ.Co.Amsterdam, 1964 p.453

34. Calculated from the formulae of Rose M.E. Phys Rev.91 610 1953

35. Lines. Thesis (BSC) Clarendon Laboratory, Oxford 1964.

36. Rado, G.T. and Suhl, H. 'Magnetism' vol. I Academic Press 1966

37. Sanctuary C.J., Private communication

38. Gerdan, E. and Braunsfurth, J. private communication

39. Shirley D.A. and Westenbarger G.A. Phys Rev 138 A170 1965

40. Campbell I.A. J.Phys C. 2 1338 1969

41. Shirley D.A. and Westenbarger A.G. Phys Rev 137 A 161 1965

42. Hanson 'Constitution of Binary Alloys'.

43. Schmelling, S.G., Ehlers, V.J., and Shugart H.A. Phys Rev 154 1142 1967

44. Crangle, J., and Goodman G.M., Bull Am Phys Soc 15, 269 1970

45. Knott T.F., Andrews, H.R., Cohen E.J., Pipkin F.M. and Santry D.C. Phys. Rev Letters 25 8 1970

46. Cracknell M.F. and Wilson G.V.J., Phys Lett. 20 569 1966

46. Fox R.A., Spanjaard D., and Stone N.J. 'Hyperfine interactions in excited nuclei' vol. 1 ed. G.Goldring and R.Kalish, p.345

48. Munnich F., Fricke K. and Koch J. Z. Physik 181 301 1964

49. Taylor H.W. and Frisken W.R. Phys Rev 114 127 1959

50. Taylor H.W. and Scott S.A. Phys Rev 114 121 1959

51. Newbolt W.B. and Hamilton J.H. Nucl Phys 53 353 1964

52. Moragnes J.A. Reyes-Suter, P., Suter T., Nucl Phys A99 652 1967

53. Korolev A.M. Izv Akad Nauk 555R Ser Fiz 31 1701 1967
[transl: Bull Acad Sci USSR Phys Ser 31 1740 1967]

54. Kumar K and Baranger M. Nucl Phys 92 608 1967; A110, 490 and 529, A122 273 and 241,1968
Phys Rev Letters 17 1146 1966

55. Krane K.S. and Steffen R.M., Phys Rev C 2 724 1970

56. Milner W.T., McGowan, F.K., Stelson P.H., Robinson R.L., Sayer R.O., Nucl. Phys A 129 687 1969

57. Westenbarger G.A., Thesis, Lawrence Radiation Laboratory, University m of California 1964

58. Friedel, J., Nuovo Cim 7 suppl 2 287 1958

59. Anderson, P.W., Phys Rev 124 41 1961

60. Koster, G.F. and Slater J.C., Phys Rev 95 1167 1954

61. Koster, G.F., Phys Rev 95 1436 1954

62. Koster G.F. and Slater J.C., Phys Rev 96 1208 1954

63. Campbell I.A., and Gomes A.A., Proc Phys Soc 91 319 1967

64. Demangeat C., and Gautier F., J.Phys C 3 S 291 1970

65. Koi Y., Tsujimura A., Hihara T., J.Phys Soc Japan 19 1493 1964

66. Campbell I.A. J. Phys C vol.3 2151 1970

67. Collins M.F. and Low G.G. Proc Phys Soc 86 535 1965

68. Riedinger R., J.Phys Chem solids 32 2087 1970

69. Hayashi E, and Shimizu M. J.Phys Soc Japan 26 1396 27, 43 1969

70. Bleaney B.I., a nd Bleaney B. 'Electricity and Magnetism' 2nd Ed. O.U.P

71. Brooks H., Phys Rev 58 909 1940

72. Fletcher G.C., Proc. Phys Soc 67A 505 1954

73. Williams H., Private communication

74. Sternheimer R.M., Phys Rev 84 244 1951, 86 316 1952, 95 736 1954

75. Bohr, A., and Weisskopf V.F. Phys Rev 77, 94 1950

76. Eisinger J., and Jaccarino V., Rev Mod Phys 30 528 1958

77. Bohr A., Phys Rev 81 331 1951

78. Perlow G.J. 'Hyperfine interactions in excited nuclei' Vol 2
ed. G.Goldring and R.Kalish

79. Perlow G.J., Johnson C.E., and Marshall W., Phys Rev 140, 1987 1965

80. Wagner F., and Zahn U., Z.Physik 233 1 1970

81. Wagner F. and Potzel W., 'Hyperfine interactions in excited nuclei'
Vol 2 ed. G.Goldring and R.Kalish

82. Van Der Bout P.A., Ehlers V.J., Nierenberg W.A. and Shugart H.A.
Phys Rev 158 1078 1967

83. Schmeling S., Ehlers V.J., Shugart H.A., Phys Rev 1 1971

84. Williams H., Private communication

85. Clogston

86. Grant R.W., Morton Kaplan, Keller, D.A., and Shirley D.A., Phys Rev.
133 4A 1964

87. Shirley D.A. in 'Hyperfine Interactions and Nuclear Radiations', edited
by E.Matthias and D.A.Shirley (North Holland Publishing Co.
Amsterdam 1968 Appendix B.

88. Houska C.R., Averbach B.L. and Cohen M., Acta Met.8 81 1960

89. Roberts L.D., and Thomson J.O. Phys Rev. 129 664 1963

90. Sanoilov B.N. Sklyarevskii V.V. Gorobchenko V.D. Eksperim Zh.
I.Teor. Fiz. 41 1783 1961; JETP 14 1267 1962

91. Shirley D.A., Phys Lett. 25A 129 1967

92. Campbell I.A., Proc Roy Soc A 311 131 1969

93. Sioshansi P., Garber D.L., King W.C., Scharenberg R.P., Steffen R.M. Wheeler R.M., Phys letters 39B 343 1972

94. Cameron J.A., Campbell I.A., Compton J.P., Lines R.A.G., and Stone N.J., Nucl.Phys 59 475 1964

95. Reid P.G.E., Sott M., and Stone N.J., Nucl Phys A129 2 273 1969

96. Templeton J.T., Thesis Clarendon Laboratory, Oxford 1967

97. Esca G., Hagn E., Butz T., a nd Kienle P., Phys Letters 36B 4 1971

98. Perlow G.J., Henning W., Olson D., and Goodman G.L., Phys Rev.Letters 23 680 1969

99. Miga M., Itoh, J., Saraswati W., J.Phys Soc Japan 31 1843 1971

100. Davies J.J. and Owen J., J.Phys C 2 1405 1969

101. Noya. H., Arima. A., and Horie. H. J. Phys soc Japan Suppl 8 1959

102. Mann J.B., Report LA-3691 Los Alamos Scientific Lab. University of California Los Alamos 1968

103. Kumar K. Phys Letters 29B 25 1969

104. King W.C., Grabowski, Z.W. and Scharenberg R.P., Phys Rev. C4 1382 1971

105. Wittenberger J.D., and Dayananda M.A., J.Appl.Phys 41 840 1970

106. Ben-Zvi I., Gilad P., Goldring G., Hillman P., Schwarzschild A. Vager Z., Phys Rev.Letters 193 373 1967

107. Aharoni A., 'Hyperfine Interactions in excited nuclei', Vol. 1 Ed. G.Goldring and R.Kalish p.75, 1971

108. Nuclear Data sheets, compiled by K.Way et al. National Academy of Sciences - National research council Washington D.C.

109. Table of Isotopes. Lederer C.M., Hollender J.M., Perlman, I. J.Wiley & Sons Inc.

110. Johns M.W., and Kawamura M., Nucl.Phys 61 385 1965

111. Kotani T., and Ross M.H., Phys Rev 113 622 1959

112. Bhattacherjee S.K., Mitra S.K., Jain H.C., Padhi H.C. Phys Rev. 159 1056 1967

113. Senbert J.W., and Wilkinson R.G. Phys Rev C. 2 721 1970

114. Bohr A., and Mottelson B.R., Nuclear Structure (W.A.Benjamin Inc. New York 1969) vol. 1 p.381

115. Marsh.J.D. Thesis, Clarendon Laboratory,Oxford.1971.

116. Spanjaard.D. Private communication.